STUDIES OF ARCTIC MIDDLE ATMOSPHERE CHEMISTRY USING INFRARED ABSORPTION SPECTROSCOPY

by

Rodica Lindenmaier

A thesis submitted in conformity with the requirements
for the degree of Doctor of Philosophy

Graduate Department of Physics
University of Toronto

Studies of Arctic Middle Atmosphere Chemistry using Infrared Absorption Spectroscopy

Rodica Lindenmaier

Doctor of Philosophy

Graduate Department of Physics
University of Toronto

2012

Abstract

The objective of this Ph.D. project is to investigate Arctic middle atmosphere chemistry using solar infrared absorption spectroscopy. These measurements were made at the Polar Environment Atmospheric Research Laboratory (PEARL) at Eureka, Nunavut, which is operated by the Canadian Network for the Detection of Atmospheric Change (CANDAC). This research is part of the CANDAC/PEARL Arctic Middle Atmosphere Chemistry theme and aims to improve our understanding of the processes controlling the stratospheric ozone budget using measurements of the concentrations of stratospheric constituents.

The instrument, a Bruker IFS 125HR Fourier transform infrared (FTIR) spectrometer, has been specifically designed for high-resolution measurements over a broad spectral range and has been used to measure reactive species, source gases, reservoirs, and dynamical tracers at PEARL since August 2006.

The first part of this research focuses on the optimization of ozone retrievals, for which 22 microwindows were studied and compared. The spectral region from 1000 to 1005 cm^{-1} was found to be the most sensitive in both the stratosphere and troposphere, giving the highest number of independent pieces of information and the smallest total error for retrievals at Eureka.

Similar studies were performed in coordination with the Network for the Detection of Atmospheric Composition Change for nine other species, with the goal of improving and harmonizing the retrieval parameters among all Infrared Working Group sites.

Previous satellite validation exercises have identified the highly variable polar conditions of the spring period to be a challenge. In this work, comparisons between the 125HR and ACE-FTS (Atmospheric Chemistry Experiment-Fourier transform spectrometer) from 2007 to 2010 have been used to develop strict criteria that allow the ground and satellite-based instruments to be confidently compared. After applying these criteria, the differences between the two instruments were generally small and in good agreement with previous ground-based FTIR/ACE-FTS comparisons. No clear bias was seen from year-to-year, and, in all cases, the difference between the measurements was within one standard deviation. The mean biases between the ACE-FTS and 125HR partial columns for 2007-2010 were -5.61 to 1.11%, -0.23 to 4.86%, -15.33 to -2.86%, -4.77 to 1.09%, and -0.34 to 5.23% for O_3, HCl, $ClONO_2$, HNO_3, and HF, respectively.

The 125HR measurements and three atmospheric models (CMAM-DAS, GEM-BACH, and SLIMCAT) were used to derive an NO_y partial column data product for Eureka. This data product includes the five primary species NO, NO_2, HNO_3, N_2O_5, and $ClONO_2$ and was used to study the seasonal and interannual variability of NO_y from 2007 to 2010. The NO_y 15-40 km partial column was found to be approximately constant through the sunlit part of the year, with greater variability during the spring. The mean partial column averaged for the spring period was $(2.5\pm0.2)x10^{16}$ molec cm^{-2}, while for the summer, it was $(2.3\pm0.1)x10^{16}$ molec cm^{-2}. The springtime evolution of NO_y and its constituent nitrogen species, was also examined for all four years. The variability of the 5-NO_y partial column was seen to be dominated by that of HNO_3.

The evolution of the individual nitrogen species was found to be consistent with the current understanding of the chemical and dynamical processes that occur in the polar stratosphere.

Unusually low ozone columns were measured at Eureka from mid-February to late March 2011 and compared to the previous 14 years of measurements by the 125HR and its predecessor, Environment Canada's Bomem DA8. The normalized O_3/HF, HCl/HF, and HNO_3/HF ratios, for which the effects of dynamics have been reduced, also showed record minima over this period. The SLIMCAT chemical transport model was used to quantify chemical ozone loss using the passive subtraction method. Chemical ozone depletion inside the vortex above Eureka was estimated to be 35%, which is the largest observed there in the past 15 years.

Acknowledgements

First and foremost I offer my sincerest gratitude to my supervisor, Dr Kim Strong, who has supported me throughout my thesis with her patience and knowledge whilst allowing me the room to work in my own way. I attribute the level of my PhD degree to her encouragement and effort, and without her this thesis, too, would not have been completed or written. One simply could not wish for a better or friendlier supervisor.

I gratefully acknowledge Dr Rebecca Batchelor for her advice, supervision, and crucial contribution, which made her a backbone of this research and this thesis. Her involvement with her originality has triggered and nourished my intellectual maturity, which I will benefit from, for a long time to come. Bec, I am grateful for all your support and hope to keep up our collaboration in the future.

I would also like to acknowledge the Network for the Detection of Atmospheric Composition Change Infrared Working Group members for their advice and their willingness to share their bright thoughts with me, which were very fruitful for shaping my own ideas and research.

Many thanks go to CANDAC leader, Prof. James Drummond for all scientific and financial support that I received over the years while completing my research in the High Arctic at Eureka. I also wish to thank Prof. Kaley Walker for leading the Canadian Arctic ACE Validation Campaigns during which we enriched our Arctic experience, collected so much useful data, and laid the basis for many life-long friendships. Thanks to CANDAC/PEARL Site Manager Pierre Fogal and operators Ashley Harrett, Alexei Khmel, Paul Loewen, Keith MacQuarrie, Oleg Mikhailov, and Matt Okraszewski, for their invaluable assistance in maintaining the Bruker 125HR and for taking measurements. The hospitality and kindness with which we were hosted every time at Environment Canada's Eureka Weather Station were always much appreciated.

Collective and individual acknowledgements are also owed to my colleagues at the University of Toronto, for giving me a pleasant time when working together with them, and for their advice and patience. I don't mention anyone particularly because I am afraid I will forget someone and that would not be right.

I gratefully thank Prof. Ted Shepherd and Prof. Kaley Walker for their constructive comments and their advice during the supervisory committee meetings and on this thesis. I am

Contents

8 Unusually low O_3, HCl, and HNO_3 Total Columns Measured at Eureka in Spring, 2011   157

9 General Conclusions and Perspectives   178

List of Tables

List of Figures

List of Acronyms

AASE Airborne Arctic Stratospheric Experiment

ACE Atmospheric Chemistry Experiment

ACE-FTS ACE-Fourier Transform Spectrometer

AMAC Arctic Middle Atmosphere Chemistry

ARCTAS Arctic Research of the Composition of the Troposphere from Aircraft and Satellites

AVK Averaging Kernel

CALIPSO Cloud-Aerosol Lidar and Infrared Pathfinder Satellite Observation

CANDAC CAnadian Network for the Detection of Atmospheric Change

CCMVal Chemistry-Climate Model Validation Activity for coupled chemistry-climate models

CFC chlorofluorocarbon

CLAES Cryogenic Limb Array Etalon Spectrometer

CMAM-DAS Canadian Middle Atmosphere Model-Data Assimilation System

CRL CANDAC Rayleigh-Mie-Raman Lidar

DMP Derived Meteorological Products

DOFS Degrees of Freedom for Signal

DU Dobson Units

EASOE European Arctic Stratospheric Ozone Experiment

ECMWF European Centre for Medium-Range Weather Forecasts

EESC Equivalent Effective Stratospheric Chlorine

ENVISAT European ENVIronmental SATellite

EPP Energetic Particle Precipitation

FWHH Full Width at Half Height

FTIR Fourier Transform InfraRed

FTS Fourier Transform Spectrometer

GEM-BACH Global Environmental Multiscale model- Belgium Atmospheric CHemistry module

GEOS-5 Goddard Earth Observing System-5

HALOE HALogen Occultation Experiment

HCFC hydroclorofluorocarbon

HgCdTe mercury cadmium telluride

HITRAN HIgh-resolution TRANsmission database

125HR the Bruker IFS 125HR Fourier transform spectrometer

ILAS Improved Limb Atmospheric Spectrometer

ILC InterLayer Correlation

ILS Instrument Line Shape

IMK-IAA Institut für Meteorologie und Klimaforschung and Instituto de Astrofísica de Andalucía

InSb indium antimonide

IPCC Intergovernmental Panel on Climate Change

IPY International Polar Year

IRWG InfraRed Working Group

ISAMS Improved Stratospheric And Mesospheric Sounder

JPL Jet Propulsion Laboratory

LIMS Limb Infrared Monitor of the Stratosphere

LT Local Time

MAP Maximum *A Posteriori* solution

MetO Met Office

MERRA Modern Era Retrospective-analysis for Research and Applications

MIPAS Michelson Interferometer for Passive Atmospheric Sounding

MIR Mid-InfraRed

MLS Microwave Limb Sounder

NASA National Aeronautics and Space Administration

NAT Nitric Acid Trihydrate

NCEP National Center for Environmental Prediction

NDACC Network for the Detection of Atmospheric Composition Change

NDSC Network for the Detection of Stratospheric Change

NH Northern Hemisphere

NIES National Institute for Environmental Studies

NIR Near-InfraRed

NOZE National OZone Expedition

ODP Ozone Depletion Potential

ODS Ozone Depleting Substance

OEM Optical Estimation Method

ØPAL Zero altitude PEARL Auxiliary Laboratory

OPD Optical Path Difference

PARIS-IR Portable Atmospheric Research Interferometric Spectrometer for the Infrared

PEARL Polar Environment Atmospheric Research Laboratory

PEARL-GBS PEARL-Ground-Based Spectrometer

POLARIS Photochemistry of Ozone Loss in the Arctic Region In Summer

PSC Polar Stratospheric Cloud

PV Potential Vorticity

RMS Root-Mean-Square

SAFIRE Surface and Atmospheric Flux, Irradiance and Radiation Extension

SAGE III Stratospheric Aerosol and Gas Experiment III grating spectrometer

SAM II Stratospheric Aerosol Measurement II satellite

SAOZ Système d'Analyse par Observation Zénithales

SCISAT SCIentific SATellite

SESAME Second European Stratospheric Arctic and Mid-latitude Experiment

SH Southern Hemisphere

SLIMCAT Single-Layer Isentropic Model of Chemistry and Transport

SNR Signal-to-Noise Ratio

SOLVE SAGE III Ozone Loss and Validation Experiment

SPARC Stratospheric Processes And their Role in Climate

sPV scaled Potential Vorticity

SSW Sudden Stratospheric Warming

STS Supercooled Ternary Solution

SZA Solar Zenith Angle

TCCON Total Carbon Column Observing Network

THESEO Third European Stratospheric Experiment on Ozone

TOMS Total Ozone Mapping Spectrometer

UARS Upper Atmosphere Research Satellite

UT-GBS University of Toronto Ground-Based Spectrometer

UV UltraViolet

UV-VIS UltraViolet-VISible

VMR Volume Mixing Ratio

WACCM Whole-Atmosphere Community Climate Model

WMO World Meteorological Organization

ZPD Zero Path Difference

Chapter 1

Introduction

The effects of climate change are increasingly evident in the Arctic, and changes are taking place significantly faster than previously thought. Climatologists forecast large changes worldwide, with climate zones shifted or completely disappearing by 2100 [*Williams et al.,* 2007].

The Canadian Network for the Detection of Atmospheric Change (CANDAC) is a network of researchers that established the Polar Environment Atmospheric Research Laboratory (PEARL) in the High Arctic, to address scientific questions raised by the changing climate. One of the main objectives of CANDAC is understanding atmospheric change over the Arctic. Measurements taken from the ground are combined with those from satellites and sondes to give a comprehensive picture of Arctic atmospheric composition, and of how it changes from season to season and from year to year.

Ozone is one of the most important trace gases in the atmosphere. It is a strong absorber of solar ultraviolet (UV) radiation at wavelengths between 200 and 300 nm (Hartley bands) and between 320 and 360 nm (Huggins bands), shielding the surface of Earth from this radiation. Since the presence of ozone in the stratosphere is vital for our existence, its study attracted public interest when it was discovered that anthropogenic activities might lead to a gradual destruction of ozone in the atmosphere. This interest became even more intense when it was discovered that stratospheric ozone levels can drop significantly in the polar regions during the spring period. The following sections describe the history of the 'ozone hole' discovery, and introduce stratospheric dynamics and chemistry needed for understanding springtime chemical ozone depletion and the processes that occur in the polar regions.

1.1 A Review of Polar Ozone Chemistry

Ozone is a naturally occurring substance that was first generated in the laboratory in 1839 by *Schönbein* [1840a, 1840b]. It was recognized as an important component of our atmosphere, as it strongly absorbs solar UV radiation [*Cornu,* 1879; *Hartley,* 1880]. Ozone was intensively studied from the early 1900s [*Fabry and Buisson,* 1913; *Dobson and Harrison,* 1926; *Fabry,* 1950; *Dobson,* 1958; *Brewer and Milford,* 1960] and the first photochemical theory for

formation and destruction of ozone was proposed by *Chapman* [1930]. This theory was based on an oxygen-only chemical scheme. In the following decades, it was discovered that stratospheric ozone was also chemically destroyed by reaction with hydrogen [*Bates and Nicolet,* 1950; *Hampson,* 1964] and nitrogen oxides [*Crutzen,* 1970, 1971; *Johnston,* 1971]. Hydrogen and nitrogen oxides can destroy odd oxygen through catalytic reactions in which the initiating active species (e.g., OH, NO) are regenerated. This means that even small amounts of these gases can significantly deplete ozone.

Later, scientists showed that chlorine [*Molina and Rowland,* 1974; *Rowland and Molina* 1975; *Stolarski and Cicerone,* 1974] and bromine [*Wofsy et al.,* 1975; *Yung et al.,* 1980; *McElroy et al.,* 1986] can also contribute to ozone destruction in the atmosphere through catalytic cycles similar to the nitrogen and hydrogen oxides. A very important step was the discovery that the anthropogenic chlorofluorocarbons (CFCs) are a major source of ozone-destroying stratospheric chlorine [*Molina and Rowland,* 1974]. The predictions for the following 50-100 years estimated at that time a global ozone loss of 5-19% [*Wuebbles,* 1983; *Cicerone et al.,* 1983; *Prather et al.,* 1984] but none predicted that the Antarctic stratosphere was more likely than any other place on the globe to experience ozone depletion.

1.1.1 Antarctic Ozone Depletion

The significant ozone depletion discovered at the British Antarctic Survey station at Halley Bay in the Antarctic spring stratosphere was first presented and documented by *Farman et al.* [1985]. The observed ozone destruction was unanticipated at that time and the study suggested that it is confined to the spring season and to southern polar latitudes. These first results were quickly confirmed by space-based measurements [*Stolarski et al.,* 1986; *Schoeberl et al.,* 1986] and by observations at other Antarctic sites [e.g., *Komhyr et al.,* 1986]. The satellite measurements showed that the seasonal depletion of springtime ozone extended over the entire continent, and the phenomenon started to be referred as the ozone 'hole' [*Krueger et al.,* 1987]. The Total Ozone Mapping Spectrometer (TOMS) program provided unique and valuable information about the geographical extent of the ozone hole over the Antarctic, and monitored its year-to-year evolution [*Stolarski et al.,* 1986]. Field campaigns were subsequently organized to study the chemistry of the Antarctic stratosphere.

The National Ozone Expedition (NOZE) in 1986 was the first major field campaign whose goal was to measure as many ozone-related chemical constituents as possible in the

Antarctic atmosphere using balloons [*Hofmann et al., 1987; Hofmann, 1988*] and ground-based measurements [*Farmer et al., 1987; Mount et al., 1987; Solomon et al., 1987a,b; Murcray et al., 1989*]. Measurements of chlorine species showed greatly enhanced ClO in the lower stratosphere (near 20 km, the observations suggested mixing ratios about 100 times greater than the 10 pptv predicted by gas phase photochemical theory) [*de Zafra et al., 1987; Farmer et al., 1987; Solomon et al., 1987a,b*], supporting the ozone depletion theory of *Farman et al.* [1985] and *Solomon et al.* [1986]. This theory suggested that HCl and $ClONO_2$ might react on the surface of 'polar stratospheric clouds' (PSCs), perturbing the gas phase chlorine in a way that could greatly accelerate ozone loss in the Arctic lower stratosphere.

The term 'polar stratospheric clouds' was introduced by *McCormick et al.* [1982], who observed high-latitude clouds in the Arctic and Antarctic stratospheres using Stratospheric Aerosol Measurement (SAM) II satellite measurements. These clouds occurred between ~12 and 25 km and were associated with cold temperatures, below ~200 K, and they constituted the key to the theory for ozone depletion. Through heterogeneous reactions on their surfaces, HCl and $ClONO_2$ would release Cl_2 and would suppress the concentration of NO_2 by forming HNO_3, so that the ClO thereby released could not reform to the $ClONO_2$ reservoir. Sunlight was required to release Cl, so ozone depletion could occur when air was cold and also sunlit. To support this theory, observations of PSCs, low amounts of NO_2 [*Noxon, 1978; Fahey et al., 1989a*] and enhanced amounts of HNO_3 measured in the polar regions [*Murcray et al., 1975; Williams et al., 1982*] and the vertical profile of the ozone depletion based on the Japanese measurements at the Syowa Station [*Chubachi et al., 1984*] were cited as evidence. The dehydration of the Antarctic atmosphere [*Kelly et al., 1989*] and its denitrification [*Fahey et al., 1989a; Wahner et al., 1989a*] were thought to be related to the solid nitric acid trihydrate and ice composition of the PSCs [*Toon et al., 1986; Hamill et al., 1986; Ramaswamy, 1988; Fahey et al., 1989a; Kinne et al., 1989*]. Based on observations, it was shown that gas phase reactive nitrogen (NO_y) [Fahey et al., 1989b] and water vapour [Kelly et al., 1989] are strongly depleted in the Antarctic stratosphere, as a consequence of sedimentation of large PSC particles.

While more ground-based measurements followed in the spring of 1987 [*Hofmann et al., 1989; Kuester et al., 1989; Carroll et al., 1989; Jaramillo et al., 1989*], supplemented with data collected from the Airborne Antarctic Ozone Experiment [*Special Edition, 1989a,b; Tuck et al., 1989; Kelly et al., 1989*], a broad range of models probed the ozone depletion theory. Two-dimensional [*Isaksen and Stordal, 1986; Chipperfield and Pyle, 1988; Brasseur and Hitchman,*

1988; *Ko et al.,* 1989; *Rodriguez et al.,* 1989; *Tie et al.,* 1997], three-dimensional [*Cariolle et al.,* 1990; *Austin et al.,* 1992; *Brasseur et al.,* 1997], and trajectory and Lagrangian studies [*Jones et al.,* 1989; *Schoeberl et al.,* 1993a] presented numerical analyses of calculated ozone trends, trying to simulate accurately the chemical perturbations occurring in the Antarctic vortex, which forms in the polar winter stratosphere.

Intensive laboratory studies helped to confirm the chemical reactions that lead to ozone destruction. *Hanson and Mauersberger* [1988] confirmed the thermodynamic stability of nitric acid trihydrate (NAT) at temperatures well above the frost point. It was also confirmed that rapid heterogeneous processes take place on surfaces similar to those present in the polar regions [*Somorjai,* 1994]. A review of the thermodynamic principles behind stratospheric heterogeneous chemistry was given by *Fairbrother et al.* [1997]. *Molina et al.* [1987] and *Tolbert et al.* [1987] carried out the first laboratory studies of stratospheric reactions on ice, and confirmed that the reaction of HCl with $ClONO_2$ takes place on water ice films. *Hanson and Ravishankara* [1994] demonstrated that the reaction is partially due to $HOCl + HCl \rightarrow Cl_2 + H_2O$, which follows the surface reaction $ClONO_2 + H_2O \rightarrow HOCl + HNO_3$. The reaction of HCl with $ClONO_2$ on NAT ice surfaces was further investigated in the laboratory, showing that its rate depended on the HCl partial pressure and the water content of the NAT surface [*Leu,* 1988; *Abbatt et al.,* 1992; *Hanson and Ravishankara,* 1993; *Peter,* 1997; *Carslaw and Peter,* 1997]. The heterogeneous reactions between bromine and chlorine that contribute to chlorine activation were also investigated [*Hanson and Ravishankara,* 1995; *Danilin and McConnell,* 1995].

1.1.2 Arctic Ozone Depletion

The question of whether similar ozone depletion was occuring in the Arctic soon arose. Measurements meant to elucidate how things happen in the northern hemisphere began in winter 1987/1988. Full moon near-UV measurements of OClO [*Solomon,* 1988] and scattered sunlight and direct moon observations of O_3 and NO_2 [*Mount et al.,* 1988] confirmed that the Arctic stratosphere was also perturbed and that ozone loss in the northern hemisphere was likely to happen. It is important to note here that differences in the pre-1970s ozone abundances in the polar vortices of southern hemisphere (SH) and northern hemisphere (NH) were first identified by *Dobson* [1968]. He attributed this to differences in atmospheric waves and circulation patterns, showing that the NH polar vortex is more disturbed by atmospheric waves forced by flow over a more variable surface topography. We now know that as a result, greater mixing and

faster downward motion take place in the NH compared to the SH, both increasing the natural wintertime Arctic ozone abundances and warming the lower stratosphere through adiabatic compression. The Arctic ozone depletion was likely to be smaller, fewer PSCs were expected in these conditions (as documented by *McCormick et al.* [1982]), and earlier (in the season) stratospheric warmings were anticipated in the north than in the south [*Pyle et al.,* 1992].

Direct observations of chemical species similar to those made in the Antarctic have shown that heterogeneous chemistry perturbs the composition of the Arctic vortex. Measurements of enhanced OClO [*Solomon et al.,* 1988; *Schiller et al.,* 1990; *Pommereau and Piquard,* 1994a; *Perner et al.,* 1994; *Pfeilsticker and Platt,* 1994] and ClO [*Brune et al.,* 1990, 1991; *Toohey et al.,* 1993; *Waters et al.,* 1993; *Bell et al.,* 1994; *Crewel et al.,* 1994; *de Zafra et al.,* 1994; *Shindell et al.,* 1994; *Donovan et al.,* 1997] were evidence of winter chlorine activation. The chlorine activation on the surface of PSCs was supported by the measured column abundances of HCl and HF [*Mankin et al.,* 1990; *Toon et al.,* 1994; *Traub et al.,* 1994]. The HCl measurements were compared to those of ClO and ClONO$_2$, strengthening the link between the enhanced ClO and conversion from its reservoirs [*Webster et al.,* 1993; *Michelsen et al.,* 1999] and displaying evidence for heterogeneous reactions on PSCs [*von Clarmann et al.,* 1993; *Adrian et al.,* 1994; *Oelhaf et al.,* 1994; *Roche et al.,* 1994; *Geller et al.,* 1995; *Yudin et al.,* 1997]. Simultaneous in situ and space-based observations of ClO and PSCs, combined with trajectory studies, further connected the reactive chlorine to heterogeneous chemistry [*Jones et al.,* 1990, *Yudin et al.,* 1997; *Dessler et al.,* 1998], confirming and strengthening the same general fingerprints of the processes observed in the Antarctic.

During the first major Arctic campaign, the Airborne Arctic Stratospheric Experiment (AASE), the PSCs were studied intensively [*Kruger,* 1990; *Hofmann,* 1990]. It was shown that PSC type I (known today to be formed by small, HNO$_3$-rich particles) and PSC type II (composed primarily of large H$_2$O-ice particles and minor amounts of HNO$_3$ as hydrates) were both present [*Browell et al.,* 1990; *McCormick et al.,* 1990]. At that time, the composition of the PSCs was not well understood. Type I PSCs were classified into two forms: those containing solid particles (nitric acid trihydrate) and those containing liquid particles (supercooled ternary solutions of nitric acid, sulfuric acid and water) [Browell et al., 1990; *Toon et al.,* 1990b]. Sporadic and limited denitrification and dehydration were also observed (in contrast with the Antarctic) [*Fahey et al.,* 1990b; *Kawa et al.,* 1990; *Khattatov et al,* 1994; *Kondo et al.,* 1994; *Oelhaf et al.,* 1994; *Rinsland et al.,* 1996; *Arnold et al.,* 1998], and in some cases denitrification

was seen without accompanying dehydration. This raised new questions regarding the mechanism of the denitrification process [*Toon et al.,* 1990a; *Gandrud et al.,* 1990; *Salawitch et al.,* 1989; *Koop et al.,* 1995]. Another contrast to the Antarctic was the rapid formation of $ClONO_2$ (consistent with the ClO decrease) by recombination of ClO with NO_2. NO_2 was photochemically released from HNO_3, after its release from the type I PSCs upon their evaporation [*Schoeberl et al.,* 1993; *Webster et al.,* 1993]. In the Antarctic, the active chlorine was seen to convert into HCl through reaction with CH_4, since nitrogen was lost by denitrification [*Toohey et al.,* 1993; *Webster et al.,* 1993].

The European Arctic Stratospheric Ozone Experiment (EASOE) measurement campaign was organized in the period November 1991 to April 1992 [*Pyle et al.,* 1994] to improve the understanding of ozone destruction in and around high northern latitudes. This was followed by other campaigns: the Second European Stratospheric Arctic and Mid-Latitude Experiment (SESAME) between 1994 and 1995, the Improved Limb Atmospheric Spectrometer (ILAS) validation balloon campaign in February-March 1997, and two major field experiments, the SAGE III Ozone Loss and Validation Experiment (SOLVE) and the Third European Stratospheric Experiment on Ozone (THESEO-2000), between 1999 and 2000. Detailed vertical profile information was obtained from balloon-borne in situ measurements for chlorine, bromine and nitrogen species [*Arnold and Spreng,* 1994; *Fabian et al.,* 1994; *Kondo et al.,* 1994; *Murcray et al.,* 1994; *Pommereau and Piquard,* 1994a,b; *Schmidt et al.,* 1994]. Measurements made by aircraft instruments provided column amounts of O_3, HCl, ClO, and HNO_3 [*Blom et al.,* 1994; *Crewell et al.,* 1994]. From the ground, millimeter-wave emission measurements [*de Zafra et al.*, 1994; *Emmons et al.,* 1994], lidar observations [*Beyerle and Neuber,* 1994; *Neuber et al.,* 1994], UV-visible spectroscopic measurements [*Fish et al.,* 1994; *Goutail et al.,* 1994], and Fourier transform infrared spectrometer measurements [*Notholt,* 1994; *Notholt et al.,* 1993, 1994, 1995a,b, 1997a,b] were made to further address questions of ozone chemistry in the Arctic.

Satellite measurements were very useful in assessing the geographical extent of these processes. Of particular note is the Upper Atmosphere Research Satellite (UARS), launched in 1991 [*Reber et al.,* 1993], which carried the Microwave Limb Sounder (MLS) to measure O_3, ClO, H_2O, HNO_3, temperature, and pressure using thermal emission techniques [*Barath et al.,* 1993]. The Cryogenic Limb Array Etalon Spectrometer (CLAES) onboard UARS was able to measure temperature, pressure, O_3, CH_4, H_2O, N_2O, NO, NO_2, N_2O_5, $ClONO_2$, CCl_3F, CCl_2F_2, and aerosol absorption coefficients using infrared emission interferometry [*Roche et al.,* 1993].

The Improved Stratospheric And Mesospheric Sounder (ISAMS) measured CO, CO_2, CH_4, NO, N_2O, NO_2, N_2O_5, HNO_3, and H_2O using pressure modulator radiometry [*Taylor et al.,* 1993]. The HALogen Occultation Experiment (HALOE) measured the vertical profiles of O_3, HCl, HF, CH_4, H_2O, NO, and NO_2, and also aerosol extinction, temperature and pressure by using the solar occultation technique [*Russell et al.,* 1993]. These four instruments provided a large quantity of information on these trace gases from 80ºN to 80ºS, these observations being used for many studies of stratospheric processes [e.g., *Dessler et al.,* 1998; *Santee et al.,* 1996, 1998].

The international Network for the Detection of Stratospheric Change (NDSC) was initiated in 1991, to observe and measure ozone, ozone-related chemicals, and meteorological variables, primarily at a globally distributed set of ground-based remote-sensing stations (including the polar regions) [*Kurylo and Solomon,* 1990; *Kurylo and Zander,* 2000]. NDSC instruments continued to monitor stratospheric ozone and related trace gases, the polar meteorological conditions occurring each year during winter-spring in both hemispheres, the evolution of the polar vortex, the extent of polar ozone depletion, and its influence on mid-latitude ozone levels.

After the first publication on Antarctic ozone loss by *Farman et al.* [1985], the World Meteorological Organization (WMO) Ozone Assessments gave more attention to polar ozone. The Ozone Trends Panel's 1988 report included an entire chapter on Antarctic ozone, extensively discussing the theories of the ozone hole originally proposed in the mid-1980s, as summarized above. The 1994 Ozone Assessment [*WMO*, 1995] report included a polar processes chapter that confirmed chlorine- and bromine-catalyzed ozone loss in the Antarctic and in the Arctic from in situ [*Anderson et al.,* 1991; *Toohey et al.,* 1993] and satellite observations [*Waters et al.,* 1993]. The 1998 Ozone Assessment [*WMO,* 1999] report included a chapter on lower stratospheric processes, pointing out a number of very low Arctic ozone years and showing that the Antarctic ozone losses were continuing. Subsequent ozone assessments [*WMO*, 2003; 2007] followed, dealing at length with the observed temperature changes over the polar regions. Satellite measurements showed a cooling of 3 K/decade in the Arctic and Antarctic middle stratosphere, and significant coolings of 1.8 K/decade at 70ºN and 1.1 K /decade at 70ºS in the lower stratosphere during spring, for the period 1979-1998.

The Ozone Assessments emphasize the high interannual variability of lower stratospheric temperatures in the Arctic. They show that despite the several cold recent northern winters 1999/2000, 2002/2003, 2004/2005, the northern winters 1998/1999, 2000/2001, 2001/2002,

2003/2004, and 2005/2006 were disturbed by stratospheric warmings (see Section 1.2.2). These reports also confirmed that the interannual varability is much weaker in the Antarctic than in the Arctic, and that the vortex is much stronger in the Antarctic and its breakup occurs later in the spring, compared to the Arctic. A compact and nearly linear relationship was shown to exist between the column ozone loss and the winter average volume of air at temperatures cold enough to activate chlorine on particle surfaces [*Rex et al.,* 2004; *Tilmes et al.,* 2004].

Arctic winter and spring ozone loss was variable between 2007 and 2011, but remained in the range comparable to the values that we have witnessed since the early 1990s. Both Arctic winters 2006/2007 [*Röseval et al.,* 2007] and 2007/2008 [*Kuttippurath et al.,* 2009] were characterized by ozone destruction on the order of 100 DU [*WMO,* 2011]. The 2010/2011 winter was characterized by prolonged cold temperatures below the PSC threshold and unusually low O_3, HCl, and HNO_3 values [Chapter 8; *Manney et al.,* 2011].

1.2 Stratospheric Dynamics and Chemistry in the Polar Regions

1.2.1 Stratospheric Circulation

Atmospheric circulation plays an important role in the vertical and latitudinal distribution of trace gases. Gases characterized by relatively long atmospheric lifetimes have their distribution governed not only by chemical processes but also by the motion of the air masses. The meridional circulation of the stratosphere is known as the Brewer-Dobson circulation [*Brewer,* 1949; *Dobson,* 1956] named after Brewer and Dobson who identified it when observing stratospheric water vapor and ozone, respectively. In the lower stratosphere, the circulation consists of a two-structure cell characterized by a rising motion across the tropical tropopause, a slow stratospheric drift towards the middle and high latitudes, and descending motion at mid-latitudes and through the polar vortex. At higher altitudes, the circulation consists of a single cell from the summer tropics into the winter hemisphere. A tropospheric return flow accounts for mass conservation. The Brewer-Dobson circulation is approximately expressed by the residual circulation [*Andrews et al.,* 1987] and is considered to be driven by the breaking and dissipation of atmospheric waves.

Figure 1.1 gives a schematic of the mean residual circulation. There is a clear difference between the summer and winter hemispheres, with the wintertime stratosphere dominated by the large-amplitude, planetary-scale Rossby waves propagating upward from the troposphere. In the "surf zone" [*McIntyre and Palmer,* 1983] these waves break intermittently, stirring the air across

large distances of the winter stratosphere. Mixing of chemical constituents by the breaking Rossby waves is an efficient transport mechanism in the surf zone.
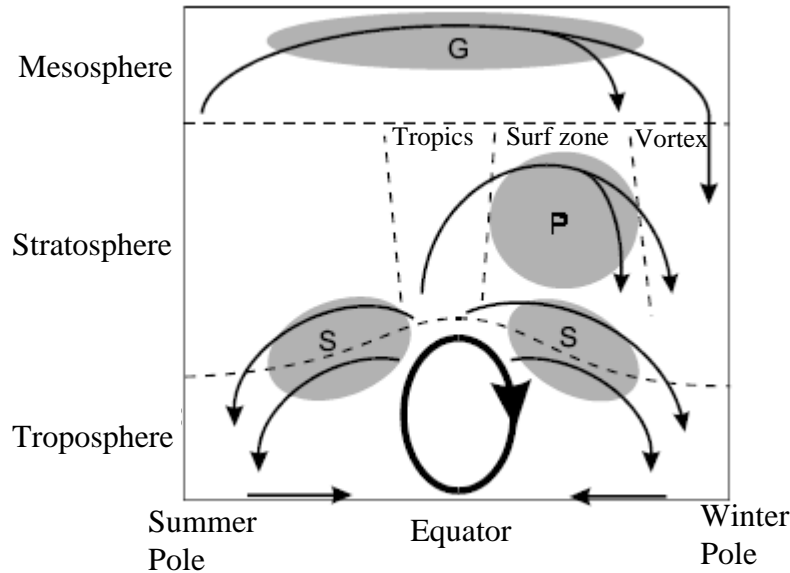
Figure 1.1 Schematic of the residual mean meridional circulation in the atmosphere. The thick line ellipse denotes the thermally-driven Hadley circulation of the troposphere. The shaded regions (labelled "S", "P", and "G") denote regions of breaking waves (synoptic- and planetary-scale waves, and gravity waves, respectively), responsible for driving branches of the stratospheric and mesospheric circulation. (This figure was reproduced from *Plumb,* 2002).

1.2.2 The Polar Vortex

Polar jets usually form at the boundary between the cold polar air and the warm air from lower latitudes. The strong thermal gradient constrains the air to flow horizontally, and because of Earth's rotation, the air speeds up and transforms into a jet stream (fast-flowing, narrow air current). In the winter hemisphere, the air above the pole becomes extremely cold as there is 24-hour darkness, generating the polar night jet stream (or polar vortex) that comprises strong eastward winds encircling the pole [*Andrews et al.,* 1987]. Acting like a barrier, these very fast winds (~80 m/s at ~60 km in the NH) isolate the air inside the vortex from mid-latitude air masses [*Schoeberl and Hartmann,* 1991; *Wallace and Hobbs,* 2006]. The barrier is impermeable to a first approximation, but not perfect, as shown by long-lived tracers whose occurrence inside the vortex was explained by mixing of surf zone air into the vortex [*Michelsen et al.,* 1998; *Kondo,* 1999; *Rex et al,* 1999; *Plumb et al.,* 2000].

The temperature inside the vortex drops as the air cools radiatively, sometimes reaching values of 195 K or less. These temperatures promote the formation of polar stratospheric clouds as will be described in the following section.

The topographical features of the NH polar region lead to stronger wave activity in the NH compared to the SH, where Antarctica is surrounded by water. As result, the NH polar vortex is usually weaker and highly variable compared to the SH. The vortex is sometimes interrupted by sudden stratospheric warmings (SSWs), when temperatures significantly increase at higher latitudes. If the temperature enhancement leads to reversal of the mean zonal winds (as a result of the inversion of the mid-latitude-to-pole temperature gradient) from eastward to westward at heights near 30 km, the stratospheric warming is called major [*e.g.*, *Chshyolkova et al.,* 2007; *Kim and Flatau,* 2010].

The NH winter polar vortex typically forms in the lower stratosphere early in November, is strongest in mid-January and typically dissipates in late March or early April [*WMO,* 2011]. Its dynamical variability changes from year-to-year and as such, quantifying Arctic ozone loss is difficult since it requires distinguishing the effects of chemical processes from transport and mixing. The period between 1989/1990 and 1997/1998 was characterized by reduced dynamical variability, with nine consecutive years without a major stratospheric warming [*Pawson et al.,* 1998; *Labitzke et al.,* 2002]. Since 1998/1999, there have been several warmer-than-average and dynamically disturbed winters: 1998/1999, 2000/2001, 2001/2002, 2003/2004, 2005/2006, 2008/2009, and 2009/2010 [*WMO,* 2007, 2011], combined with cold winters in 1999/2000 [*Mellqvist et al.,* 2002; *Müller et al.,* 2003], 2002/2003 [*WMO,* 2007], 2004/2005 [*Jin et al.,* 2006; *Rösevall et al.,* 2008], and 2006/2007 [*Rösevall et al.,* 2007], and 2007/2008 [*WMO,* 2011]. During winter 2010/2011, another cold and strong Arctic vortex formed, leading to the first genuine 'ozone hole' to appear in the NH [*Manney et al.*, 2011].

1.2.3 Polar Stratospheric Clouds

The background stratospheric aerosols formed by liquid-phase binary sulfuric acid/water (H_2SO_4/H_2O) droplets are found globally throughout the stratosphere [*Junge et al.,* 1961; *Junge and Manson,* 1961]. Inside the vortex, where temperatures are very low, these take up HNO_3 and H_2O [*Carslaw et al.,* 1994; *Tabazadeh et al.,* 1994] transforming into ternary $HNO_3/H_2SO_4/H_2O$

droplets, usually referred to as supercooled ternary solution (STS) PSCs. H_2O ice and solid hydrates of HNO_3 are other forms that PSC particles may take [*Voigt et al.,* 2000].

Based on their optical parameters, PSCs are classified in type I and type II, with type I (which form below ~195 K) being further divided into type Ia and Ib. Type Ia particles have dimensions of 1 µm or greater, are less spherical and have a small total volume concentration. Type Ib particles are of approximately 0.5 µm diameter, are almost spherical, and have a large volume concentration, and are likely to take up most of the atmospheric HNO_3 [*Lowe and MacKenzie,* 2008]. Other gaseous species, including the halogen reservoir species HCl, HBr, HOCl, and HOBr also dissolve into the stratospheric H_2SO_4/H_2O droplets. Thermodynamical models developed to model the equilibrium properties of liquid stratospheric droplets [*Carslaw et al.,* 1994; *Cox et al.,* 1994; *Tabazadeh et al.,* 1994] showed a rapid change in particle composition at about 4-5 K above the ice frost point, from almost binary H_2SO_4/H_2O solutions to almost binary HNO_3/H_2O solutions [*Lowe and MacKenzie,* 2008].

Type II PSCs consist of large crystalline particles ($\geq$ 10 µm) which only exist below the stratospheric ice frost point of ~188 K [*Poole and McCormick,* 1988]. The main composition of type II PSCs is water ice [*Turco et al.,* 1989], but since these ice crystals nucleate from HNO_3-rich particles, their compositions and lifecycles are different and more complicated than those of simple H_2O ice crystals.

During the polar winter, a mixture of liquid binary or ternary droplets and solid particles, NAT and H_2O, of various sizes and number densities can be found in the stratosphere [*Toon et al.,* 2000; *Drdla et al.,* 2003]. It has been shown that the chlorine activation rates on stratospheric particles depend on the uptake coefficient on the particle and the particulate surface area density [*Lowe and MacKenzie,* 2008]. These are generally much higher for the STS compared to the NAT PSC particles, making liquid particles much more efficient in chlorine activation [*Portmann et al.,* 1996; *Lowe and MacKenzie,* 2008]. In the Arctic, the STS PSCs are common, but the temperature distribution and the volume of air in which the PSCs can exist depend very much on the dynamical situation of each winter [*Pawson and Naujokat,* 1999]. As a consequence, ozone loss in the Arctic vortex can vary considerably from year to year depending on changes in meteorological conditions [*Rex et al.,* 2004].

1.2.4 Heterogeneous and Polar Stratospheric Chemistry

The use of chlorofluorocarbons during the past decades has led to a pronounced increase in the stratospheric chlorine content, and even after their international regulation, they represent the most abundant halogenated source compounds in the atmosphere. Chlorine is released from CFCs in the stratosphere through photochemical destruction and transported in reservoir forms poleward due to the Brewer-Dobson circulation. Under the very cold conditions specific to the polar regions, they play a key role in the chemical destruction of ozone. It is important to understand the partitioning of chlorine between reservoir forms like HCl and $ClONO_2$ that are inert with regard to ozone, and the active forms like Cl and ClO.

During the winter, as the air above the pole cools down, the polar vortex forms and the temperatures decrease. When they reach the condensation point of nitric acid (~195 K), these conditions promote the formation of PSCs, as discussed in the previous sections. These clouds provide surfaces for the fast heterogeneous reaction that combines HCl and $ClONO_2$, releasing the active chlorine (R28, Table 1.1). In the meantime, NO_2 concentrations are suppressed, so the released chlorine cannot return to its reservoir form. Laboratory studies showed that heterogeneous activation of chlorine can occur by other reactions (R31 and R34) [*Ravishankara and Hanson,* 1996]. When the sun returns, the chlorine molecule is broken into Cl atoms and can destroy ozone in catalytic cycles like those involving the nitrogen and hydrogen oxides, as shown in Table 1.1. *Wofsy et al.* [1975], *Yung et al.* [1980], *Tung et al.* [1986] and *McElroy et al.* [1986] showed that bromocarbons play also important role in the ozone chemical depletion. The coupling of bromine and chlorine chemistry (as shown in Table 1.1) leads to a similar net cycle as in the case involving the ClO dimer, Cl_2O_2. Ozone depletion is very rapid, and thousands of ozone molecules are destroyed while Cl and Br molecules are recycled.

As the days become longer, the temperature increases and the PSCs evaporate, releasing HNO_3. This will release the NO_2 molecule through photolysis, which will further react with ClO to reform the $ClONO_2$ reservoir (R26). In the Arctic, this reaction is faster than the competing reaction of active chlorine to form HCl (R24). The resulting repartitioning of the chlorine in the Arctic typically results in enhanced $ClONO_2$ and sustained low values of HCl for some time after PSCs have disappeared [*Santee et al.,* 2008].

Table 1.1 Key chemical processes and catalytic cycles (reproduced from *Solomon,* 1999).

Chemical Process	Reaction Number
Chapman Chemistry[a]	
$O_2 + h\nu \rightarrow 2O$	R1
$O + O_2 + M \rightarrow O_3 + M$	R2
$O_3 + h\nu \rightarrow O_2 + O(^1D)$	R3
$O(^1D) + M \rightarrow O + M$	R4
$O_3 + h\nu \rightarrow O_2 + O$	R5
$O + O + M \rightarrow O_2 + M$	R6
$O + O_3 \rightarrow 2O_2$	R7
Illustrative Odd Hydrogen Catalytic Cycles[b]	
$O + OH \rightarrow O_2 + H$	R8
$H + O_2 + M \rightarrow HO_2 + M$	R9
$O + HO_2 \rightarrow O_2 + OH$	R10
Net Cycle 1: $O + O + M \rightarrow O_2 + M$	R6
$OH + O_3 \rightarrow HO_2 + O_2$	R11
$HO_2 + O_3 \rightarrow OH + 2O_2$	R12
Net Cycle 2: $2O_3 \rightarrow 3O_2$	R13
Illustrative Odd Nitrogen Catalytic Cycle[c]	
$NO + O_3 \rightarrow NO_2 + O_2$	R14
$O + NO_2 \rightarrow NO + O_2$	R15
Net Cycle 3: $O + O_3 \rightarrow 2O_2$	R7
Illustrative Odd Chlorine Catalytic Cycles[d]	
$Cl + O_3 \rightarrow ClO + O_2$	R16
$ClO + O \rightarrow Cl + O_2$	R17
Net Cycle 4: $O + O_3 \rightarrow 2O_2$	R7
$Cl + O_3 \rightarrow ClO + O_2$	R16
$Cl + O_3 \rightarrow ClO + O_2$	R16
$ClO + ClO + M \rightarrow Cl_2O_2 + M$	R18
$Cl_2O_2 + h\nu \rightarrow Cl + ClO_2$	R19
$ClO_2 + M \rightarrow Cl + O_2 + M$	R20
Net Cycle 5: $2O_3 \rightarrow 3O_2$	R13
Illustrative Cl-Br Catalytic Cycle[e]	
$Cl + O_3 \rightarrow ClO + O_2$	R16
$Br + O_3 \rightarrow BrO + O_2$	R21
$BrO + ClO \rightarrow Br + ClO_2$	R22
$ClO_2 + M \rightarrow Cl + O_2 + M$	R20
Net Cycle 5: $2O_3 \rightarrow 3O_2$	R13
Some Important Coupling and Reservoir Reactions	
$ClO + NO \rightarrow Cl + NO_2$	R23
$Cl + CH_4 \rightarrow HCl + CH_3$	R24
$HO_2 + ClO \rightarrow HOCl + O_2$	R25
$ClO + NO_2 + M \rightarrow ClONO_2 + M$	R26
$OH + NO_2 + M \rightarrow HNO_3 + M$	R27
Key Heterogeneous Reactions	
$HCl + ClONO_2 \rightarrow HNO_3 + Cl_2$	R28
$N_2O_5 + H_2O \rightarrow 2HNO_3$	R29
$ClONO_2 + H_2O \rightarrow HNO_3 + HOCl$	R30
$HCl + HOCl \rightarrow H_2O + Cl_2$	R31
$BrONO_2 + H_2O \rightarrow HNO_3 + HOBr$	R32
$HCl + BrONO_2 \rightarrow HNO_3 + BrCl$	R33
$HCl + HOBr \rightarrow H_2O + BrCl$	R34

[a]*Chapman* [1930].
[b]*Bates and Nicolet* [1950]; *Hampson* [1964].
[c]*Crutzen* [1970]; *Johnston* [1971].
[d]*Stolarski and Cicerone* [1974]; *Molina and Molina* [1974].
[e]*McElroy et al.* [1986]; *Tung et al.* [1986].

Simultaneous observations of ClO, HCl, ClONO$_2$, NO, NO$_2$, HNO$_3$ and other gases can give us useful information about the Arctic springtime stratosphere. Combining the measurements provided by all the instruments deployed at Eureka and those from satellites, help us to understand the meteorological conditions specific to each year and the evolution of ozone and related trace gases.

1.3 Current Issues and Future Predictions

The Montreal Protocol, strengthened through five Amendments, is considered a successful environmental protection agreement for the phase out of ozone-depleting substances (ODSs). As a result of this Protocol, ODS abundances are expected to decline, while ozone is expected to recover by the end of this century [*WMO*, 2007; 2011].

The sum of chlorine and bromine derived from the tropospheric abundances of ODSs and weighted to reflect their potential influence on ozone in different parts of the stratosphere gives the Equivalent Effective Stratospheric Chlorine (EESC). The EESC abundance differs from region to region in the atmosphere, being controlled by its input into the stratosphere from the troposphere, mixing, and transport processes. Figure 1.2 shows the EESC derived for the mid-latitude and polar stratospheric regions relative to peak abundances plotted as a function of time [*WMO*, 2011]. It is clearly seen that the polar EESC (blue curve) had decreased by approximately 5% from its peak value in 2002 by the end of 2008, this value representing 10% of the decrease required to return to the 1980 levels in the polar regions. One important concern is that emissions inferred for CFCs from global observed changes did not decline in the period from 2005 to 2008 as rapidly as projected in the A1 scenario of the 2006 Ozone Assessment [*WMO*, 2011].

The HCFC production in developing countries and East Asia increased in the 2005-2008 period, this increase coinciding with a doubling of the HCFC-142b emissions by 2008, compared to what the A1 scenario of the 2006 Ozone Assessment predicted. There are also indications that the estimated lifetimes for some ODSs may be longer than those predicted in the 2006 Ozone Assessment [*WMO*, 2007] (e.g., CFC-11 for which the lifetime is 56-64 years instead of the estimate of 45 years used in WMO (2007) [*Douglass et al.,* 2008]), requiring revisions and recalculation of their ozone depletion potentials (ODP) [*WMO*, 2011].
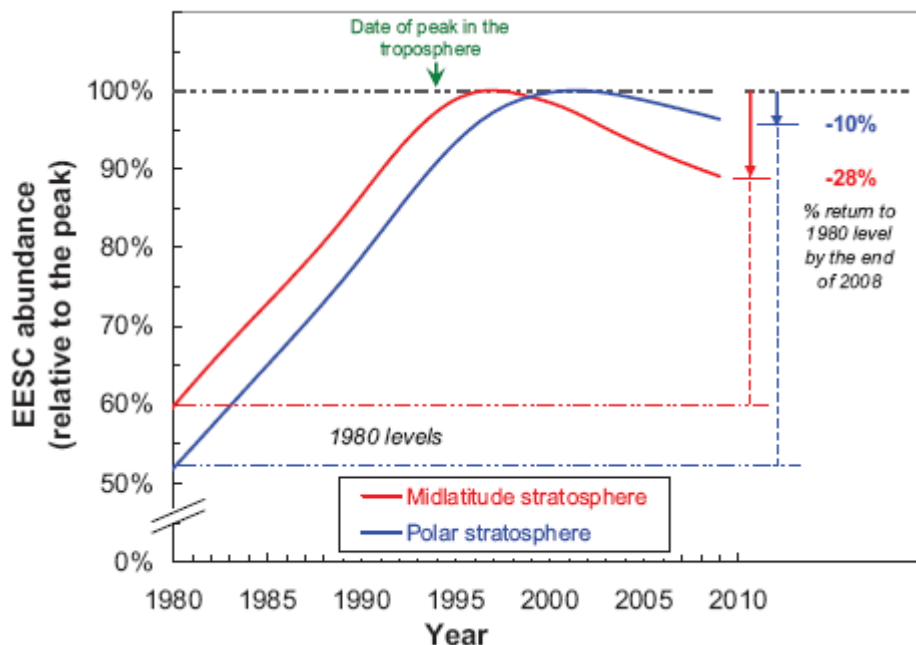
Figure 1.2 EESC derived for the mid-latitude (red) and polar (blue) stratospheric regions relative to peak abundances plotted as a function of time. The peak abundances are ~1950 ppt and ~4200 ppt for the mid-latitude and polar stratosphere, respectively. The percentages indicate the observed change in EESC by the end of 2008 relative to the change needed for EESC to reach the 1980 abundances. (This figure was reproduced from *WMO,* 2011).

N_2O, an important ozone-depleting and greenhouse gas, has been shown to be the most important ODS emitted today [*Ravishankara et al.,* 2009]. N_2O emissions are not controlled by the Montreal Protocol, and future anthropogenic emissions of N_2O may increase if the production of biofuels is enhanced [*Crutzen et al.,* 2008]. Using the IPCC A2 scenario for the 21st century, *Portmann and Solomon* [2007] computed an 8% ozone decrease by 2100 in the 20 to 40 km altitude range from changes in N_2O alone (these are estimated to be 0.8 ppb/yr). One target of the Kyoto Protocol is the limitation of future N_2O emissions. This will result in enhanced recovery of the depleted ozone layer and will reduce the anthropogenic forcing of the climate system.

The stratospheric Brewer-Dobson circulation is expected to accelerate as a consequence of climate change, especially in the NH, leading to an increase in the stratosphere-to-troposphere ozone flux [*Hegglin and Shepherd,* 2009]. As shown in Figure 1.3, this increase is predicted to be as much as 2.6%/decade in the NH and 0.8%/decade in the SH and is attributed in both hemispheres to climate change. This transport-induced ozone increase is expected to lead to a decrease in the ultraviolet index at high latitudes in the NH and an increase in the tropics, with

consequences for the tropospheric radiative forcing, air quality, and human health [*Hegglin and Shepherd,* 2009].
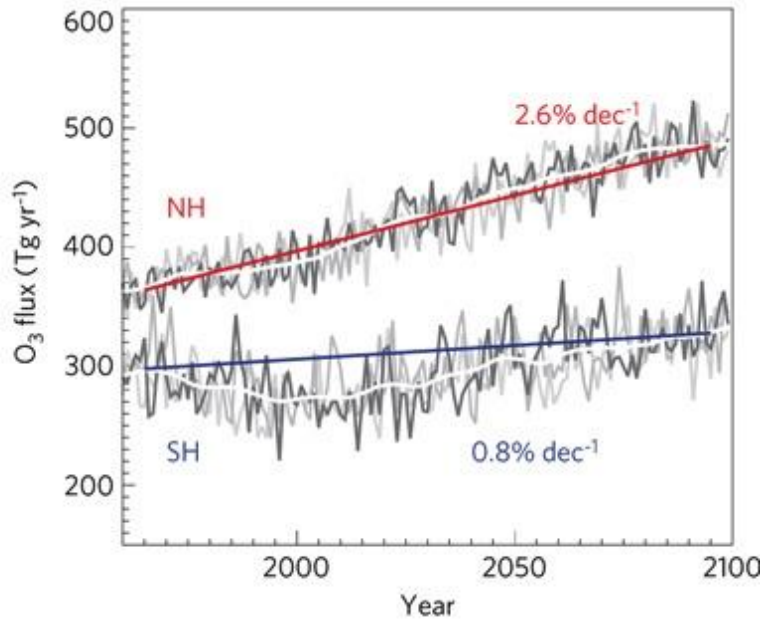
Figure 1.3 The evolution of annual mean stratosphere-to-troposphere ozone flux obtained from CMAM (Canadian Middle Atmosphere Model) simulations (grey lines) for the 1960 to 2100 time period. The white line indicates the five-year running ensemble mean, while the red and blue lines indicate the trends for the two hemispheres. The effects of ozone depletion/recovery were excluded in computing these trend lines. (This figure was reproduced from *Hegglin and Shepherd,* 2009).

A tendency toward cooling of the "cold" Arctic winters is discussed by *Rex et al.* [2006]. They show that the volume of air at temperatures below the PSC threshold (V_{PSC}) reaches a maximum approximately once in five years, and is closely correlated with the potential for ozone loss. Although this previously seen trend is somewhat questioned in the *WMO* [2011] report due to the lack of a new peak in the past five years (Figure 1.4), this winter (2010/2011) the V_{PSC} was the largest on record [*Manney et al.,* 2011].

Chemistry-Climate Models (CCMs) are important tools used to project the future evolution of ozone [*WMO,* 2007, 2011]. Simulations from 17 CCMs were recently examined to study the evolution of stratospheric ozone through this century [*SPARC CCMVal,* 2010]. There is significant interest in the effects of greenhouse gas (GHG) emissions on the future evolution of stratospheric ozone, and different scenarios were used to predict their evolution. It is well known

that GHGs warm the troposphere while they cool the stratosphere. Lower stratospheric temperatures result in slower gas-phase ozone loss cycles [*Haigh and Pyle,* 1982], hence in higher ozone concentrations. On the other hand, a cooler Arctic stratosphere will enhance PSC formation, chlorine activation and ozone depletion. Therefore, it is difficult to predict the future evolution of ozone and efforts are made to simulate this evolution based on various GHG emission scenarios. Figure 1.5 shows the long-term evolution of stratospheric ozone and equivalent stratospheric chlorine (ESC) as referenced to 1960 values [*WMO 20 Questions: update 2010,* 2011]. The uncertainties in the model projections are also included. While the global annual mean stratospheric ozone is predicted to return to 1980 levels by 2030, this is expected to happen earlier in the NH (2020 in the NH midlatitudes and 2025 in the Arctic) and later in the SH (2035 in the SH midlatitudes and 2050 in the Antarctic) and tropics (2040).
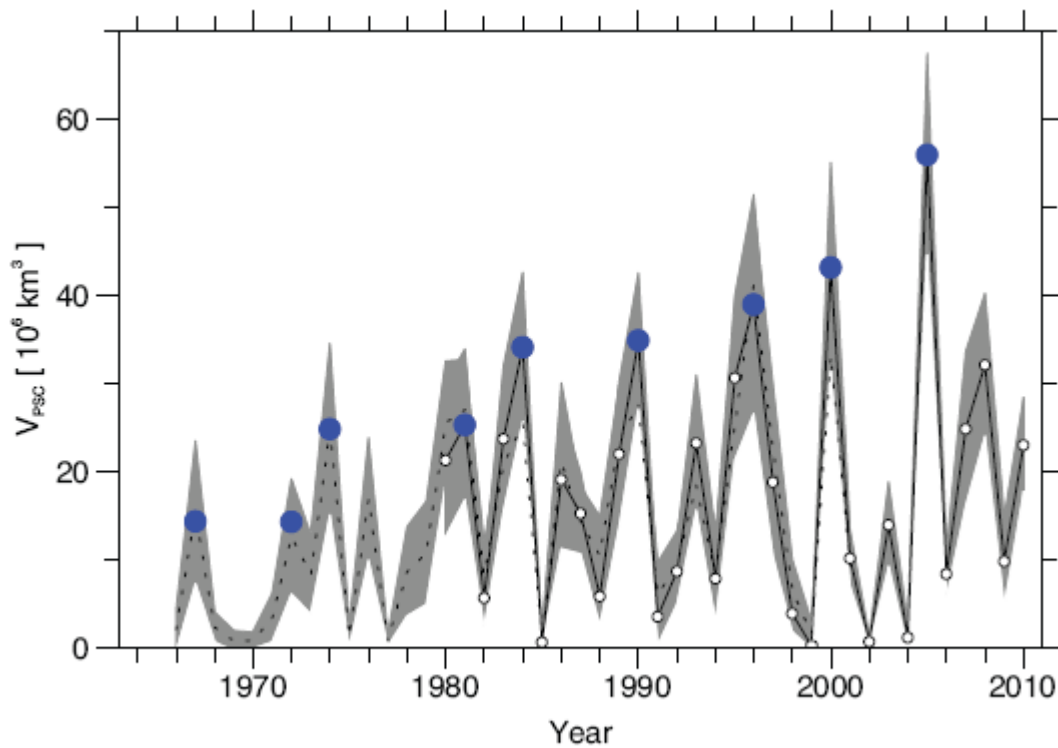
Figure 1.4 Evolution of V_{PSC} (km^3) for the Arctic over the past four decades obtained from the ECMWF (solid line) and Free University of Berlin (dotted line) data. The blue circles represent the maximum values of V_{PSC} during five-year intervals. The gray shading represents the uncertainty of V_{PSC}. (This figure was reproduced from *WMO,* 2011).
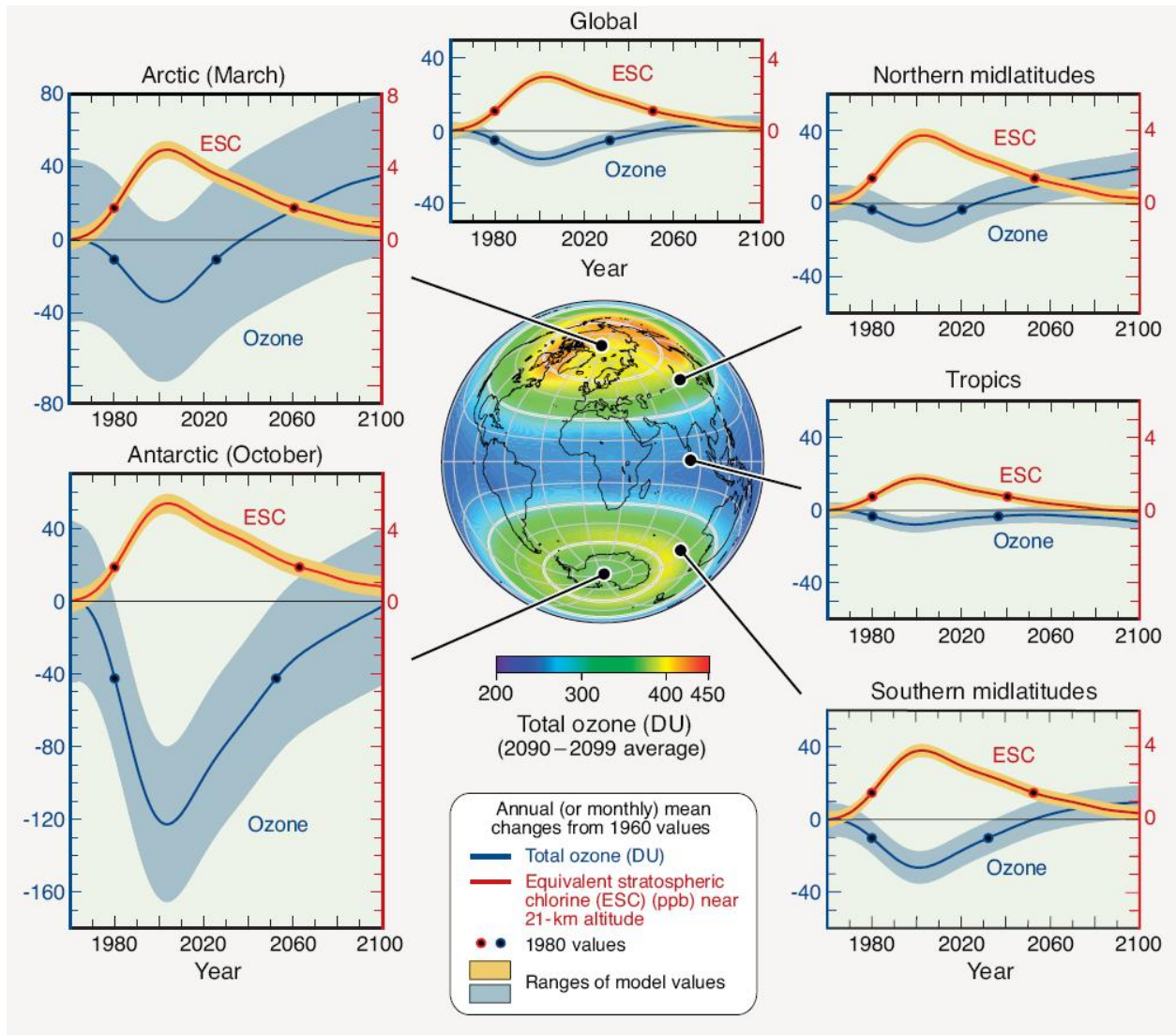
Figure 1.5 Long-term changes in ozone and equivalent stratospheric chlorine (ESC). Regional and global projections are shown for total ozone and ESC for the period 1960–2100, referenced to 1960 values. The globe in the center shows average total ozone projections for the last decade of the 21st century. Total ozone depletion increased after 1960 as ESC values steadily increased throughout the stratosphere. ESC values have peaked and are now in a slow decline. All the projections show maximum total ozone depletion around 2000, coincident with the highest abundances of ESC. Thereafter, total ozone increases, except in the tropics, as ESC slowly declines. In all the projections except the Antarctic and the tropics, total ozone returns to 1960 values by midcentury, which is earlier than expected from the decrease in ESC alone. The earlier returns are attributable to climate change, which influences total ozone through changes in stratospheric transport and temperatures. In the tropics, in contrast, climate change causes total ozone to remain below 1960 values throughout the century. In the Antarctic, the effect of climate change is smaller than in other regions. As a result, Antarctic total ozone in springtime mirrors the changes in ESC, with both closely approaching 1960 values at century's end. The dots on each curve mark the occurrences of 1980 values of total ozone and ESC. Note that the equal vertical scales in each panel allow direct comparisons of ozone and ESC changes between regions. (This figure was reproduced from *WMO*, 2011, *20 Questions: update 2010*).

1.4 Thesis Objectives

This work is part of CANDAC efforts to better understand the changing Arctic atmosphere. The main research themes of CANDAC at PEARL are the study of Arctic tropospheric transport and air quality, the Arctic radiative environment (impacts of clouds, aerosols and diamond dust), the chemistry of the Arctic middle atmosphere, and waves and coupling processes. The overall goal of the Arctic Middle Atmosphere Chemistry (AMAC) theme is to improve our understanding of the processes controlling the stratospheric ozone budget and its future evolution, using measurements of the concentrations of stratospheric constituents. This work is part of the collective AMAC effort, and the scientific objectives of this work were:

- To implement and optimize retrievals for ozone and other stratospheric gases from spectra recorded by the new Bruker 125HR Fourier transform infrared spectrometer at Eureka.

- To explore ways of improving the satellite validation method for the highly variable spring meteorological conditions. For this purpose, the Canadian Arctic Atmospheric Chemistry Experiment (ACE) Validation Campaigns were conducted each spring at Eureka.

- To study the evolution (seasonal, annual) of ozone and other stratospheric gases related to ozone and ozone depletion, to better understand the chemical and dynamical processes that control ozone abundances and the changes in these processes over time.

- To compare measurements with atmospheric model results for model validation purposes and for deriving an NO_y data product for Eureka. Model comparisons were also used to quantify the chemical ozone depletion during spring 2011.

1.5 Personal Contribution

Work on the material of this thesis began with my first trip to Eureka, in July 2006, when the Bruker 125HR instrument was installed at PEARL. Since its installation, I have shared with Dr. Rebecca Batchelor (2006-2009) the operation and maintenance of the instrument and the guidance of the CANDAC operators in operating, troubleshooting, and winterizing the instrument. Since November 2009, I have had primary responsibility for the instrument. I was an ACE Validation Campaign team member for five consecutive years 2007-2011, and also

participated in the summer 2007 Aura Campaign. In July 2010, I visited Eureka for maintenance and relocation of the instrument with Bruker engineer Gregor Suravicz.

After learning and implementing the retrieval technique using SFIT2, I started to produce time series of ozone and related trace gases. I then focused on the error analysis, and contributed with IDL coding to develop the error calculation for our retrievals together with Dr. Rebecca Batchelor. Results from my first ozone retrievals and error analysis were included in *Batchelor et al.* [2009].

My work was further focused on ozone retrievals. I optimized the ozone retrievals for Eureka with the results published in *Lindenmaier et al.* [2010]. I co-led, with Dr. Thomas Blumenstock from the Karlsruhe Institute of Technology, the ozone retrieval harmonization effort among the Network for the Detection of Atmospheric Change (NDACC, former NDSC) Infrared Working Group (IRWG) stations. I also performed tests with the Eureka data to evaluate the IRWG recommendations for other nine gases as part of the harmonization initiative.

I developed a strict comparison method for springtime 125HR ACE-FTS comparisons, and wrote the IDL coding that improved the old 'closely spaced in location and time' coincidence criterion. The results were published as part of a paper by *Batchelor et al.* [2010].

Recently, I derived an NO_y data product from the Bruker 125HR measurements that contains the five primary species: NO, NO_2, HNO_3, N_2O_5, and $ClONO_2$. I developed the coding for comparing these species with three atmospheric models and the ACE-FTS measurements. These results were published in *Lindenmaier et al.* [2011a].

I also led the analysis of the 125HR 2011 spring measurements and I quantified the chemical ozone depletion above Eureka from February 23 to April 6. These results are summarized in the paper submitted to *Atmospheric Chemistry and Physics* on October 3, 2011 [*Lindenmaier et al.,* 2011b].

During my Ph.D., I also analyzed data that were contributed to studies by *O'Neill et al.* [2008], *Adams et al.* [2011], *Kohlhepp et al.* [2011], *Wespes et al.* [2011], and *Wunch et al.* [2011].

1.6 Thesis Outline

After the description of the stratospheric circulation and polar stratospheric chemistry given here in Chapter 1, a brief description of the site and of the instrument follows in Chapter 2. The retrieval technique, retrieval algorithm, and error analysis are described in Chapter 3. A detailed

analysis of the parameters used for ozone retrievals at Eureka is presented in Chapter 4. Through this work, the best parameters for retrievals at Eureka were identified, as those giving the greatest amount of information for both the troposphere and stratosphere, and the smallest total error. Efforts have been also made to implement the new harmonized parameters recommended by the NDACC IRWG for ozone and nine other species. These results are discussed in Chapter 5.

For comparisons of the Bruker 125HR measurements with satellite data, a new comparison methodology was developed and is described in Chapter 6. Comparisons from four Canadian Arctic ACE Validation Campaigns conducted during the springs of 2007-2010 are shown for Bruker 125HR and ACE-FTS total columns of O_3, HCl, HNO_3, $ClONO_2$, and HF. Chapter 7 is dedicated to developing an NO_y partial column data product from the FTIR measurements at Eureka, which is used to assess the seasonal and interannual variability of reactive nitrogen. The results are also compared to three atmospheric models and satellite data.

Unusually low O_3, HCl, and HNO_3 column measurements at Eureka during spring 2011 are shown and compared to measurements from the previous 14 years of measurements by the 125HR and its predecessor, Environment Canada's Bomem DA8, in Chapter 8. The ozone loss was also quantified using the passive subtraction method and SLIMCAT. Chapter 9 briefly summarizes the results of the thesis and outlines recommendations for future work.

Chapter 2

The Bruker 125HR Fourier Transform Infrared

Spectrometer

2.1 CANDAC and PEARL

The polar regions are an essential element of the entire Earth system. They both respond to and drive changes elsewhere on the planet. The Arctic is one of the hardest parts of the Earth system to study because of the very few Arctic stations dedicated to measurement acquisition, and without measurements, it is difficult to monitor and explain the processes that occur. CANDAC has established PEARL to make long-term atmospheric measurements in the high Arctic, in order to address issues within three broad areas of air quality, ozone, and climate change.

The PEARL Ridge Laboratory is located on Ellesmere Island at Eureka, Nunavut (80.05ºN, 86.42ºW), at 610 m above sea level (Figure 2.1). There are two additional laboratories at Eureka, the Zero Altitude PEARL Auxiliary Laboratory (ØPAL) located at sea level near Environment Canada's Eureka Weather Station, and the Surface and Atmospheric Flux, Irradiance and Radiation Extension (SAFIRE), located at 5 km from the Weather Station.

One of the key instruments contributing to the AMAC theme is the Bruker IFS 125HR FTIR spectrometer (henceforth referred to as the 125HR), which we installed at PEARL in July 2006. The 125HR has been specifically designed for high-resolution measurements over a broad spectral range. Using the Sun or Moon as a source, an FTIR records interferograms that can be converted into absorption spectra and analyzed to obtain the column amount of an atmospheric constituent and some information about its vertical distribution. Column amounts and vertical profiles of molecules such as O_3, HCl, HF, NO, NO_2, $ClONO_2$, HNO_3, CH_4, C_2H_6, N_2O, CFC-11, CFC-12, CO, and OCS are derived from the spectra using spectral fitting techniques. Most of these molecules have a role to play in either the ozone destruction cycle or global warming. The FTIR can also be used to detect and quantify the presence of some volatile organic compounds (VOCs) that are the by-product of biomass burning and anthropogenic activities such as combustion. Using the instrument, we are recording a long-term data set of Arctic chemical composition measurements that will contribute to a better understanding of ozone loss at Eureka,

of the links between ozone depletion and climate change, and of the transport of tropospheric pollutants.
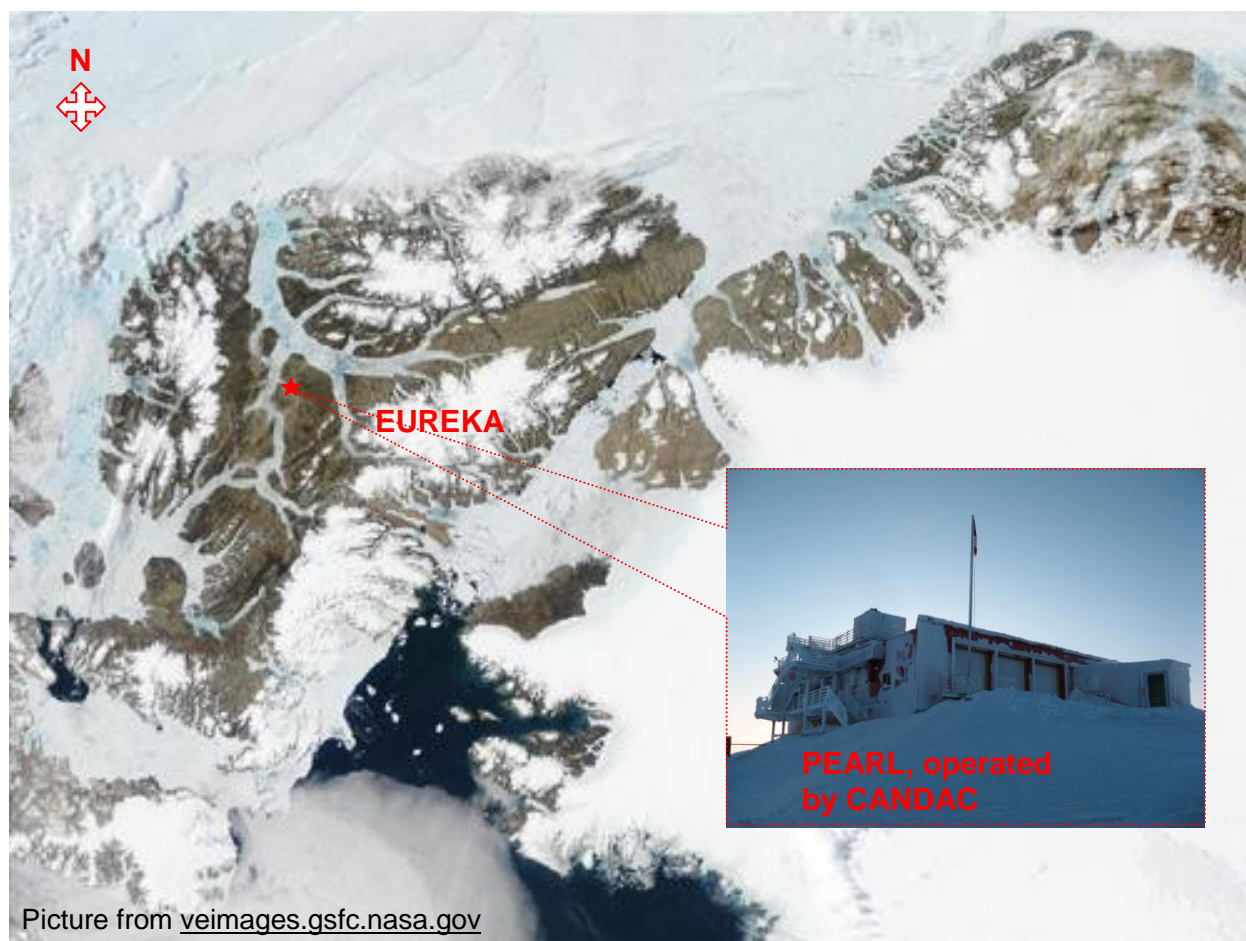
Figure 2.1. Ellesmere Island and Eureka, NU (80.05ºN, 86.42ºW). The PEARL Ridge Laboratory at Eureka is shown in the inset photo.

2.2 The Michelson Interferometer

The science of Fourier transform interferometry was initiated in 1880, when Albert Michelson invented the interferometer [*Bell,* 1972]. It remains the back-bone of many interferometers used today. The optical diagram of the basic Michelson interferometer is shown in Figure 2.2.

The beam coming from the source is reflected or transmitted by a beamsplitter into two perpendicular directions. In one direction the beam is reflected off a stationary mirror, and in the other direction the beam is reflected off a moving mirror. This moving mirror introduces a path difference between the two beams, which, after reflection off their respective mirrors are recombined and directed towards the detector. The detector produces an intensity signal modulated by the optical path difference (OPD) of the two interfering beams. Assuming that the refractive index of the air is 1 and that the moving mirror is displaced by distance x parallel to the optical axis, the path difference between the two beams will be $2x$. For any discrete wavenumber v_i, constructive interference will occur whenever the OPD is an integer multiple of the wavelength λ_i:

$$2x = n\lambda_i = n/v_i \quad (n = 0, 1, 2, 3, ...), \tag{2.1}$$

while destructive interference will occur for any OPD that is an odd multiple of the half wavelength. If R is the coefficient of reflection and T is the coefficient of transmission of the beamsplitter, the electromagnetic wave at the location of the detector can be described by the superposition of the two beams by the relation:

$$A(x_1, x_2, v) = RTA_0(v)\left\{e^{i(\omega t - 2\pi v x_1)} + e^{i(\omega t - 2\pi v x_2)}\right\}, \tag{2.2}$$

where A_0 is the amplitude of the waves, x_1 and x_2 denote the optical path for the two waves. The intensity of the interferogram $I(x_1, x_2, v)$ is a real quantity given by the square modulus

$$\begin{aligned} I(x_1, x_2, v) &= A(x_1, x_2, v)A*(x_1, x_2, v) \\ &= 2|RT|^2 A_0^2(v)\left\{1 + \cos(2\pi v(x_1 - x_2))\right\}. \end{aligned} \tag{2.3}$$

and it is the quantity measured by the detector.

The beam of a frequency-stabilized monochromatic laser is added to the interferometer, and helps to determine the exact position of the moving mirror while recording the interferogram. Knowing the exact frequency of the laser and by counting the interference fringes of the laser beam, the relative displacement of the moving mirror can be calculated. For a monochromatic light source, the interference pattern recorded by the detector is a sine wave, since the two beams move in and out of phase as a result of the optical path difference. The solar beam is a multi-wavelength source, and the observed interference pattern is in this case the summation of all sine waves corresponding to each wavelength. The point where all wavelengths of the solar light constructively interfere is known as the 'zero path difference' (ZPD) and corresponds to the point where the path length is identical for both beams. This corresponds to a

maximum signal on the detector, and becomes weaker as the moving mirror moves away from this point. The pattern of intensity versus path difference that the detector records while the moving mirror moves from the ZPD to the end of the arm is called the interferogram. The Fourier transform of the interferogram yields the frequency information of the incident light, the spectrum.
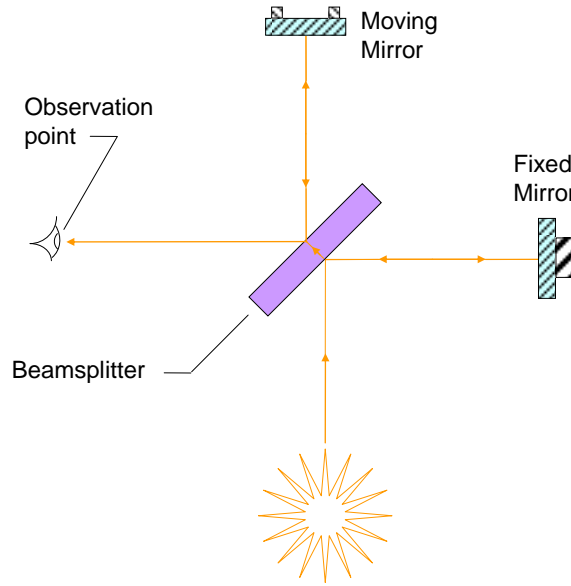
Figure 2.2. Schematic of the optical path of the solar beam (orange lines) in a Michelson interferometer. The beamsplitter splits the beam into two equal parts, directing them towards the fixed and moving mirrors. The reflected beams return to the beamsplitter and recombine into one beam that is directed towards the observation point.

If we denote the OPD between the two secondary beams by $x = x_1 - x_2$, the square amplitude of the light wave by $S(v) = A_0^2$, and extend the description to non-monochromatic sources, we find the intensity $\tilde{I}(x)$ recorded in the interferogram by applying the superposition principle, *i.e.* by integrating $I(x)$ over all wavenumbers:

$$\tilde{I}(x) = 2|RT|^2 \int_0^{+\infty} S(v)\{1 + \cos(2\pi vx)\}dv$$

$$= 2|RT|^2 \left\{ \int_0^{+\infty} S(v)\cos(0)dv + \int_0^{+\infty} S(v)\cos(2\pi vx)dv \right\}.$$

(2.4)

The first integral term in the equation above (constant in x) gives the intensity of the interferogram for a path difference of zero where the maximum of the interferogram is located,

while the second integral describes the modulation of the signal as a function of OPD. For an ideal beamsplitter, for which the incident light is split into two equal beams, $|R^2| = |T^2| = \frac{1}{2}$ and Equation 2.4 can be rewritten as

$$\left[\tilde{I}(x) - \frac{1}{2}\tilde{I}(0) \right] = \frac{1}{2}\int_0^{+\infty} S(\nu)\cos(2\pi\nu x)d\nu .$$ (2.5)

Since $\tilde{I}(x)$ is a directly measurable quantity (real in the mathematical sense), $S(\nu)$ has to be Hermitian [Bell, 1972], *i.e.*, $S*(\nu) = S(-\nu)$. Accounting for this and applying Euler's theorem to the right hand side of Equation 2.5 we obtain

$$\begin{aligned}
\left[\tilde{I}(x) - \frac{1}{2}\tilde{I}(0) \right] &= \frac{1}{2}\int_0^{+\infty} \text{Re}\left[S(\nu)e^{i2\pi\nu x} \right]d\nu \\
&= \frac{1}{2}\int_0^{+\infty}\left[\left\{ \frac{1}{2}S(\nu)e^{i2\pi\nu x} \right\}^* + \frac{1}{2}S(\nu)e^{i2\pi\nu x} \right]d\nu \\
&= \frac{1}{4}\int_{-\infty}^0 S(\nu)e^{i2\pi\nu x}d\nu + \frac{1}{4}\int_0^{+\infty} S(\nu)e^{i2\pi\nu x}d\nu \\
&= \frac{1}{4}\int_{-\infty}^{+\infty} S(\nu)e^{i2\pi\nu x}d\nu .
\end{aligned}$$ (2.6)

The relationship between the interferogram and the spectrum is given by the Fourier integral pair:

$$\begin{aligned}
I(x) &= \tilde{I}(x) - \frac{1}{2}\tilde{I}(0) = \frac{1}{4}\int_{-\infty}^{+\infty} S(\nu)e^{i2\pi\nu x}d\nu \\
S(\nu) &= 4\int_{-\infty}^{+\infty} I(x)e^{-i2\pi\nu x}dx .
\end{aligned}$$ (2.7)

Because the real spectrometer has a finite OPD, L, (due to the finite size of the arm holding the moving mirror), the interferogram can be recorded only with a finite step size Δx. Mathematically, the finite OPD can be introduced in Equation 2.7 by multiplying with a function $B(x)$ that is equal to 1 throughout the [-L, L] interval, and 0 elsewhere:

$$\tilde{S}(\nu) = 4\int_{-\infty}^{+\infty} I(x)B(x)e^{-i2\pi\nu x}dx .$$ (2.8)

The function $B(x)$ is the boxcar or instrumental line shape (ILS) function. Any other even function that is positive and continuous throughout [-L, L] and zero outside [-L, L] can be used instead of $B(x)$. The boxcar function is the simplest function and preserves the maximum

information from the interferogram for a given OPD. The Fourier transform, $b(v)$, of the ILS

$B(x) = 1$ for $x \in [-L, L]$ is [*Bell*, 1972]:

$$\mathcal{F}^{-1}\{B(x)\} = b(v) = \frac{\sin(2\pi vL)}{2\pi vL} = \mathrm{sinc}(2\pi vL) \,. \tag{2.9}$$

Using the convolution theorem of the Fourier theory and Equations 2.8 and 2.9, we obtain the

relation for the convolved spectrum:

$$\widetilde{S}(v) = S(v) \otimes b(v) \,. \tag{2.10}$$

This equation shows that the instrumental spectrum is given by the convolution of the idealized

spectrum produced by infinite OPD with the ILS function. Therefore, the ILS plays an important

role in the characterization of the instrument. Investigating how the ILS deviates from the ideal

case gives important information about the instrument optical alignment, scan mirror stability,

and sampling errors.

The modulation efficiency is a measure of the integrity of the signal strength on the

detector as a function of OPD. If the Jacquinot advantage (described below) is not totally

achieved, it means that there is a dispersion of radiation in the internal optics of the instrument.

The dispersion will be larger at greater OPD, and is known as self-apodization of the

interferometer. It is expected that there will be always some loss due to the self-apodization of

the instrument, but a higher value can indicate a misalignment of the optical components or the

inability of the moving mirror to remain perpendicular to the fixed mirror.

During the derivation of Equation 2.7, it was assumed that any phase changes induced by

the optical components of the instrument are compensated for prior to the beam reaching the

detector. In practice, this cannot be perfectly realized, and phase errors usually occur. The ideal

interferogram is perfectly symmetric, while that affected by a small phase error will be slightly

asymmetric relative to the ZPD. Mathematically, the resulting spectrum becomes a complex

spectrum, with the tangent of the phase angle given by the ratio of the real and imaginary parts of

the spectrum.

Interferometers have several advantages over prism or diffraction grating spectrometers.

The more commonly known or traditional advantages are the Jacquinot and the Fellgett

advantages. Compared to the best grating spectrometers, about 200 times more power can be put

through the interferometer (for the grating spectrometers, the power through the instrument is

limited by the area of the entrance slit). Jacquinot realized and wrote about the throughput

advantage (known as the Jacquinot advantage or étendue), stating that in a lossless optical

system, the brightness of an object equals the brightness of the image. In other words, the étendue, a property of an optical system that represents the dispersion of the beam of radiation, is conserved [*Jacquinot and Dufour,* 1948].

The other advantage of a Fourier transform spectrometer arises from the multiplex or Fellgett advantage [*Fellgett,* 1951; 1958]. This is based on the fact that an interferometer receives information from the entire range of a given spectrum during each time element of a scan, while the older scanning grating instruments or prism spectrometers receive information only in the narrow band of the spectrum that lies on the exit slit of the instrument at that particular time element of the scan. This means that an FTS spectrum can be measured relatively quickly in comparison to traditional dispersive spectroscopy, and multiple scans can be co-added together in a short period of time.

The large resolving power of the interferometer is a result of these two advantages and depends linearly on the relative displacement of the instrument's movable mirror. The longer the scanning arm, the higher the resolution.

Several criteria have been used to define the resolution of FTIR spectrometers, from which the most widely used are the Rayleigh criterion and the full width at half-height (FWHH). The Rayleigh criterion was first used to define the resolution of the diffraction-limited grating spectrometer, whose ILS is represented by a triangular function (in the frequency domain this becomes a sinc^2 function). The Rayleigh criterion states that "*two adjacent spectral lines of equal intensity, each with a $\mathrm{sinc}^2 \pi \tilde{v} L$ shape, are considered to be just resolved when the center of one line is at the same frequency as the first zero value of the other*" [*Griffiths,* 2002]. The resolution is then $1/L$ and the resulting curve has a dip of 20% of the maximum intensity (Figure 2.3(a)). If the same criterion is applied to lines having $\mathrm{sinc} 2\pi \tilde{v} L$ shape, it is found that the lines are not resolved (Figure 2.3(b)). Under the FWHH criterion, two lines of equal intensity and half-width will be resolved only when the spacing between the lines is greater than the FWHH of either line. In the case of triangular function, the FWHH is $0.9/L$ (Figure 2.3(c)), and the lines are just resolved at this resolution. For lines having $\mathrm{sinc} 2\pi \tilde{v} L$ shape, the FWHH is $0.6/L$ (Figure 2.3(d)), and they are not resolved when they are separated by this amount. For these lines a dip of approximately 20% is found when they are separated by $0.73/L$ (Figure 2.3(e)). Because the value of the resolution depends on the apodization function and the resolution criterion applied, $1/L$ is usually chosen as the 'nominal resolution' of the instrument. Bruker Optics uses the

FWHH of the ideal monochromatic line after triangular apodization to specify the spectral resolution of the 125HR, *i.e.*, $0.9/L$. This convention is followed here, but the true resolution is higher than stated, as boxcar apodization is used.
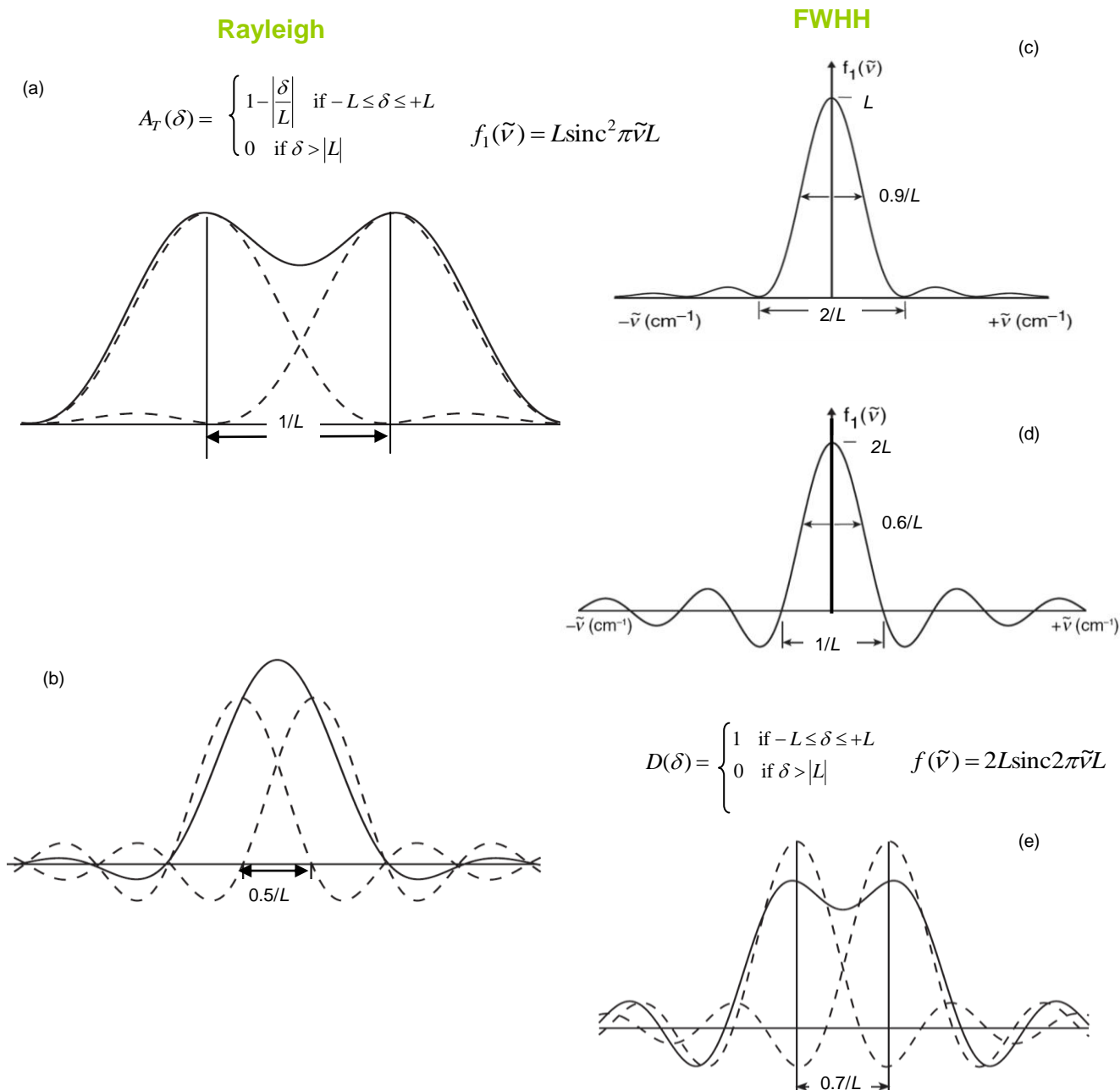
Figure 2.3 (a) Resultant (solid line) of adding two $\mathrm{sinc}^2\pi\tilde{v}L$ functions (dashed lines) of equal amplitude separated by $1/L$; (b) Resultant (solid line) of two $\mathrm{sinc}2\pi\tilde{v}L$ functions (dashed lines) of equal amplitude separated by $0.5/L$; (c) $\mathrm{sinc}^2\pi\tilde{v}L$ ILS function computed for triangularly apodized interferogram; (d) Fourier transform of a boxcar function of unit amplitude extending from $-L$ to $+L$; (e) Resultant (solid line) of two $\mathrm{sinc}2\pi\tilde{v}L$ functions (dashed lines) of equal amplitude separated by $0.7/L$; (This figure was reproduced from *Griffiths and de Haseth*, 2007).

2.3 The Bruker 125HR FTIR

The 125HR is a permanently aligned modified Michelson scanning interferometer optimized for solar absorption spectroscopy in the infrared. It records spectra at a resolution of up to 0.0024 cm^{-1} (where resolution is defined as 0.9/maximum optical path difference, and the maximum optical path difference for the PEARL 125HR is 372 cm). The beamsplitter is permanently aligned at 30-degree incidence, with a repeatable locking mount that allows easy exchange and automatic recognition of either of its two beamsplitters: the potassium bromide (KBr) beamsplitter for mid-infrared (MIR) measurements from 450 to 4800 cm^{-1}, and the calcium fluoride (CaF$_2$) beamsplitter for near-infrared (NIR) measurements from 1200 to 15000 cm^{-1}. A helium neon laser is used for precise location of the scanning mirror, which uses a DC motor and a linear drive unit for smooth gliding along its track. MIR interferograms are recorded on either of two liquid-nitrogen-cooled detectors: the photovoltaic indium antimonide (InSb) or photoconductive mercury-cadmium-telluride (HgCdTe) detector. These detectors are sensitive to radiation from 1850 to 10000 cm^{-1} (5 to 1 μm) and 600 to 6000 cm^{-1} (16 to 1.6 μm) respectively, and are typically used in conjunction with one of eight standard NDACC narrow bandpass filters (listed in Table 2.1) which limit the wavenumber range of the spectra, thus increasing the signal-to-noise ratio. NIR interferograms are recorded on the indium-gallium-arsenide (InGaAs) detector, which is sensitive to radiation from 4000 to 15000 cm^{-1}. The whole system is operated under vacuum, with a Duniway ISP-250B dry scroll pump used to maintain the pressure at less than 1 hPa. Sunlight comes from a previously installed, custom-built active solar tracker located on the roof of PEARL, previously used for the Bomem DA8 FTIR. From July 2006 to July 2010, the instrument was in the northern wing of the laboratory. After installation, the solar beam coming from the tracker was picked up by four mirrors arranged such that they directed the beam towards the last 45º mirror in the front of the instrument's input window (as shown in Figure 2.4). After the DA8 was removed in 2009, two mirrors were removed and the solar beam was directed towards the instrument as shown in Figure 2.5. During a service visit in July 2010, the instrument was relocated and realigned, and other two mirrors were removed. The new configuration is shown in Figure 2.6.

The tracking mirror reflects the solar beam down into the laboratory, from where it is redirected into the instrument. A small part of the solar beam is collected by a tiny mirror and directed into a sensitive photomultiplier tube, which works as a quadrant diode system (see Figure 2.7). The output from the photomultiplier activates the azimuth and elevation motors that

drive the tracking mirror, such that the most intense part of the solar disk is tracked by the mirror.
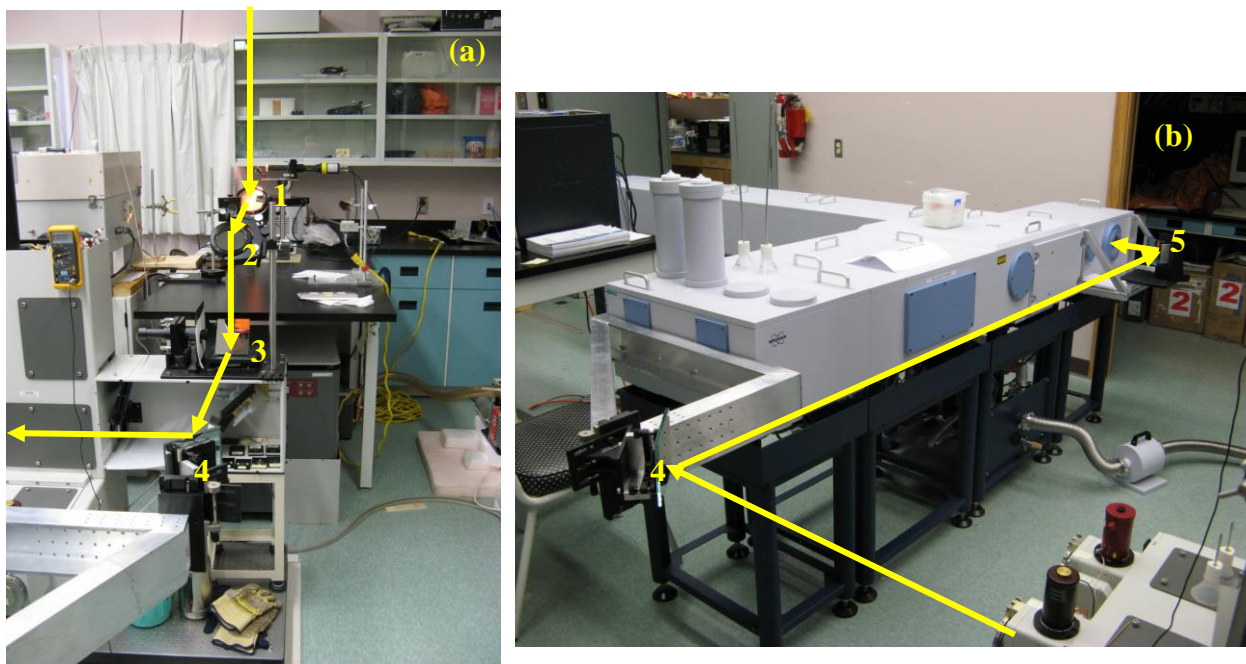
Figure 2.4. The Bruker 125HR setup from July 2006 to March 2009. (a) The beam comes from the solar tracker on the roof and is redirected by the four pickup mirrors towards the instrument. (b) The beam is redirected from the last pickup mirror (#4) towards the 45°mirror located in the front of the instrument's input window.

Table 2.1. NDACC narrow bandpass filters used at Eureka for MIR solar measurements.

Filter number	Wavenumber range (cm^{-1})	Wavelength range (µm)
1	3950 – 4300	2.32 − 2.53
2	2700 – 3500	2.85 − 3.70
3	2420 – 3080	3.25 − 4.13
4	1950 – 2700	3.70 − 5.13
5	1800 – 2200	4.55 − 5.55
6	700 – 1350	7.40 − 14.28
7*	700 – 1000	10.00 − 14.28
8*	1000 – 1400	7.14 − 10.00

* these filters were installed in August 2007.
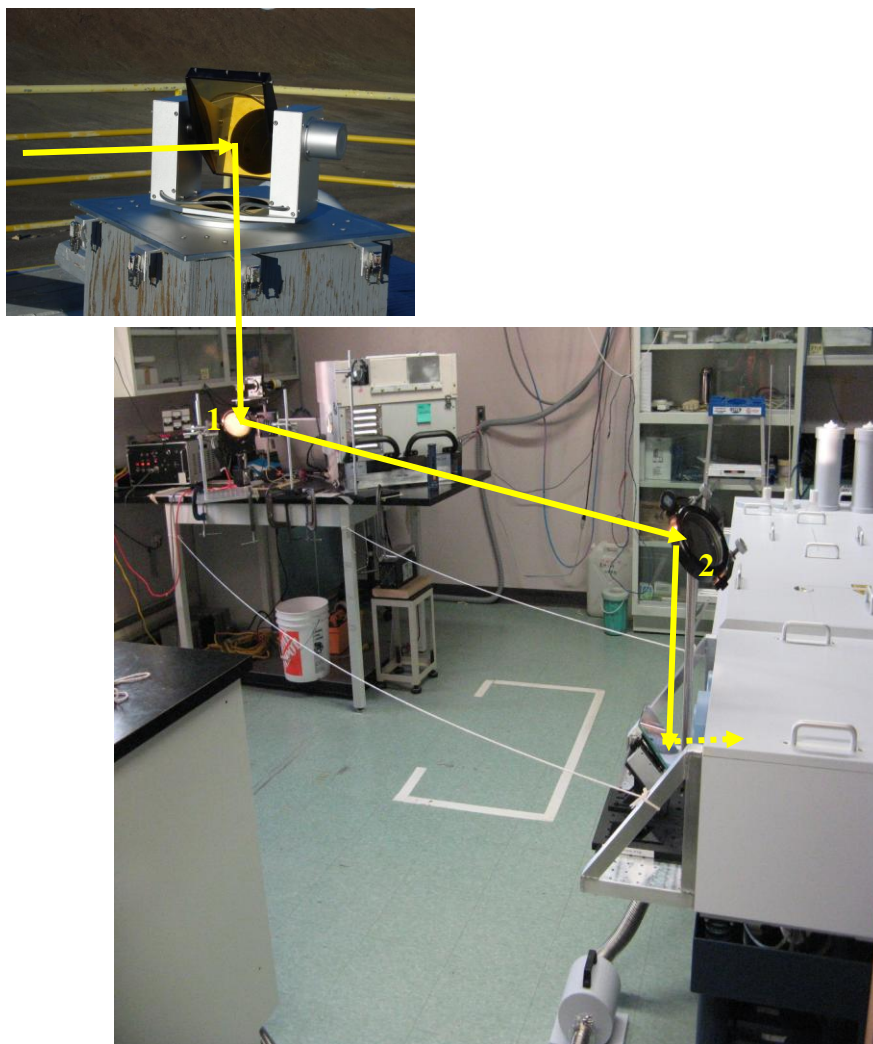
Figure 2.5 The Bruker 125HR setup from March 2009 to July 2010. The top photo shows the solar tracker on the roof, and the bottom photo shows the two pickup mirrors that direct the solar beam (yellow line) to the input window of the instrument.

In the new location of the instrument, the beam coming from the solar tracker hits the 45º flat mirror located in the front of the input window of the instrument. From this mirror, the beam enters the instrument and is directed through the input aperture towards the beamsplitter (see Figure 2.8). Here, the beam is split and sent to the fixed and moving mirrors. The moving mirror is translated on a hybrid bearing which maintains the beam integrity over extremely long OPDs. Upon return, due to the difference in the optical path, the two beams will interfere. The recombined beam is then directed towards the detectors. The instrument has a sample compartment where gas cells can be inserted into the beam before it reaches the detector. The laser controls the position of the moving mirror and is used to determine the data sampling

positions. The monochromatic beam produced by the frequency-stabilized HeNe laser is modulated by the interferometer. In the case of uniform scanner motion, a sinusoidal signal is generated.
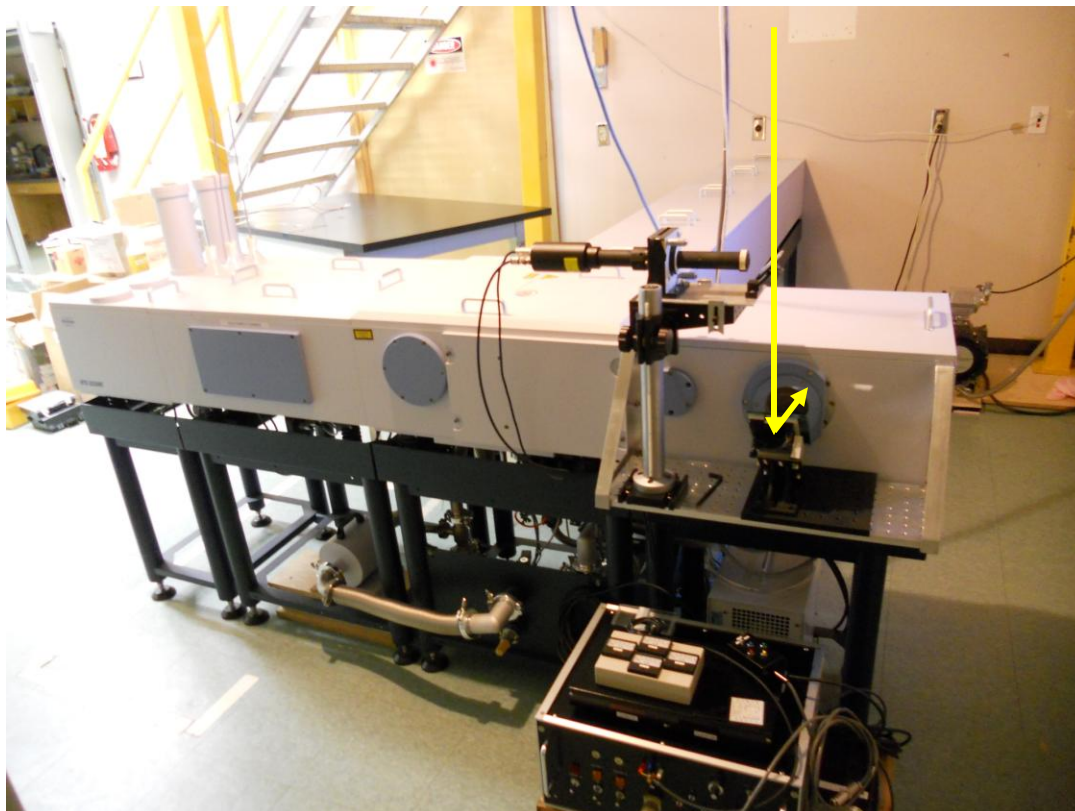
Figure 2.6. The instrument setup from July 2010 onwards.

2.4 Performance of the 125HR

Approximately every two months, an NDACC cell containing a known amount of HBr gas [*Coffey et al.,* 1998] is placed in the sample compartment, and a spectrum is recorded using the internal mid-infrared source. Cell # 30 used at Eureka and was obtained from NIES (National Institute for Environmental Studies) in Japan from the second batch of cells produced by NDACC. It is a 2-cm-long sealed glass cell with 2.5 cm diameter fused sapphire windows and contains HBr at a nominal pressure of ~2 mbar. The HBr spectrum consists of 50 co-added scans and is recorded at the resolution of 0.0035 cm^{-1} that is currently used for solar spectra acquisition. A similar spectrum is recorded without the cell, and a transmission spectrum is generated by taking the ratio of the cell spectrum to the background spectrum. This eliminates systematic features associated with water vapor absorption and detector nonlinearity. 14

microwindows in the transmission spectrum, each containing a single HBr absorption feature, are simultaneously fitted using the LINEFIT 9.0 code, as described by *Hase et al.* [1999] (a typical fit is shown in Figure 2.9). The modulation efficiency and phase error as a function of OPD are adjusted until the fit residual is minimized.
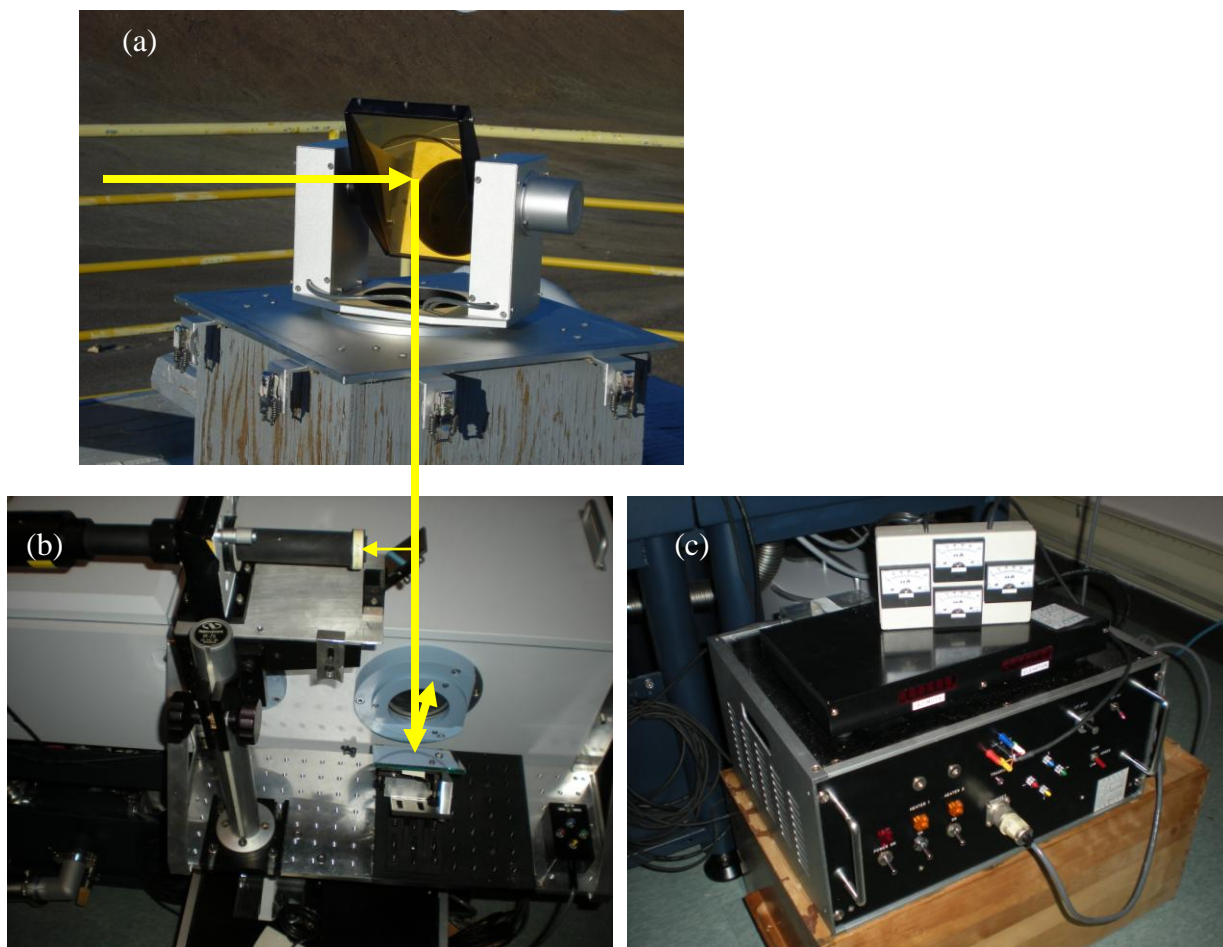
Figure 2.7 The solar tracker used with the 125HR: (a) The tracking mirror, (b) the photomultiplier tube and the tiny pick-off mirror that takes a small part of the solar beam (yellow line) redirecting it into the tube, and (c) the control unit for the solar tracker.

The ILS recorded in August 2011 is shown in Figure 2.10. It is not significantly different from the ILS obtained during previous analyses. There is a slight asymmetry due to the small phase error of ~18x10^{-3} rad at ~70 cm (Figure 2.11). The modulation efficiency (normalized to 1 at ZPD) is increasing slowly then decreases by 0.75% at the maximum OPD. The increase of the modulation efficiency above 1, which corresponds to the ideal instrument with the nominal field-of-view (defined as the radius if the aperture divided by the focal length of the collimator), is

possibly not real according to *Hase et al.* [1999]. They attributed this effect to a slightly smaller field-of-view that is due to an additional black coating on the field-stop apertures, which reduces the nominal aperture value. To date, the instrument has maintained near-perfect alignment, with the modulation efficiency along its path in excess of 98%. Figure 2.12 shows the modulation efficiencies for each HBr cell analysis since installation, while Figure 2.13 shows the corresponding phase errors (less than 0.04 radians, with a peak at approximately 60 cm).
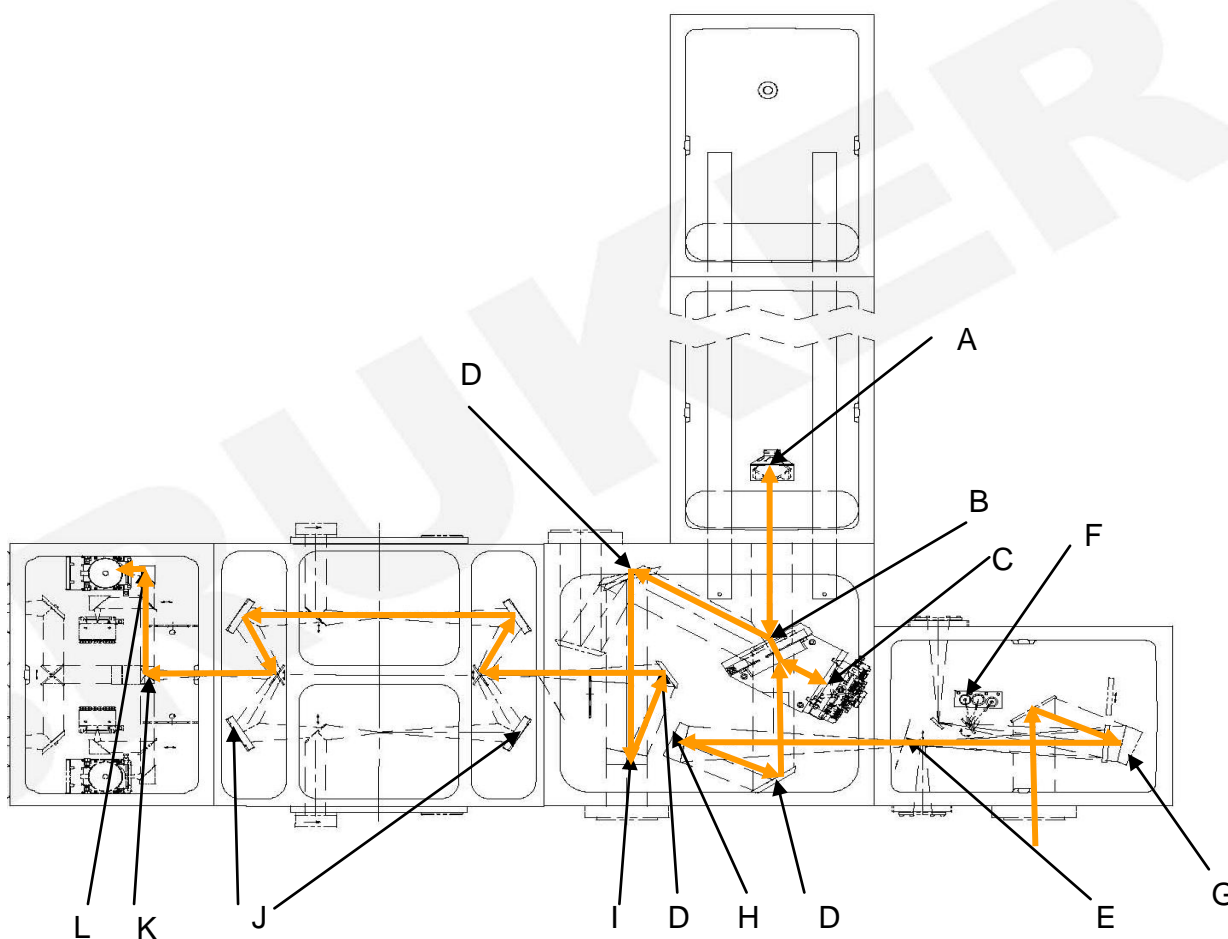
Figure 2.8. Schematic diagram showing the optical path of the solar beam (orange lines) inside the instrument, where A is the scanner with movable retroreflecting mirror, B the beamsplitter, C fixed retroreflecting mirror, D folding mirror, E input aperture, F internal sources, G spherical mirror, H and K collimating parabolic mirrors, I and L focusing parabolic mirrors, and J toroidal mirror. The beam is shown originally by the dashed black lines on which the orange lines were superimposed for a clearer view. (From the Bruker Optics User Manual, 2006)
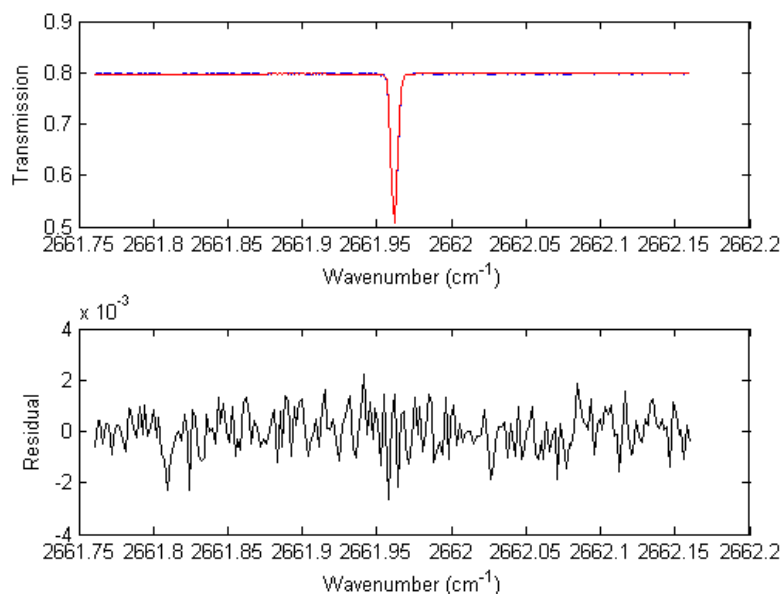
Figure 2.9. Typical fit for a HBr line (top panel) and the corresponding residual (bottom panel). The measured spectrum is shown in blue, while the calculated spectrum is red.

Figure 2.14 (top panel) shows the evolution of the modulation efficiency at 257 cm versus time for all 26 cell measurements shown in Figure 2.12, and the evolution of the maximum phase error (bottom panel) for the same measurements. The x axis indicates the corresponding dates in the form yymmdd. The modulation efficiency is very stable as discussed above, with a very small increase at the end of 2009 and beginning of 2010. This coincides with the instrumental upgrade for NIR measurements, when the mirrors were slightly realigned. The second increase corresponds to a realignment performed in August 2011, after the failure and replacement of the stepper motor that switches the position of the mirror that sends the beam to the two MIR detectors. The phase error has larger variation, and has a decreasing tendency. Note the improvements when the instrument was realigned.

During each ILS analysis, the HBr gas column in the cell is also retrieved, allowing for the direct monitoring of its stability. Figure 2.15 shows a slow decrease (of ~2.4%) of the retrieved HBr column amounts, indicating that the HBr concentration in the cell is decreasing perhaps due to slight cell leakage.
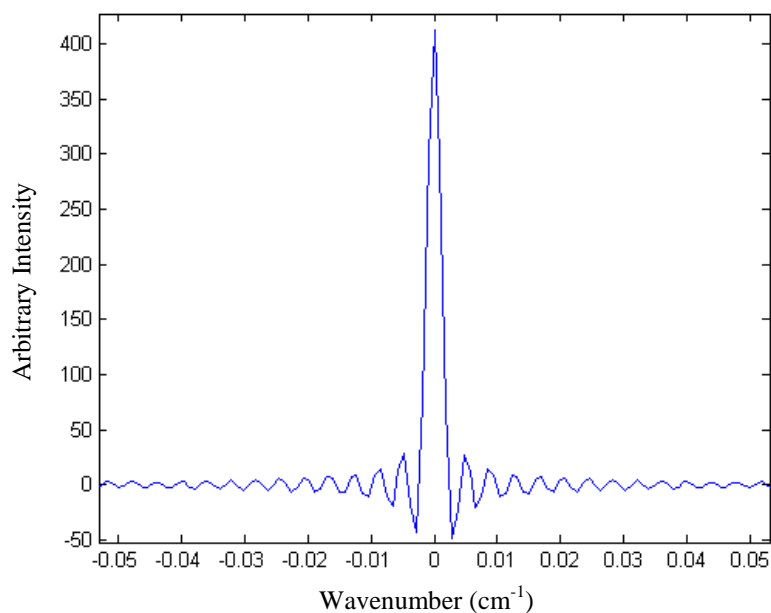
Figure 2.10. ILS obtained from the HBr cell measurement performed on 18 August 2011 with the 125HR using LINEFIT v9.0. 50 scans were acquired, at scanner temperature of 19.5 $^{\circ}$C, with aperture 1.15 mm, preamp. A, filter 3, resolution = 0.0035 cm^{-1}, OPD = 257 cm, and boxcar apodization.
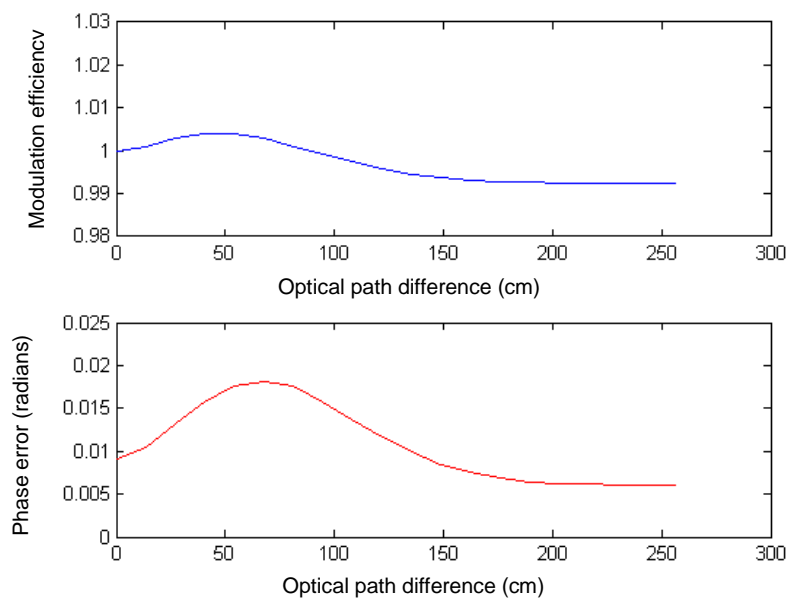
Figure 2.11. The modulation efficiency (top panel) and phase error (bottom panel) derived using LINEFIT v9.0 for the HBr cell measurement performed on 18 August 2011.
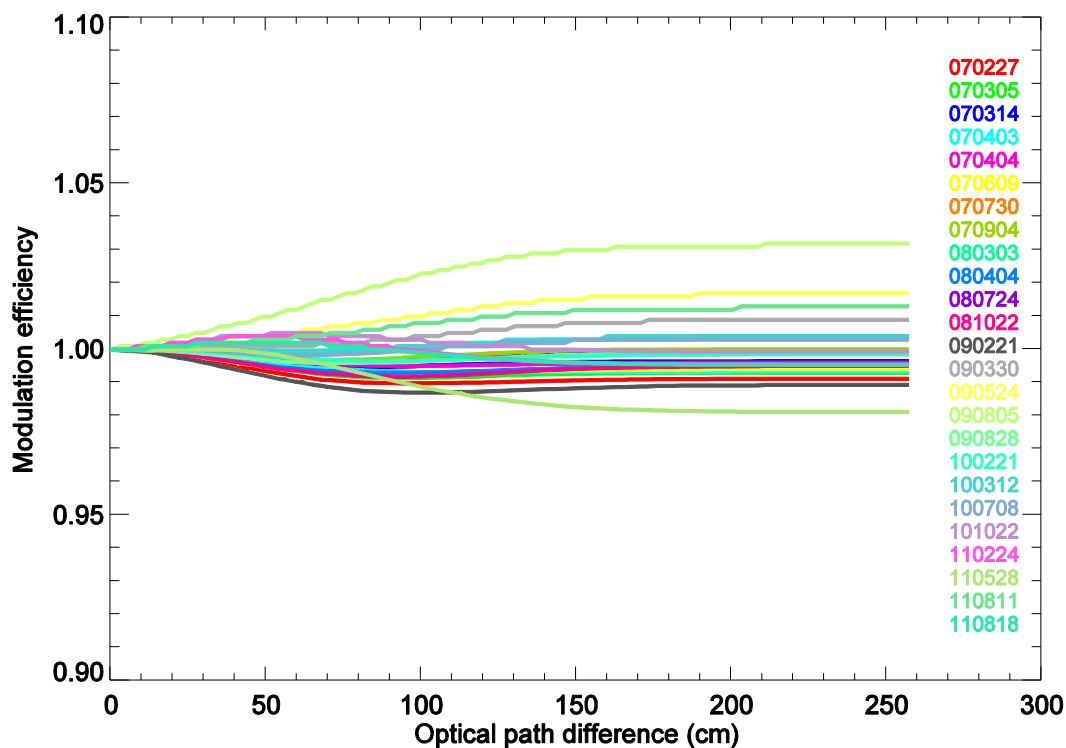
Figure 2.12 The modulation efficiency of the 125HR for the HBr cell measurements performed on the dates shown in the legend (yymmdd).
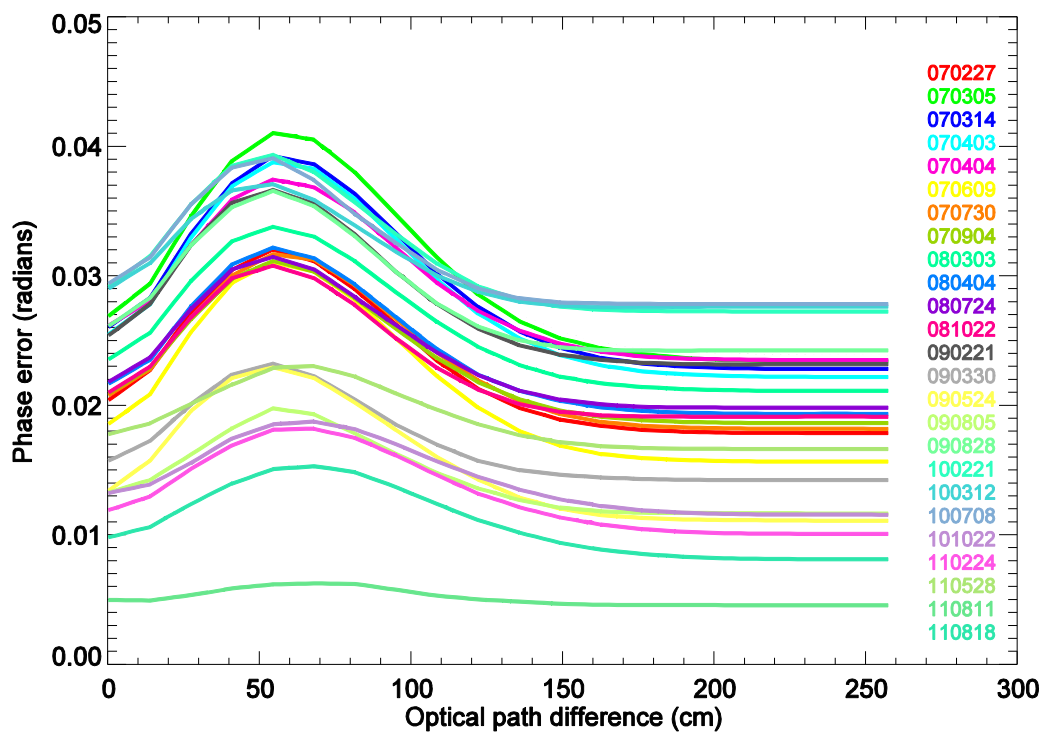
Figure 2.13. Same as Figure 2.12 but for the phase error.
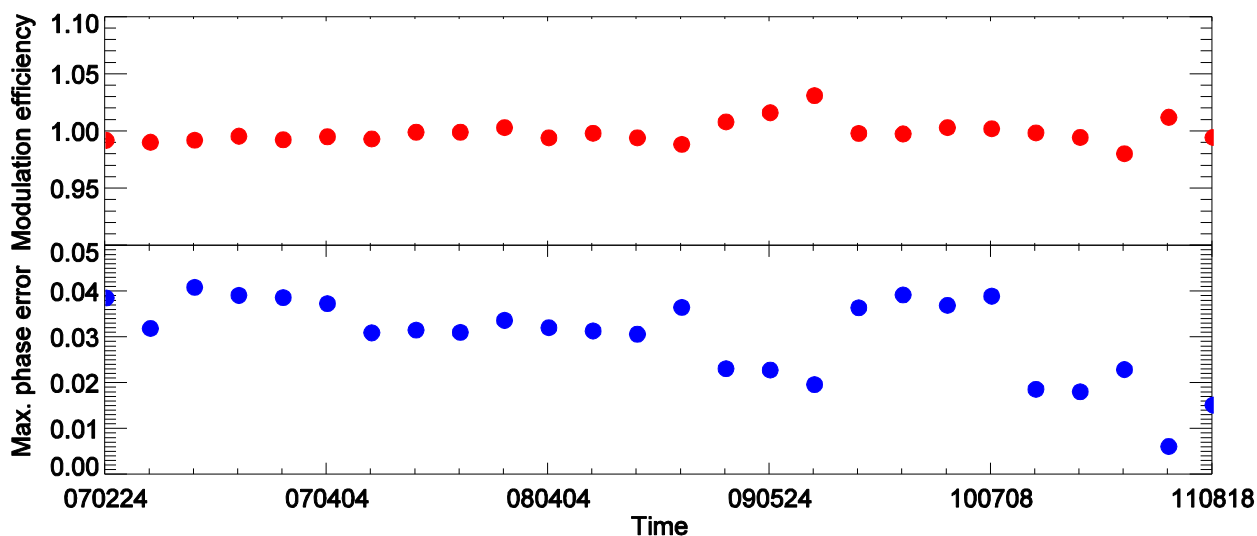
Figure 2.14 Modulation efficiency at 257 cm OPD (red circles) and maximum phase error (blue circles) from February 2007 to August 2011. The x axis indicates the dates of the cell measurement in the form yymmdd (correspond to the dates shown in Figure 2.12).

2.5 Atmospheric Measurements

The IFS 125HR is completely software controlled. OPUS^{TM} version 6.5 spectroscopic software is used to control the instrument and perform measurements. Routine direct-sun absorption measurements are made whenever possible during the sunlit parts of the polar year (approximately February 21 to October 20). Measurements are only possible when clouds are very thin or the sky is clear. In standard operation, the 125HR measures through each of its filters in turn, utilizing a macro to adjust the preamplifier gain to maximize the signal. From July 2006 to March 2009, four scans at 0.0035 cm^{-1} resolution (maximum optical path difference = 257 cm), recorded in both the forward and backward scanning directions and taking in total approximately eight minutes, were recorded and co-added for each spectrum. Beginning March 2009 only two scans were made, taking in total approximately four minutes at the same resolution.

In addition to routine daily measurements, the 125HR has participated in eight campaigns, during which measurements were tailored to meet the goals of the campaigns. These campaigns have included: the 2007, 2008, 2009, 2010, and 2011 Canadian Arctic ACE Validation Campaigns, when the 125HR was operated in conjunction with the University of Waterloo Portable Atmospheric Research Interferometric Spectrometer for the Infrared (PARIS-

IR) and the Environment Canada Bomem DA8 during the 2007 and 2008 campaigns; a 125HR –
DA8 intercomparison exercise in July 2007, as described by *Batchelor et al.* [2010]; an NDACC
NASA Aura satellite validation campaign in August and September 2007, when coordinated
measurements were made at NDACC FTIR sites around the globe; and during a NASA
ARCTAS overflight in April 2008, when the instrument made measurements in the near-infrared
in support of the Total Carbon Column Observing Network (TCCON) [*Washenfelder et al.,*
2006]. The instrument was upgraded for NIR measurements in August 2009 and had a service
visit in July 2010.

Figure 2.15. HBr columns retrieved for cell #30 used to characterize the 125HR alignment. The x axis indicates the dates of the cell measurement in the form yymmdd (correspond to the dates shown in Figure 2.12).
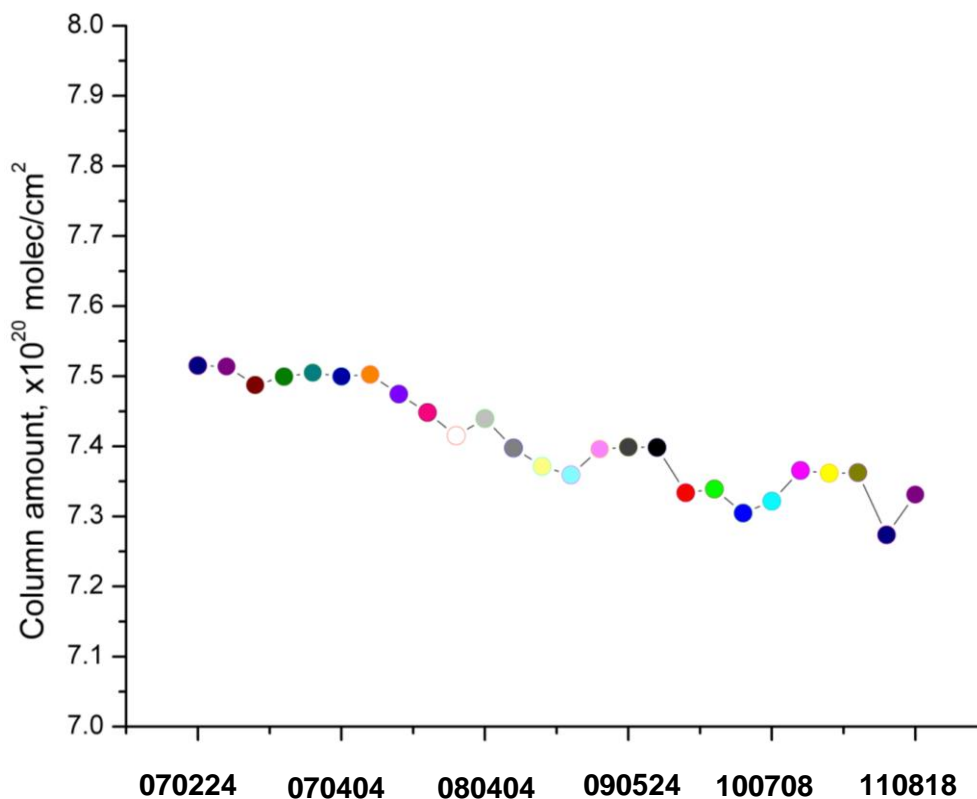
Chapter 3

Trace Gas Retrievals

3.1 Retrieval Theory

The retrieval of a volume mixing ratio (VMR) profile for an atmospheric gas using the absorption spectrum recorded by a ground-based instrument relies on inverse theory. The inverse problem involves finding the best representation of the desired parameter, the retrieved profile in our case, given the measurements made and any appropriate prior information that may be available. It is important to understand and describe the information content of the measurement, to find the relationship between the true and the retrieved state using the inverse method, and to perform an error analysis of the measuring system. The retrieval of a VMR profile from a solar absorption spectrum is an ill-posed problem, because the spectral absorption features contain information to determine the gas concentrations only for a few independent vertical layers. At the same time, the observation geometry and the maximum spectral resolution are factors that limit the vertical resolution of a ground-based instrument. The Optimal Estimation Method (OEM) developed by *Rodgers* [1976, 1999, 2000] is a suitable procedure for solving the under-determined problem of deriving the VMR profile of a target gas from an observed absorption spectrum.

To examine the information content of our measurements, we consider the measurements assembled into a vector $\mathbf{y}$ (the measurement vector) with m elements, and the unknowns into a state vector $\mathbf{x}$ with n elements, describing the state of the atmosphere [*Rodgers,* 2000]. The process of measurement will be described by the forward model, which describes the physics of the measurement process. The relationship between the measurement vector and the state vector can be written as

$$\mathbf{y} = \mathbf{F(x,b)} + \mathbf{\varepsilon} \tag{3.1}$$

where $\mathbf{F(x,b)}$ is the forward model, and $\mathbf{\varepsilon}$ represents the measurement error. $\mathbf{b}$ includes all the parameters which influence the retrieval but are not retrieved (temperature and pressure profiles, absorption cross sections of the atmospheric gases, and instrument profile).

To determine the information content of our measurement, it is convenient to do a linearization of the forward model about the reference state $\mathbf{x}_a$, which is our best estimate of the

true atmosphere, considering that $\mathbf{F(x)}$ is linear within the error bounds of the retrieval. $\mathbf{x}_a$ is the best estimate of the state vector, called the *a priori*, and $\hat{\mathbf{b}}$ is the best estimate of $\mathbf{b}$. We consider $\mathbf{c}$ to include any additional parameters used in the retrieval that do not appear in the forward model.

With these assumptions, and defining the inverse model $\mathbf{I}$, or the retrieval, as the process in which the retrieved profile $\hat{\mathbf{x}}$ is determined from $\mathbf{y}$, we can write that

$$\hat{\mathbf{x}} = \mathbf{I(y,\hat{b},c)} = \mathbf{I(F(x,b)} + \varepsilon, \hat{\mathbf{b}}, \mathbf{c}) . \tag{3.2}$$

Linearizing about $\mathbf{x}_a$, we have

$$\hat{\mathbf{x}} = \mathbf{I[F(x_a,\hat{b}),\hat{b},c]} + \frac{\partial \mathbf{I}}{\partial \mathbf{y}} \frac{\partial \mathbf{F}}{\partial \mathbf{x}} (\mathbf{x} - \mathbf{x_a}) + \frac{\partial \mathbf{I}}{\partial \mathbf{y}} \frac{\partial \mathbf{F}}{\partial \mathbf{b}} (\mathbf{b} - \hat{\mathbf{b}}) + \frac{\partial \mathbf{I}}{\partial \mathbf{y}} \varepsilon . \tag{3.3}$$

We can define the gain matrix, $\mathbf{G}$ as

$$\mathbf{G} = \frac{\partial \mathbf{I}}{\partial \mathbf{y}} \tag{3.4}$$

which shows the sensitivity of the retrieval to the measurement. The partial derivative of the forward model with respect to the state vector defines the $m \times n$ weighting function matrix $\mathbf{K}$

$$\mathbf{K} = \frac{\partial \mathbf{F}}{\partial \mathbf{x}} \tag{3.5}$$

and shows the sensitivity of the forward model to the state vector. Its columns show the change in the measured spectrum that results from a change in the state profile at each of the altitudes in the vector and its rows show the part of the profile that is represented by each measurement [*Rodgers,* 1990]. The partial derivative of the forward model with respect to the forward model parameters shows similarly the sensitivity of the forward model to the forward model parameters

$$\mathbf{K_b} = \frac{\partial \mathbf{F}}{\partial \mathbf{b}} . \tag{3.5'}$$

If we ignore for a moment the measurement errors, we can relate the retrieval to the unknown profile by a transfer function T [*Rodgers,* 1990]:

$$\hat{\mathbf{x}} = \mathbf{I[F(x,b),b,c]} = \mathbf{T(x,b,c)} . \tag{3.6}$$

Studying this transfer function provides a way of understanding the nature of the retrieved state vector. The averaging kernel matrix is defined as

$$\mathbf{A} = \frac{\partial \mathbf{T}}{\partial \mathbf{x}} = \frac{\partial [\mathbf{I(F(x,b),b,c)}]}{\partial \mathbf{x}} = \mathbf{GK} \tag{3.7}$$

and characterizes the combined forward model and retrieval system with respect to the true atmosphere. The rows of the **A** matrix are the averaging kernels (smoothing functions), which describe what proportion of each of the altitude layers in the true profile is included in the determination of the retrieved profile at each layer, in other words they represent the sensitivity of the retrieved state to the true state.

For an ideal observing system, **A** will be a unit matrix, showing that the retrieval at a given altitude comes from that altitude only, but this is not usually the case. The shape of the averaging kernels gives us information about the vertical resolution and can be difficult to interpret if the shape is other than a simple peak. The area under the averaging kernel is found to be approximately unity at levels where the retrieval is accurate [*Rodgers,* 2000]. Summing the elements of each row determines the area under the averaging kernel (also called sensitivity), which is indicative of the fraction of the retrieval that comes from the measurement rather than from the *a priori* [*Vigouroux et al.,* 2008].

Using the definitions above, we find for the retrieved profile:

$$\widehat{\mathbf{x}} = \mathbf{I}[\mathbf{F}(\mathbf{x_a}, \widehat{\mathbf{b}}), \widehat{\mathbf{b}}, \mathbf{x_a}, \mathbf{c}] + \mathbf{A}(\mathbf{x} - \mathbf{x_a}) + \mathbf{GK_b}(\mathbf{b} - \widehat{\mathbf{b}}) + \mathbf{G\varepsilon}. \tag{3.8}$$

Following *Rodgers* [2000], if the measurements were not made, *a priori* would be our only knowledge, so the method will return the *a priori*, or

$$\mathbf{I}[\mathbf{F}(\mathbf{x_a}, \widehat{\mathbf{b}}, \mathbf{c}), \widehat{\mathbf{b}}, \mathbf{x_a}, \mathbf{c}] = \mathbf{x_a} \tag{3.9}$$

and the retrieved profile can be written as the linear combination of the *a priori* profile and the true profile with additional error contributions:

$$\widehat{\mathbf{x}} = \mathbf{x_a} + \mathbf{A}(\mathbf{x} - \mathbf{x_a}) + \mathbf{GK_b}(\mathbf{b} - \widehat{\mathbf{b}}) + \mathbf{G\varepsilon}. \tag{3.10}$$

The procedure for finding the solution $\widehat{\mathbf{x}}$ is to find the probability of obtaining the VMR profile **x** from the measurement **y** using Bayes' theorem:

$$\mathbf{P}(\mathbf{x}|\mathbf{y}) = \frac{\mathbf{P}(\mathbf{x}, \mathbf{y})}{\mathbf{P}(\mathbf{y})}, \tag{3.11}$$

where $\mathbf{P}(\mathbf{x}|\mathbf{y})$ is the conditional probability of obtaining **x** given **y**, $\mathbf{P}(\mathbf{y})$ is the probability of obtaining **y**, and $\mathbf{P}(\mathbf{x}, \mathbf{y})$ is the joint probability of obtaining **x** and **y**. This is described in depth by *Rodgers* [2000], and we will focus here on the results. Assuming Gaussian error statistics, the possible solutions are selected by weighting the measurement and the *a priori* information, the optimal solution being the maximum *a posteriori* solution (MAP). This corresponds to the most

likely state that maximizes the probability density function (*pdf*). Equation 3.10 can then be written as

$$\hat{\mathbf{x}} = \mathbf{x_a} + \mathbf{S_a}\mathbf{K^T}(\mathbf{K}\mathbf{S_a}\mathbf{K^T} + \mathbf{S_\varepsilon})^{-1}\mathbf{K}(\mathbf{x} - \mathbf{x_a}) \tag{3.12}$$

where $\mathbf{S_a}$ and $\mathbf{S_\varepsilon}$ represent the *a priori* and the measurement error covariance matrices, respectively, and $\mathbf{K}$ the Jacobian matrix. This equation assumes not only Gaussian error probabilities, but also a linear relationship between $\mathbf{x}$ and $\mathbf{y}$ ($\mathbf{y} = \mathbf{K}\mathbf{x}$). In general, there is a non-linear relationship $\mathbf{y} = \mathbf{F(x)}$ between the spectrum $\mathbf{y}$ and the profile $\mathbf{x}$, so the most probable solution is given by equating the derivative of the posterior *pdf* to zero:

$$\nabla_\mathbf{x}\left[-2\ln P(\mathbf{x}|\mathbf{y})\right] = \nabla_\mathbf{x}\left\{[\mathbf{y} - \mathbf{F(x)}]^\mathbf{T}\mathbf{S_\varepsilon}^{-1}(\mathbf{y} - \mathbf{F(x)}) + (\mathbf{x} - \mathbf{x_a})^\mathbf{T}\mathbf{S_a}^{-1}(\mathbf{x} - \mathbf{x_a}) + \mathbf{C}\right\} \tag{3.13}$$

$$= \nabla_\mathbf{x}\left[(-\mathbf{F(x)})\right]^\mathbf{T}\mathbf{S_\varepsilon}^{-1}(\mathbf{y} - \mathbf{F(x)}) + \mathbf{S_a}^{-1}(\mathbf{x} - \mathbf{x_a}) \tag{3.14}$$

$$= -\left[\nabla_\mathbf{x}\mathbf{F(x)}\right]^\mathbf{T}\mathbf{S_\varepsilon}^{-1}(\mathbf{y} - \mathbf{F(x)}) + \mathbf{S_a}^{-1}(\mathbf{x} - \mathbf{x_a}) = \mathbf{0}, \tag{3.15}$$

where $\mathbf{C}$ is a constant.

The value of $\mathbf{y}$ is obtained from $\mathbf{x}$ by solving Equation 3.15; the difficulty in numerically solving this equation depends on the degree of nonlinearity of the forward model, $\mathbf{F(x)}$. The gradient of the cost function, $\mathbf{J(x)}$, defined as

$$\mathbf{J(x)} = (\mathbf{y} - \mathbf{K}\mathbf{x})^\mathbf{T}\mathbf{S_\varepsilon}^{-1}(\mathbf{y} - \mathbf{K}\mathbf{x}) + (\mathbf{x} - \mathbf{x_a})^\mathbf{T}\mathbf{S_a}^{-1}(\mathbf{x} - \mathbf{x_a}) \tag{3.16}$$

where $\mathbf{K(x)} = \nabla_\mathbf{x}\mathbf{F(x)}$, gives

$$\nabla_\mathbf{x}\mathbf{J(x)} = -\left[\nabla_\mathbf{x}\mathbf{F(x)}\right]^\mathbf{T}\mathbf{S_\varepsilon}^{-1}(\mathbf{y} - \mathbf{F(x)}) + \mathbf{S_a}^{-1}(\mathbf{x} - \mathbf{x_a}). \tag{3.17}$$

A straightforward numerical method for finding the zero of the gradient of the cost function is the Newtonian iteration, and for $\nabla_\mathbf{x}\mathbf{J(x)} = \mathbf{0}$, the (i+1)[th] iteration of $\mathbf{x}$ gives

$$\mathbf{x}_{i+1} = \mathbf{x}_i - \left[\nabla_\mathbf{x}\nabla_\mathbf{x}\mathbf{J(x}_i)\right]^{-1}\nabla_\mathbf{x}\mathbf{J(x}_i). \tag{3.18}$$

Substituting the cost function and rearranging to express $\mathbf{x}_{i+1}$ as a departure from $\mathbf{x}_a$ rather than $\mathbf{x}_i$, we find that

$$\mathbf{x}_{i+1} = \mathbf{x_a} + \{\mathbf{S_a}^{-1} + [\nabla_\mathbf{x}\mathbf{F(x}_i)]^\mathbf{T}\mathbf{S_\varepsilon}^{-1}\nabla_\mathbf{x}\mathbf{F(x}_i)\}^{-1}[\nabla_\mathbf{x}\mathbf{F(x}_i)]^\mathbf{T}\mathbf{S_\varepsilon}^{-1}\{\mathbf{y} - \mathbf{F(x}_i) + [\nabla_\mathbf{x}\mathbf{F(x}_i)](\mathbf{x}_i - \mathbf{x_a})\} \tag{3.19}$$

$$= \mathbf{x_a} + \mathbf{S_a}\{[\nabla_\mathbf{x}\mathbf{F(x}_i)]^\mathbf{T}\{\nabla_\mathbf{x}\mathbf{F(x}_i)\mathbf{S_a}[\nabla_\mathbf{x}\mathbf{F(x}_i)]^\mathbf{T} + \mathbf{S_\varepsilon}\}^{-1}\{(\mathbf{y} - \mathbf{y}_i) + [\nabla_\mathbf{x}\mathbf{F(x}_i)](\mathbf{x}_i - \mathbf{x_a})\} \tag{3.20}$$

in which $\mathbf{y}_i = \mathbf{F(x}_i)$ is produced by the forward model using the ith estimate of the VMR profile. A convergence criterion is needed to terminate the iterations. Usually the calculated spectrum $\mathbf{y}_i = \mathbf{F(x}_i)$ is compared to the measured spectrum, and the difference between the two is required to be smaller than the estimated error times a tolerance factor.

3.2 Error Analysis

To evaluate the errors, we rewrite Equation 3.6 including the errors in the measurements and model parameters

$$\widehat{\mathbf{x}} = \mathbf{I}\big[\mathbf{F}(\mathbf{x},\mathbf{b}), \Delta\mathbf{f}(\mathbf{x},\mathbf{b},\mathbf{b'}) + \mathbf{\varepsilon}, \mathbf{b}, \mathbf{c}\big], \tag{3.21}$$

where $\Delta\mathbf{f}(\mathbf{x},\mathbf{b},\mathbf{b'})$ is the difference between the best known forward model and the perfect forward model (the error in the forward model relative to the real physics). $\mathbf{b'}$ represents parameters of the forward function, $\mathbf{f}(\mathbf{x},\mathbf{b},\mathbf{b'})$, that have been ignored in constructing the approximate forward model $\mathbf{F}(\mathbf{x},\mathbf{b})$, and $\mathbf{c}$ again represents any additional parameters used in the retrieval that do not appear in the forward model. Replacing the forward function by the forward model including the error term we find

$$\widehat{\mathbf{x}} = \mathbf{I}(\mathbf{F}(\mathbf{x},\mathbf{b}) + \Delta\mathbf{f}(\mathbf{x},\mathbf{b},\mathbf{b'}) + \mathbf{\varepsilon}, \widehat{\mathbf{b}}, \mathbf{c}). \tag{3.22}$$

Linearizing the forward model about $\mathbf{x} = \mathbf{x}_a$ and $\mathbf{b} = \widehat{\mathbf{b}}$ we obtain

$$\widehat{\mathbf{x}} = \mathbf{I}(\mathbf{F}(\mathbf{x}_a,\widehat{\mathbf{b}}) + \mathbf{K}(\mathbf{x} - \mathbf{x}_a) + \mathbf{K}_b(\mathbf{b} - \widehat{\mathbf{b}}) + \Delta\mathbf{f}(\mathbf{x},\mathbf{b},\mathbf{b'}) + \mathbf{\varepsilon}, \widehat{\mathbf{b}}, \mathbf{c}) \tag{3.23}$$

and further linearizing about $\mathbf{y}$ we obtain

$$\widehat{\mathbf{x}} = \mathbf{I}\big[\mathbf{F}(\mathbf{x}_a,\widehat{\mathbf{b}}), \widehat{\mathbf{b}}, \mathbf{x}_a, \mathbf{c}\big] + \mathbf{G}\big[\mathbf{K}(\mathbf{x} - \mathbf{x}_a) + \mathbf{K}_b(\mathbf{b} - \widehat{\mathbf{b}}) + \Delta\mathbf{f}(\mathbf{x},\mathbf{b},\mathbf{b'}) + \mathbf{\varepsilon}\big]. \tag{3.24}$$

Substituting Equations 3.7 and 3.9 in 3.24 and rearranging, we obtain the expression for the error in $\widehat{\mathbf{x}}$:

$$\begin{aligned} \widehat{\mathbf{x}} - \mathbf{x} &= (\mathbf{A} - \mathbf{I}_n)(\mathbf{x} - \mathbf{x}_a) \quad \text{...smoothing error} \\ &+ \mathbf{G}\mathbf{K}_b(\mathbf{b} - \widehat{\mathbf{b}}) \quad \text{...model parameter error} \\ &+ \mathbf{G}\Delta\mathbf{f}(\mathbf{x},\mathbf{b},\mathbf{b'}) \quad \text{...forward model error} \\ &+ \mathbf{G}\mathbf{\varepsilon} \quad \text{...retrieval noise} \end{aligned} \tag{3.25}$$

where $\mathbf{I}_n$ is the n by n unity matrix.

Since we do not know the true state, the error covariance matrices over an ensemble of states will be used to determine the total error in our observations

$$\mathbf{S}_s = (\mathbf{A} - \mathbf{I}_n)\mathbf{S}_a(\mathbf{A} - \mathbf{I}_n)^{\mathbf{T}} \tag{3.26}$$

$$\mathbf{S}_f = \mathbf{G}\mathbf{K}_b\mathbf{S}_b\mathbf{K}_b^{\mathbf{T}}\mathbf{G}^{\mathbf{T}} \tag{3.27}$$

$$\mathbf{S}_m = \mathbf{G}\mathbf{S}_\varepsilon\mathbf{G}^{\mathbf{T}} \tag{3.28}$$

where $\mathbf{S}_b = \in\{(\mathbf{b} - \widehat{\mathbf{b}})(\mathbf{b} - \widehat{\mathbf{b}})^{\mathbf{T}}\}$ is the error covariance matrix of $\mathbf{b}$. $\mathbf{S}_s$ is the error covariance of the smoothing of the real VMR profile using the averaging kernel matrix. It is a systematic error

on short time scales, but random on long time scales. This is because its estimate is only correct as S_a (the covariance matrix built up of our best estimate of the covariance of the atmosphere about the *a priori* profile) becomes the covariance of a real ensemble of atmospheric VMR profiles and x_a gives the true mean atmospheric VMR profile. The model parameter error covariance, S_f, is caused by biases in forward model parameters, and can contain both random errors (from temperature and pressure profile, solar zenith angle) and systematic errors (from spectroscopic parameters). The forward model error is a systematic error usually neglected, since calculating it without knowing x and b is very difficult. S_m is a random error and is the error covariance induced by the random measurement noise propagating into the retrievals.

As previously mentioned, the measurement is a vector with *m* elements. These elements could be linearly dependent and some of them not relevant to the quantity that we are trying to determine. The number of independent pieces of information contained in the measurement is called by *Rodgers* [2000] "degrees of freedom for signal", d_s or DOFS. In the presence of errors, these pieces of information will have an associated uncertainty, which may be so large that they make the measurement worthless. The "degrees of freedom for noise", d_n, represents the number of independent pieces of information which are not useful. Determining the trace of the averaging kernel matrix, **tr(A)**, is a simple way to calculate d_s [*Rodgers,* 2000].

3.3 The SFIT2 Retrieval Algorithm

The SFIT2 profile retrieval algorithm used in this work was developed by C. P. Rinsland (NASA Langley Research Center) and B. J. Connor (National Institute of Water and Atmospheric Research, New Zealand). It is widely used for the analysis of ground-based solar absorption spectra and "*is based on the fitting of a calculated spectrum to the recorded one by means of adjustment to the target gas profile and supplementary instrument-related parameters*" (*Pougatchev et al.,* 1995). SFIT2 employs the OEM discussed above [*Rodgers,* 1976, 1990, 2000]. The solution is found iteratively, and the iteration is performed until the difference between two successive iteration changes the calculated spectrum by less than the estimated error times a tolerance factor. The tolerance factor for our retrievals was chosen to be 0.1 and the estimated measurement error given by the inverse of the signal-to-noise ratio of the measurement.

The forward model of SFIT2 is "*a multi-layer, multi-species, line-by-line transfer model which was developed for the analysis of FTIR spectra*" [*Pougatchev et al.,* 1995]. The model

assumes that the layers are homogeneous and in local thermodynamic equilibrium; it also assumes a Voigt line shape function, refractive ray-tracing calculations, and ILS function calculations (including the effects of apodization, maximum OPD, finite field-of-view) [*Pougatchev et al.,* 1995].

Prior to performing the retrieval, some input information has to be prepared: a) a model atmosphere; b) line parameters; c) instrumental parameters, and d) small regions of the spectrum, called microwindows, where the target gas has absorption lines. The atmospheric profile (P, T) for the SFIT2 analysis can be provided by the user or a ray-tracing program, *fscatm,* can be used to produce this profile [*Gallery et al.,* 1983]. In this work, daily pressure-temperature profiles were obtained from the average of the twice-daily radiosondes launched at Eureka, supplemented with the National Centre for Environmental Prediction (NCEP) profiles above the maximum altitudes of the radiosondes, and with the 1976 U.S Standard Atmosphere profile above 50 km [*Batchelor et al.,* 2009]. *fscatm* converts pressure, temperature and *a priori* VMR profiles specified on 61 layers to density-weighted pressure, temperature and VMR profiles on a 38-layer grid used by SFIT2 for the Eureka retrievals. It also provides the air mass distribution (the number of molecules as a function of altitude) for each model atmosphere. The 38-layer retrieval grid increases by approximately 4% in thickness for each successive layer, from 0.8 km thickness at 1 km to 13 km at 100 km. The HITRAN 2004 and updates spectroscopic linelist [*Rothman et al.,* 2005] was used for line-by-line calculations of the atmospheric spectrum. A single set of *a priori* VMR profiles was used to eliminate the variations in the long-term trend caused by the use of different (*e.g.,* seasonal) *a priori* VMR profiles.

The absorption spectra are converted to binary format prior to the retrieval. There is also a *meta-data* file associated with each spectrum containing information about the site, latitude, longitude, solar zenith angle, maximum path difference, field-of-view, imposed apodization, *etc*. A *binput* file is also created to give information about what molecules are fitted and the *a priori* uncertainty of mixing ratios in each layer. For the interfering species only, profile scaling is done. The *binput* file also contains the calculation and forward model parameters, *a priori* and uncertainties, solar spectrum parameters (if the solar spectrum is to be included), and also information for each microwindow.

The user must construct the measurement noise and *a priori* covariance matrices $(\mathbf{S}_\varepsilon, \mathbf{S}_a)$ used in the iterative retrieval scheme. A realistic estimation is necessary, since together with the weighting function matrix $\mathbf{K}$, these determine the quantity and vertical distribution of the

independent pieces of information in the retrieval. While the actual signal-to-noise ratios (SNRs) of the spectra are very high (sometimes exceeding 1000), the *ad hoc* SNR is a fitting parameter that defines the measurement noise covariance $\mathbf{S}_\varepsilon$ with diagonal elements set to $1/(\text{SNR})^2$. The *ad hoc* SNR is usually tuned to ensure optimal fitting of the calculated to the measured spectra by plotting the "trade-off curve" of the root-mean-square (RMS) fitting residual against SNR for each gas. The use of low values of SNR results in high RMS residuals when insufficient information comes from the measurements. As the SNR is increased, the RMS residual decreases, as the measurement contributes more to the retrieval, then levels off, at which point the retrieval is attempting to fit noise. An *ad hoc* value of the SNR near the elbow of this curve ensures that the retrieval is not being under or over fitted.

During the iterative retrieval, the model atmosphere is used in each iteration to calculate the infrared absorption spectrum for the target gas (and for the significantly absorbing interfering species) in one or multiple bandpasses or microwindows. To organize and automate the SFIT2 analysis on large data sets, a program called *zephyr2* [*Wood et al.*, 2000] was used. The result of the retrieval is the full vertical profile of the target gas, the state vector $\hat{\mathbf{x}}$ consisting of 38 target gas profile elements. For the major interfering species, only the scaling factors applied to the *a priori* profiles are retrieved. The forward model parameters, *i.e.*, the wavenumber shift, background slope, solar line shifts, and phase error are also retrieved.

3.4 Implementation of SFIT2

The SFIT2 retrieval algorithm version 3.92c, released on March 19, 2007 was implemented in April 2007 (see Section 3.4) and used along with the error calculation (see Section 3.5) implemented during summer 2007 for retrievals at Eureka [*Batchelor et al.,* 2009]. The results discussed in this work were obtained using this version of SFIT2 along with the HITRAN 2004 and updates spectroscopic linelist. The following sections discuss the input parameters used for the retrievals.

3.4.1 *A priori* **profiles**

The starting point in building the *a priori* profiles for Eureka [*Keeyoon Sung,* personal communication] was the *a priori* VMR set used at the high-latitude NDACC site at Kiruna, Sweden [*Meier et al.,* 2004a,b]. Most of these *a priori* VMR profiles were updated using a variety of climatological data sets. For O_3, HCl, HF, NO, NO_2, CH_4, and H_2O, more than 7000

HALOE profiles from 1991 to 2005 were used [http://haloedata.larc.nasa.gov/home/ index.php; *Brühl et al.,* 1996; *Gordley et al.,* 1996; *Park et al.,* 1996; *Russell et al.,* 1996a,b; *Randel et al.,* 2002]. Monthly mean VMRs reported in the SPARC2000 compilations were used for N_2O and HNO_3 [http://www.sparc.sunysb.edu/ html/updates.html; *Randel et al.,* 2002], while MIPAS VMR profiles from 2002 to 2004 were used for $ClONO_2$ [*Höpfner et al.,* 2007]. For each species, the *a priori* profiles were taken to be the zonally averaged mean VMR profiles of the climatological data sets available at latitudes higher than 65ºN. The mean profiles were calculated taking into account the non-uniform temporal distribution of input profiles, to eliminate sampling biases, *i.e.,*

$$\bar{\mathbf{x}} = \frac{1}{n(s)} \sum_s \frac{1}{n(m)} \sum_m \frac{1}{n(y)} \sum_y \frac{1}{n(k)} \sum_k \mathbf{x}_{kyms} \, , \tag{3.29}$$

where n is the number of profiles available and the indices are s for sunset/sunrise mode, m for month from March through September, y for year of observation, and k for altitude index in the data available at latitudes higher than 65ºN [*Keeyoon Sung,* personal communication]. Figure 3.1 shows the *a priori* profiles for the gases retrieved on a regular basis at Eureka.

The same data sets were used to calculate VMR variances as a function of altitude. From these, the largest values were adopted as the diagonal elements of the *a priori* $\mathbf{S_a}$ covariance matrix to ensure that $\mathbf{S_a}$ encompassed the full range of observed variability. For $ClONO_2$, whose VMR profile experiences substantial seasonal variations (by a factor of two or greater), a covariance of 100% was used [*Keeyoon Sung,* personal communication].

For ozone only, the $\mathbf{S_a}$ covariance matrix diagonal elements were not constant for each altitude level. They were determined from the 16-year mean (1993-2008) Environment Canada ozonesonde measurements at Eureka for the sunlit February-September period. Figure 3.2 shows all 1275 individual profiles, along with the mean profile and the one standard deviation from the mean. Figure 3.3 illustrates the one standard deviation from the mean, when the mean was calculated in three different ways: (1) monthly mean profiles were calculated from which yearly means and finally the total mean were calculated; (2) yearly means were calculated from individual profiles, followed by the total mean calculation; (3) the mean was calculated from all individual profiles. Based on these results, the $\mathbf{S_a}$ covariance matrix diagonal elements were set at 30% from ground to 6 km and from 17-35 km, and gradually increases in between, peaking at 75% at 10 km. Average HALOE ozone data from the same months were used above 35 km for

both $\mathbf{x_a}$ and $\mathbf{S_a}$ [*Brühl et al.,* 1996]. Above 35 km, the $\mathbf{S_a}$ diagonal elements were kept constant at 30%.
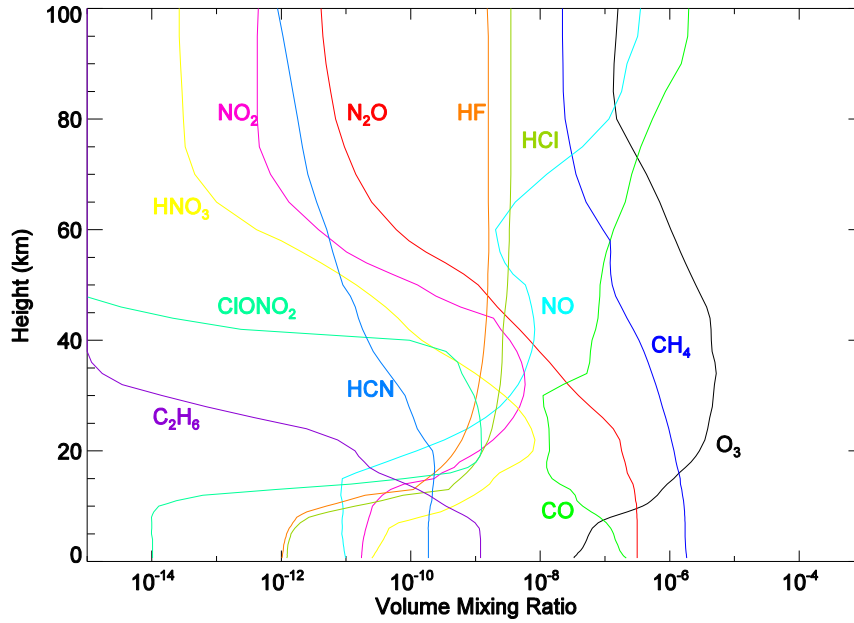
Figure 3.1. Eureka *a priori* profiles for the ten NDACC target gases, and NO and NO_2, determined as described in the text.

An interlayer correlation (ILC) parameter was also determined from correlation matrices calculated using the same climatological data sets. The ILC values were determined by examining plots of the correlation matrix, $\mathbf{R}$, (not shown here) of the VMRs from the climatological data used to derive $\mathbf{x_a}$, calculated using

$$\mathbf{R} = \frac{1}{N}\left[\mathbf{S}_a^{-1}(\mathbf{x}_a - \bar{\mathbf{x}}_a)(\mathbf{x}_a - \bar{\mathbf{x}}_a)^{\mathrm{T}}\mathbf{S}_a^{-\mathrm{T}}\right], \tag{3.30}$$

where $\mathbf{x_a}$ and $\bar{\mathbf{x}}_a$ are the individual and mean VMR profiles from the climatological data, respectively. $\mathbf{S_a}$ is the diagonalized covariance of $\mathbf{x_a}$, and N is the total number of individual profiles. This ILC was then used to generate the off-diagonal elements of $\mathbf{S_a}$ during the retrieval, based on a Gaussian distribution, which is a widely used approach in the NDACC IRWG. The diagonal values of $\mathbf{S_a}$ and the ILC for each retrieved gas is given in Table 3.1.

3.4.2 Microwindows

A complete set of microwindows has been defined based on synthetic spectra simulated with the constructed *a priori* VMR set and on averaging kernel information obtained in

preliminary retrievals from the Eureka DA8 FTIR [*Dejian Fu* and *Keeyoon Sung,* personal communication]. Since the inclusion of more lines in the fit provides a better constraint on the parameters to be determined in the spectrum fitting, wider microwindows or simultaneous fit of multiple microwindows were employed for the retrieved trace gases. The microwindows used for the Eureka 125HR retrievals are listed in Table 3.1, along with the corresponding interfering species.
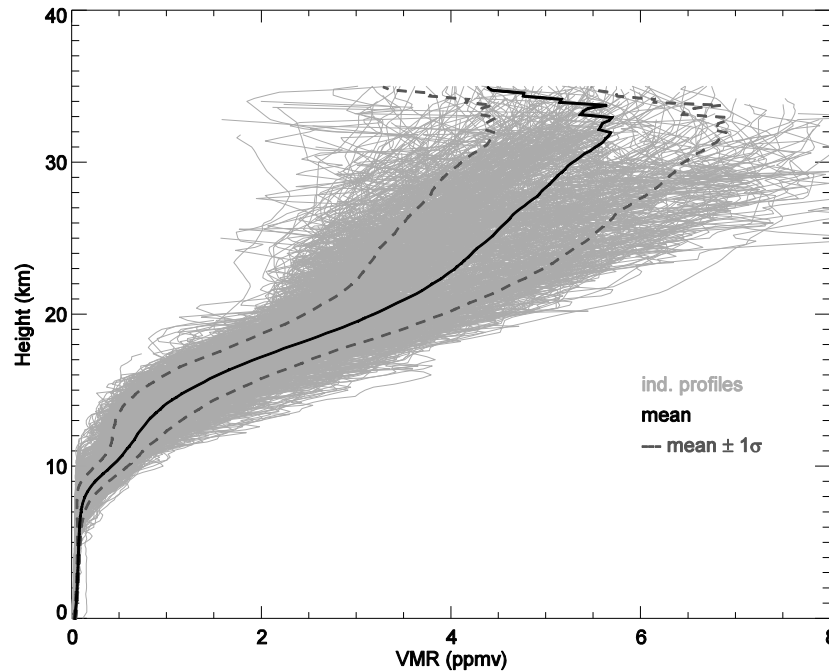
Figure 3.2. Ozonesonde VMR profiles (light grey) from 1993 to 2008. The mean profile is shown with the black solid line, while the black dashed lines indicate ± one standard deviation from the mean.

3.5 Implementation of Error Analysis

The error calculations for retrievals at Eureka are based on the methodology described in Section 3.2 and implemented as described by *Batchelor et al.* [2009]. In addition to the smoothing (S_s) and measurement (S_m) errors, forward model parameter errors are calculated using a perturbation method and our best estimate of the uncertainties in temperature (S_{temp}), line intensity (S_{lint}), air-broadened half width (S_{lwdth}), and solar zenith angle (S_{sza}). K_b (in Equation 3.27) is determined using a small perturbation of the parameter, while S_b is described by our best estimate of the uncertainty in that parameter. As an example, for the error resulting from the uncertainty in solar zenith angle (S_{sza}), an uncertainty of 0.125° is used, corresponding to the maximum change in solar zenith angle from the center point where the solar zenith angle was

calculated to the end of a four-minute measurement. In the same way, uncertainties resulting from the line parameters are determined by perturbing each of the line intensities and the air-broadened half widths for all lines of the species of interest. In this case, S_b is determined from the maximum uncertainty in the line parameter given in HITRAN 2004 [*Rothman et al., 2005*]. If the uncertainty in the line parameter is unknown, a 20% uncertainty is used. Interference errors, as described by *Rodgers and Connor* [2003] have been calculated to account for uncertainties in retrieval parameters (*i.e.*, wavelength shift, instrument line shape, background slope and curvature, and phase error) and in the interfering gases simultaneously retrieved. These interference errors are referred to as S_{int1} and S_{int2}, respectively.
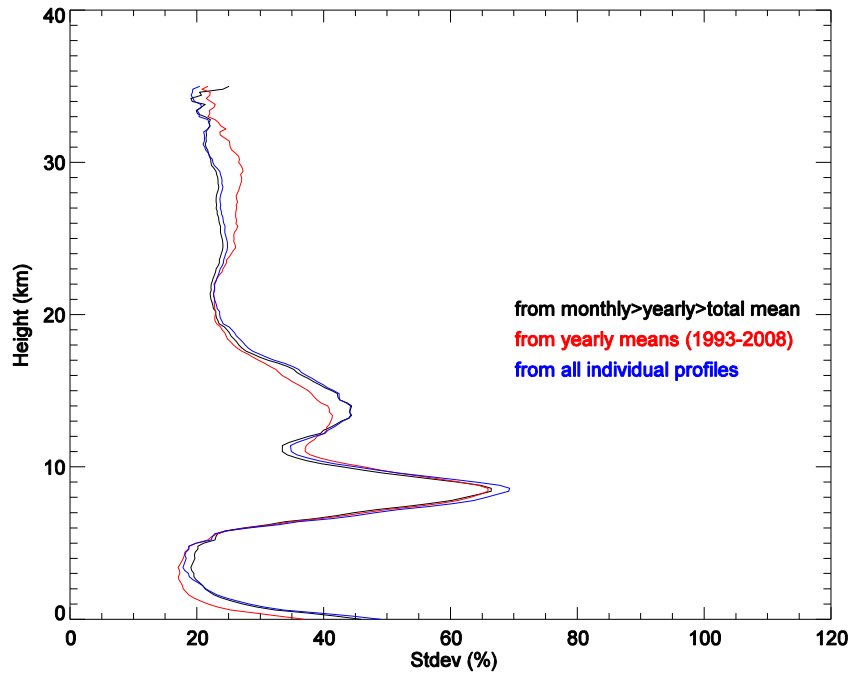
Figure 3.3. One standard deviation from the mean derived from all 1275 ozonesondes launched at Eureka from 1993 to 2008. The means were calculated as described in the text and are color coded as shown in the legend.

The total error (S_{TOTAL}) has been determined by adding all components in quadrature:

$$S_{TOTAL} = \left\{ (S_m^2 + S_{temp}^2 + S_{int1}^2 + S_{int2}^2 + S_{sza}^2) + S_{lint}^2 + S_{lwdth}^2 + S_s^2 \right\}^{1/2} . \qquad (3.31)$$

In many cases, however, it is useful to exclude the smoothing error (because this can be accounted for when doing comparisons) and the spectroscopic line parameter errors (because

Table 3.1 Summary of the retrieval parameters used for the 125HR. Multiple microwindows listed for a single gas are fitted simultaneously. Interfering species are scale-fitted, and are shown for each microwindow. The S_a covariance matrix diagonal elements are constant for all layers except for ozone (see explanation in the text). The ILC and the *ad hoc* signal-to-noise ratio are also specified.

Target gas	Microwindow(s) (cm^{-1})	Interfering species	Target gas S_a (%)	ILC (km)	Interfering gases S_a (%)	SNR
O_3	1000.00-1005.00	H_2O, CO_2, $O_3(676)$, $O_3(667)$, $O_3(686)$, $O_3(668)$, C_2H_4	min 30 max 75*	4	100	100
HCl	2775.72-2775.80	O_3, CH_4, N_2O				
	2821.40-2821.62	HDO, N_2O	50	4	100	100
	2925.75-2926.05	CH_4, NO_2, OCS, O_3				
HNO_3	867.50-870.00	H_2O, OCS, NH_3	100	4	100	100
HF	4038.78-4039.10	H_2O, CH_4, HDO	50	5	100	100
$ClONO_2$	779.85-780.45	CO_2, O_3, HNO_3	100	4	100	100
HCN	3268.00-3268.38	H_2O	50	4	100	200
	3287.00-3287.48	H_2O				
C_2H_6	2976.50-2977.20	H_2O, CH_4, O_3	30	1	100	200
CO	2057.684-2058.00	O_3, CO_2, OCS				
	2069.56-2069.76	O_3, CO_2, OCS				
	2157.507-2159.144	O_3, N_2O, H_2O, OCS	20	4	100	200
N_2O	2481.30-2482.60	H_2O, HDO,CO_2, O_3, CH_4				
	2526.40-2528.20	H_2O, HDO,CO_2, O_3, CH_4	50	7	100	70
	2537.85-2538.80	H_2O, HDO,CO_2, O_3, CH_4				
	2540.10-2540.70	H_2O, HDO,CO_2, O_3, CH_4				
CH_4	2613.70-2615.40	H_2O, HDO, NO_2, CO_2				
	2650.60-2651.30	H_2O, HDO, NO_2, CO_2				
	2835.50-2835.80	H_2O, HDO, NO_2, CO_2	20	4	100	70
	2903.60-2904.03	H_2O, HDO, NO_2, CO_2				
	2921.00-2921.60	H_2O, HDO, NO_2, CO_2				

* The S_a covariance matrix diagonal elements for ozone were set at 30% from the ground to 6 km and from 17-100 km, and gradually increases/decreases between 6 and 18 km, peaking at 75% at 10 km.

these are truly systematic), and as such, we define the total random error ($\mathbf{S_{totr}}$) as the sum of the measurement error, interference errors, and errors due to uncertainties in solar zenith angle and temperature, added in quadrature (represented by the sum within the round brackets in Equation 3.31):

$$\mathbf{S_{totr}} = (\mathbf{S_m^2} + \mathbf{S_{temp}^2} + \mathbf{S_{int1}^2} + \mathbf{S_{int2}^2} + \mathbf{S_{sza}^2})^{1/2}. \tag{3.32}$$

Chapter 4

An Evaluation of Infrared Microwindows for Ozone

Retrievals at Eureka

4.1 Introduction

The focus of this chapter is the evaluation of ozone retrievals from mid-infrared measurements made with the 125HR at Eureka. This work has been published in the Journal of Quantitative Spectroscopy and Radiative Transfer [*Lindenmaier et al.,* 2010]. Particular emphasis has been placed on the selection of microwindows within which ozone is fitted. Many different microwindows containing ozone absorption features have been used by different groups for retrieval of ozone in the past. Until recently, narrow microwindows were used due to computational limitations, *e.g.*, the 1002.6-1003.2 cm^{-1} microwindow used by *Pougatchev et al.* [1995] and the 2107.80-2107.86 cm^{-1} microwindow used by *Hamdouni et al.* [1997]. With recent advances in computational processing power, retrievals over broader microwindows encompassing multiple ozone absorption features have become possible. It has been demonstrated by *Barret et al.* [2002] and *Schneider et al.* [2008] that using broader microwindows increases the degrees of freedom for signal.

Table 4.1 summarizes the mid-infrared ozone microwindows that have been used in ground-based FTIR spectroscopy, demonstrating the lack of consistency in the literature. In the 2400 to 3100 cm^{-1} region, one or more narrow microwindows are usually used. This is due to the high number of non-ozone absorption lines that affect the retrieval. The number of interfering species is much smaller in the 600 to 1400 cm^{-1} region, and therefore, the microwindows tend to be broader in this region.

In this study, spectral simulations were first performed for intervals of 30 cm^{-1} that contained strongly absorbing ozone lines and relatively few absorption lines due to interfering species. From these intervals, 22 smaller microwindows were then identified (as discussed in Section 4.4.1), overlapping with or extending the previously used ozone microwindows listed in Table 4.2. These 22 microwindows were evaluated to determine which is the most appropriate

Table 4.1. Infrared microwindows previously used for ozone retrievals. References are specified along with the spectral range used and the interfering species when they were available. The numbers in brackets for O_3 define its isotopes, with 6, 7, and 8 indicating ^{16}O, ^{17}O, and ^{18}O, respectively.

Reference	Spectral range (cm^{-1})	Interfering species (if available)
Vigouroux et al. [2008], Senten et al. [2008]	1000 - 1005	H_2O, CO_2, C_2H_4, O_3(668), O_3(686)
Wunch et al. [2007], Taylor et al. [2007]	3039.90 - 3040.60	H_2O, CH_4
	2775.68 - 2776.30	CH_4, CO_2, HCl, N_2O
	2778.85 - 2779.20	CH_4, HDO, N_2O
	2781.57 - 2782.06	CH_4, HDO, N_2O, CO_2
Yamamori et al. [2006], Kagawa et al. [2007]	3051.29 - 3051.90	H_2O, CH_4, HDO, CH_3D
Sung et al. [2007], Fu et al. [2007]	2775.78 - 2775.88	HCl, N_2O, CH_4
	2775.68 - 2776.30	
	2778.90 - 2779.50	CH_4, CO_2, HCl, N_2O, HDO, solar lines
	2781.54 - 2782.09	
	1104.78 - 1105.08	CH_3D, CHF_2Cl, CCl_2F_2, H_2CO_2, HDO, O_3(668)
	1119.73 - 1119.95	CHF_2Cl, N_2O, O_3(668)
	1121.67 - 1122.03	O_3(668), H_2CO_2, CHF_2Cl, N_2O, H_2O
	1122.84 - 1123.06	O_3(668), H_2CO_2, CHF_2Cl, CH_3D, CH_4, H_2O
	3039.80 - 3041.70	CH_4, H_2O, CH_3D
Griesfeller et al. [2006]	782.561 - 782.861	not available
	788.850 - 789.369	
	1000.0 - 1005.0	
Hase et al. [2004], Schneider et al. [2007, 2008]	782.56 - 782.86	H_2O, CO_2, solar lines
	788.85 - 789.37	H_2O, CO_2, solar lines
	993.3 - 993.9	H_2O, CO_2, O_3(668), O_3(686)
	1000.0 - 1005.0	
	1007.3 - 1009.0	H_2O, CO_2, O_3 - all isotopologues
	1011.1 - 1013.6	
Meier et al. [2005]	3039.75 - 3040.55	CH_4, H_2O
	3045.08 - 3045.38	CH_4
Barret et al. [2002]	1002.567 - 1003.2	O_3(668), O_3(686)
	1000.0 - 1005.0	O_3(668), O_3(686), H_2O
Notholt et al. [2000]	1002.58 - 1003.50	H_2O
	1003.90 - 1004.38	H_2O
	1004.58 - 1005.00	H_2O
Goldman et al. [1999]	3045.08 - 3045.38	
	3027.42 - 3027.60	
Hamdouni et al. [1997]	2107.80 - 2107.86	not available
	2780.81 - 2780.96	
	3037.32 - 3037.80	
Pougatchev et al. [1996, 1995]	1002.567 - 1003.203	
Rinsland et al. [1996]	764.03 - 764.43	
	773.20 - 773.38	
	781.08 - 781.25	CO_2
	1127.60 - 1129.50	HDO, CH_4
	1146.40 - 1146.56	
	1146.55 - 1147.40	N_2O, H_2O, HDO
	1155.39 - 1155.56	
	1162.85 - 1163.50	
	1163.34 - 1163.48	
	1167.50 - 1167.75	
	2083.50 - 2084.72	H_2O, CO_2
	2754.55 - 2755.45	HDO, CH_4, solar lines
	2778.90 - 2779.20	
	2781.60 - 2781.86	HDO
	2792.65 - 2793.28	N_2O, HDO, solar
	3040.00 - 3040.90	H_2O, CH_4
Adrian et al. [1991], Wegner et al. [1998]	996.5 - 998.5	H_2O, CO_2
	2768.0 - 2773.0	HDO, H_2O, N_2O, CH_4
	2773.0 - 2776.0	CH_4, N_2O, HDO, HCl

for ozone retrievals at our high Arctic site, identifying the spectral region that provides the highest DOFS and the smallest total error. The sensitivity of the retrieval to the stratosphere and troposphere for each microwindow was also investigated.

4.2 The Retrieval Method

The retrieval method used for this study was described in the previous chapter. For this study, the *a priori* covariance matrix $\mathbf{S_a}$, which constrains the retrieval to the *a priori,* was set to 70% on the diagonal with a Gaussian 4-km interlayer correlation from 0.6 to 100 km. The 70% uncertainty represents the maximum variability in ozone observed in the Eureka ozonesonde data record (1σ on the 16-year mean). For the interfering species, the *a priori* diagonal covariances were set to 100% with no interlayer correlation.

The optimal value of the signal-to-noise ratio as a fitting parameter, used to determine the retrieval noise covariance matrix, was chosen after constructing the trade-off curves of the RMS fitting residual as a function of SNR for each microwindow as described in Section 3.3. The total error ($\mathbf{S_{TOTAL}}$) has been determined, as described in Section 3.5, by adding all components in quadrature and not taking into account differences between the random and systematic components (Equation 3.31).

4.3 Methodology

A series of 30 cm^{-1} intervals in the NDACC filter 6 (600-1400 cm^{-1}) and filter 3 (2400-3100 cm^{-1}) regions, corresponding to the HgCdTe and InSb detectors respectively, were investigated. Simulations were used to identify the interfering species for each spectral interval that was studied. The *a priori* VMR profiles and the pressure and temperature profiles used in the simulations were the same as those used in the retrievals (discussed in Sections 4.2 and 3.4, respectively). The mean absorptions for ozone and the interfering species were calculated for each interval of interest. This was very useful in selecting the microwindows where the ozone lines were strong enough for retrieval and minimally influenced by interfering species. The key interfering species that should be considered for each region were also identified. Examples of simulations are shown in Figures 4.1 and 4.2. Figure 4.1 shows a simulation for the 1142–1146 cm^{-1} spectral region, where the N$_2$O lines are interfering strongly with the O$_3$ lines due to overlap
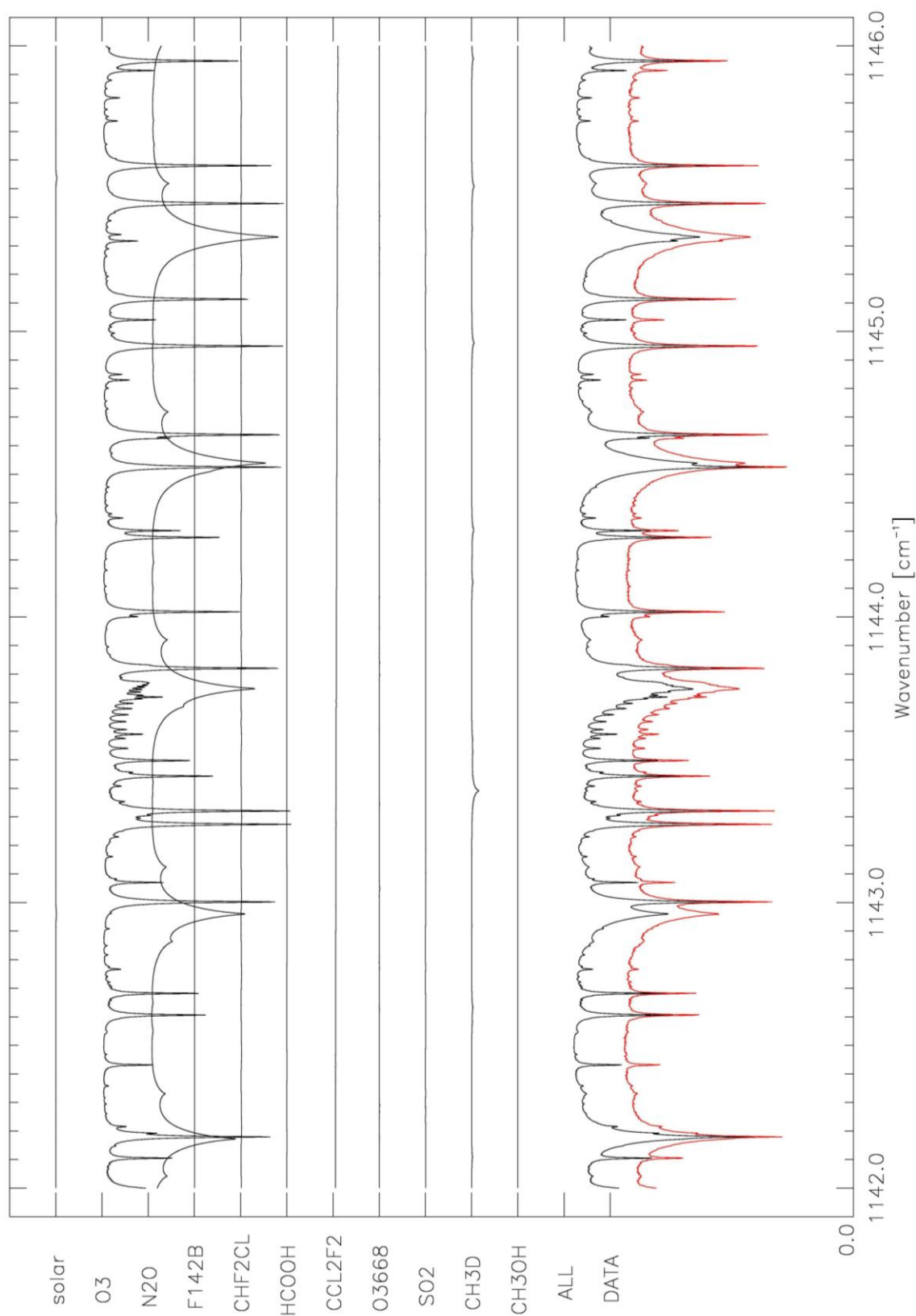
Figure 4.1. Example of simulation for the 1142.0–1146.0 cm⁻¹ spectral region for a spectrum recorded on August 30, 2007. The interfering species are indicated on the y axes, being shifted vertically for clarity. The bottom black line represents the simulated spectrum (considering the contribution of all species), while the red line shows the measured spectrum.
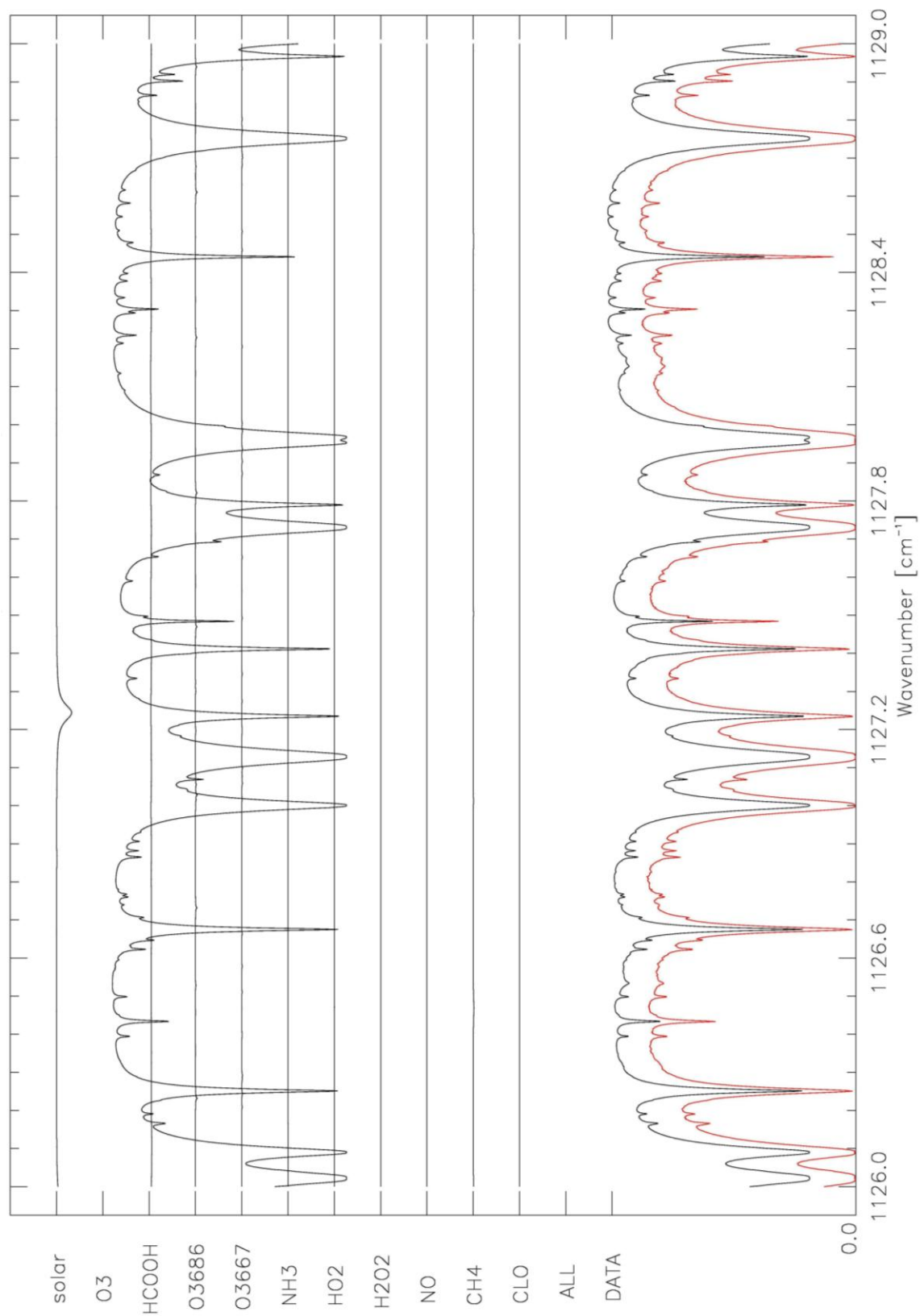
Figure 4.2. Same as Figure 4.1 but for the 1126.0–1129.0 cm⁻¹ spectral region.

of the spectral lines, and is therefore not a good region for O$_3$ retrievals. Figure 4.2 shows the simulation for the 1126–1129 cm^{-1} spectral region, where the interfering species make a very small contribution to the final spectrum, making this region more suitable for O$_3$ retrievals.

After the initial definition of the spectral regions of interest, preliminary retrievals were performed and the RMS fitting residuals were examined for systematic features indicative of issues with the spectroscopic parameters in the HITRAN database. These results were used to refine the choice of microwindows. In total, 22 microwindows and multi-microwindows (meaning that more than one microwindow is fitted simultaneously) were chosen in our study for further analysis and are presented in Table 4.2, along with the values of the ad hoc SNR determined from the trade-off curves for each microwindow combination and the interfering species included in each case. The microwindow designation for each microwindow combination, as listed in column two, approximates the spectral region, with the letter "m" identifying a multi-microwindow fit.

4.4 Results and Discussion

4.4.1 Comparison of Microwindows

Retrievals were performed using spectra recorded during August 2007 and March 2008 using each of the 22 microwindows listed in Table 4.2. Figure 4.3 shows typical fits for a selection of 12 of these microwindows. It is evident that the number and depth of the absorption lines is very different from one microwindow to the other (*e.g.*, 782 compared to 1123). Systematic features in the residual tend to correspond to poor spectral parameters in the HITRAN database, often corresponding to CH$_4$ features. These have been avoided in many cases by removing badly affected regions. In the case of microwindow 3041, the simultaneous retrieval of O$_3$ with CH$_4$ could not remove the spikes in the residual, corresponding to CH$_4$ spectral lines. These residuals may also in part be due to the use of the Voigt line shape in the forward model. Use of a line-shape model that accounts for line-mixing effects can significantly improve the fitting residuals for some spectra [*Mondelain et al.,* 2007]. This has not, however, been investigated in this work. For microwindow 3051m, two narrow microwindows were used in order to exclude regions having similar spikes (not shown in Figure 4.3). Most of the microwindows in the filter 3 region (2400-3100 cm^{-1}) are dominated by interfering species, making it difficult to obtain good retrievals, as seen from the larger fitting residuals.

The vertical sensitivity (indicating the fraction of the retrieval at each altitude that comes from the measurement rather than the *a priori*) of each microwindow was examined using the VMR averaging kernels, which are shown in Figure 4.4 for 20 of the 22 microwindows. These show that microwindows 3023, 3041, 3045, and 3051m display almost no sensitivity in the troposphere, while 984m, 1000, and 1123 are sensitive in this region.

Table 4.2. List of ozone microwindows examined in this work, their designation and spectral range, the ad hoc SNR used in the retrieval, and the interfering species included in the retrievals. The microwindow designation for each microwindow combination, as listed in column two, approximates the spectral region, with the letter "m" identifying a multi-microwindow fit. The numbers in brackets for O$_3$ define its isotopes, with 6, 7, and 8 indicating ^{16}O, ^{17}O, and ^{18}O, respectively.

	Microwindow designation	Spectral range (cm^{-1})	SNR	Interfering species
1	782	780.70 - 783.10	100	CO$_2$, H$_2$O, HNO$_3$, ClONO$_2$, C$_2$H$_2$, CCl$_4$, COF$_2$, C$_2$H$_6$, HCN, solar
		785.55 - 790.30		CO$_2$, H$_2$O, HNO$_3$, ClONO$_2$, C$_2$H$_2$, CCl$_4$, C$_2$H$_6$, HCN, solar
2	984	984.47 - 985.28	100	O$_3$(686), CO$_2$, O$_3$(668), H$_2$O, C$_2$H$_4$
3	984m	984.47 - 985.90	100	O$_3$(686), CO$_2$, O$_3$(668)
		986.10 - 988.09		O$_3$(686), O$_3$(668), CO$_2$, C$_2$H$_4$
		988.30 - 990.00		O$_3$(686), O$_3$(668), CO$_2$, H$_2$O, C$_2$H$_4$
4	987	986.10 - 988.10	100	O$_3$(686), CO$_2$, O$_3$(668), C$_2$H$_4$
5	988	988.70 - 990.00	100	O$_3$(686), CO$_2$, O$_3$(668)
6	1000	1000.00 - 1004.5	100	H$_2$O, CO$_2$, O$_3$(676), O$_3$(667), O$_3$(686), O$_3$(668), C$_2$H$_4$
7	1088	1088.10 - 1091.00	100	CO$_2$, H$_2$O, O$_3$(668), CCl$_3$F, CCl$_2$F$_2$, HCOOH, CHF$_2$Cl
8	1090	1085.70 - 1091.00	100	CO$_2$, H$_2$O, O$_3$(668), CCl$_3$F, CCl$_2$F$_2$, HCOOH, CHF$_2$Cl
9	1106	1101.70 - 1106.50	100	CCl$_2$F$_2$, H$_2$O, CCl$_3$F, CHF$_2$Cl, HDO, HCOOH, O$_3$(668)
10	1119	1112.00 - 1117.40	100	H$_2$O, CCl$_2$F$_2$, CH$_3$D, CHF$_2$Cl, HDO, HCOOH, O$_3$(668)
11	1119m	1112.00 - 1117.40	100	H$_2$O, CCl$_2$F$_2$, CH$_3$D, CHF$_2$Cl, HDO, HCOOH, O$_3$(668)
		1118.85 - 1120.50		N$_2$O, H$_2$O, CCl$_2$F$_2$, CH$_3$D, CHF$_2$Cl, SO$_2$, HDO, HCOOH
12	1123	1123.85 - 1133.92	100	N$_2$O, H$_2$O, CCl$_2$F$_2$, CH$_3$D, CHF$_2$Cl, SO$_2$, HDO, HCOOH, solar
13	1146m	1138.00 - 1140.85	100	N$_2$O, H$_2$O, CCl$_2$F$_2$, CH$_3$D, CHF$_2$Cl, SO$_2$, HDO, CH$_4$
		1142.65 - 1148.80		N$_2$O, H$_2$O, CCl$_2$F$_2$, CH$_3$D, CHF$_2$Cl, SO$_2$, HDO, CH$_4$
14	1148	1142.65 - 1148.80	100	N$_2$O, H$_2$O, CCl$_2$F$_2$, CH$_3$D, CHF$_2$Cl, SO$_2$, HDO, CH$_4$
15	1170	1175.80 - 1180.50	100	CH$_4$, H$_2$O, CCl$_2$F$_2$, CH$_3$D, SO$_2$, HDO, N$_2$O, HNO$_3$, HCFC-142b
16	2775	2766.50 - 2775.50	200	CH$_4$, N$_2$O, CO$_2$, H$_2$O, HDO, HCl, solar
17	3023	3023.35 - 3023.85	200	H$_2$O, CH$_4$, CH$_3$D, CH$_3$Cl, C$_2$H$_4$
18	3023m	3023.70 - 3024.07	170	H$_2$O, CH$_4$, CH$_3$D, CH$_3$Cl, C$_2$H$_4$
		3039.75 - 3040.55		H$_2$O, CH$_4$, CH$_3$D, CH$_3$Cl, C$_2$H$_4$
		3045.09 - 3040.65		H$_2$O, CH$_4$, CH$_3$D, CH$_3$Cl, HDO, C$_2$H$_4$
19	3040m	3023.40 - 3023.55	170	H$_2$O, CH$_4$, CH$_3$D, CH$_3$Cl, C$_2$H$_4$, N$_2$O, solar
		3040.90 - 3041.01		CH$_4$, H$_2$O, CH$_3$D, CH$_3$Cl, HDO,N$_2$O, C$_2$H$_4$, solar
		3042.85 - 3043.16		H$_2$O, CH$_4$, CH$_3$D, CH$_3$Cl, HDO, HCl, solar
		3044.25 - 3044.50		H$_2$O, CH$_4$, CH$_3$D, CH$_3$Cl, HDO, HCl, solar
20	3041	3039.91 - 3042.20	170	H$_2$O, CH$_4$, CH$_3$D, CH$_3$Cl, solar
21	3045	3044.20 - 3045.74	170	CH$_4$, H$_2$O, CH$_3$D, CH$_3$Cl, HDO,N$_2$O, C$_2$H$_4$, solar
22	3051m	3051.35 - 3051.52	150	CH$_4$, H$_2$O, CH$_3$D, HDO, solar
		3051.77 - 3051.88		CH$_4$, H$_2$O, CH$_3$D, HDO, solar
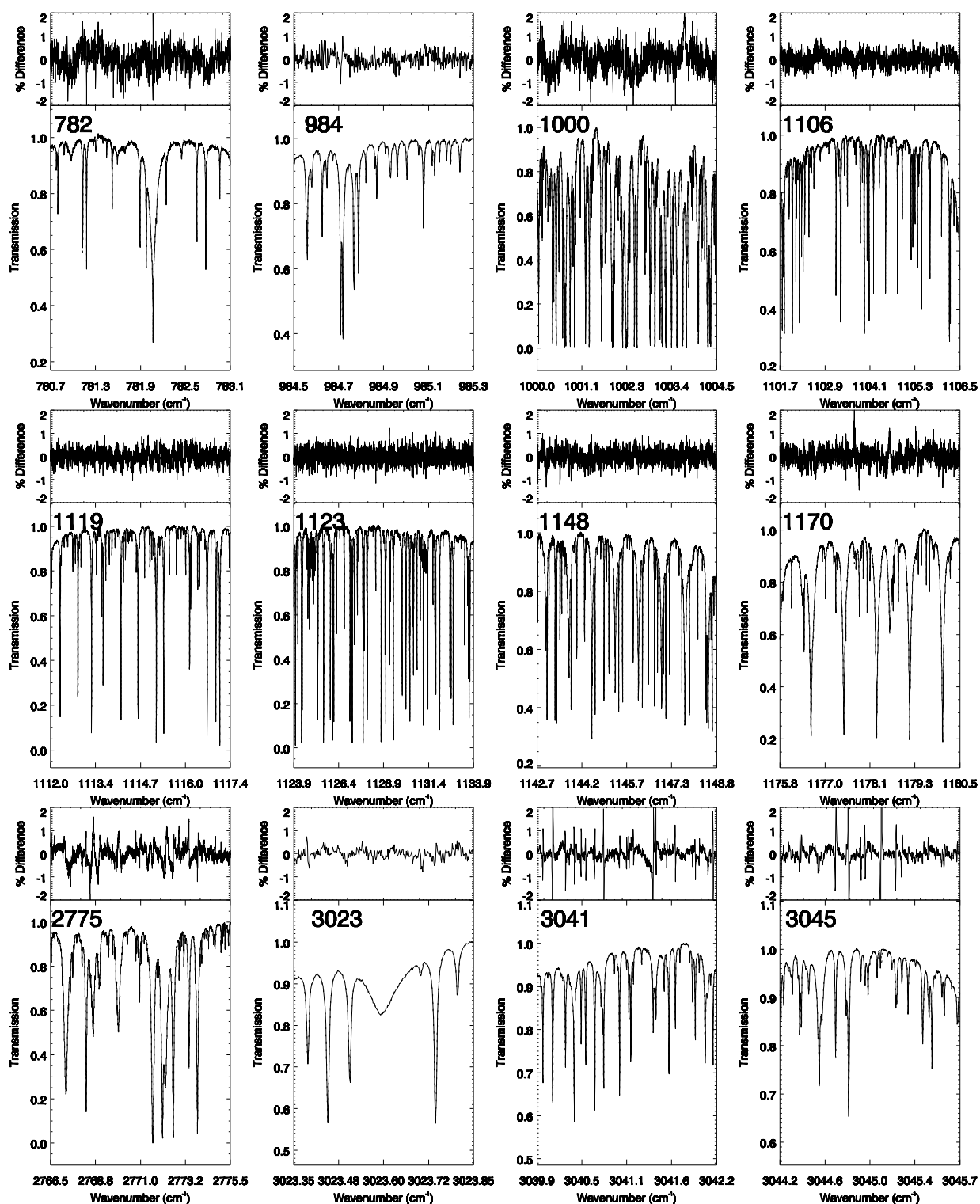
Figure 4.3. Examples of fits and residuals for 12 of the 22 ozone microwindows studied. The spectra were recorded on August 30, 2007. The measured spectra are indicated by the solid line, and the calculated spectra are indicated by the dashed line (generally not visible). The residuals are calculated as the difference between the measured and calculated spectra.
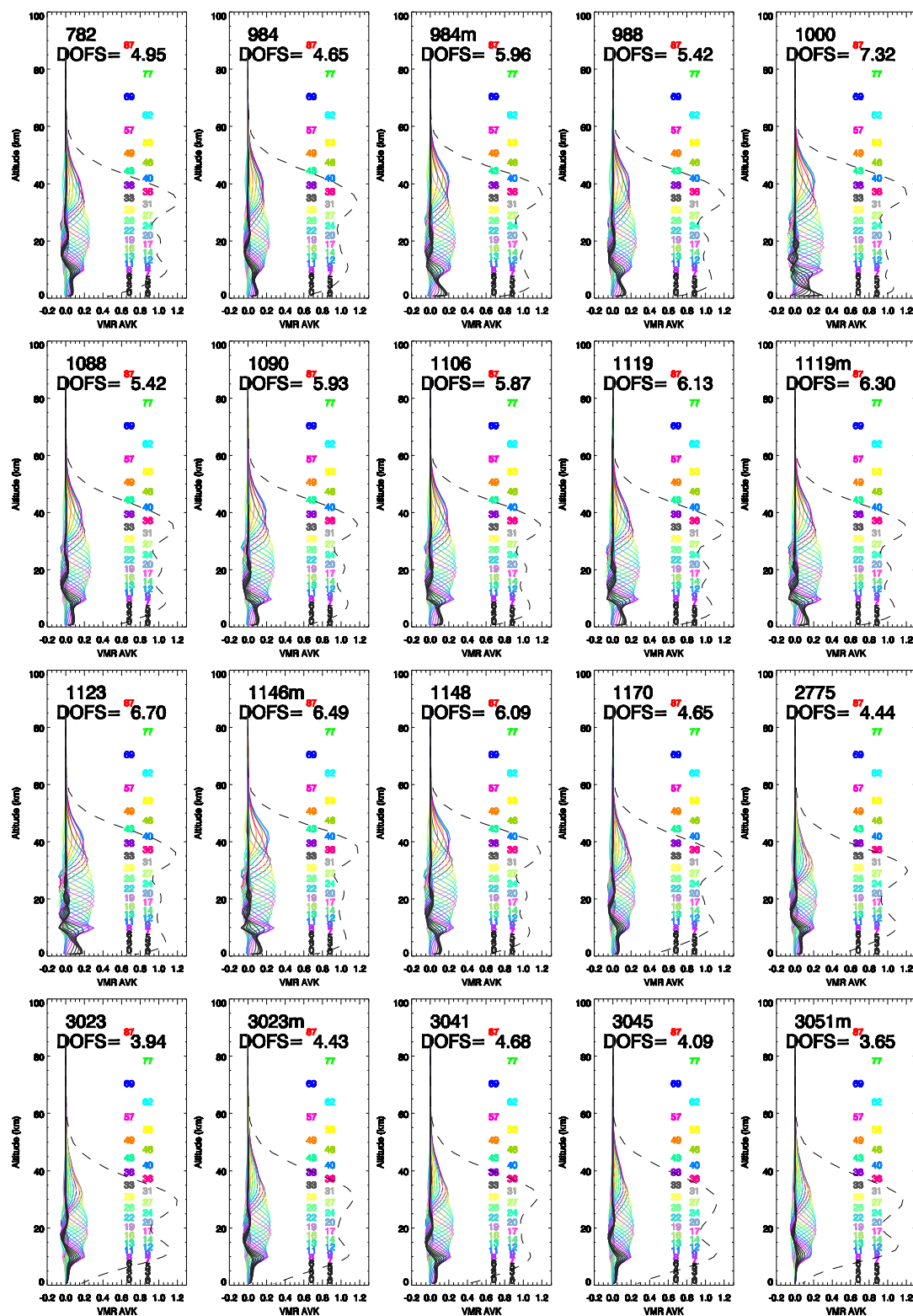
Figure 4.4. Ozone VMR averaging kernels for spectra recorded on August 30, 2007 for 20 of the 22 microwindows studied. Each color corresponds to one of the 38 retrieved layers, with the altitude of each layer in km indicated on the right of each panel. The dashed line shows the sensitivity of the retrieval to the measurement. The DOFS is given for each microwindow.

The filter 6 spectral interval (600-1400 cm^{-1}) is more suitable for broad microwindows as the number of strongly interfering species is smaller. As a result of having fewer interfering species, we can additionally fit minor species with very small interference, resulting in better retrievals and smaller residuals. Examples of microwindows with high total column DOFS and high tropospheric sensitivity are 1000, 1119, 1123, and 1146m. The DOFS for the microwindows in the filter 6 spectral region are, in general, higher by at least 1, sometimes by 2 or 3, compared to the DOFS for microwindows in the filter 3 spectral region. This is explained by the larger number of lines and greater range of intensities in the filter 6 region, which allows us to probe different altitudes of the atmosphere.

Figure 4.5 presents the 0.6-8 km partial column (dotted lines), 8-50 km partial column (dashed lines), and the total column (solid lines) averaging kernels. Most of the filter 6 microwindows are seen to have significant tropospheric column averaging kernels, while the filter 3 microwindows have much smaller tropospheric column averaging kernels, as seen for example for 3051m. The stratospheric column averaging kernels show only small differences for each microwindow, and are close to 1 between 8 and 50 km in all cases.

Scatter plots of columns retrieved in pairs of microwindows were constructed to assess the correlations of the tropospheric, stratospheric, and total columns. All spectra recorded from March 1 to April 8, 2008, corresponding to the Canadian Arctic ACE Validation Campaign (to be discussed in Section 4.5) were used. Pairs of measurements were considered matched if they were made within one hour of each other. Results are shown for microwindow 1000 versus 1123, 3023m, and 3051m, where microwindows 1000 and 1123 are sensitive in both the tropospheric and stratospheric regions, while 3023m is less sensitive in the troposphere and 3051m is only sensitive in the stratosphere. The top row of Figure 4.6 (panels a-c) shows the scatter plots and linear fits for the stratospheric partial columns, 8-50 km. In general, for the stratosphere, there is a good correlation for each pair, with the correlation coefficient (R) and slope (S) being very close to 1, and the intercept (I) being very small. While there is good correlation in all three cases, it is marginally better for the 1000 and 1123 pair than for the 1000 and 3023m or 3051m pairs, as expected by the sensitivity shown in Figure 4.5.

The middle row of Figure 4.6 (panels d-f) shows similar plots for the tropospheric partial columns, 0.6-8 km. As expected from the sensitivity plots, the tropospheric information is more varied from microwindow to microwindow. For the first pair of microwindows, 1000 versus
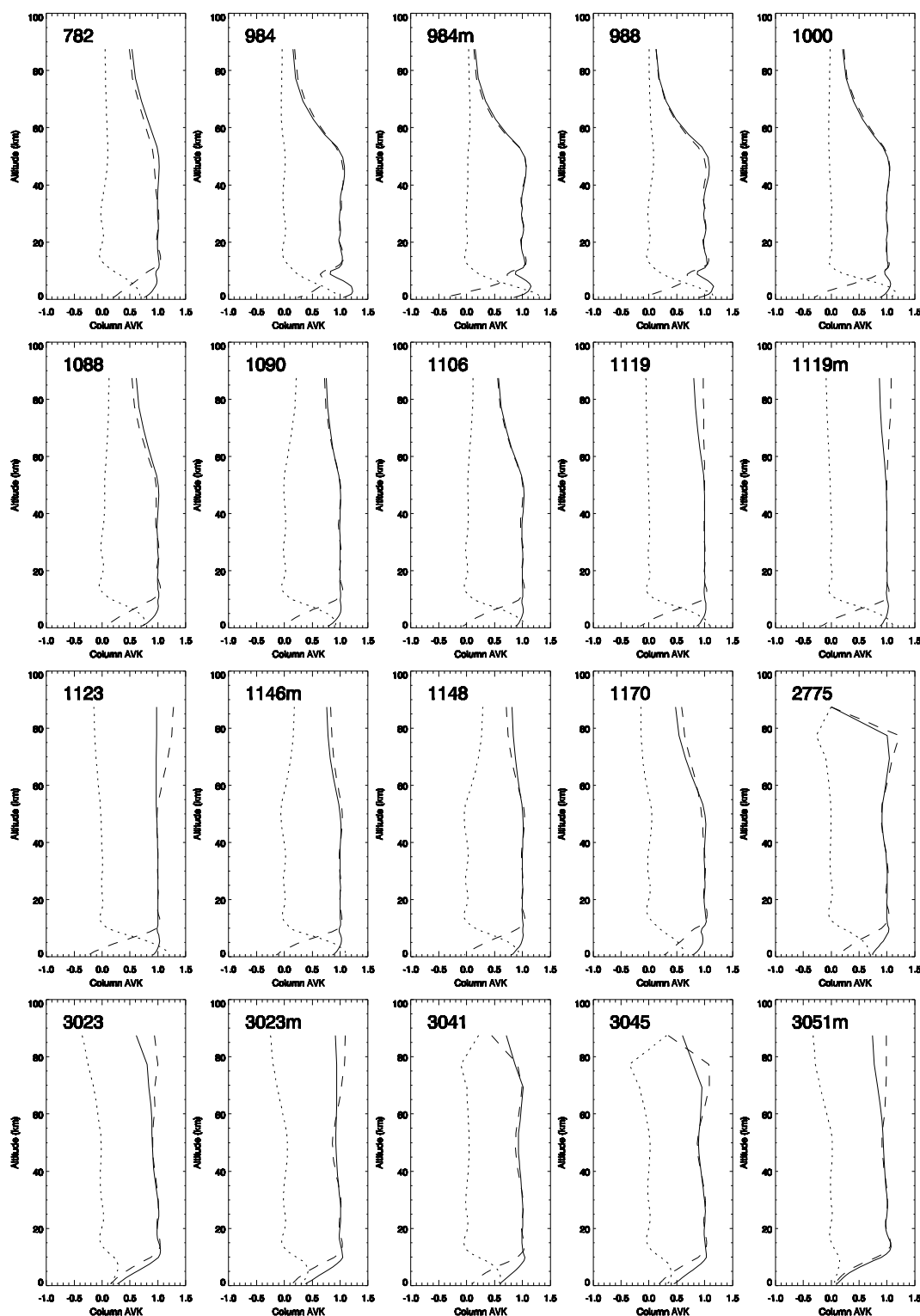
Figure 4.5. Ozone column averaging kernels for spectra recorded on August 30, 2007 for 20 of the 22 microwindows studied. The solid line indicates the total column (0.6-100 km) averaging kernel. The dotted line corresponds to the tropospheric partial column (0.6-8 km) and the dashed line to the stratospheric partial column (8-50 km).
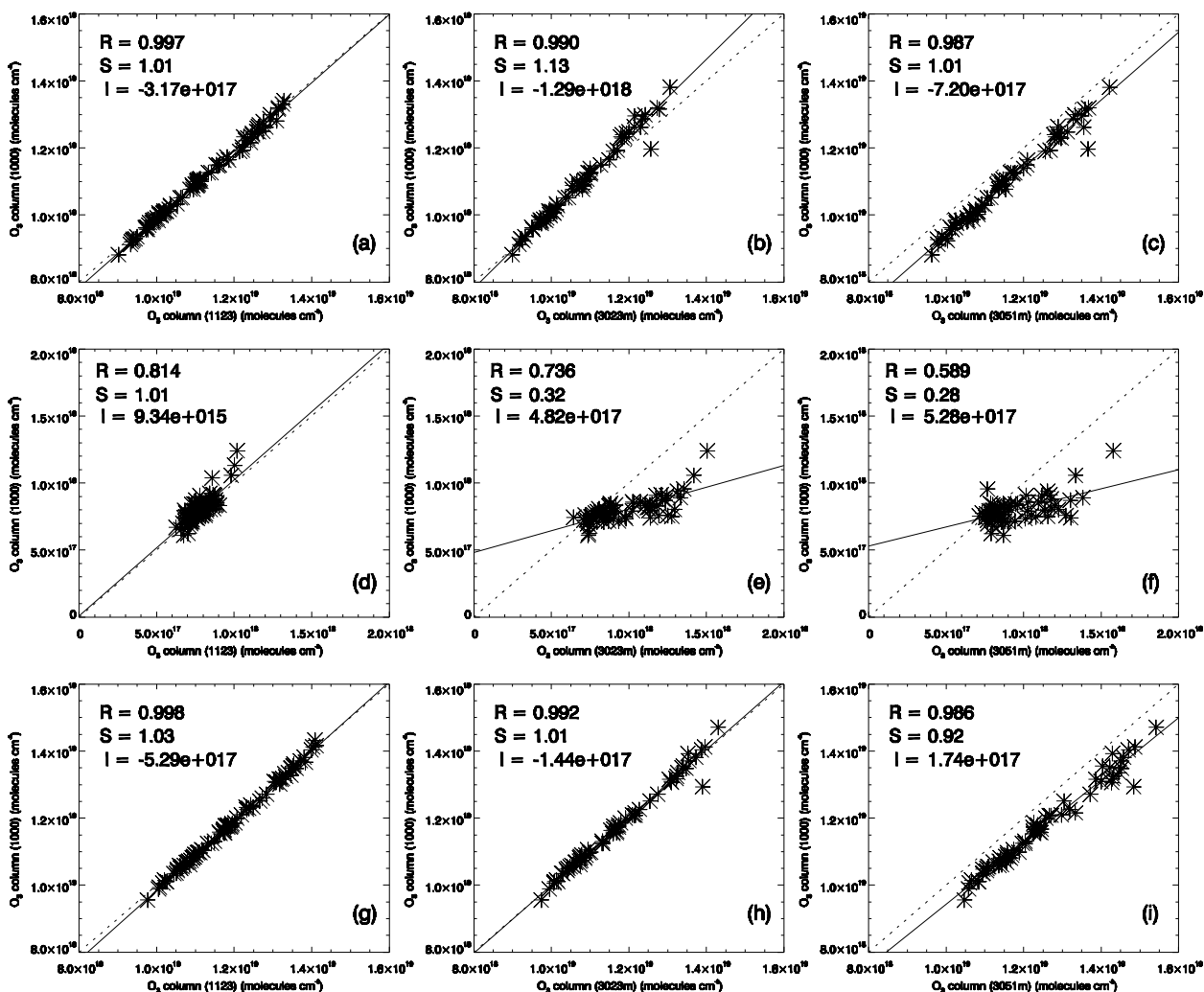
Figure 4.6. Top row: scatter plots for pairs of microwindows for the stratospheric ozone partial columns (8-50 km). (a) microwindow 1000 vs. 1123, (b) 1000 vs. 3023m and (c) 1000 vs. 3051m. Middle row (d-f): same as above but for the tropospheric ozone partial column (0.6-8 km). Bottom row (g-i): same as above but for the ozone total column (0.6-100 km). The spectra were recorded in spring 2008 (March 1 to April 8). The correlation coefficient (R), slope (S) and intercept (I) are given for each comparison. The solid black line shows the best fit for the comparison, and the dotted line shows the 1:1 line.

1123, both of which contain information in the troposphere, the agreement is good. For the latter two pairs of microwindows, the correlations are not so good, as expected.

For the total columns from 0.6 to 100 km, the correlations are given in the bottom row of Figure 4.6 (panels g-i). These plots are very similar to those for the stratosphere, with excellent correlations. The slope of 0.92 in panel (i) versus 1.01 for the stratospheric partial columns in panel (c) for the 1000 versus 3051m pair can be attributed to the differences in the total column

averaging kernels for microwindow 1000 versus 3051m (shown in Figure 4.5). The total column scatter plots show that the choice of microwindow(s) is less critical if the measurement of interest is total column ozone than if vertical information is of interest. This is highlighted in Figure 4.7, which shows the percentage difference between the columns retrieved for each of these microwindows with respect to microwindow 1000, along with the mean and standard deviation. The percentage difference between the total columns is given by

$$\%\,Diff \;=\; 100\% * \left[(MW1000 - MWx)/(MW1000 + MWx)*0.5\right], \tag{4.2}$$

where $MW1000$ represents the total column retrieved using microwindow 1000 and MWx represents the total column using one of the other previously mentioned microwindows.
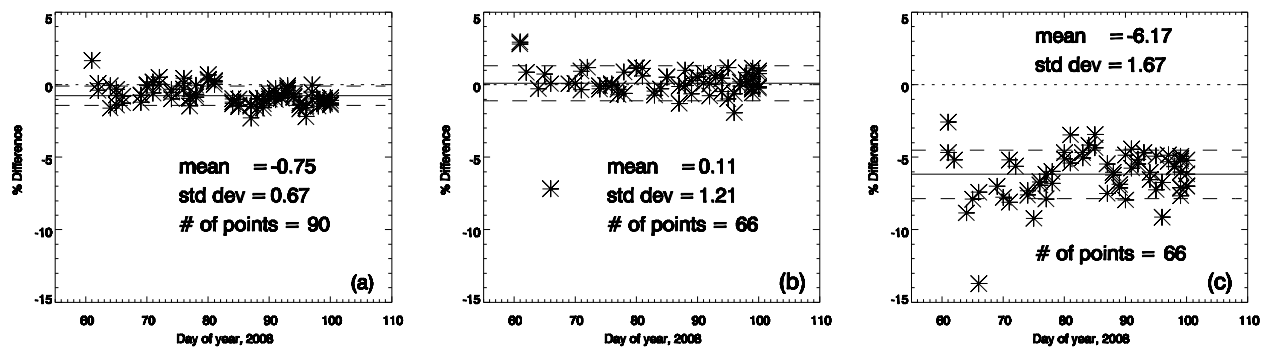
Figure 4.7. Percentage differences for the ozone total columns for microwindow 1000 versus (a) 1123, (b) 3023m, and (c) 3051m. The percentage difference is calculated using Equation 4.2. The mean percentage difference (solid line), standard deviation (dashed lines), and number of points compared are given for each case. The dotted line shows the zero difference.

The mean differences for microwindow 1000 versus 1123 and 3023m (Figure 4.7, panels a and b) are less than 1%, indicating that the retrieved columns are almost identical. For the 1000 versus 3051m pair (panel c), the percentage difference is larger than in the previous two cases, at -6.17%. The scatter, represented by the standard deviation, is also greater for this microwindow pair, suggesting that the 3051m retrievals are not as consistent as the other microwindows. A list of mean differences for the ozone total columns and their standard deviations for microwindow 1000 versus each of the other 21 microwindows is given in Table 4.3.

Table 4.3. Mean differences, given by Equation 4.2, in the ozone total columns and their standard deviations (both in %), for the 1000 microwindow compared with each of the other 21 microwindows, for spring 2008. The number of spectra compared was 90 for the filter 6 microwindows and 66 for the filter 3 microwindows.

Microwindow designation	Mean difference (%)	Standard deviation (%)
782	2.04	1.39
984	0.27	1.04
984m	0.96	0.82
987	1.35	0.75
988	0.44	0.73
1088	-0.41	1.07
1090	-0.44	1.02
1106	0.27	1.22
1119	-0.23	1.06
1119m	-0.44	0.99
1123	0.75	0.67
1146m	0.36	0.82
1148	0.32	0.95
1170	-0.16	1.17
2775	6.16	2.15
3023	0.23	1.88
3023m	0.11	1.21
3040m	-1.58	1.97
3041	3.11	1.85
3045	-4.03	1.50
3051m	-6.17	1.67

4.4.2 Error Budget

Table 4.4 provides the error budget for the ozone total columns calculated as discussed in Sections 3.4 and 4.2, for all 22 of the microwindows studied. For the filter 6 region, a spectrum recorded on August 30, 2007 at 10:20:55 local time (LT) at a SZA of 73.07° was used. For the filter 3 region, a spectrum recorded on the same day at 11:21:42 LT, at a SZA of 71.78° was used. The choice of these spectra was based on the fact that August 30 was a very clear day, optimal for FTS measurements.

Measurement errors (S_m) vary from 0.23% for microwindow 1000 to 3.48% for 3051m and are generally higher for the filter 3 microwindows. Microwindows 984, 984m, 987, 988, and 3040m, have the largest uncertainties (approx. 2 to 2.5%) due to temperature (S_{temp}), while 1088, 1090, 1106 and 1146m have the smallest values ($\leq$0.20%). The uncertainties due to the retrieved

instrument parameters (S_{int1}) and the retrieved interfering species (S_{int2}) are higher in the filter 3 region, as expected from the narrower microwindows and the larger interference from other gases. The uncertainties resulting from changes in the SZA (S_{sza}) are very similar for all the microwindows, as expected from the identical time required for each measurement. The uncertainties coming from the spectroscopic parameters (S_{lint} and S_{lwdth}) have similar values across the microwindows, however microwindow 1000 has less than half the uncertainty of the other microwindows for the line intensity (4.24%), but a larger uncertainty for the line width (0.4%) compared to the other filter 6 microwindows. The line width difference could be due to saturation effects, since this microwindow contains the largest number of lines with nearly 100% absorption compared to the other microwindows. Smoothing errors (S_s) vary from 0.13% for microwindow 1123 to 3.6% for microwindow 3051, and are in general higher for the filter 3 microwindows.

Table 4.4. The error budget for ozone total column (0.6-100 km) for August 30, 2007: SZA= 73.07° for the filter 6 (600-1400 cm^{-1}) region, SZA= 71.78° for the filter 3 (2400-3100 cm^{-1}) region. The covariance matrices are defined in the text.

MW	S_m (%)	S_{temp} (%)	S_{int1} (%)	S_{int2} (%)	S_{sza} (%)	S_{totr} (%)	S_{lint} (%)	S_{lwdth} (%)	S_s (%)	S_{TOTAL} (%)	DOFS
782	1.42	1.40	0.03	0.18	0.80	2.16	12.37	0.11	0.56	12.57	4.95
984	1.70	2.53	0.39	0.09	0.68	3.15	10.15	0.12	1.48	10.73	4.65
984m	0.72	1.96	0.05	0.08	0.61	2.17	9.14	0.10	0.97	9.45	5.97
987	0.96	2.03	0.03	0.06	0.60	2.32	9.09	0.09	1.15	9.45	5.47
988	0.89	2.13	0.09	0.004	0.61	2.39	9.10	0.10	1.08	9.47	5.43
1000	0.23	0.69	0.01	0.003	0.27	0.77	4.24	0.40	0.33	4.34	7.32
1088	1.17	0.09	0.31	0.25	0.71	1.43	11.04	0.05	0.33	11.14	5.42
1090	0.83	0.10	0.17	0.15	0.69	1.10	10.82	0.05	0.21	10.88	5.94
1106	0.70	0.13	0.21	0.02	0.75	1.06	11.42	0.02	0.20	11.47	5.87
1119	0.61	0.58	0.09	0.04	0.79	1.16	11.76	0.12	0.27	11.82	6.14
1119m	0.54	0.63	0.07	0.03	0.78	1.14	11.65	0.13	0.25	11.71	6.31
1123	0.30	0.41	0.04	0.01	0.74	0.89	11.03	0.17	0.13	11.06	6.71
1146m	0.64	0.20	0.08	0.05	0.70	0.98	10.98	0.04	0.21	11.03	6.50
1148	0.93	0.34	0.09	0.09	0.69	1.22	10.87	0.05	0.39	10.95	6.09
1170	1.76	0.65	0.20	0.18	0.64	1.10	11.10	0.14	0.65	11.29	4.65
2775	1.15	1.28	0.01	0.35	0.50	1.83	11.53	0.24	0.29	11.68	4.45
3023	2.68	0.95	1.78	0.23	0.65	3.43	10.54	0.59	2.30	11.34	3.95
3023m	2.08	1.24	1.50	0.24	0.77	2.96	12.46	0.60	1.78	12.94	4.44
3040m	3.40	2.11	2.72	2.57	0.73	5.53	12.58	1.48	1.24	13.88	3.73
3041	1.53	1.19	0.38	0.79	0.71	2.24	11.54	0.07	0.40	11.77	4.69
3045	2.27	1.61	0.38	0.42	0.71	2.93	11.81	0.65	1.50	12.27	4.10
3051m	3.48	1.00	3.72	0.81	0.62	5.30	10.15	1.16	3.60	12.06	3.65

The total error column, S_{TOTAL}, clearly shows that microwindow 1000 has the smallest uncertainty of the 22 microwindows (4.34%). This microwindow also has the largest information content as shown by the DOFS in the last column (7.32). Similar results are shown in Tables 4.5 and 4.6, which give the error budgets calculated for the spectra mentioned above, for the stratospheric (8-50 km) and tropospheric (0.6-8 km) columns, respectively. As for the total column calculations, microwindow 1000 is seen to have the highest DOFS and lowest errors for both partial columns.

Table 4.5. The error budget for stratospheric ozone partial column (8-50 km), for the same spectra as in Table 4.4.

MW	S_m (%)	S_{temp} (%)	S_{int1} (%)	S_{int2} (%)	S_{sza} (%)	S_{totr} (%)	S_{lint} (%)	S_{lwdth} (%)	S_s (%)	S_{TOTAL} (%)	DOFS
782	1.79	0.19	0.04	0.12	0.87	2.01	13.29	0.61	2.70	13.72	4.44
984	2.74	2.55	0.43	0.17	0.67	3.83	10.01	0.45	3.72	11.35	4.01
984m	1.52	1.58	0.08	0.11	0.54	2.26	8.23	0.61	2.30	8.86	4.95
987	1.95	1.92	0.04	0.12	0.56	2.79	8.48	0.61	2.65	9.33	4.55
988	1.93	1.67	0.10	0.02	0.55	2.61	8.32	0.50	2.68	9.14	4.58
1000	0.55	0.52	0.03	0.02	0.22	0.79	3.36	0.90	1.29	3.79	5.86
1088	1.42	1.02	0.39	0.19	0.74	1.95	11.52	0.56	1.50	11.79	4.80
1090	1.28	1.74	0.32	0.15	0.73	2.31	11.46	0.66	1.32	11.78	5.18
1106	1.34	1.70	0.46	0.03	0.78	2.35	12.06	0.74	1.54	12.41	5.04
1119	0.94	1.70	0.14	0.03	0.80	2.11	12.00	1.00	1.23	12.29	5.22
1119m	0.84	1.70	0.09	0.02	0.80	2.06	11.92	1.03	1.18	12.20	5.36
1123	0.68	1.85	0.04	0.02	0.77	2.12	11.58	1.04	1.14	11.87	5.63
1146m	1.07	2.36	0.24	0.07	0.70	2.69	10.95	0.50	1.22	11.36	5.57
1148	1.25	1.56	0.26	0.12	0.68	2.14	10.94	0.50	1.58	11.26	5.33
1170	1.94	0.29	0.07	0.16	0.66	2.08	11.43	0.53	2.73	11.94	4.19
2775	1.48	1.39	0.12	0.19	0.71	2.17	12.38	1.41	1.08	12.69	3.91
3023	2.03	1.27	1.74	0.12	0.68	3.04	11.30	1.21	2.21	11.98	3.76
3023m	1.37	1.69	1.00	0.06	0.80	2.52	13.02	1.54	2.06	13.51	4.11
3040m	2.85	2.25	2.11	1.57	0.80	4.56	13.53	2.06	1.22	14.47	3.63
3041	1.29	1.68	0.59	0.19	0.77	2.34	12.65	1.49	1.01	12.99	4.19
3045	1.79	1.71	0.71	0.15	0.76	2.69	12.57	1.65	2.10	13.13	3.79
3051m	2.95	1.31	2.94	0.68	0.66	4.46	10.85	1.51	2.61	12.11	3.57

Similar calculations (not shown) have been performed for spectra recorded during spring 2008, when the sun is lower and the instrument consequently looks through more atmosphere. In all cases, the relative results for the microwindows were similar, but the DOFS were higher and the total errors smaller (e.g., 7.58 and 1.52% for the total column using microwindow 1000), reflecting the additional information contained in the deeper absorption features.

Table 4.6. The error budget for tropospheric ozone partial column (0.6-8 km), for the same spectra as in Table 4.4.

MW	S_m (%)	S_{temp} (%)	S_{int1} (%)	S_{int2} (%)	S_{sza} (%)	S_{totr} (%)	S_{lint} (%)	S_{lwdth} (%)	S_s (%)	S_{TOTAL} (%)	DOFS
782	16.32	11.83	0.18	1.96	0.36	20.25	6.57	4.08	19.63	29.24	0.61
984	19.08	2.60	7.88	2.25	0.81	20.94	12.01	3.62	22.59	33.26	0.72
984m	9.99	4.92	0.48	0.38	1.29	11.23	18.76	6.37	21.34	31.21	1.11
987	12.15	2.97	0.09	0.44	1.06	12.56	15.51	6.16	21.19	29.76	1.01
988	17.80	7.25	0.90	0.24	1.34	19.29	19.40	5.70	23.87	36.75	0.94
1000	5.94	5.93	0.12	0.13	0.94	8.46	14.75	5.55	14.76	23.19	1.63
1088	16.86	7.83	0.55	2.28	0.49	18.74	8.14	4.79	14.42	25.46	0.72
1090	13.42	9.97	0.56	1.46	0.53	16.80	7.90	5.11	12.19	22.79	0.87
1106	12.75	12.12	1.37	0.23	0.63	17.66	7.94	6.59	13.53	24.52	0.94
1119	13.95	9.31	0.37	0.73	0.74	16.81	10.77	11.38	16.97	28.56	1.04
1119m	11.74	8.01	0.47	0.57	0.72	14.25	10.75	10.97	15.49	26.05	1.08
1123	7.25	11.29	0.004	0.11	0.53	13.43	7.82	9.65	14.10	23.10	1.22
1146m	13.55	19.79	1.31	1.12	0.71	24.06	10.84	6.79	14.52	30.88	1.04
1148	21.77	11.77	1.70	2.37	0.80	24.94	9.68	8.25	21.96	35.58	0.88
1170	24.97	5.65	1.71	0.85	0.42	25.68	7.62	4.94	29.93	40.47	0.55
2775	15.63	3.73	1.05	3.90	0.99	16.60	5.52	9.49	9.97	22.26	0.64
3023	19.13	2.84	5.91	1.42	0.29	20.28	3.16	6.90	36.98	42.85	0.27
3023m	27.25	5.52	14.34	2.78	0.53	31.41	6.59	12.90	40.63	53.36	0.42
3040m	21.57	2.45	19.99	18.36	0.14	34.76	1.70	7.49	23.39	42.60	0.16
3041	14.82	4.26	1.46	6.82	0.35	16.93	4.60	10.83	9.35	22.64	0.60
3045	21.76	5.58	5.34	4.30	0.16	23.49	4.45	11.22	32.97	42.24	0.40
3051m	16.49	2.63	21.02	3.57	0.20	27.08	3.15	3.36	44.35	52.16	0.13

Combining the information gained from the averaging kernels, column scatter plots and error analysis, it is clear that the 1000 microwindow, covering the broad spectral range 1000 to 1004.5 cm^{-1} is the best choice for ozone retrievals using the Bruker 125HR at Eureka.

4.5 Comparison with Other Instruments

Since 2004, there has been an annual springtime Canadian Arctic ACE validation campaign at Eureka (*e.g., Kerzenmacher et al.,* 2005). During this time, intensive ozone measurements are made with a variety of instruments, including FTIR spectrometers, ultraviolet-visible (UV-VIS) spectrometers, Brewer spectrophotometers, and ozonesondes. During the 2008 campaign, three FTIR spectrometers measured side-by-side, sharing the same solar beam [*Fu et al.,* 2011]. These included the Bruker 125HR, the Bomem DA8 FTIR [*Farahani et al.,* 2007, *Fast et al.,* 2011] and the Portable Atmospheric Research Interferometric Spectrometer for the Infrared (PARIS-IR) [*Fu et al.,* 2007]. In addition, two UV-VIS instruments, Brewer spectrophotometer #21 [*Savastiouk and McElroy,* 2005], located at the Eureka Weather Station,

and the SAOZ (Système d'Analyse par Observation Zénithale) [*Pommereau and Goutail,* 2005] were in operation.

Figure 4.8 shows the ozone total column time series measured with each of these instruments during the 2008 campaign. In addition, ozone total columns determined from regularly launched ozonesondes and from profiles recorded with the ACE-FTS [*Bernath et al.,* 2005] onboard the SCISAT satellite are shown. For ozonesondes, the total column was calculated including the corrections made for ozone above the altitude of the highest measurement. For the ACE-FTS, the column between the lowest measurement altitude and the surface was determined using ozonesonde values from that day. Ozone from the ground-based FTIRs was retrieved using the 1000 microwindow described in Section 4.4. A detailed comparison of the measurements made with the FTIR instruments, including the ACE-FTS, is presented in Chapter 6, showing that the Bruker 125HR agrees, with a mean difference of less than 2%, with both the DA8 and PARIS-IR and less than 4% with ACE-FTS [*Batchelor et al.,* 2010].
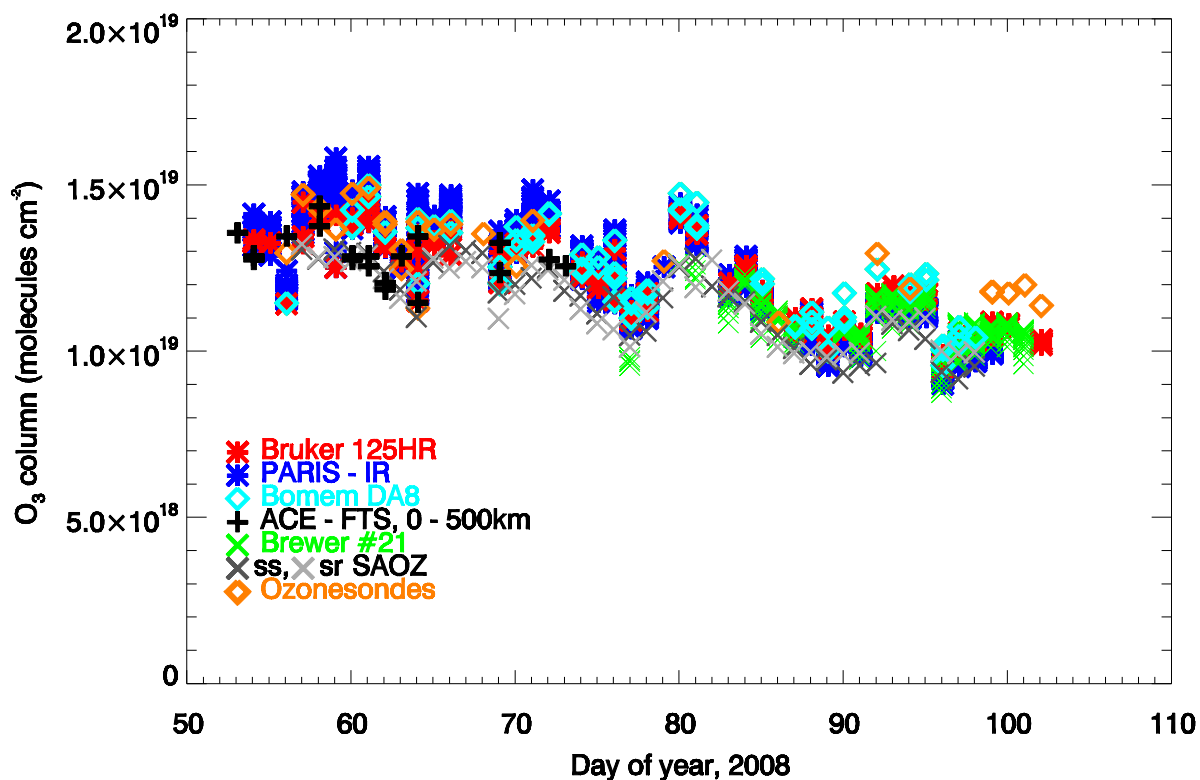
Figure 4.8. Ozone total columns at Eureka retrieved during spring 2008. All ground-based FTIR results used microwindow 1000. The ACE-FTS measurements were acquired within 500 km of PEARL as measured from the ACE-FTS 30-km tangent altitude.

The Brewer spectrophotometer is an instrument widely used to measure ozone with high accuracy, so we will focus on comparing the Bruker 125HR values to it. The correlation and percentage difference plots for the Bruker 125HR versus Brewer #21 are shown in Figure 4.9. For this comparison, all direct sun Brewer measurements made within one hour of each Bruker 125HR spectrum were considered. Good agreement is seen, with both the correlation coefficient and slope close to 1. The mean difference is 0.66%, being similar in magnitude to the difference between FTIR and Brewer measurements (1.9%) recorded at Izaña [*Schneider et al.,* 2005]. The differences were calculated with a relation similar to Equation 4.2:

$$\% Diff = 100\% * \left[(MW1000 - IN)/(MW1000 + IN) * 0.5 \right], \qquad (4.3)$$

where *IN* stands for the instrument compared with the Bruker 125HR.
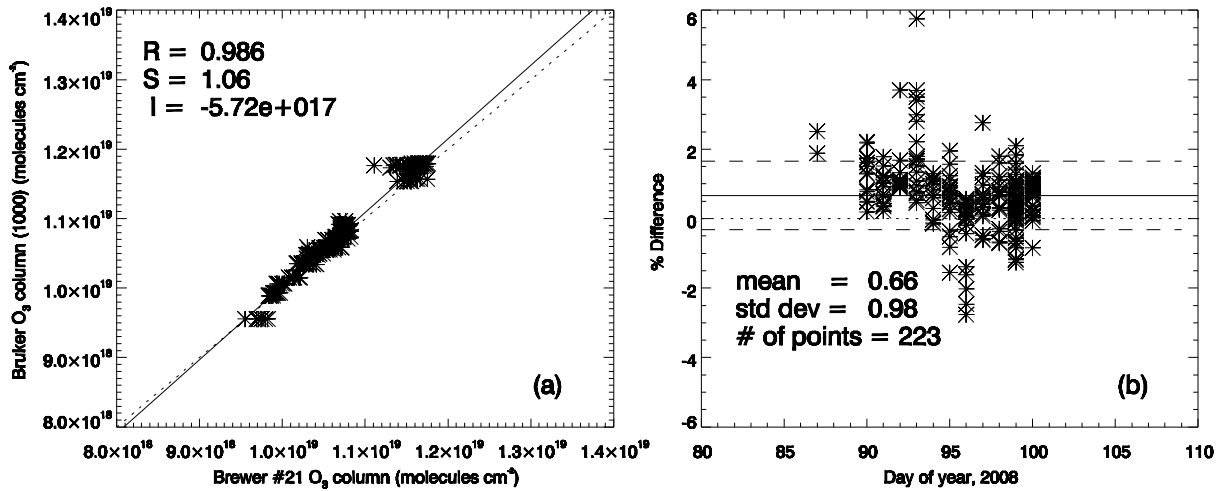
Figure 4.9. (a) Scatter plot for ozone total columns retrieved with microwindow 1000 and Brewer #21. The correlation coefficient (R), slope (S) and intercept (I) are given for the comparison. The solid black line shows the best fit for the comparison, and the dotted line shows the 1:1 line. (b) Corresponding percentage differences were calculated using Equation 4.3. The mean percentage difference (solid line), standard deviation (dashed lines), and number of points compared are also shown.

Results of the comparisons with the SAOZ spectrometer are shown in Figure 4.10 for sunrise and sunset. For each day, all spectra recorded with the Bruker 125HR before local noon were compared with the sunrise SAOZ measurements, and those recorded after local noon with the sunset SAOZ measurements. The correlation coefficients are again close to 1, with a slightly better correlation for the sunset measurements than the sunrise ones. The mean differences between the instruments for sunset and sunrise are 7.94% and 8.36% respectively, showing that

the Bruker 125HR gives higher column values than the SAOZ spectrometer, similar to differences of 4-7% shown by *Fraser et al.* [2007]. This offset is clearly seen in Figure 4.8, and is most likely related to the very different observing geometry of the two instruments. SAOZ views scattered sunlight from the twilight zenith-sky, while the Bruker 125HR is solar pointing, with an atmospheric path that can extend hundreds of kilometers in the direction of the sun.
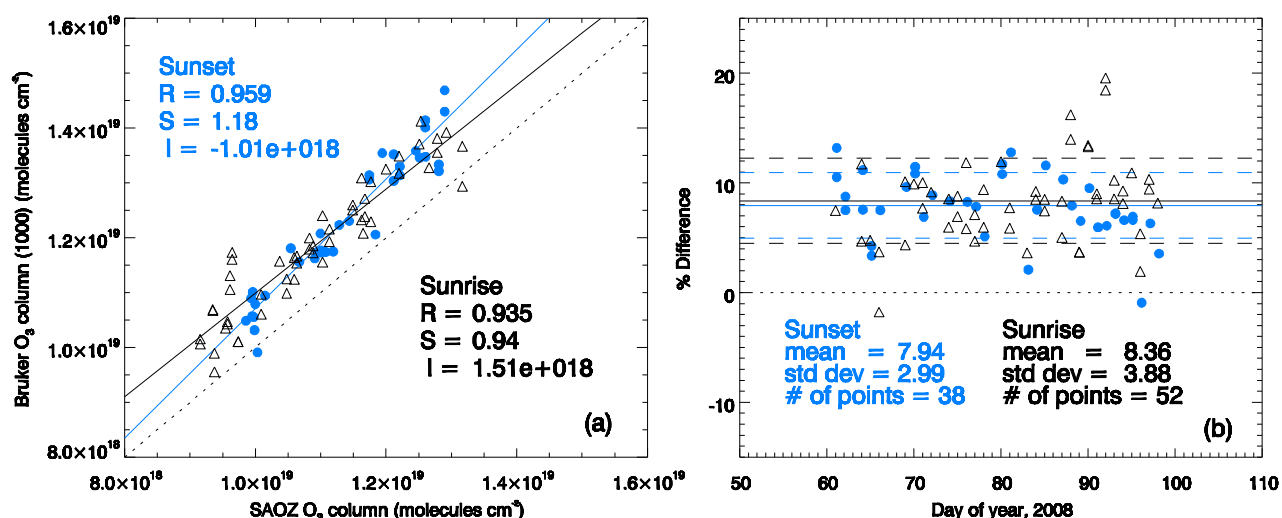
Figure 4.10. Same as Fig. 4.9, but for microwindow 1000 versus SAOZ. Blue represents SAOZ sunset values, gray represents SAOZ sunrise values.

Ozonesondes are launched daily during the spring campaigns and once a week throughout the rest of the year. For the 2008 campaign, ozonesonde columns are compared with the Bruker 125HR in Figure 4.11. The correlation coefficient for this comparison is 0.941, the slope is 1.16 and the intercept is of order 10^{18} molec/cm^2. The mean difference in column of -6.94% indicates that the ozonesonde columns are larger than the columns obtained with the 1000 microwindow, while the standard deviation (4.23%) indicates some scatter in the column differences (similar comparisons were done by *Schneider et al.* (2005) and *Barret et al.* (2002), who found 9% and 6 to -9% relative differences, respectively). These results may again be related to the different air masses being sampled by the two instruments, as the Arctic stratosphere is highly variable in time and space at this time of the year.
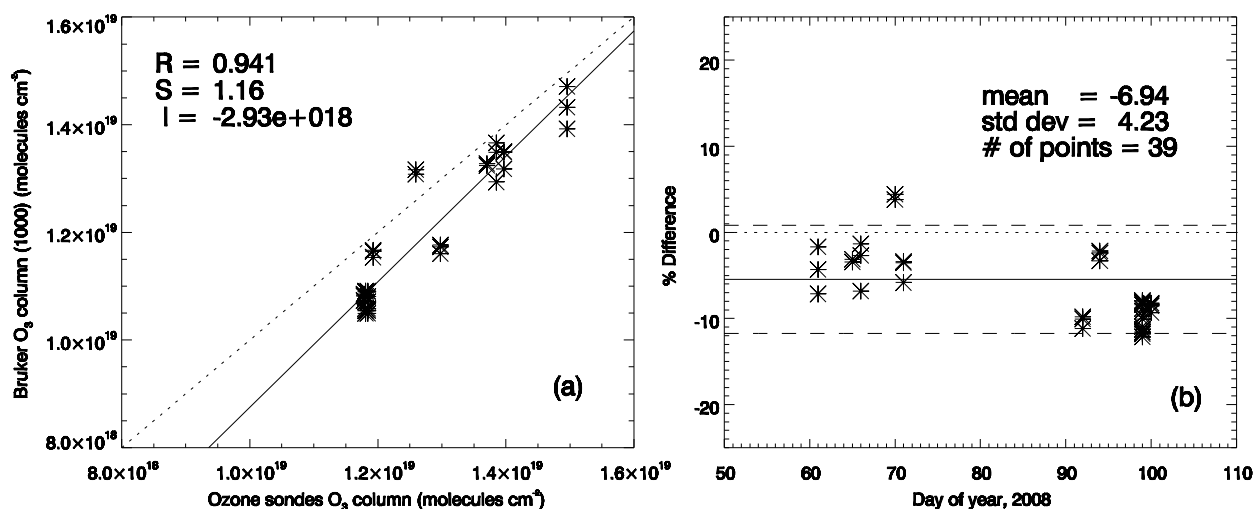
Figure 4.11. Same as Fig. 4.9, but for microwindow 1000 versus ozonesondes.

4.6 Conclusions

The purpose of the study described in this chapter was to optimize the ozone retrievals for mid-infrared FTIR measurements made with the Bruker 125HR at Eureka. In particular, the choice of retrieval microwindow(s) has been investigated by examining 22 different spectral regions. Averaging kernels, DOFS, and error budgets were determined for each microwindow, using both spring and summer spectra. The filter 6 region (600-1400 cm^{-1}) shows more sensitivity in both the stratosphere and troposphere than the filter 3 region (2400-3100 cm^{-1}), with a somewhat smaller total error and higher DOFS. Microwindow 1000 (1000-1004.5 cm^{-1}) was shown to have the highest sensitivity to both the stratosphere and troposphere. The quantity of information given by this microwindow is very high, with close to 7 DOFS for the total column, and more than 1.5 DOFS for the tropospheric partial column. The total error for the total column is one-third to one-half of the total error found for the other microwindows. These results support the choice of this microwindow for the evaluation of tropospheric and stratospheric ozone trends over Western Europe performed by the European ground-based FTIR network UFTIR (Upper Free Troposphere observations from a European ground-based FTIR network) [*Vigouroux et al.,* 2008] and by *Barret et al.* (2002), *Griesfeller et al.* (2006), *Schneider et al.* (2008), and *Senten et al.* (2008) from Table 4.1. The results of this study were provided to the NDACC IRWG in the context of its harmonization initiative and contributed to this microwindow being selected as the standard for use by all IRWG sites.

Ozone measurements retrieved using the 1000 microwindow were compared with several other instruments at Eureka during the spring 2008 Canadian Arctic ACE validation campaign. These comparisons showed mean agreement of approximately 2% with the two additional ground-based FTSs, 4% with the satellite-based ACE-FTS, 0.7% with the Brewer spectrophotometer, 8% with the SAOZ spectrometer, and 7% with the ozonesondes. The higher differences for the latter two comparisons are likely indicative of the different air masses being sampled by these instruments.

Chapter 5

NDACC IRWG Parameter Implementation for Eureka

5.1 Trace Gas Retrievals at Eureka

Ten species have been retrieved at Eureka on a regular basis since the 125HR was installed: O_3, HCl, HF, $ClONO_2$, HNO_3, N_2O, CH_4, C_2H_6, HCN, and CO. The vertical profiles of volume mixing ratio for these species are weighted by airmasses in each retrieval layer and integrated to give the total or partial columns. Details of the input parameters, *e.g.,* microwindows, interfering gases, *a priori* covariance, SNR, and ILC are given in Table 3.1.

Results for the first four years of measurements at Eureka, from July 2006 to August 2010, were submitted to the NDACC archive in September 2010 and data from August 2010 to October 2011 were submitted in February 2012. This database is publicly accessible and can be used for research purposes. The submitted time series of total columns, and stratospheric (10-50 km) and tropospheric (0-10 km) partial columns (available depending on the retrieved species) are plotted in Figure 5.1. The time series in Figure 5.1 indicate that variability is greater in the spring period, when the polar vortex is often overhead and conditions are driven by vortex dynamics and ozone depletion chemistry. During the summer, perturbations of trace gases may result from transport of pollutants from lower latitudes. Photochemistry also plays an important role in the observed trends, as the days grow from 24-hour darkness in February to 24-hour daylight in May and vice versa starting in late August until late October.

For HCl, HF, HNO_3, and $ClONO_2$ there is no information coming from the measurement in the troposphere, hence no partial columns were calculated, but for N_2O, CO, and CH_4, two independent pieces of information come from this region. For ozone, the microwindow identified in Chapter 4 was extended to 1005.0 cm^{-1} to support the choice of this microwindow by the IRWG as a result of its harmonization initiative. Neither the total error, nor the DOFS changed significantly from the results in Chapter 4 for this extended range. These O_3 retrievals are sensitive to both the stratosphere and troposphere.

An estimate of the mean uncertainty in the measurements has been made using the procedure described in Section 3.5 and a subset of representative spectra, and is given in Table 5.1. The mean DOFS was also calculated for all spectra (late February to late October) and is given for the total and partial columns.
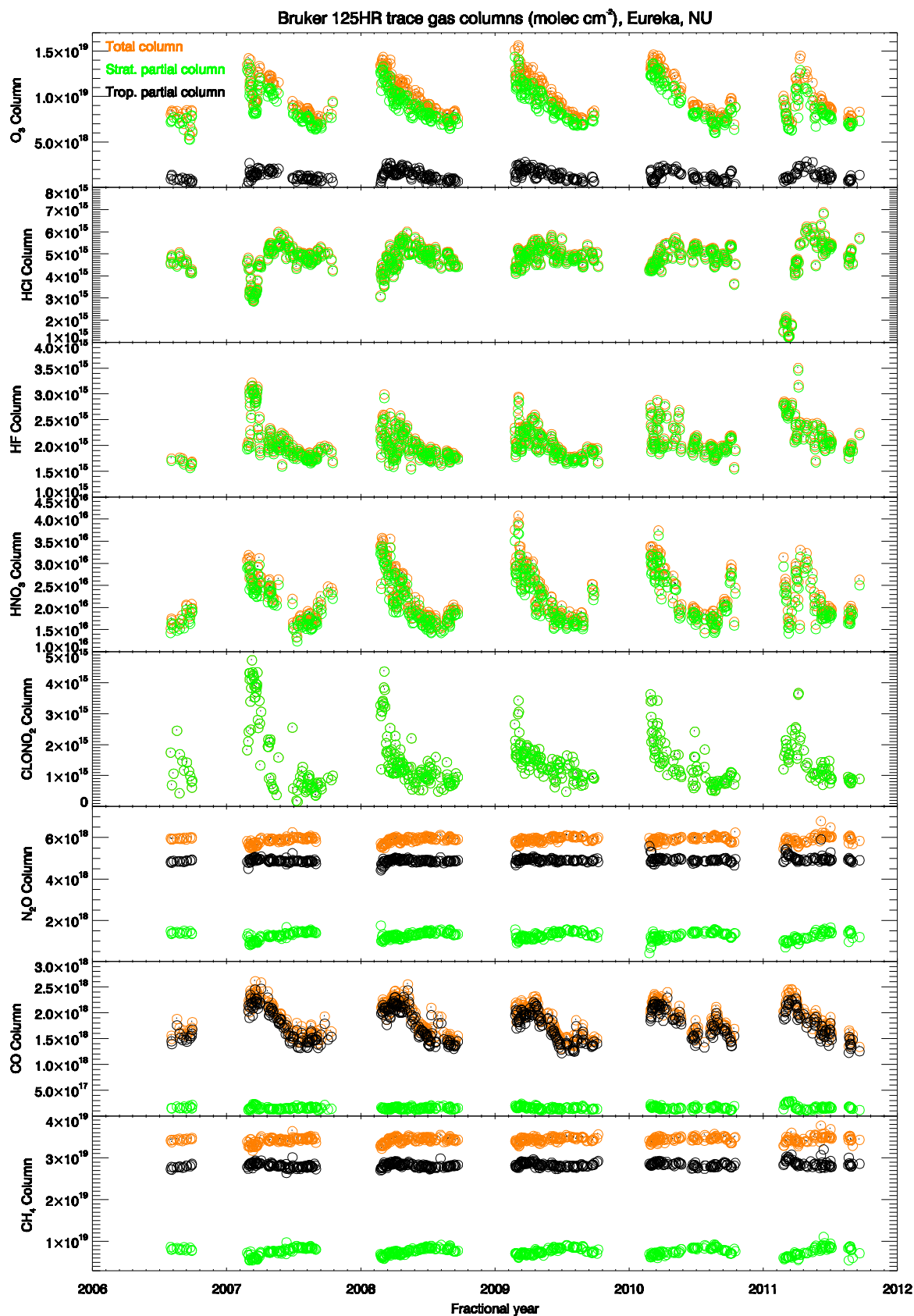
Figure 5.1 Total column (orange), stratospheric (green) and tropospheric (black) partial columns in molec cm^{-2} for the July 2006 - October 2012 period, submitted to the NDACC data archive.

Table 5.1 Mean total error calculated as described in the text for the total columns and stratospheric (10-50 km) and tropospheric (0.6-10 km) partial columns, for the species submitted to the NDACC archive. The mean DOFS was also calculated for all spectra for the same columns.

Target gas	S_{TOTAL} (%) (0.6-100 km)	S_{TOTAL} (%) (10-50 km)	S_{TOTAL} (%) (0.6-10 km)	Mean DOFS (0.6-100 km)	Mean DOFS (10-50 km)	Mean DOFS (0.6-10 km)
O_3	4.3	3.8	23.0	6.4	4.4	2.0
HCl	4.2	4.3	–	2.4	2.4	0.0
HF	5.0	5.1	–	2.2	2.2	0.0
HNO_3	16.2	17.1	–	2.3	2.2	0.1
$ClONO_2$	15.0	15.0	–	0.8	0.8	0.0
N_2O	3.9	11.9	4.2	4.1	1.8	2.3
CO	1.8	14.6	1.7	2.8	0.6	2.2
CH_4	14.0	28.0	16.7	3.5	1.5	2.0

5.2 NDACC

Established in 1991, the Network for the Detection of Stratospheric Change [*Kurylo and Solomon,* 1990; *Kurylo and Zander,* 2000] focused on observing and measuring stratospheric ozone, ozone-related chemicals, and meteorological variables, at a globally distributed set of ground-based remote-sensing stations. The network includes lidars and ultraviolet, visible, infrared, and microwave instruments for total column and vertical profile measurements, as well as in situ aircraft and balloon sounding instruments.

After ten years of careful and comprehensive worldwide observations of a large number of atmospheric parameters, scientists met at the NDSC 2001 Symposium, held in Arcachon, France on 24-27 September 2001. Their conclusion was that during the first decade, the NDSC had made important progress in understanding the changes in stratospheric ozone and in associating these changes with tropospheric chemistry and climate [*NDSC 2001 Symposium Report,* http://www.ndsc.ncep.noaa.gov/news/ndsc_01sym .html].

While the NDSC continues to monitor changes in the stratosphere with a focus on the ozone layer and its evolution, it now also evaluates trends in both stratospheric and tropospheric composition, investigates links between climate change and atmospheric composition, validates space-based measurements of the atmosphere, organizes scientific field campaigns, and contributes to the testing and the improvement of atmospheric models. To better reflect these priorities and the expanded tropospheric and stratospheric coverage, the network changed its

name to the Network for the Detection of Atmospheric Composition Change in 2007 [*NDACC Newsletter,* 2007; http://www.ndacc.org/].

Today, NDACC comprises more than 70 high-quality remote-sensing research stations (Figure 5.2) and consists of nine working groups, representing the various techniques that are used in the network: Dobson and Brewer, FTIR, Lidar, Microwave, Ozone and Aerosol sondes, Satellite, Spectral UV, Theory and Analysis, and UV-visible, with observational capabilities as shown in Figure 5.3. It celebrated twenty years of global atmospheric research at the international Symposium held on November 7-10, 2011 in Saint Paul, Reunion Island, France.

Figure 5.2. Location of the NDACC research stations (reproduced from NDACC home page, http://www.ndacc.org).

The infrared working group (IRWG) comprises a network of more than twenty high-resolution FTIR spectrometers that are part of the NDACC. The acquired atmospheric absorption spectra are used to retrieve the concentration of more than twenty trace gases such as O_3, HCl, HF, NO, NO_2, $ClONO_2$, HNO_3, CH_4, C_2H_6, N_2O, CFC-11, CFC-12, CO, and OCS. The PEARL 125HR was certified as an NDACC instrument in January 2009, based on a formal certification process (details can be found in *Batchelor et al.,* 2009).

Figure 5.3. Observational capabilities of the NDACC. Ripples indicate approximate vertical resolution, plain bars represent column measurements (reproduced from NDACC home page, http://www.ndacc.org).

5.3 The IRWG Harmonization Initiative

At the recommendation of the IRWG, all the FTIR sites are making efforts to standardize the retrieval parameters for the species retrieved and archived by our community. Prior to this, each site developed its own retrieval parameters based on its particularities (*e.g.,* a set of retrieval parameters that works well for a tropical site might not be ideal for an Arctic site), largely independently. The NDACC IRWG has adopted a two-step approach in the harmonization process. As a first step, a microwindow (or set of microwindows) was recommended for each of the ten primary IRWG species: O_3, HCl, HF, $ClONO_2$, HNO_3, N_2O, CH_4, C_2H_6, HCN, and CO, and all stations had to compare the results obtained using these recommended microwindows with those obtained using their previously chosen microwindow. For each gas, a coordinating committee was formed, responsible for collecting the results from all sites and deciding on the final choice. The recommended microwindows and corresponding interfering species are given in Table 5.2. The results of this first part of the harmonization exercise were presented at the IRWG Annual Meeting in 2009.

Table 5.2 Microwindows recommended by the NDACC IRWG for O_3, HCl, HF, $ClONO_2$, HNO_3, N_2O, CH_4, C_2H_6, HCN, and CO, and the corresponding interfering species.

Target gas	Microwindow(s) (cm^{-1})	Interfering species
O_3	1000.00-1005.00	H_2O, CO_2, O_3(676), O_3(667), O_3(686), O_3(668), C_2H_4
HCl	2727.73-2727.83	O_3, HDO
	2775.70-2775.80	O_3, N_2O
	2925.80-2926.00	CH_4, NO_2, O_3
HNO_3	867.05-870.00	H_2O, OCS, NH_3
	872.25-874.00	H_2O, OCS, NH_3
HF	4000.86-4001.10	O_3, H_2O
	4038.81-4039.07	H_2O, CH_4, HDO
	4109.77-4110.07	H_2O, CH_4, HDO
$ClONO_2$	780.12-780.32	CO_2, O_3, HNO_3, H_2O, CCl_4
HCN	3268.05-3268.40	H_2O
	3287.10-3287.35	H_2O
	3299.40-3299.60	H_2O
C_2H_6	2976.66-2976.95	H_2O, O_3
	2983.20-2383.55	H_2O, O_3
	2986.50-2986.95	H_2O, O_3
CO	2057.684-2058.00	O_3, CO_2, OCS
	2069.56-2069.76	O_3, CO_2, OCS
	2157.507-2159.144	O_3, N_2O, H_2O, OCS
N_2O	2481.30-2482.60	H_2O, HDO, CO_2, O_3, CH_4
	2526.40-2528.20	H_2O, HDO, CO_2, O_3, CH_4
	2537.85-2538.80	H_2O, HDO, CO2, O_3, CH_4
	2540.10-2540.70	H_2O, HDO, CO_2, O_3, CH_4
CH_4	2613.70-2615.40	H_2O, HDO, NO_2, CO_2
	2650.60-2651.30	H_2O, HDO, NO_2, CO_2
	2835.50-2835.80	H_2O, HDO, NO_2, CO_2
	2903.60-2904.03	H_2O, HDO, NO_2, CO_2
	2921.00-2921.60	H_2O, HDO, NO_2, CO_2

The second step in the harmonization initiative involved the testing of new *a priori* profiles and *a priori* uncertainties, along with a new layering scheme and extended altitude range. The new *a priori* profiles were generated using the Whole-Atmosphere Community Climate Model (WACCM), a comprehensive numerical model developed at the National Center for Atmospheric Research [*Sassi et al.,* 2002] that spans the range of altitudes from Earth's surface to the thermosphere. Using the 40-year (1980-2020) average of the profiles from the WACCM run for each species, *a priori* profiles were created for each NDACC site. The one standard deviation from the mean was also provided to be used as input for the $\mathbf{S_a}$ covariance matrix. In addition, the recommended altitude range was extended from ground level to 120 km and the altitude grid was increased to 48 layers. The resulting retrievals were compared with those obtained using the original parameters at each station and were presented at the IRWG Annual Meeting in 2010. Based on the averaging kernels, fit quality, DOFS, errors, *etc.*, decisions can be made on the set of parameters that is the most appropriate for implementation in retrievals at Eureka. This chapter summarizes the results of the comparison exercise obtained for all ten species above. Note that the full $n \times n$ $\mathbf{S_a}$ covariance matrix on the site-specific grid, also provided with the WACCM *a priori* profiles for each gas, was not tested. Results from other sites suggested that this did not give as good results as the WACCM 1σ $\mathbf{S_a}$.

Three combinations of parameters were used in the "step two" tests: these are identified by case number in Table 5.3.The results of the harmonization exercise will be discussed for each gas in the following sections.

Table 5.3 The three sets of parameters compared in the second part of the IRWG harmonization exercise. All $\mathbf{S_a}$ matrices include off-diagonal elements using a Gaussian interlayer correlation length as discussed in the text.

Case #	*a priori* profiles	Sa covariance matrix (%)	Altitude range (km)	Altitude grid (layers)
1	Eureka	Eureka (Section 3.4.1)	0.6-100	38
2	WACCM	Eureka (Section 3.4.1)	0.6-120	48
3	WACCM	1σ based on WACCM	0.6-120	48

5.4 Retrieval parameter harmonization for ozone

As shown in the previous chapter, ozone microwindows were intensively studied and the most appropriate microwindow for retrievals at Eureka was found to be 1000-1004.5 cm^{-1} [*Lindenmaier et al.,* 2010]. The microwindow recommended by the IRWG extended this to 1005 cm^{-1}, and 1000-1005 cm^{-1} was used for all results discussed below. The ozone time series presented at the 2009 IRWG Annual Meeting is shown in Figure 5.4.

The top panel shows the total ozone columns from August 2006 to May 2009, for the sunlit part of each year. The annual cycle of ozone driven by the Brewer-Dobson circulation can be clearly distinguished, with large values during late winter/early spring, slowly dropping during the summer to minimum values, then increasing again during the fall. Greater variability is seen during each spring, these being explained by the more dynamically active meteorological conditions during spring compared to the summer. The presence of the cold polar vortex can also promote chemical reactions that may result in ozone depletion.
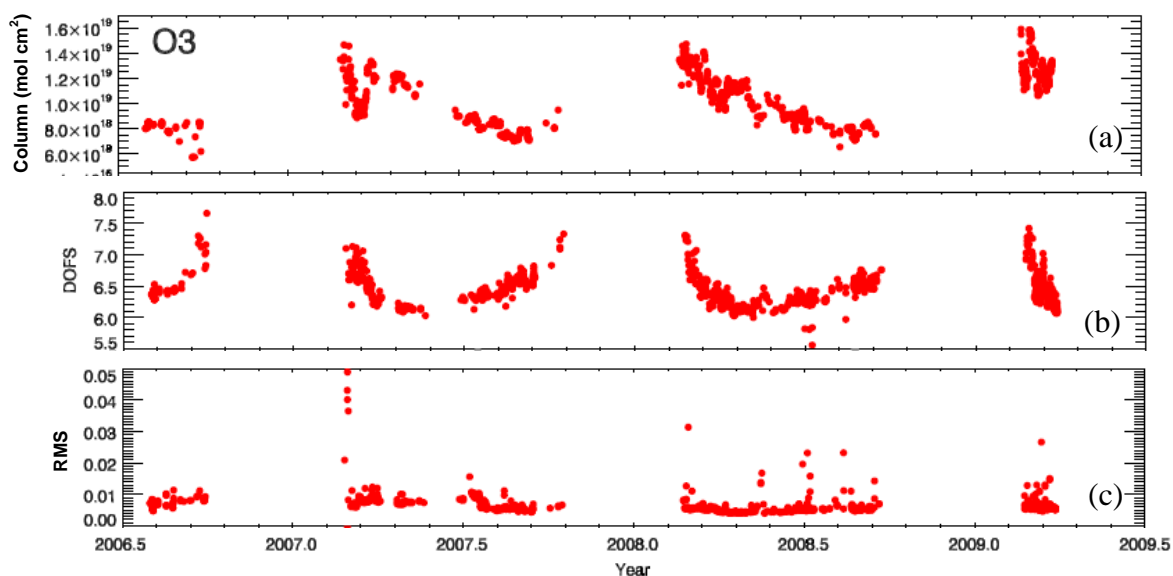
Figure 5.4. (a) Ozone total columns, (b) DOFS, and (c) RMS fitting residuals for August 2006 to May 2009.

The DOFS (panel (b)) are larger during the spring and fall compared to summer, as at these times of the year the solar zenith angles are larger. When sampling through more atmosphere (large SZA), more information is retrieved compared to measurements at small SZA. The RMS fitting residuals (bottom panel) are in general small, in the range 0.005 to 0.01, with some higher values in the spring. These are due to the noisier spectra recorded on the very first

days after polar sunrise, when the sun is very low, and the instrument sampled through haze and thin clouds.

The *a priori* profiles used in the second step of the harmonization exercise are presented in Figure 5.5. In this figure and subsequent plots of the *a priori* profiles and $\mathbf{S_a}$ for other gases, the profiles are plotted on both log and linear scale to show the structures at small VMRs. Panels (a), (b), and (c) correspond to cases 1, 2, and 3, respectively (summarized in Table 5.3). For the troposphere, the *a priori* profiles evolve similarly, peaking at ~35 km in all cases. Above this altitude, the decrease is faster for the WACCM *a priori* profile. There is also a very sharp feature (decrease followed by an increase) at ~95 km that was brought to the attention of the IRWG at the 2010 Annual Meeting.

Figure 5.5. The *a priori* profiles (solid line) used in the second part of the IRWG harmonization exercise for ozone. The dashed lines indicate the *a priori* profile variability given by $\mathbf{S_a}$ for each altitude. Panels (a), (b), and (c) correspond to cases 1, 2, and 3, respectively, as specified in Table 5.3. The profiles are plotted on both log scale (left panels) and linear scale (right panels).

The WACCM-based 1σ $\mathbf{S_a}$ covariance matrix used in case 3 constrains the retrieved profile more in the stratosphere and less in the mesosphere, compared to the original $\mathbf{S_a}$ covariance matrix (cases 1 and 2).

To obtain a good estimate of the measurement noise covariance matrix, RMS versus SNR trade-off curves were constructed for cases 2 and 3. For case 1, trade-off curves were constructed for all gases when the original Eureka retrieval parameters were chosen, and are not shown in this study. For ozone, the resulting *ad hoc* SNR for case 1 is 100. Typical ozone trade-off curves are shown in Figures 5.6 and 5.7 for cases 2 and 3, respectively. For each case, the evolution of the DOFS against SNR is also shown. For case 2, the 4-km Gaussian interlayer correlation used in case 1 was first tested. This led to oscillations in the trade-off curve. By reducing the ILC to 3 km, the oscillations were eliminated and an *ad hoc* SNR of 80 was chosen for these retrievals. Similar results were found for case 3, *i.e.*, a 3-km Gaussian ILC was more appropriate.
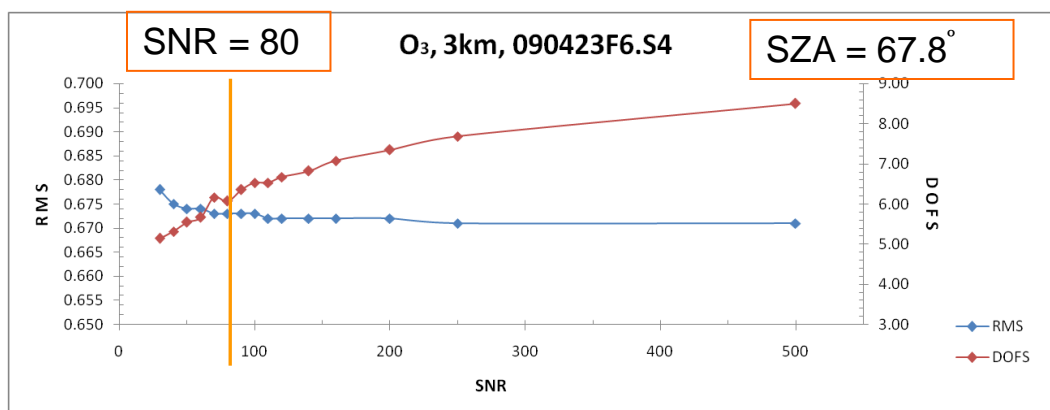
Figure 5.6. RMS fitting residual trade-off curves for case 2, for spectrum 090423F6.S4.
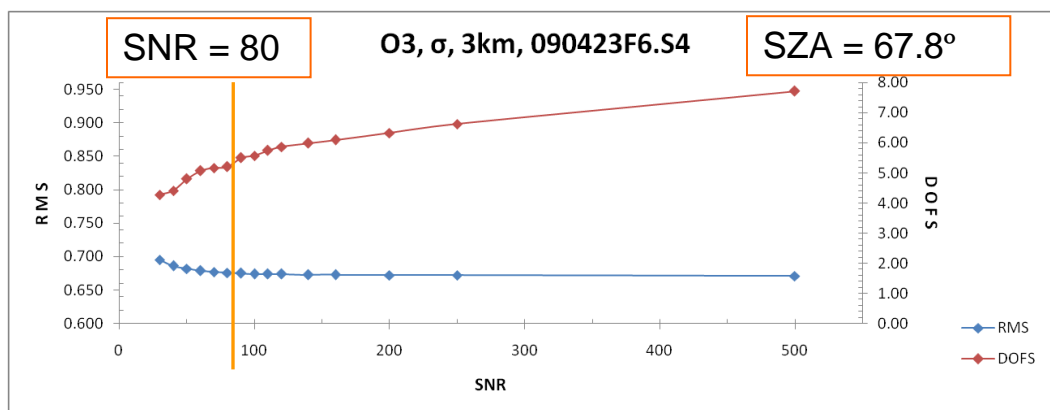
Figure 5.7. Same as Figure 5.6 but for case 3.

The layer and column averaging kernels for each case are shown in Figure 5.8. Panels (a) show the layer averaging kernels (left panel) and the column averaging kernels (right panel) for case 1. The DOFS are the highest for this case, with the highest sensitivity near ground level compared to the other two cases. The column AVKs are also more stable and are close to 1 for each partial and total column. For case 2, panels (b), the sensitivity is good up to 50 km, as seen in both plots, with column AVKs close to 1 up to 50 km. Compared to these AVKs, those obtained for case 3 give less information. The layer averaging kernels in Figure 5.8 (c) are more uniform in peaking around 0.2 and show more sensitivity in the tropospheric region, while the partial column AVKs have more pronounced oscillations above 40 km. These might be a consequence of the larger S_a values above ~55 km for case 3, mentioned above in the *a priori* profile comparison.

Figure 5.8. Layer averaging kernels (left panels) and column averaging kernels (right panels) for: case 1 (a), case 2 (b), and case 3 (c), for spectrum 090423F6.S4, SZA=67.8°. For the layer AVKs, the height of the layer is specified on the left with numbers (height given in km) colored as the corresponding kernel. The column AVKs are colored according to the partial column range shown in the legend.

An example of retrieved profiles for the three cases is shown in Figure 5.9. For all three cases, the retrieved profile displays two maxima, one at ~20 km, the other at ~35 km. The value of the higher peak is the largest for case 2, and the smallest for case 3. This reflects the way the retrieval puts the information at different altitudes, according to the averaging kernels. Above 55 km, the retrieved profile coincides with the *a priori* profile (except case 3, for which this is true above ~70 km), as according to the averaging kernels, at these altitudes there is no sensitivity to the measurement.
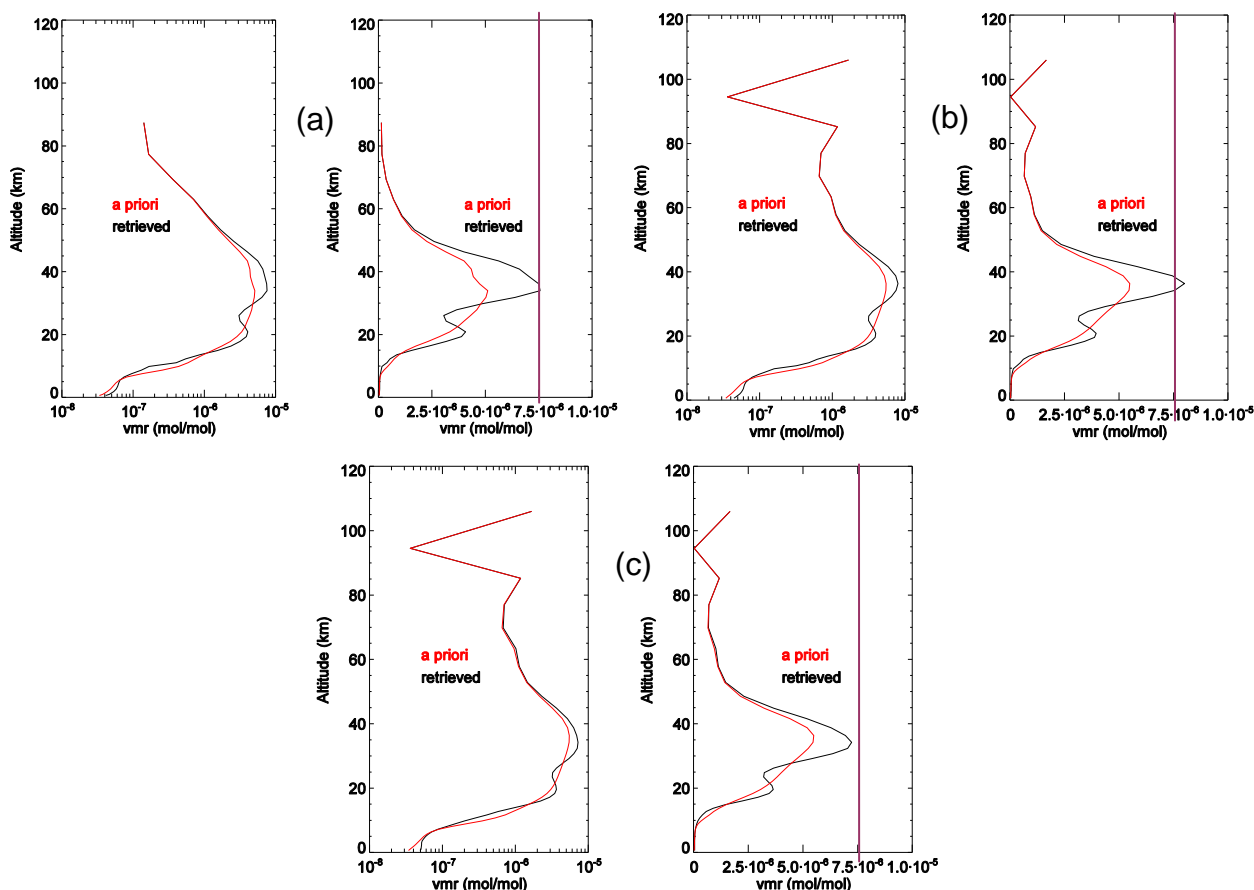
Figure 5.9. Retrieved ozone profiles (black) for: (a) case 1, (b) case 2, and (c) case 3, for spectrum 090423F6.S4, SZA=67.8°. The *a priori* profiles are shown in red. The profiles are plotted on both log (left panels) and linear (right panels) scales. The purple vertical line indicates the maximum of 7.5×10^{-6} in the retrieved profile for case 1.

Total columns were also calculated and compared for all three cases listed in Table 5.3 for all 2009 data. Figure 5.10 (a) to (d) shows the comparison for cases 1 and 2. The mean difference between the total columns is $(0.16 \pm 0.19)\%$, the original retrieval method used at

Eureka (case 1) giving slightly larger total column values. The mean percentage difference was calculated using the relation

$$\Delta_{12}\% = \frac{100}{N}\sum_{i=1}^{N}\left[2(\text{case } 1_i - \text{case } 2_i)/(\text{case } 1_i + \text{case } 2_i)\right], \tag{5.1a}$$

where case 1 and case 2 represent the total columns calculated using the parameters in Table 5.3 for these two cases, for spectrum i. The DOFS are also slightly higher for the original retrieval method (case 1), while the RMS fitting residuals are approximately the same in both cases. Figure 5.10 (e) to (h) shows the comparison for cases 2 and 3. The mean percentage difference between the total columns calculated using these two approaches is very small, (-0.14±0.26)%, as shown in panel (f). For this comparison, the mean percentage difference was calculated using a similar equation to Equation 5.1a:

$$\Delta_{23}\% = \frac{100}{N}\sum_{i=1}^{N}\left[2(\text{case } 2_i - \text{case } 3_i)/(\text{case } 2_i + \text{case } 3_i)\right], \tag{5.1b}$$

where case 2 and case 3 represent the total column calculated using the parameters in Table 5.3 for these two cases, for spectrum i. The DOFS differ by ~1, being larger for the retrievals in case 2. The RMS fitting residuals are very similar for both approaches.

To conclude, retrievals made in cases 1 and 2 give similar results (total columns, DOFS, and RMS fitting residual values). However, the layer averaging kernels show more sensitivity in the troposphere for case 1. The column averaging kernels for case 3 have more oscillations and the DOFS are smaller by ~1 compared to the other two cases. Based on these results, the original Eureka *a priori* profile combined with the Eureka S_a (case 1) gives the best averaging kernels, DOFS and RMS fitting residual values. Of the two WACCM tests, the results are better for case 2, with S_a based on real variability in the Eureka ozonesonde record.

5.5 Retrieval Parameters Tested for Other Gases

Analyses similar to ozone were made for all gases. This section will summarize the results of implementing the IRWG recommendations with Section 5.5.1 and Section 5.5.2 describing results from the first step and the second step of the harmonization initiative, respectively.
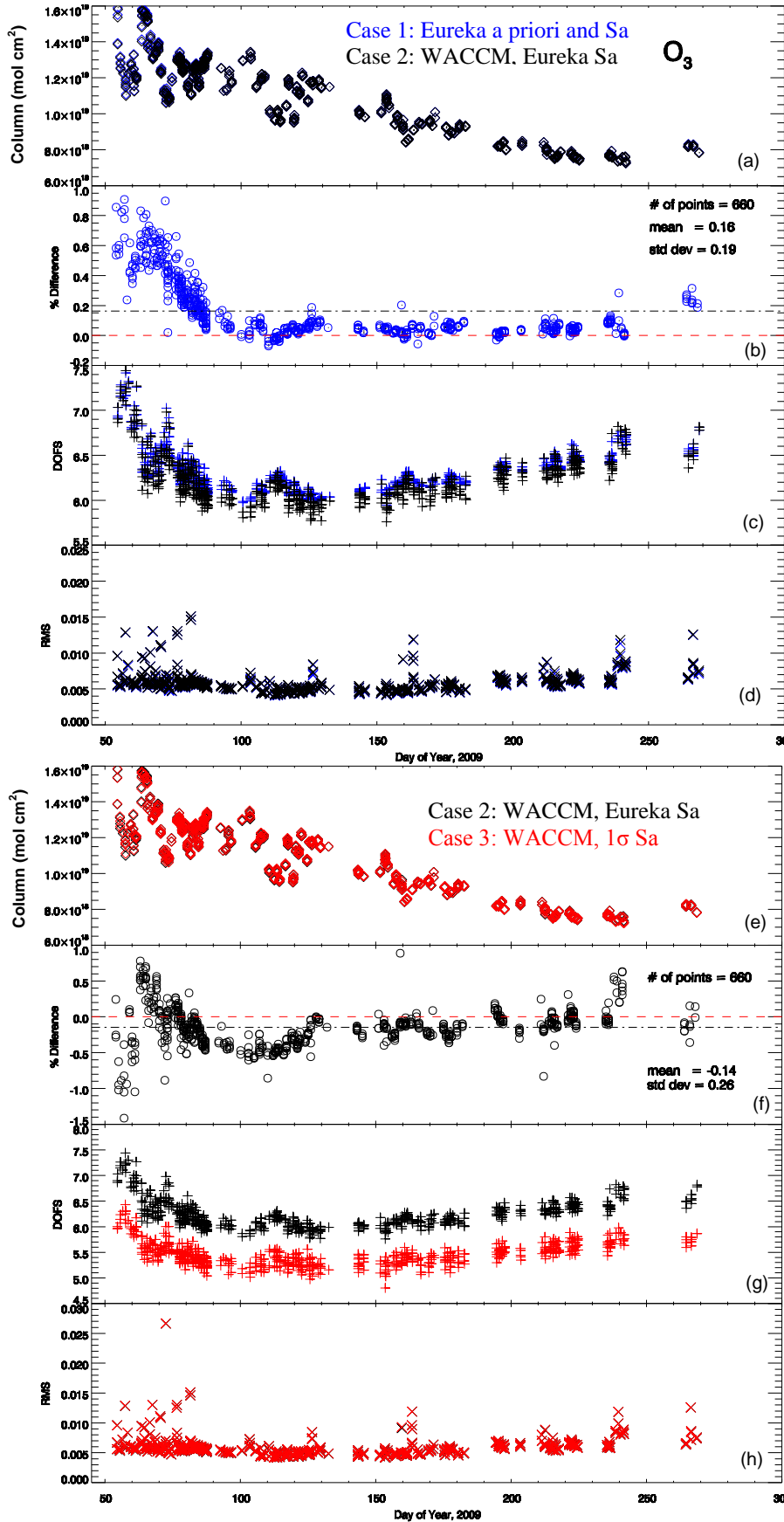
Figure 5.10. (a) Total ozone column, (b) % difference calculated using Equation 5.1a, (c) DOFS, and (d) RMS fitting residual comparison for columns calculated using cases 1 (blue) and 2 (black) for the sunlit part of 2009. The number of points compared, the mean % difference, and the standard deviation for this comparison are given in panel (b). Panels (e), (f), (g), and (h) are the total column, % difference, DOFS, and RMS fitting residual, respectively for the comparison of columns calculated using cases 2 (black) and 3 (red), for the same period. Here, the % difference was calculated using Equation 5.1b, and the results are shown in panel (f).

5.5.1 Evaluation of Recommended Microwindows

For ozone, CO, N$_2$O, and CH$_4$, the recommended microwindows were already in use for retrievals at Eureka, as seen by comparing Tables 3.1 and 5.2. Example of fits for both sets of microwindows for all ten gases studied are shown in Appendix A. Total columns were calculated for all ten gases using the original Eureka microwindows (Table 3.1) and the IRWG-recommended microwindows (Table 5.2) and compared for August 2006 to April 2009. Figure 5.11 shows the total column time series for all ten species. The test retrieval is shown with red circles in all cases. Note that HCN time series start only in July 2007, when filter 2 was installed in the instrument. For each of the six species for which the recommended microwindows differed from those used for the original Eureka retrievals, the percentage difference is shown in Figure 5.12 along with the mean percentage difference, the standard deviation, and the number of points compared. The mean percentage difference was calculated as:

$$\Delta\% = \frac{100}{N} \sum_{i=1}^{N} \left[(test_i - original_i)/test_i \right] \tag{5.2}$$

where $test_i$ is the total column calculated for the test microwindows and $original_i$ is the total column calculated using the original Eureka microwindows, for pair i. There is no significant difference for HCl. For HNO$_3$, HF, and C$_2$H$_6$ there is a slight positive bias, while for HCN the bias is negative. For ClONO$_2$ the positive bias is larger, and comes mostly from summertime measurements. During summer, there is less ClONO$_2$ compared to spring, and it is very difficult to retrieve as the DOFS decrease well below 1.

Figure 5.13 shows the DOFS for all ten retrieved species. While there is no significant difference for HF, HCl, and HCN, for HNO$_3$ the DOFS corresponding to the test microwindows are slightly larger. Note that the DOFS for HCl and HF do not follow the usual pattern (large values for large SZA, and decreasing values as the SZAs decrease). This is because the retrievals, both test and Eureka, were made with too high an ILC (4 and 5 km, respectively). This was accounted for in the second part of the harmonization evaluation. For ClONO$_2$, the DOFS corresponding to the test microwindows are smaller by ~0.2, especially during the summer period. For C$_2$H$_6$ the test retrieval gives a better result, the DOFS being larger by ~0.5.

The RMS fitting residual results are shown in Figure 5.14. Slightly higher RMS values can be seen for HF and C$_2$H$_6$ for the test microwindows, while for the other gases the RMS values are very similar for the test and original microwindows. In general, the RMS fitting
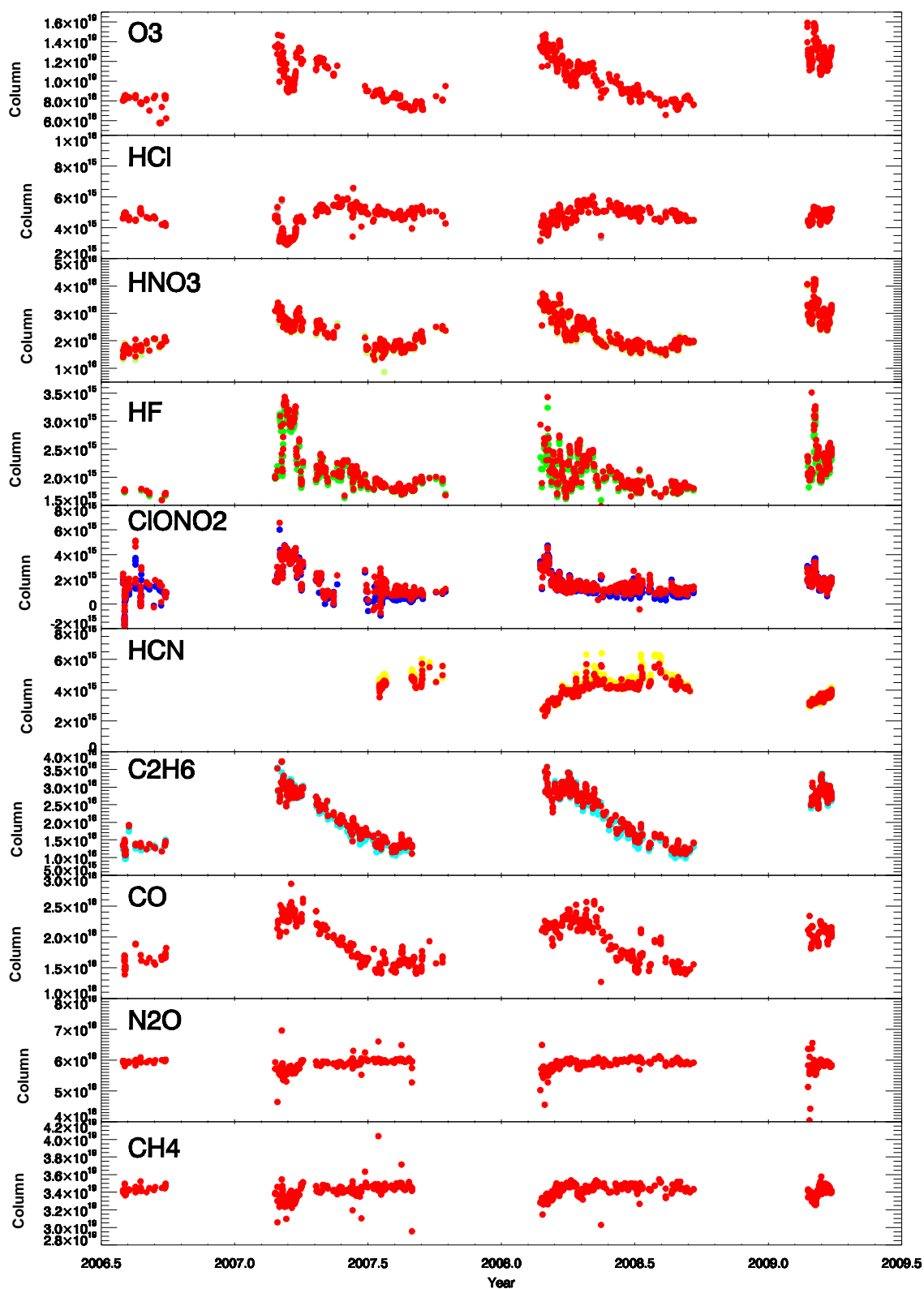
Figure 5.11. Total column amounts in molec cm^{-1} for the ten gases for which the microwindow harmonization evaluation was made. In all cases, the red circles represent the IRWG test results, while the other colors represent the original Eureka results.
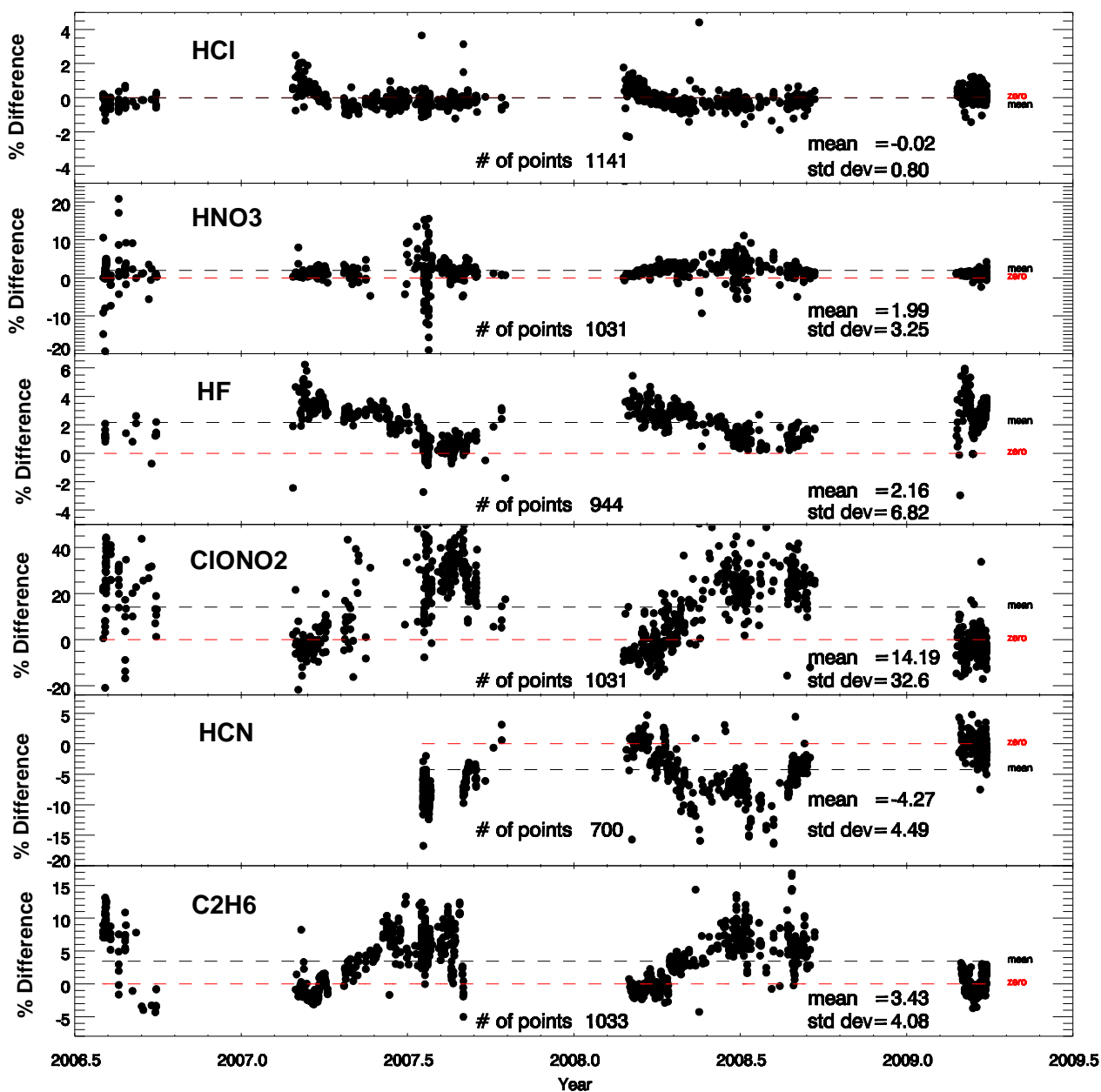
Figure 5.12. Percentage difference for the total columns of HCl, HNO$_3$, HF, ClONO$_2$, HCN, and C$_2$H$_6$ retrieved with the IRWG test microwindows and with the original Eureka microwindows. The mean percentage difference is calculated as shown in Equation 5.2. The standard deviation and the number of points are also shown.
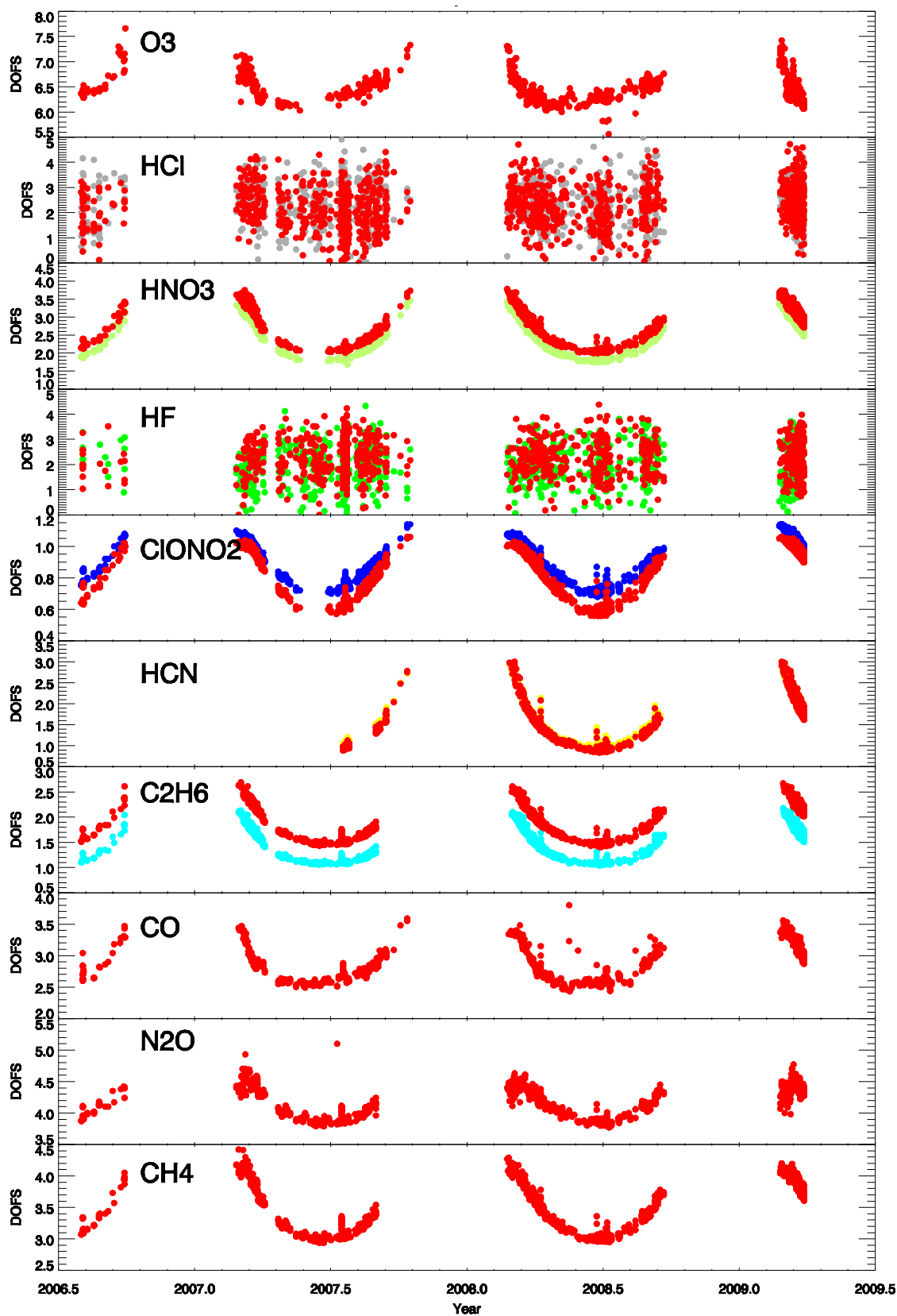
Figure 5.13. The DOFS for the retrievals shown in Fig. 5.11. Red circles represent the test microwindow results, and the colored circles represent the original Eureka results.
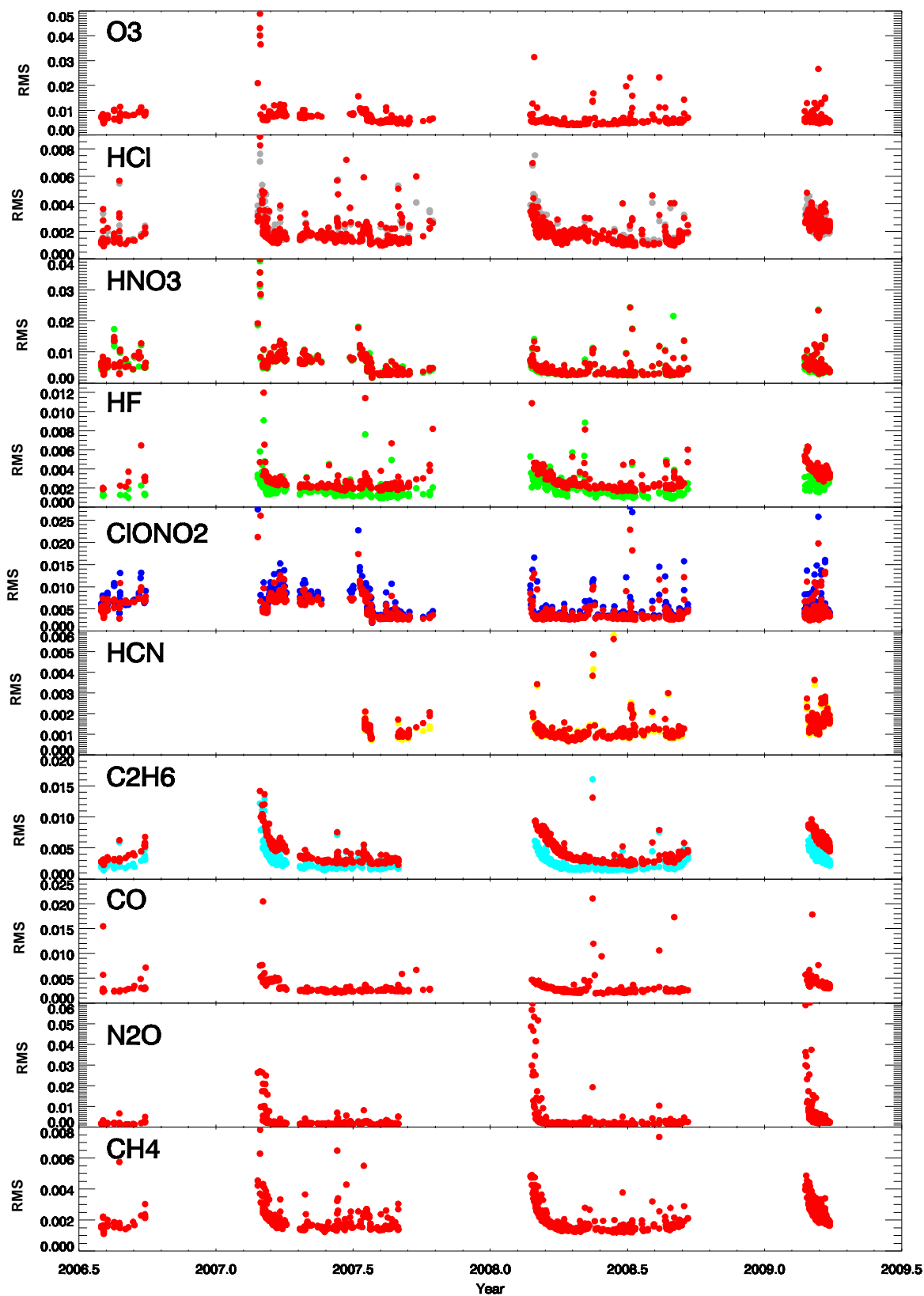
Figure 5.14. RMS fitting residuals corresponding to the retrievals shown in Fig. 5.11. Red circles represent the test microwindow results, and the colored circles represent the original Eureka results.

residual values are larger in the spring or when the meteorological conditions are not optimal for measurements.

The use of the recommended microwindows led to significant improvement for C_2H_6. In contrast, $ClONO_2$ retrievals made with the recommended microwindow were worse and should not be adopted without further evaluation. For the other eight gases there is no significant difference, and we agree that the IRWG-recommended microwindows are appropriate for Eureka.

5.5.2 Evaluation of Recommended *a priori* Profiles

The second part of the evaluation exercise was done for eight gases only. For HF, no WACCM output was provided, while for HCN, the microwindow selection for retrievals was not finalized. The ozone results were presented in detail in Section 5.4, and for the other gases only a selection of the significant results are given below. More plots (*a priori* profiles, averaging kernels, RMS versus SNR trade-off curves, and retrieved profiles) are provided in Appendix A.

As mentioned earlier, the original ILC for **HCl** was too large. When building the trade-off-curve to determine the correct *ad hoc* SNR for the retrievals in case 2, convergence was not reached for a SNR higher than 120 for the recommended microwindows. Since there was no significant difference between the results obtained using the original Eureka microwindows and those obtained using the recommended ones (as presented in the previous section), the original Eureka microwindows were used for the second part of the exercise. The ILC was reduced first to 3 km and then further to 2.5 km. The latter was adopted, as it resulted in smooth RMS fitting residuals and DOFS curves. Similar results were obtained for case 3 and an *ad hoc* SNR of 150 was chosen for cases 2 and 3 for the HCl retrievals. Table 5.4 indicates the ILC and SNR used for all cases in the second part of the evaluation exercise for all trace gases analyzed.

The HCl total columns retrieved for all three cases listed in Table 5.3 were compared for 2009 and the results are shown in Figure 5.15. Panels (a) to (d) correspond to the comparison between case 1 and case 2. The HCl total columns are given in panel (a), with blue and black corresponding to cases 1 and 2, respectively. The column amounts for case 2 are larger than those obtained for the original Eureka parameters (case 1), as seen in panel (a), the mean percentage difference being (-3.17±1.43)% (b). The DOFS (c) are also larger for case 2 compared to case 1, by ~0.6. The RMS fitting residuals (d) are not very different, slightly larger for case 1 during the spring and early summer. The comparison between cases 2 (black) and 3

(red), shown in panels (e) to (h), give similar total columns (e) and a very small mean percentage difference between the two approaches, (0.09 ± 0.58)% (f). The DOFS, shown in panel (g), differ consistently by ~0.8, being larger for the retrievals in case 2. The RMS fitting residuals (h) are very similar for both cases.

Based on these results, case 2 is clearly the best for HCl retrievals at Eureka. Example of fits, layer and column averaging kernels, *a priori* profiles, RMS fitting residual trade-off curves, and retrieved profiles are provided in Appendix A (Figures A.1 to A.8).

Table 5.4. Summary of the ILC and SNR used for cases 1, 2, and 3 during the evaluation exercise step two.

Target gas	Case 1 ILC (km)	Case 1 SNR	Case 2 ILC (km)	Case 2 SNR	Case 3 ILC (km)	Case 3 SNR
O_3	4	100	3	80	3	80
HCl	4	100	2.5	150	2.5	150
HNO_3	4	100	4	150	4	150
HF	5	100	–	–	–	–
$ClONO_2$	4	100	4	120	4	120
HCN	4	200	–	–	–	–
C_2H_6	1	200	1	250	1	250
CO	4	200	4	300	4	250
N2O	7	70	7	100	7	100
CH4	4	70	4	100	4	100

For **HNO₃**, the averaging kernels for case 2 peak higher (are larger) in the 8-15 km region compared to the other two cases (Figure A.14), indicating more sensitivity in this altitude range. At higher altitudes, from 20-30 km, case 1 gives more information (also noticeable in the profile plots in Figure A.15). The cause of the oscillations noticeable above 35 km for the column averaging kernels for case 2 is not clear and needs to be further investigated. Another issue found during these retrievals was the large number (18%) of convergence failures for retrievals made in case 2 and 3, compared to 3% for case 1.

The HNO_3 total columns retrieved for all three cases listed in Table 5.3 were compared for 2009 and the results are shown in Figure 5.16. Panels (a) to (d) correspond to the comparison between case 1 and case 2, following the format of Figure 5.10. The columns (a) for case 2 are slightly larger than those obtained for the original Eureka parameters (case 1), the mean
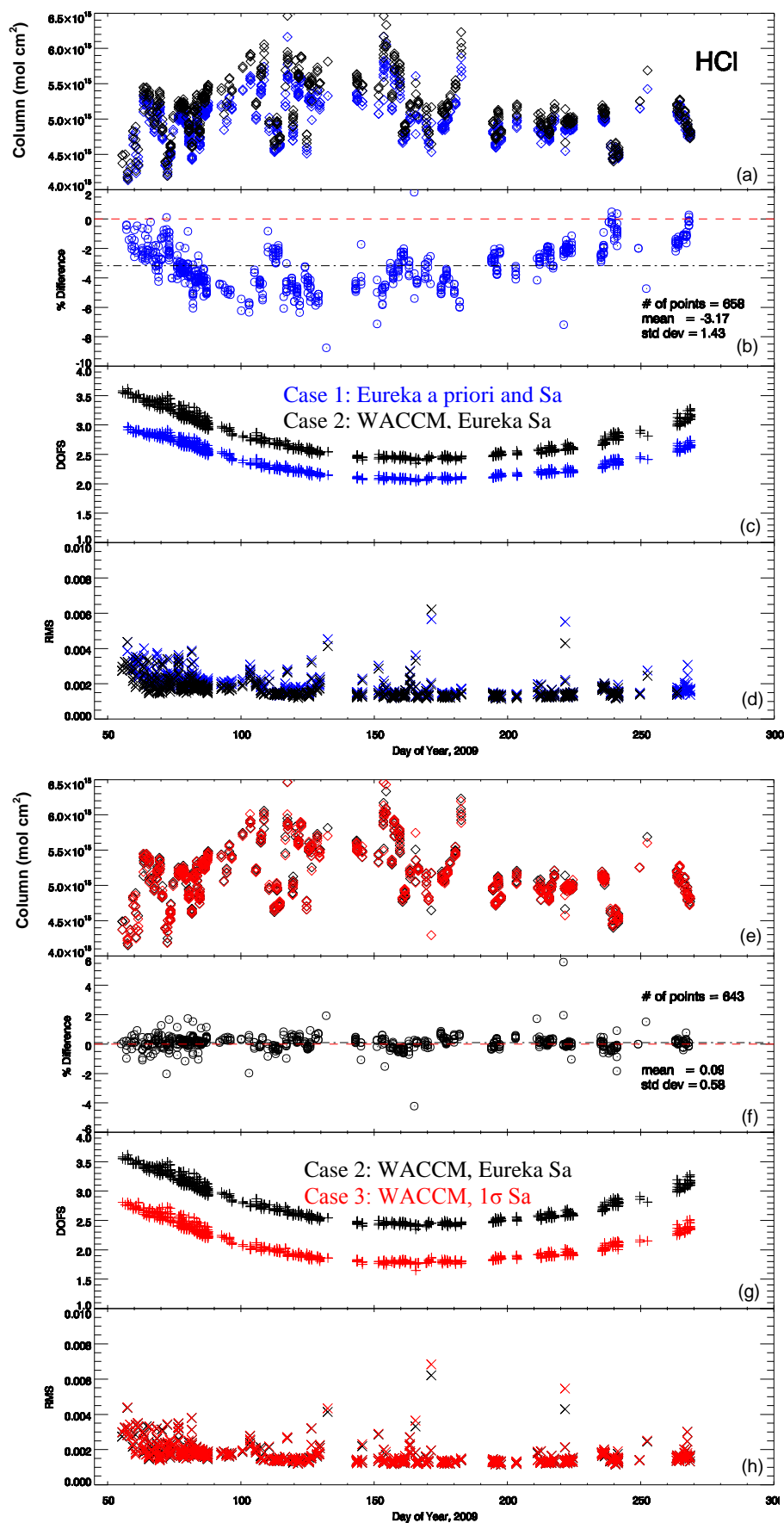
Figure 5.15. Same as Figure 5.10 but for HCl.
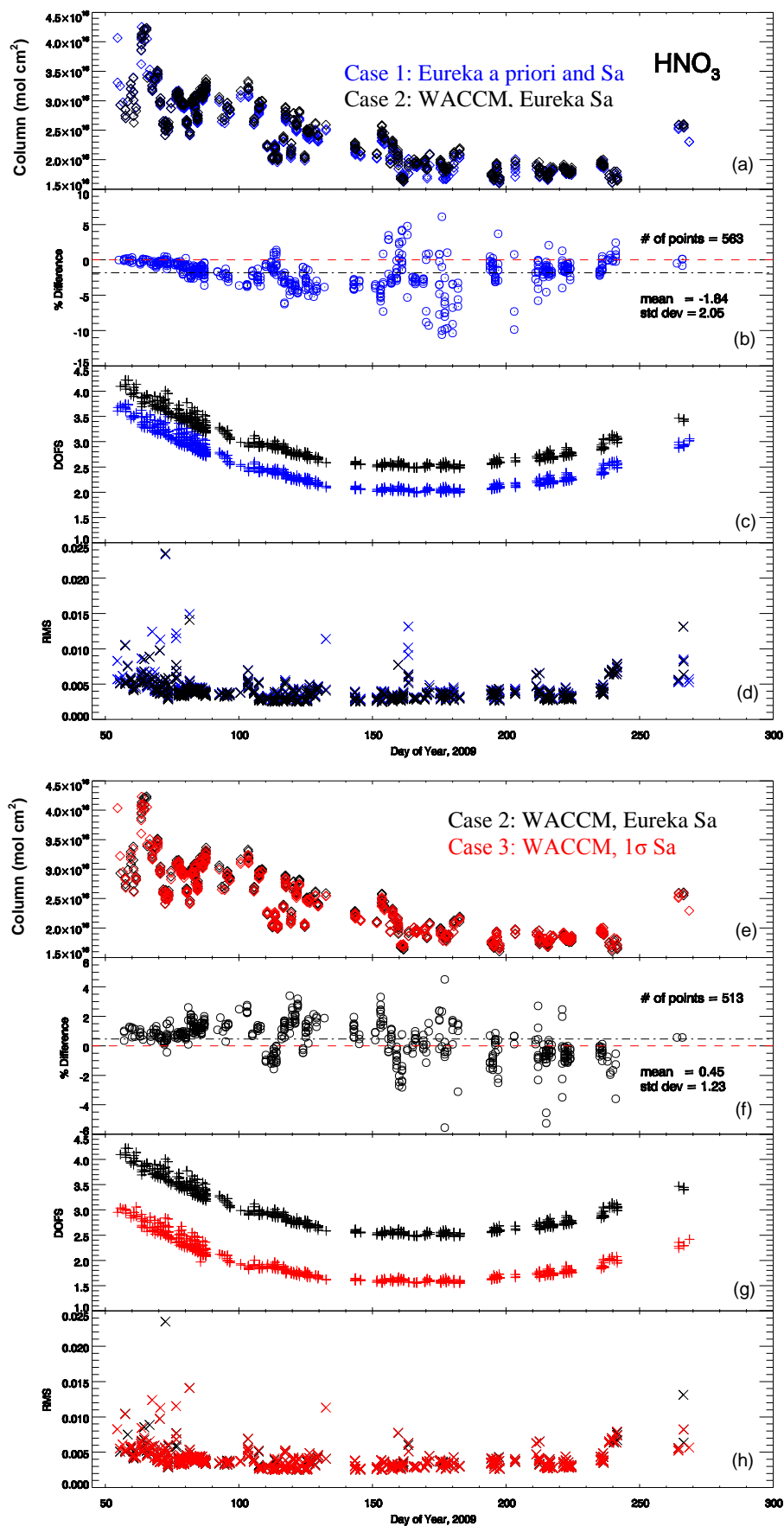
Figure 5.16. Same as Figure 5.10 but for HNO₃.

percentage difference being (-1.84±2.05)% (b).   The DOFS (c) are also larger for case 2 compared to case 1, by ~0.5. The RMS fitting residuals (d) are not very different. The comparison between cases 2 (black) and 3 (red), shown in panels (e) to (h), give similar total columns (e) with a mean percentage difference between the two approaches of (0.457±1.23)% (f).

The DOFS (g), differ consistently by ~1, being larger for the retrievals in case 2. The RMS fitting residuals (h) are very similar for both cases. Overall, retrievals made using case 2 are better than case 3 and the original Eureka setup (case 1). In conclusion, case 2 would be a good choice for retrievals at Eureka, however, more work should be focused on reducing the oscillations in the column averaging kernels.

Since for **ClONO$_2$** the IRWG recommended microwindow gave worse results for Eureka, the second step of the evaluation exercise was done using the original Eureka microwindows. Examining the *a priori* profiles (Figure A.22) we find that in case 1, this peaks at ~20 km compared to ~23 km in the other two cases. Also, the peak VMR for case 1 is approximately twice that for cases 2 and 3 (WACCM underestimating Arctic ClONO$_2$ compared to Eureka *a priori*). The layer averaging kernels (Figure A.24) peak at the same height in all three cases; the retrieval cannot distinguish the individual layers, and all information comes from the partial column from 15 to ~30 km.

The ClONO$_2$ total columns retrieved for all three cases listed in Table 5.3 were compared for 2009 and the results are shown in Figure 5.17. Panels (a) to (d) again correspond to the comparison between case 1 and case 2. The columns (a) for case 2 are smaller than those obtained for the original Eureka parameters (case 1), the mean percentage difference being (2.47±16.6)% (b). Note the large standard deviation during the summer, when the ClONO$_2$ concentration is very small and the retrieval error is large (exceeding 50%). The DOFS (c) are also smaller for case 2 compared to case 1, by ~0.35 during the summer and ~0.15 during spring and fall. The RMS fitting residuals are not very different, as seen in panel (d). The comparison between cases 2 (black) and 3 (red), shown in panels (e) to (h), give larger total columns for case 3 (e) with a mean percentage difference between the two approaches of (-2.55±13.90)% (f). The DOFS, shown in panel (g), differ by ~0.25 during summer and fall and by ~0.15 in the spring, being larger for the retrievals in case 2. The RMS fitting residuals (h) are very similar for both cases. To conclude, retrievals made using the original Eureka *a priori* profiles and S_a (case 1) give the best results and should be used for retrievals at Eureka.
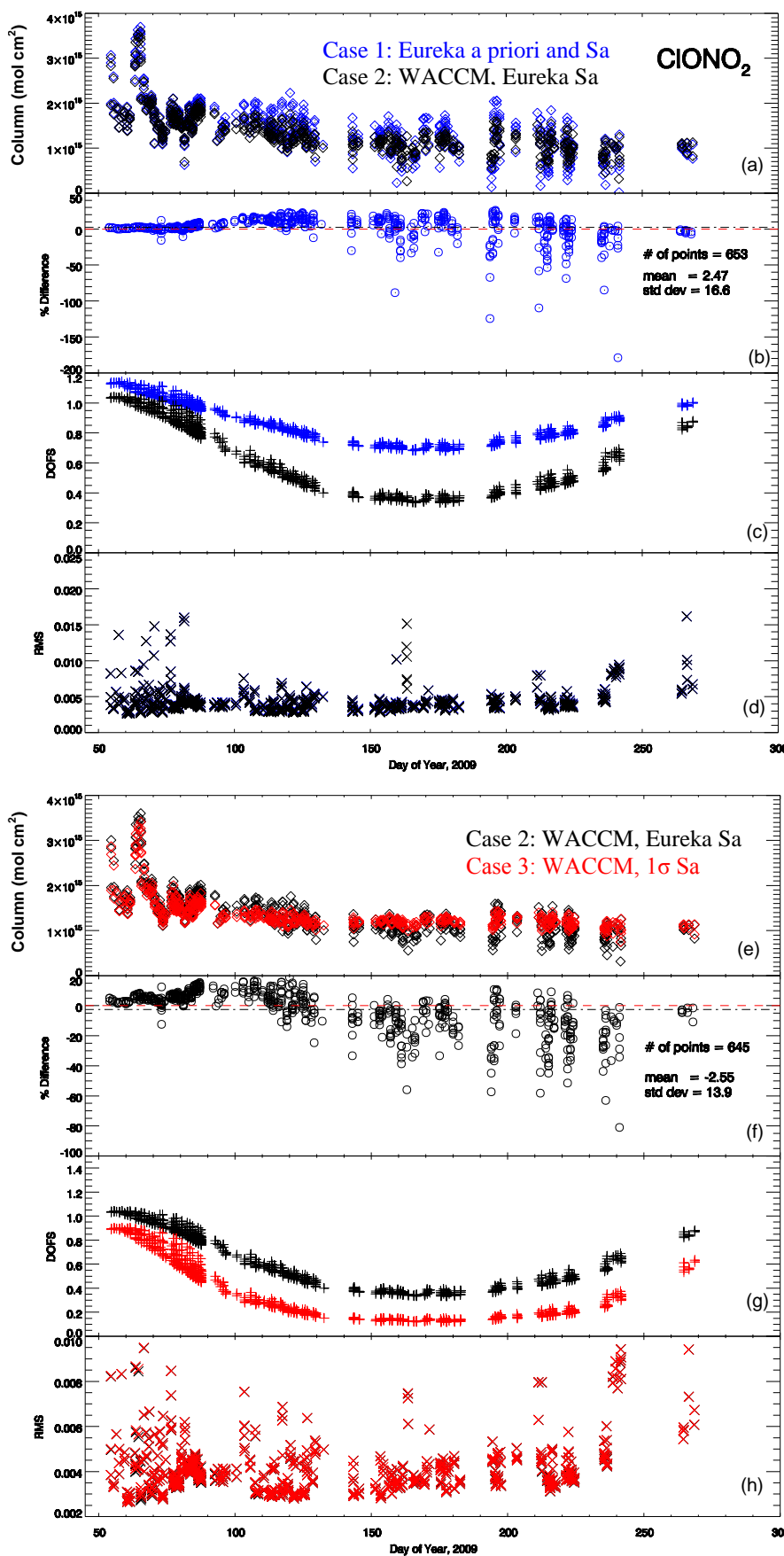
Figure 5.17. Same as Figure 5.10 but for ClONO$_2$.

For **C$_2$H$_6$**, the *a priori* profiles (Figure A.32) have the same value at ground level and decrease smoothly with altitude for all three cases. At ~22 km, the *a priori* profile for case 1 decreases faster than those in cases 2 and 3, remaining constant above 30 km. For cases 2 and 3 the *a priori* profiles continue to decrease above 30 km. The averaging kernels (Figure A.34) for all three cases show that there is no information coming from the measurement above 20 km, and below this altitude, case 1 display the largest peak at ~7 km. For this case, in the tropospheric region the information content of the retrieval is higher compared to cases 2 and 3. It is not clear why the column averaging kernels for case 2 display large oscillations above 15 km. The retrieved profiles (Figure A.35) peak at ~6 km in all cases, with smaller VMRs in cases 2 and 3 compared to case 1.

The C$_2$H$_6$ total columns retrieved for all three cases listed in Table 5.3 were compared for 2009, and the results are shown in Figure 5.18. Panels (a) to (d) correspond to the comparison between case 1 and case 2. The columns (a) for case 2 are similar with those obtained for case 1, the mean percentage difference being (-0.19±1.46)% (b). The DOFS (c) are slightly larger for case 2 compared to case 1, by ~0.1. The RMS fitting residuals (d) are also similar, as seen in panel (d). The comparison between cases 2 (black) and 3 (red), shown in panels (e) to (h), give slightly larger total columns for case 3 (e) the mean percentage difference between the two approaches being (-1.24±1.71)% (f). The DOFS, shown in panel (g), are slightly smaller for case 3 compared to case 2 by ~0.1. The RMS fitting residuals (h) are similar for both cases. Overall, retrievals made using the original Eureka parameters (case 1) give the best result, but only marginally.

CO results were particularly interesting and are discussed in more detail here. Figure 5.19 shows the *a priori* profiles for all three cases. We notice differences between the *a priori* profiles: for cases 2 and 3 they evolve more smoothly from 10 to 40 km compared to case 1, and also increase more sharply above 40 km. Above 25 km, the elements of the **S$_a$** covariance matrix for case 3 are larger than for cases 1 and 2, giving more freedom to the retrieval. Typical averaging kernels are shown in Figure 5.20. The differences in the layer averaging kernels are significant. For cases 2 and 3, the sensitivity is much higher in the upper stratosphere and mesosphere, with lower sensitivity in the troposphere compared to the original Eureka parameters (case 1). The averaging kernels suggest that the retrieval does better with a constant 20% **S$_a$** (case 2) than the WACCM-based 1 σ for **S$_a$** (case 3) (see the shape of the layer averaging kernels for case 3 between 5 and 15 km). The column averaging kernels for cases 2
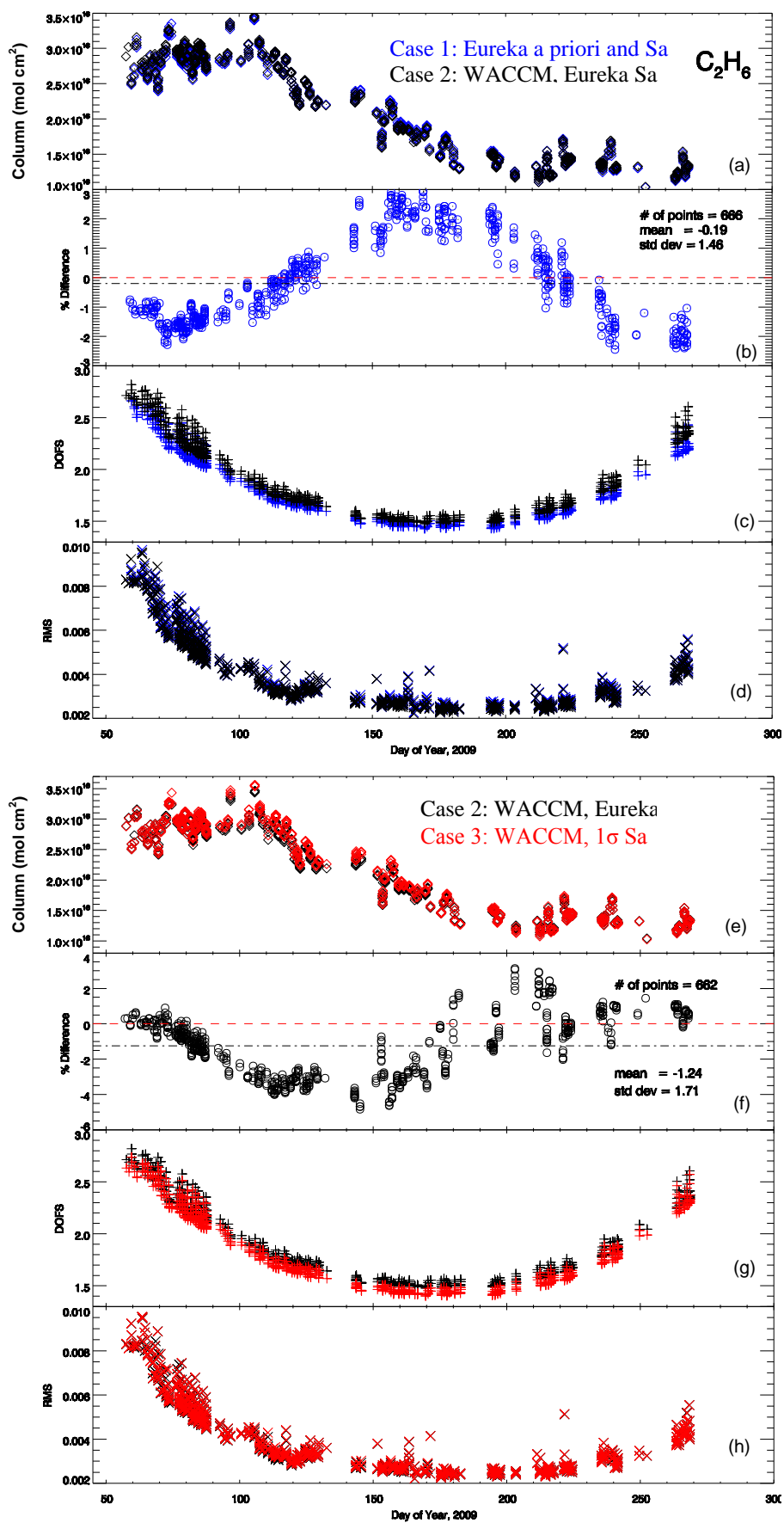
Figure 5.18. Same as Figure 5.10 but for C_2H_6.

and 3 show slight oscillations above 30 km, but this might be due to the higher sensitivity in the stratosphere-mesosphere region.

The retrieved profiles shown in Figure 5.21 confirm that the information is weighted differently, displaying more sensitivity in the stratosphere-mesosphere for cases 2 and 3. However, from 50 to ~64 km for case 2 and from 35 to 58 km for case 3, the VMR becomes negative, indicating oscillations of the retrieved profiles at these altitudes. The cause of these oscillations is not clear but could be related to the magnitude of the *a priori* values, these being larger by approximately one order of magnitude for cases 2 and 3 compared to case 1. The total columns are very similar for all three cases (Figure 5.22) with mean differences of (0.14±0.40)% and (0.17±0.22)%   for comparisons of the retrievals made for cases 1 vs. 2 and 2 vs 3, respectively. The RMS fitting residuals are also very similar for all three cases, while the DOFS are much higher for cases 2 and 3 compared to case 1 (panels (c) and (g)).

From these results, the conclusion is that case 2 would be the best choice for our retrievals at Eureka. However, a more detailed study should be carried out, to insure that these results are correct, and the information believed to come from the upper stratosphere-mesosphere is real.

For **N_2O**, the *a priori* profiles (Figure A.42) have the same value from ground level to ~10 km, then decrease smoothly (less smoothly for case 1) with altitude for all three cases. We notice differences in the $\mathbf{S_a}$ covariance values from ground level to ~35 km, these constraining the retrieval more for case 3 compared to cases 1 and 2. The averaging kernels (Figure A.44) for case 2 indicate more information from 8 to 20 km compared to case 1, for which information comes from the ground to ~25 km. For case 3, most of the information comes from 8-18 km. It is not clear why the column averaging kernels show oscillations above 25 km for all cases, these being stronger for cases 1 and 2. The retrieved profiles (shown in Figure A.45) display oscillations in the troposphere and lower stratosphere for cases 1 and 2 compared to case 3. These are not due to over-fitting the retrieval (as seen in the trade-off curves in Figure A.43). Rather, the retrieved profile in both cases could move with more freedom around the *a priori* profile due to less constraining $\mathbf{S_a}$ values for cases 1 and 2 (Figure A.42). Also, the ILC should be further investigated for N_2O, as its value is much larger (7 km) than for any other gas (typically 3-4 km) retrieved at Eureka.
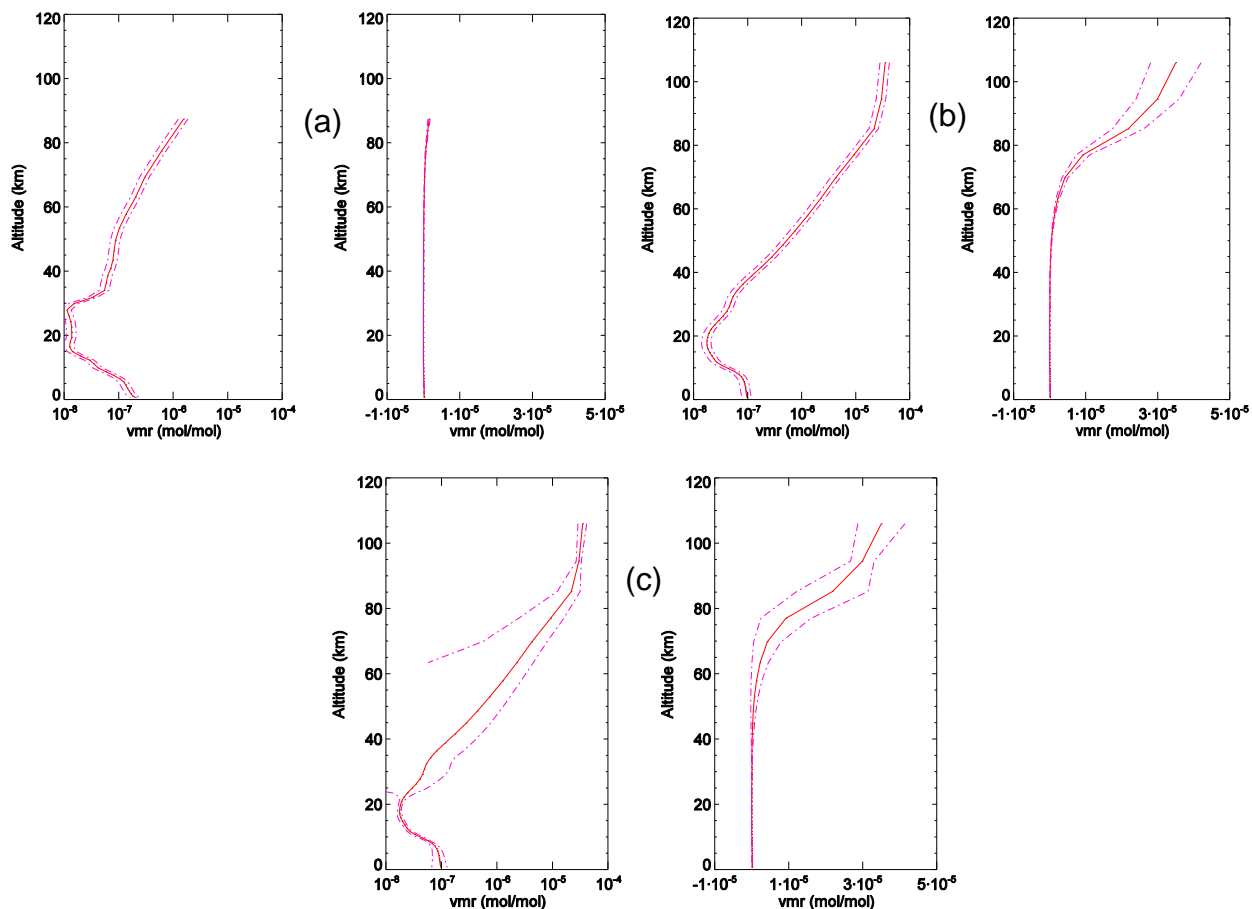
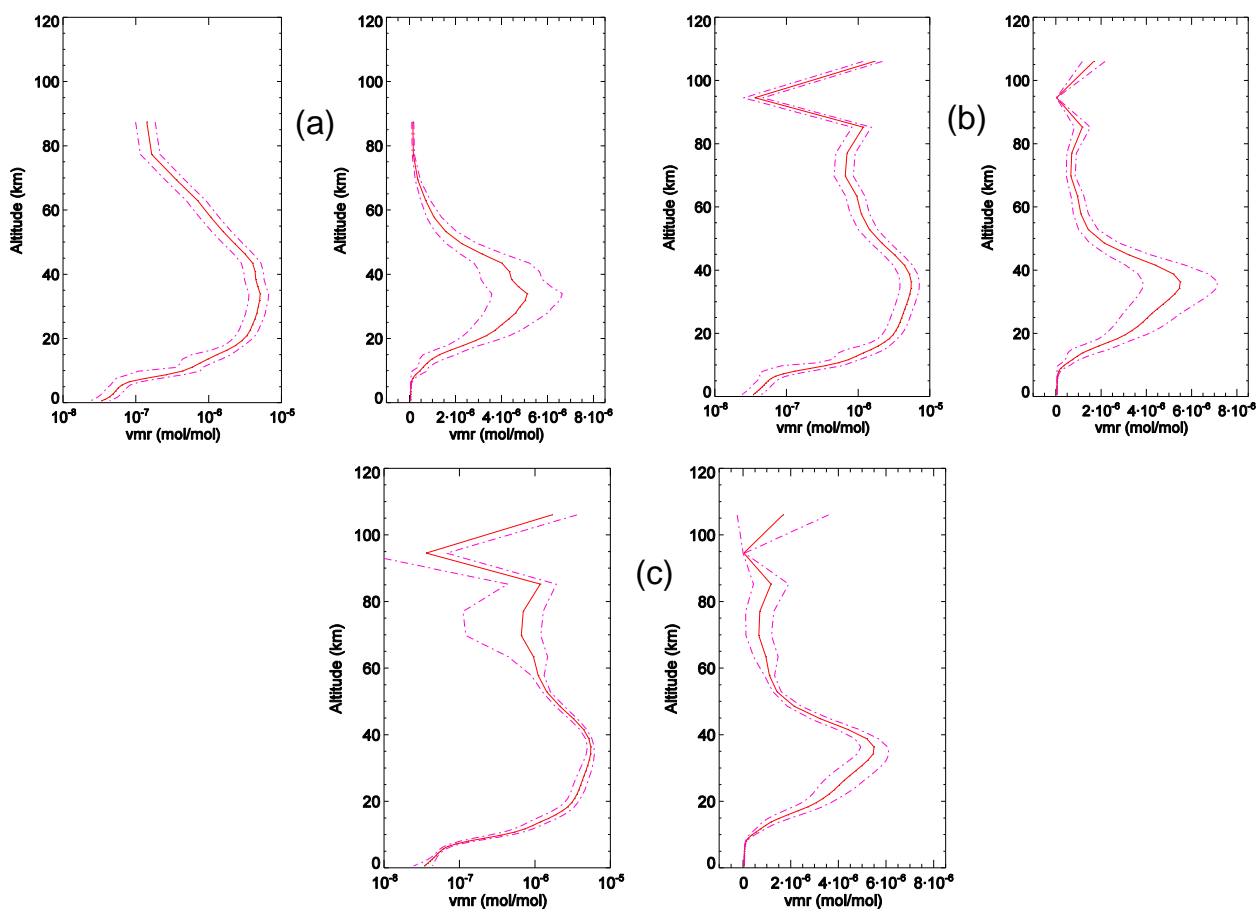Figure 5.19. The *a priori* profiles (solid line) used in the second part of the IRWG harmonization exercise for CO. The dashed lines indicate the *a priori* profile variability given by $\mathbf{S}_a$ for each altitude. Panels (a), (b), and (c) correspond to cases 1, 2, and 3, respectively, as specified in Table 5.3. The profiles are plotted on both log (left panels) and linear (right panels) scales.

The N_2O total columns retrieved for all three cases listed in Table 5.3 were compared for 2009, and the results are shown in Figure 5.23. Panels (a) to (d) correspond to the comparison between case 1 and case 2. The columns for case 2 are similar to those obtained for case 1, the mean percentage difference being $(0.13\pm0.11)\%$ (b). The DOFS (c) are larger for case 2 compared to case 1, by ~0.2. The RMS fitting residuals (d) are also similar. The comparison between cases 2 (black) and 3 (red), shown in panels (e) to (h), give slightly larger total columns for case 2 (e) the mean percentage difference between the two approaches being $(0.30\pm0.26)\%$ (f). The DOFS, shown in panel (g), are consistently larger for case 2 compared to case 3 by ~2. The RMS fitting residuals (h) are similar for both cases. Overall, retrievals made for case 2 give

the best results and the parameters used for this retrieval approach are recommended for retrievals at Eureka.
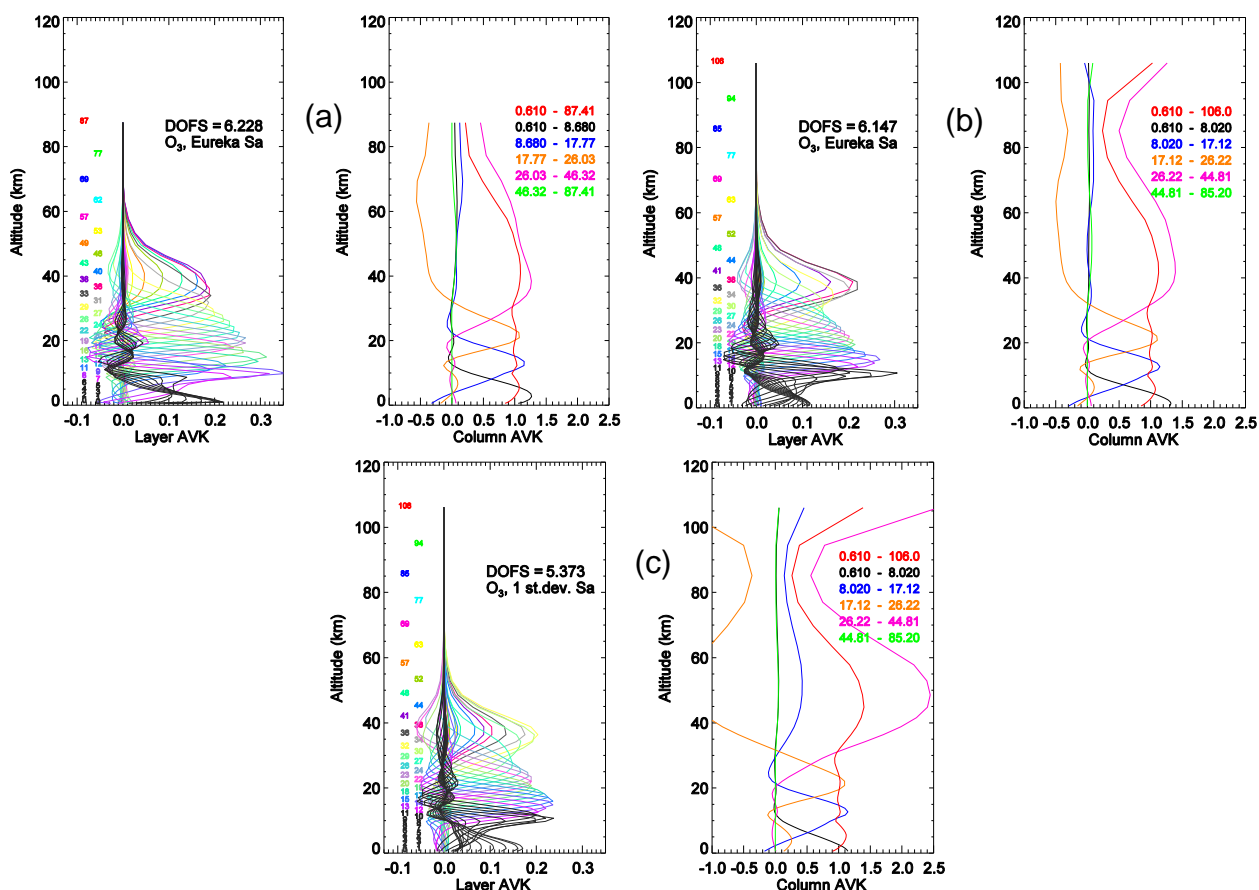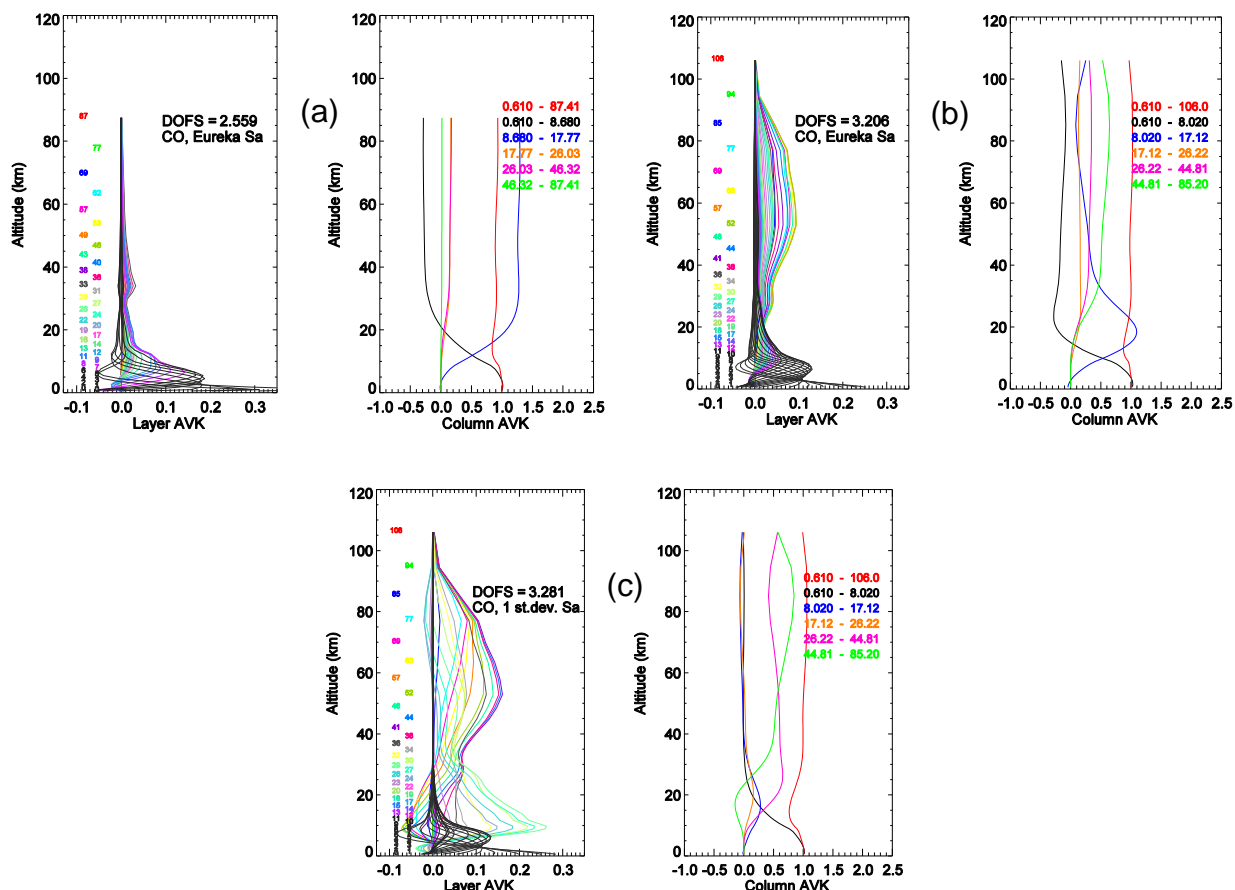

Figure 5.20. CO layer averaging kernels (left panels) and column averaging kernels (right panels) for: (a) case 1, (b) case 2, and (c) case 3, for spectrum 090615F5.S3, SZA=56.80º. For the layer AVKs, the height of the layer is specified on the left with numbers (height given in km) colored as the corresponding kernel. The column AVKs are colored according to the partial column range shown in the legend.

CH$_4$ is the last species discussed here. For CH$_4$, the *a priori* profiles (Figure A.48) have the same value at ground level, and decrease smoothly (less smoothly and faster for case 1) with the altitude for all three cases. At ~77 km, a sharp decrease is seen in the *a priori* profiles for cases 2 and 3 compared to case 1, followed by an increase above 95 km. As for N$_2$O, we notice differences in the **S$_a$** covariance values from ground level to ~60 km, these constraining more the retrieval for case 3 compared to cases 1 and 2. The layer averaging kernels (Figure A.50) for case 1 give the most information from ground level to ~5 km compared to the other two cases, and are similar to those for case 2 above this altitude. For case 3, the layer averaging kernels

peak almost uniformly (at ~0.1) from ground to ~18 km, and then evolve similarly to the other two cases. Above 40 km, the layer averaging kernels indicate that no information comes from the measurement. The column averaging kernels look good for case 1, but they oscillate above 30 km for the other two retrievals (cases 2 and 3, being stronger for case 2). The retrieved profiles (shown in Figure A.51) give the largest VMR value at ground level for case 1. All three retrieved profiles display a peak in the troposphere at ~7 km (less visible for case 3 because it is more constrained than the other two cases).
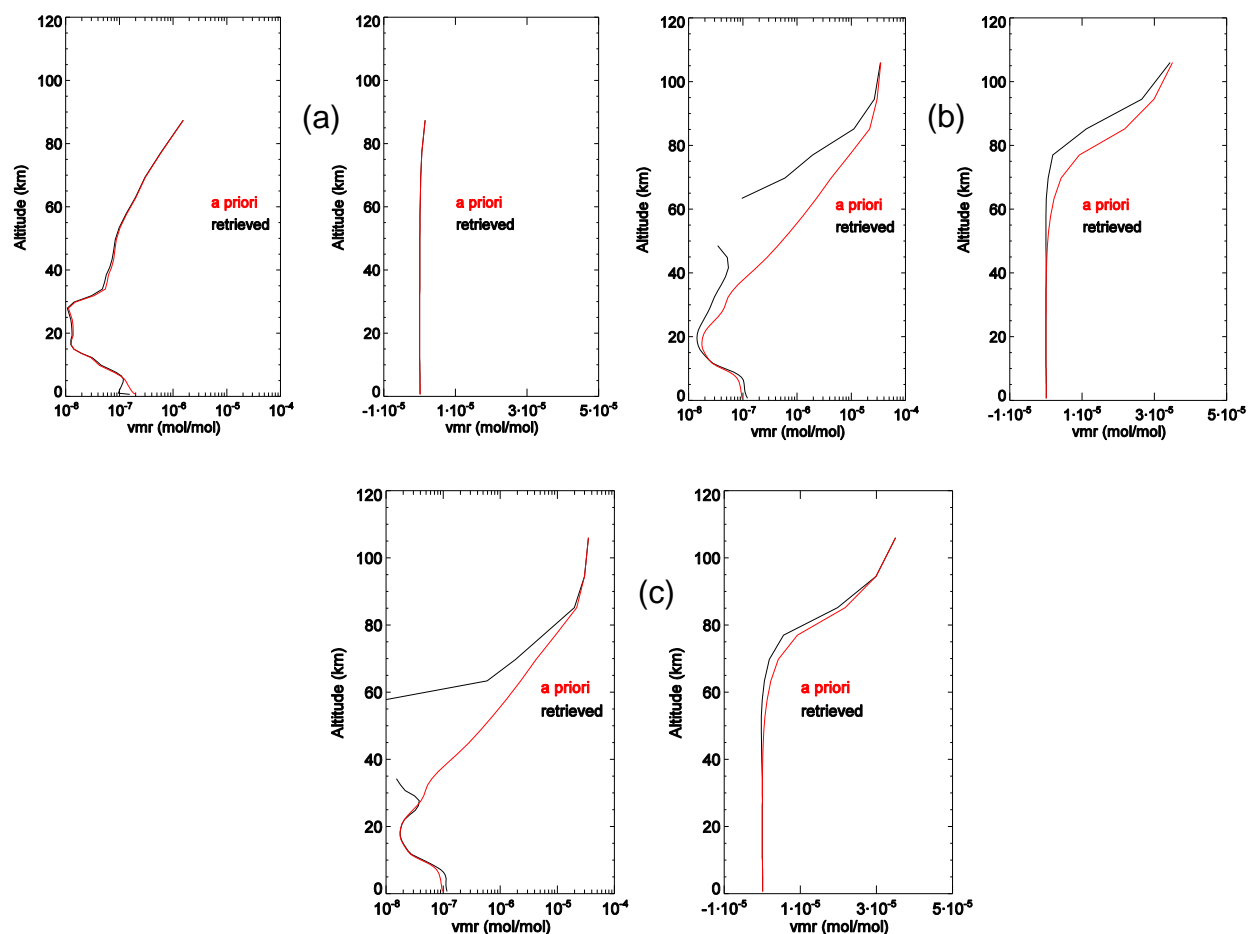
Figure 5.21. CO retrieved profiles (black) for (a) case 1, (b) case 2, and (c) case 3 for spectrum 090615F5.S3, SZA=56.80°. The *a priori* profiles are shown in red. The profiles are plotted on both log (left panels) and linear (right panels) scales.

The CH_4 total columns retrieved for all three cases listed in Table 5.3 were compared for 2009, and the results are shown in Figure 5.24. Panels (a) to (d) correspond to the comparison
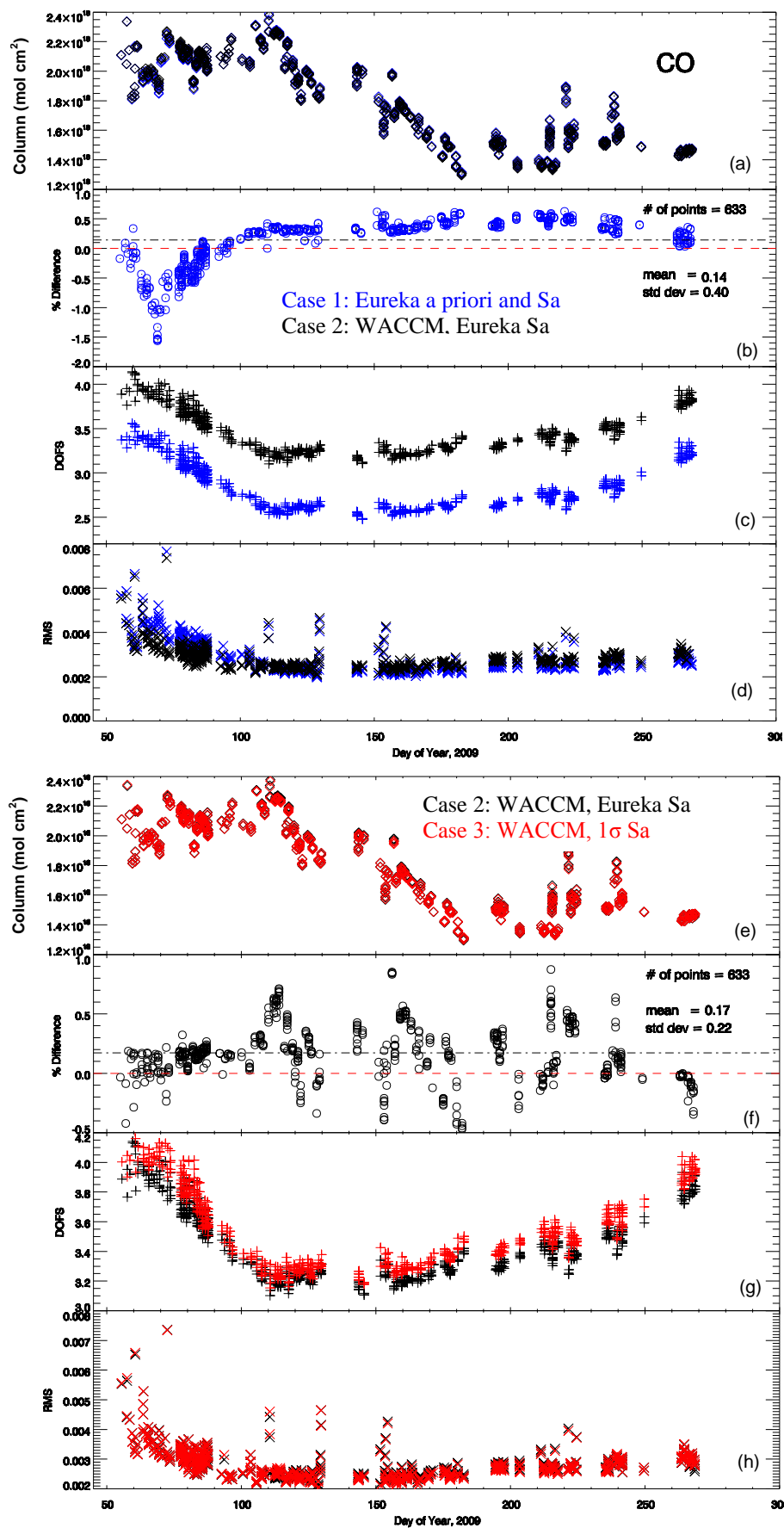
Figure 5.22. Same as Figure 5.10 but for CO.
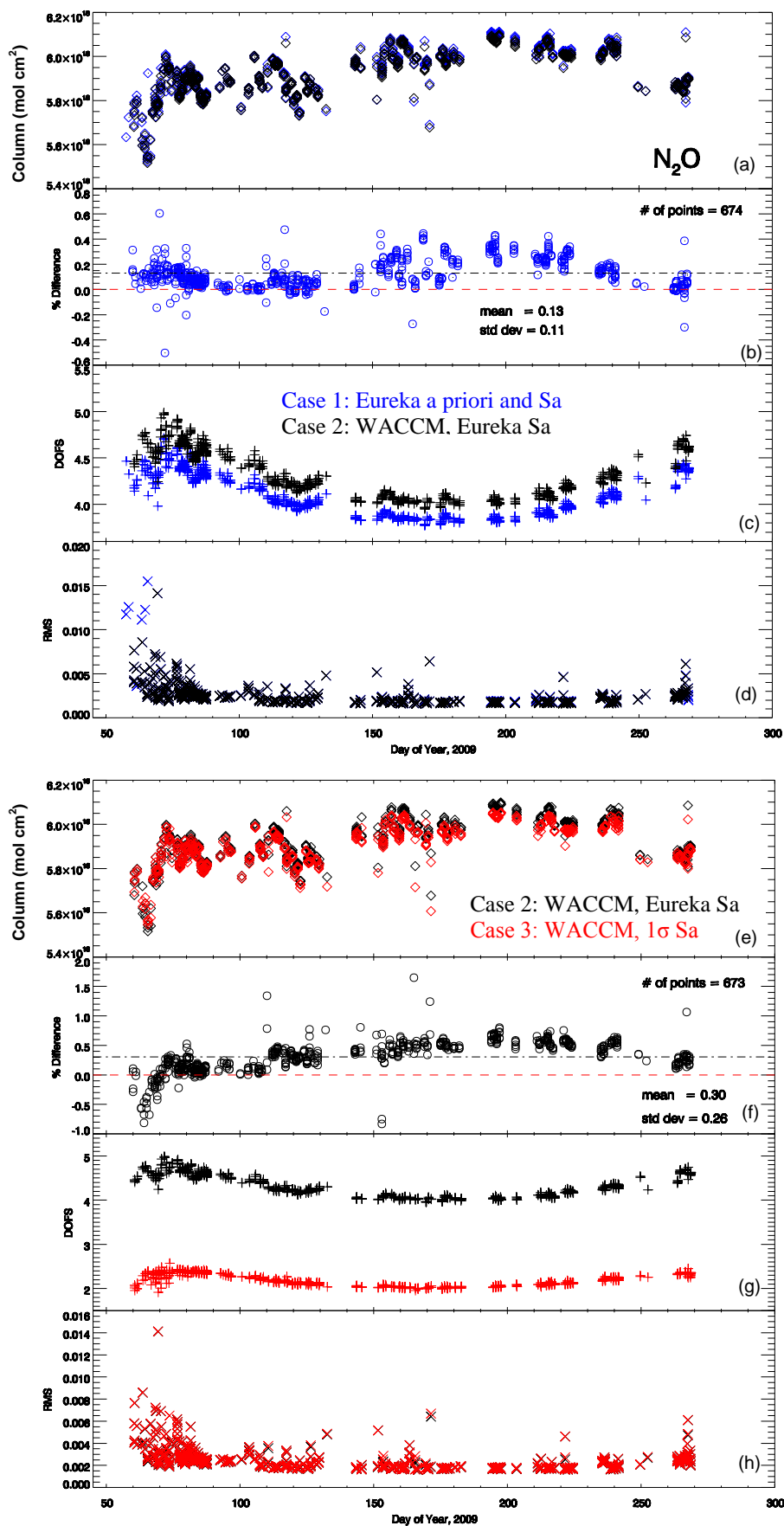
Figure 5.23. Same as Figure 5.10 but for N₂O.
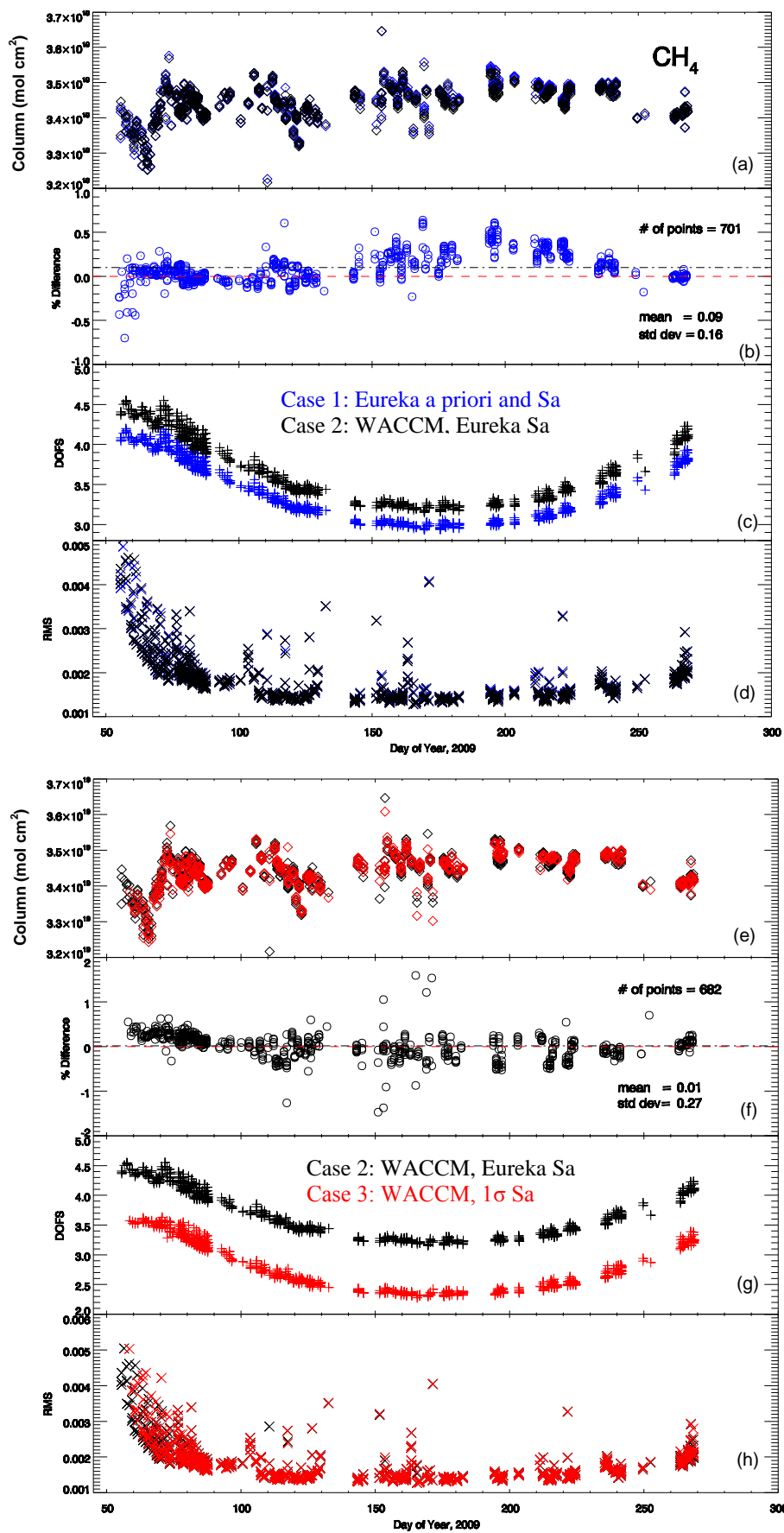
Figure 5.24. Same as Figure 5.10 but for CH_4.

between case 1 and case 2. The columns (a) for case 2 are similar to those obtained for the original Eureka parameters (case 1), the mean percentage difference being (0.09±0.16)% (b). The DOFS (c) are consistently larger for case 2 compared to case 1, by ~0.3. The RMS fitting residuals (d) are similar. The comparison between cases 2 (black) and 3 (red), shown in panels (e) to (h), give again similar total columns (e) the mean percentage difference between the two approaches being (0.01±0.27)% (f). The DOFS (g), are consistently larger for case 2 compared to case 3 by ~1. The RMS fitting residuals (h) are similar for both cases.

During the last IRWG Annual Meeting (June 2011), a detailed analysis of CH_4 retrievals was presented (for Garmisch and Wollongong) where retrievals using different microwindow-HITRAN linelist combinations were compared [*Sussmann et al.,* 2011]. It was decided that all sites will contribute to this study (for Eureka, PhD student Joseph Mendonca is working on this evaluation exercise), and the analysis is currently ongoing.

5.6 Conclusions

This study was useful in identifying the retrieval parameters that work well for our Arctic conditions. For O_3, we found that the IRWG-recommended microwindow works very well, but would prefer the original Eureka a priori profiles and $\mathbf{S_a}$. For HCl, step one gave similar results for both original and IRWG microwindows, however step two was completed using the original Eureka microwindows. Case 2 gave the best results for the retrieval parameter evaluation. For HNO_3, the IRWG microwindows worked better and the WACCM parameters gave good results for case 2. The microwindow comparison for HF gave similar results for both the IRWG recommended and original Eureka microwindows. The second part of the evaluation was not completed as WACCM parameters were not provided for HF. For $ClONO_2$, the original Eureka microwindows and retrieval parameters gave the best results. For HCN, the microwindow evaluation needs to be finalized and the second part of the harmonization evaluation completed. The IRWG microwindows for C_2H_6 gave clearly good results compared to the original ones, but for the second step of the evaluation, the original Eureka parameters were better. For C_2H_6, the poor state of spectroscopy at 3 μm has been in the attention of scientists for the last decade [*Rothman et al.,* 2003; 2005; 2009; *Lattanzi et al.,* 2011]. HITRAN 2008 contains lines for just nine strongest PQ branches, and work is ongoing to develop an empirical pseudo-linelist (PLL) containing 80,000 lines to represent the C_2H_6 absorptions in the 3 μm region (work in progress was presented by Geoff Toon at the 2011 IRWG Meeting). For CO and N_2O, the IRWG

microwindows were already used at Eureka and the WACCM parameters gave good results for case 2. The microwindows and linelist to be used for CH_4 retrievals are still under evaluation.

A summary of the results for step one and two of the harmonization exercise for each gas is made in Table 5.5, along with recommendations for future work where appropriate.

Table 5.5 Current status of evaluation of Eureka retrieval parameters recommended by the IRWG for the harmonization initiative.

Target gas	Step one: microwindow choice	Step two: WACCM, case # giving best results	Comments	Future work
O_3	✓	case 1		!
HCl	✓	case 2		!
HNO_3	✓	case 2		Investigate oscillations in column averaging kernels and convergence issues, !
HF	✓	not evaluated	Waiting on HF WACCM parameters	Finalize step two
$ClONO_2$	Original Eureka microwindows	case 1		!
HCN	?	not evaluated	HCN waiting on improved microwindows	Finalize steps one and two
C_2H_6	✓	case 1	Waiting on improved linelist	!
CO	✓	case 2		!
N_2O	✓	case 2		! Check/confirm ILC
CH_4	? under review by IRWG	case 2	Waiting on Final selection of CH_4 microwindows and linelist	!

✓ indicates IRWG-recommended microwindow is acceptable/improves the results.

? indicates that step one has not been finalized.

! indicates error analysis should be done.

Chapter 6

ACE-FTS Validation at Eureka During IPY and Beyond

6.1 Introduction

Ground-based instruments that measure the chemical composition of the atmosphere, through techniques such as solar-absorption spectroscopy, provide a key data set for the validation of satellite remote-sensing instruments [*e.g.*, *Dils et al.,* 2006; *Kerzenmacher et al.,* 2008; *Mahieu et al.,* 2008; *Vigouroux et al.,* 2008; *Wolff et al.,* 2008; *Dupuy et al.,* 2009]. Biases and differences in the total columns measured by ground-based and satellite instruments are, however, difficult to quantify due to the range of viewing geometries and resolution of the individual instruments considered for comparison. Even when side-by-side, total column densities of key stratospheric trace gases measured by ground-based FTIR spectrometers may exhibit differences of several percent, even during times of stable atmospheric conditions and when retrieval algorithms are made as consistent as possible [*Goldman et al.,* 1999; *Griffith et al.,* 2003; *Meier et al.,* 2005; *Wunch et al.,* 2007; *Batchelor et al.,* 2009; *Batchelor et al.,* 2010]. Validation of the ACE-FTS becomes very challenging particularly during the highly-variable Arctic spring-time. Comparisons made under these conditions thus require a comprehensive understanding of both the validating instrument and the viewing geometry with respect to polar vortex dynamics.

The Canadian Arctic ACE Validation Campaigns have been carried out during the polar sunrise period at PEARL since 2004 [*Kerzenmacher et al.,* 2005; *Fraser et al.,* 2008; *Fu et al.,* 2011]. The 2007, 2008, 2009, and 2010 campaigns extended from mid-February until mid-April, and were additionally complemented by instrumentation installed at PEARL by CANDAC during 2006. One of these additions was the Bruker 125HR FTIR spectrometer. This allowed simultaneous measurements of atmospheric composition to be made throughout the 2007 and 2008 campaigns by four Fourier transform spectrometers: three ground-based and one satellite-borne. Note that the Bomem DA8 FTIR spectrometer was removed prior to the 2009 campaign.

This chapter focuses on the validation of ACE-FTS data acquired during the International Polar Year Canadian Arctic ACE Validation Campaigns of 2007 and 2008, and beyond during the 2009 and 2010 campaigns using the 125HR. Meteorological conditions were quite different

during the four campaigns, with many measurements in 2007 being made inside the polar vortex where heterogeneous chemistry and ozone-depleting processes were occurring. A polar stratospheric warming prior to the start of the campaign in 2008, however, resulted in most of those measurements being made outside the vortex. *Manney et al.* [2009b] describe a major SSW in January 2009 that was the strongest and most prolonged on record. In 2009, most of the measurements were made on the vortex edge. A polar stratospheric warming prior to the start of the 2010 campaign again resulted in measurements mostly on the edge of the vortex. As such, the four years provide a range of atmospheric conditions for the intercomparisons. Key stratospheric trace-gas species O_3, chlorine reservoirs HCl and $ClONO_2$, fluorine reservoir HF and nitrogen reservoir HNO_3 are investigated. Derived meteorological data along the instruments' line-of-sight are used to account for the changing conditions of the polar stratosphere, and a comprehensive set of measurement comparison criteria are identified for satellite validation near the polar vortex edge. This work was published in *Batchelor et al.* [2010].

6.2 ACE-FTS

The Atmospheric Chemistry Experiment (or SCISAT) Canadian satellite mission was launched in August 2003 and orbits the Earth in a 74º inclined circular orbit at an altitude of 650 km [*Bernath et al.,* 2005]. Working in solar occultation, the ACE instruments provide profile information from 85ºN to 85ºS for temperature, pressure, and more than 30 atmospheric species. The satellite makes measurements over Eureka during polar sunrise (February-March), when ozone depletion chemistry can be observed, and again near polar sunset in September-October.

The primary ACE instrument is a high-resolution (0.02 cm^{-1}) Fourier transform spectrometer (henceforth the ACE-FTS), that has a similar spectral range to the 125HR, from 750 to 4400 cm^{-1}, but a considerably higher vertical resolution due to the limb-sounding geometry [*Bernath et al.,* 2005]. Pressure and temperature profiles are determined from the ACE-FTS spectra (based on a detailed CO_2 analysis) and further used to retrieve trace gas volume mixing ratio profiles with a nonlinear least squares fitting algorithm described by *Boone et al.* [2005]. The data set used for this comparison is v2.2 with updates for O_3 and N_2O_5. The ACE-FTS data set has recently been reprocessed with a new version of the retrieval algorithm, v3, which is being validated.

6.3 Derived Meteorological Products

Solar absorption measurements sample the air mass between the sun and the instrument along the line-of-sight. During the spring period, the solar zenith angle is large, and as such, the air mass being sampled at a given altitude may be a considerable distance from the instrument itself. To account for this, especially when considering the polar vortex and changes in chemistry occurring around its edge, meteorological products are derived at locations along the line-of-sight using the GEOS Version 5.0.1 (GEOS-5) analyses [*Reinecker et al.,* 2007]. These products are Derived Meteorological Products (DMPs), and in this work, have been calculated for both the ground- and satellite-based measurements at series of altitudes in the stratosphere, namely at 14, 18, 20, 22, 24, 26, 30, 36 and 46 km, with ground-based line-of-sight calculations as described in *Fu et al.* [2011] and satellite-based calculations as described in *Manney et al.* [2007]. The DMPs include temperature, pressure, winds, potential temperature and scaled potential vorticity. A full description of the data set used can be found in *Manney et al.* [2007]. Scaled potential vorticity (sPV) from the DMPs has been used in this work to differentiate the extra- and inner-vortex air masses at each altitude. sPV is the PV scaled in vorticity units, providing a field with a similar range of values at altitudes throughout the stratosphere [e.g., *Dunkerton and Delisi,* 1986; *Manney et al.,* 1994; *Manney et al.,* 2007 and references therein]. An sPV value of 1.2×10^{-4} s^{-1} was used as a proxy for the outer edge of the polar vortex and an sPV value of 1.6×10^{-4} s^{-1} was used for the inner edge, as these values are typically in the vortex edge region in the stratosphere [*Manney et al.,* 2008].

6.4 Methodology

Total column densities of O_3, HCl, $ClONO_2$, HNO_3 and HF spanning the region between the ground and 100 km have been determined from the 125HR spectra. The retrieval method was described in Chapter 3 and the input parameters are the original Eureka parameters given in Table 3.1. A summary of the spectral microwindows that have been fitted for each of the retrievals is presented in Table 6.1. The DOFS, defined as the trace of the averaging kernel, as well as an estimated error in the total column are also given. The errors have been calculated for each of the gases as described in Section 3.5 (using Equation, 3.31 but not including the smoothing error $\mathbf{S_s}$) using a set of representative spectra recorded at the beginning of March, when the solar zenith angles are typically > 80º.

The validation of ACE-FTS has been carried out using spectra coincident with those acquired by the 125HR. Spectra were considered coincident if the 125HR and ACE-FTS measurements were recorded within 12 hours and the distance between the ACE 30-km tangent point and PEARL was less than 1000 km.

Due to the difference in altitude sensitivity between the two instruments, partial, rather than total, column densities have been compared using ACE-FTS profiles smoothed to the resolution of the 125HR, as described by Equation 6.1 [*Rodgers and Connor,* 2003]:

$$\mathbf{x}_s = \mathbf{x}_a + \mathbf{A}(\mathbf{x}_h - \mathbf{x}_a) \ , \tag{6.1}$$

where $\mathbf{x}_s$ represents the smoothed ACE-FTS profile, $\mathbf{x}_a$ the 125HR *a priori* profile, $\mathbf{A}$ the 125HR averaging kernel matrix, and $\mathbf{x}_h$ the original ACE-FTS profile.

Table 6.1. Summary of retrieval microwindows and interfering species used in this study, with estimated total uncertainty and DOFS for the 125HR. Multiple microwindows are fitted simultaneously where more than one region is specified. Interfering trace gas species are scale fitted, unless profile fitting is indicated by a (P). Total uncertainty has been calculated for the spring period, with individual uncertainties resulting from measurement, model parameter errors, and spectroscopic line parameter errors added in quadrature. The DOFS are also representative values for spectra recorded at the beginning of March, when solar zenith angles are typically > 80°.

Gas	Microwindow(s) (cm^{-1})	Interfering Species	Total Uncertainty (%)	DOFS
O_3	$1000.0 - 1005.0$	H_2O, CO_2, $O_3(676)$, $O_3(667)$, $O_3(686)$, $O_3(668)$, C_2H_4	3.8	7.5
HCl	$2775.72 - 2775.8$ $2821.4 - 2821.62$ $2925.75 - 2926.05$	O_3, CH_4, N_2O HDO, N_2O CH_4, NO_2, OCS, O_3	3.3	3
$ClONO_2$	$779.85 - 780.45$ $782.55 - 782.87$ $938.3 - 939.3$	O_3 (P), CO_2 (P), HNO_3 O_3 (P), CO_2 (P), H_2O, HNO_3 CO_2 (P)	3.8	1
HNO_3	$867.5 - 870.0$	H_2O, OCS, NH_3	8.1	3.5
HF	$4038.78 - 4039.1$	H_2O, CH_4, HDO	5.8	2.5

Each ACE-FTS profile was linearly interpolated from the 1-km ACE grid to the 38-layer altitude grid used for the 125HR retrievals, and then smoothed with the 125HR averaging kernel and *a priori* profile corresponding to the matching 125HR spectrum. In the tropospheric region where no ACE-FTS data were available, the profile values were filled with the corresponding 125HR *a priori* profile for the calculation. Partial columns were then determined for each measurement pair for the altitude range for which ACE-FTS data existed for that measurement and where the sensitivity of the 125HR measurement, as determined from the sums of each row of the averaging kernel matrix, was at least 0.5 [*Vigouroux et al.,* 2008; *Kerzenmacher et al.,* 2008; *Wolff et al.,* 2008].

Comparisons were made for O_3, HCl, HF, HNO_3, and $ClONO_2$, with the mean, standard deviation, and standard error of the differences between each pair of ACE-FTS and 125HR partial column values calculated. While the exact altitude range included in the partial column varied from pair to pair, these typically ranged from approximately 6-43 km (O_3), 8-38 km (HCl), 15-26 km ($ClONO_2$), 8-29 km (HNO_3) and 10-43 km (HF). Attempts to quantify the causes of differences in the partial columns determined from each spectrometer were investigated using the DMPs described in Section 6.3, and were used to further enhance the coincidence criteria, as discussed below.

6.5 Results and Discussion

Figure 6.1 shows the partial columns, the percentage differences between the ACE-FTS and 125HR measurements (using (ACE-FTS − 125HR)/125HR), the distance between the two measurements, and the sPV for each of the gases for 2007 (top) and 2008 (bottom) respectively. The sPV along the line-of-sight has been determined for both the ACE-FTS and the 125HR as described in Section 6.3. From the number density profiles of each gas, it was determined that peak values were typically at approximately 18 km, thus sPV values from that altitude were used as a proxy for the dynamical conditions being experienced for each measurement.

From the plot, we can see that while sometimes the partial columns measured by the two spectrometers are similar, at other times there are considerable differences. Occasionally these differences can be explained by either the physical distance between the measurements or by the fact that one measurement is recorded inside the polar vortex while the other is recorded outside (for example HCl measurements on day 64 of 2007). At other times, however, this does not ful-
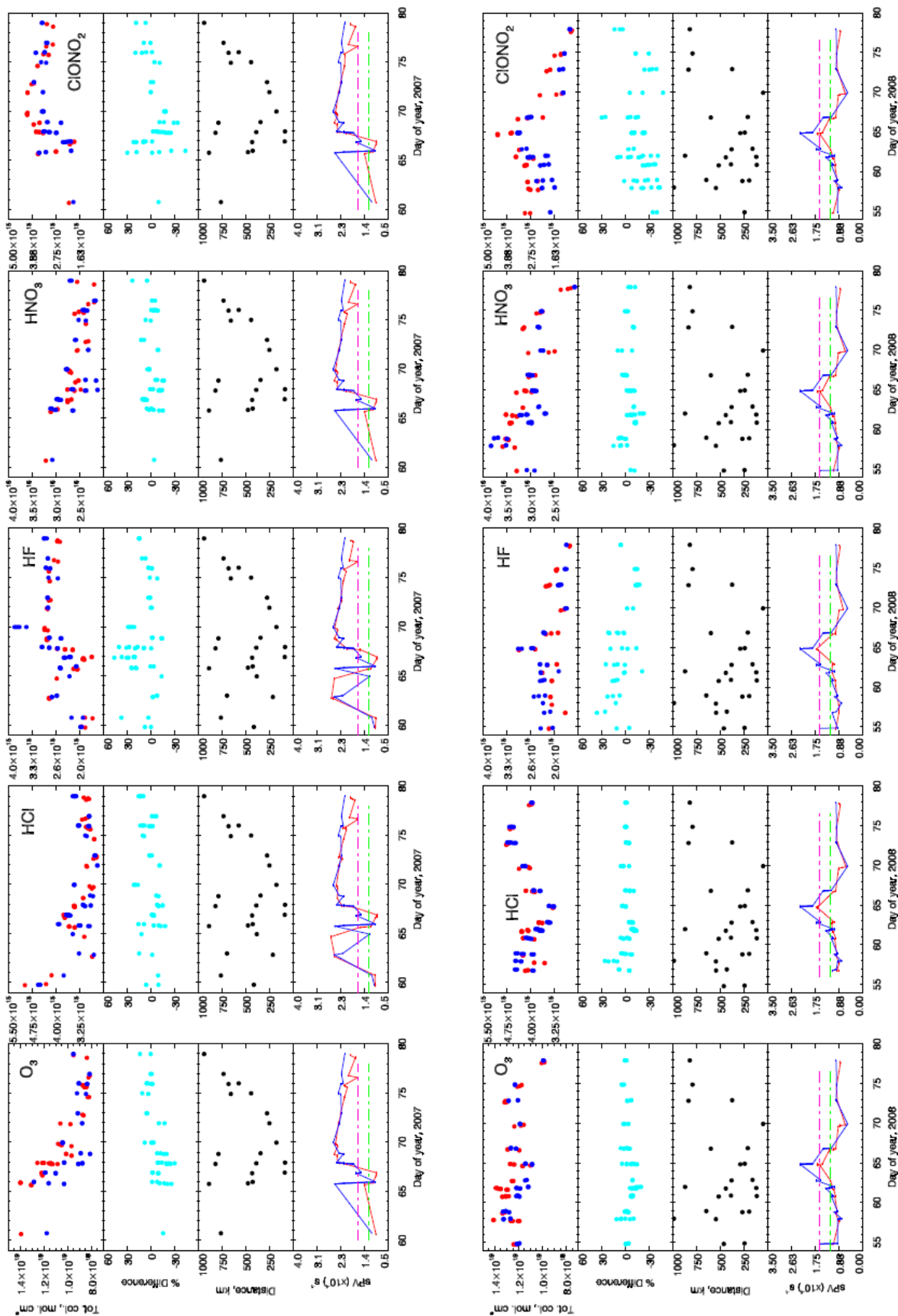
Figure 6.1. Time series from 2007 (top plots) and 2008 (bottom plots) for (from left to right) O₃, HCl, HF, HNO₃ and ClONO₂. For each sub-plot, from top to bottom: partial columns determined for ACE-FTS (blue) and 125HR (red); the percentage difference between the ACE-FTS and 125HR partial columns ((ACE-FTS − 125HR)/125HR); the distance between the two measurements as measured from the ACE 30-km tangent point to PEARL; and the sPV for both ACE-FTS (red) and 125HR (blue) at 18 km. The vortex edge region is marked by green dashed (outer) and magenta dashed (inner) lines.

ly explain the differences (for example on day 70 of 2007 for the HF measurements). The differences observed between the ACE-FTS and 125HR using these simple time and location criteria, i.e., 12 hours and 1000 km (from the ACE 30-km tangent point to PEARL) are shown in Table 6.2.

From Table 6.2, some significant differences in the mean and especially in the standard deviation can be seen between the two years, with the more dynamically variable 2007 in most cases showing greater scatter in the differences (as seen by the standard deviation) than in the more dynamically quiet 2008. We believe this reflects the number of measurements which capture spectra measured in different locations relative to the location of the polar vortex. While the mean differences determined by this comparison are comparable to those determined in previous ACE-FTS validation exercises, we took the investigation a step further to better identify measurement pairs that should be comparable due to well-matched atmospheric conditions, thus improving our confidence in the quality of the comparison.

Table 6.2. Mean percentage differences between ACE-FTS and 125HR partial columns (calculated as described in the text), one standard deviation from the mean (also as a percentage), the standard error on the mean, and the number of pairs of measurements (n) used in these calculations, for both 2007 and 2008. Note that the partial column altitude ranges varied for each individual comparison, but were typically around 6-43 km (O_3), 8-38 km (HCl), 15-26 km ($ClONO_2$), 8-29 km (HNO_3) and 10-43 km (HF).

	2007				2008			
	Mean (%)	Standard deviation (%)	Standard error (%)	n	Mean (%)	Standard deviation (%)	Standard error (%)	n
O_3	-7.45	10.60	1.56	46	-4.26	6.30	0.81	60
HCl	0.28	9.76	1.30	56	-1.93	7.67	0.94	67
$ClONO_2$	-4.94	15.98	2.41	44	-17.6	16.92	2.22	58
HNO_3	-1.55	8.66	1.32	43	-4.90	7.85	1.05	56
HF	10.57	15.11	1.98	58	3.41	14.37	2.24	41

Looking first at the distance criterion, we determined that the 1000-km criteria, as measured from the ACE 30-km tangent point to the station, was not a particularly accurate representation of the distance between the actual air masses being sampled. Based on the derived meteorological product determinations of the longitude and latitude along the lines-of-sight of the ACE-FTS and 125HR measurements, we found that some measurements meeting the 1000 km criteria were actually sampling air masses that were more than 1000 km apart, while other

measurements which sampled air masses that were closer than 1000 km together were being excluded. An example of this is shown in Figure 6.2, which shows the 2007 O_3 comparison distance measurements based on the ACE 30-km tangent point to PEARL distance (black) together with the distance based on the 18-km altitude along the lines-of-sight of the measurements (orange). In order to ensure all measurements that were within 1000 km of each other throughout the partial column were included, our ACE-FTS measurement sample was expanded to include all measurements within 2000 km of PEARL (based on the 30-km tangent point altitude), in order to subsequently filter them to 1000 km based on the distance between measurement points within the partial column. We also investigated the time criterion, but found little difference in the combinations that would be used for the comparison if the time criterion was set for 6, 12 or 18 hours. This was a result of the limitation of sunlight for the ground-based instruments and the sunrise/sunset viewing geometry of the ACE-FTS.
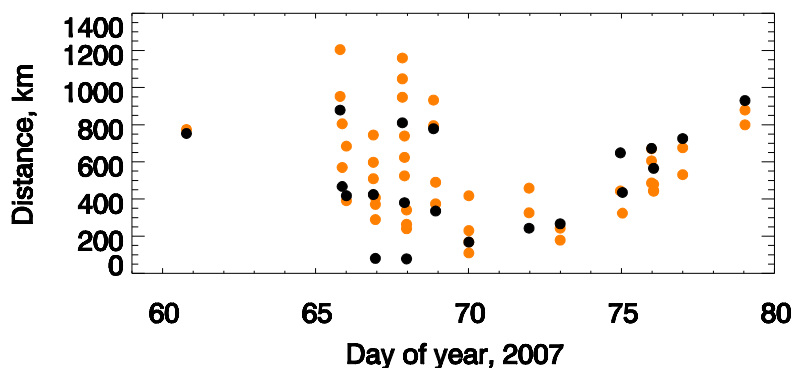
Figure 6.2. Distance between comparable ACE-FTS and 125HR measurements, as measured from the ACE 30 km-tangent point to PEARL (black) and from the measurement location at 18 km for both measurements (orange).

To further refine the comparison, for each pair, a plot of the sPV at each of the eight DMP altitudes along the line-of-sight for each instrument was constructed, with only those altitudes within the corresponding partial column altitude range being considered. Additional plots showing the temperature at each DMP location, the retrieved volume mixing ratio, and the distance between the measurement points were constructed. Examples of two of these plots, one showing a good match, and one showing a poor match, are shown in Fig. 6.3 and Fig. 6.4 respectively.
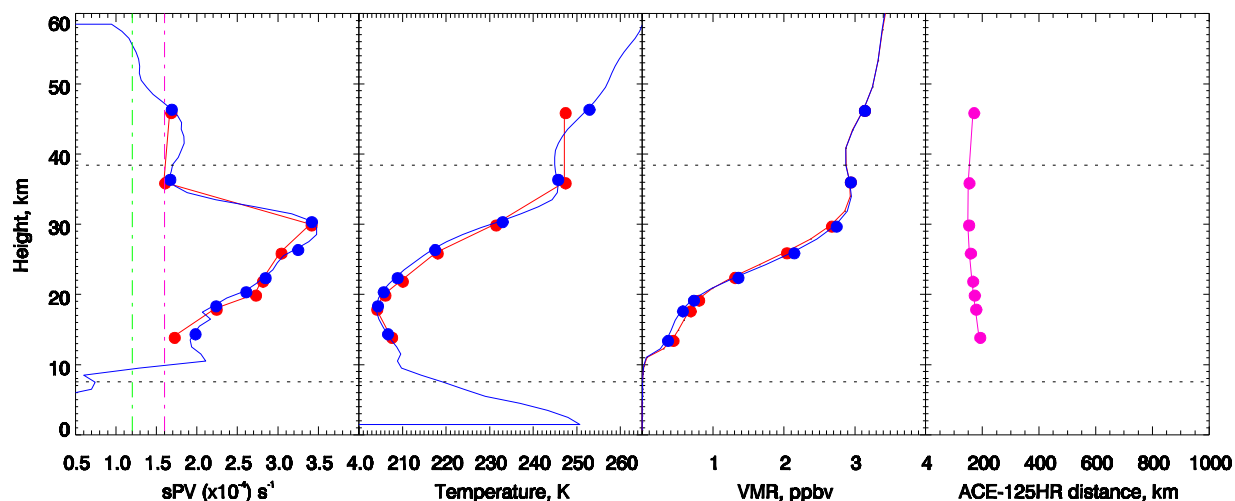
Figure 6.3. Sample plots for determining the comparability of ACE-FTS and 125HR measurements. Plots from left to right show (a) the sPV (with inner and outer edge of the vortex marked with magenta and green dashed lines respectively), (b) temperature, (c) HCl VMR profile (where the ACE-FTS profile has been smoothed to match the 125HR), and (d) distance between ACE-FTS and 125HR measurements, with data being determined from DMPs along the lines-of-sight of each instrument. Dotted lines indicate the altitude range for the partial column used in this comparison. ACE-FTS information is shown in blue, and 125HR is shown in red. The dots indicate the values at altitudes of 18, 20, 22, 24, 26, 30, 36, and 46 km along the line-of-sight. This example shows a well-matched comparison between HCl measurements made on 13 March 2007. The difference in the 9.82-38.40 km partial columns is 1.4%.
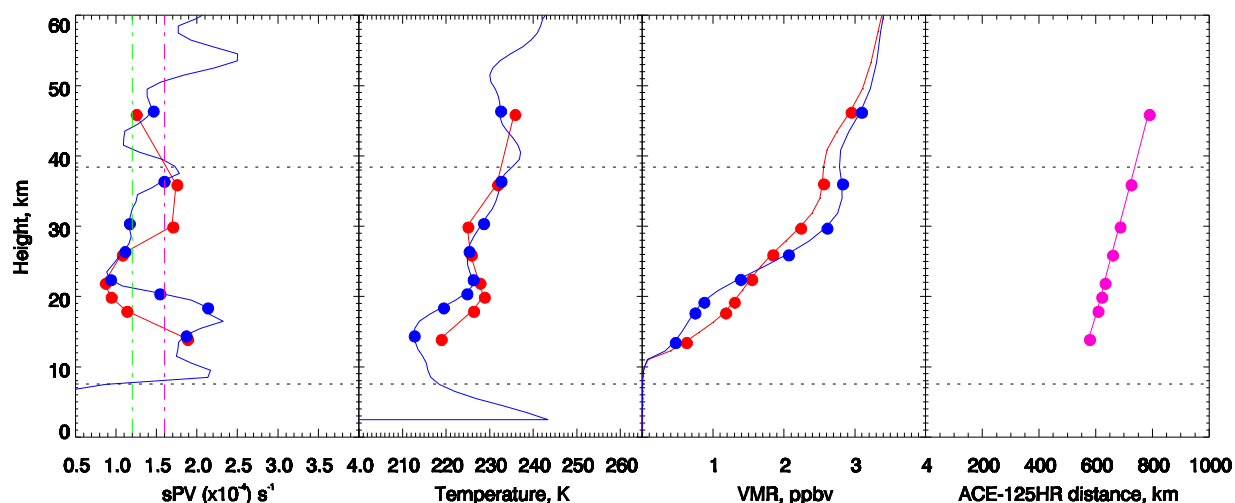
Figure 6.4. As for Fig. 6.3, but demonstrating a less-well-matched comparison pair recorded on 6 March 2007. Note the differences in sPV at 30 and 18 km, with the two instruments each sampling a combination of air masses located inside and outside the polar vortex. The difference between the two measurements over the 11.02-38.40 km partial column is 10.0%.

From these plots, we were able to determine whether the measurement conditions being sampled by the two instruments were similar throughout the height range of each comparison. The sPV and temperature profiles provided key information on the air mass with respect to the polar vortex and likely chemical processing conditions within, while the distance plot provided a measure of the physical separation of the sampled air masses. The retrieved VMR profiles provided additional information on where in the partial column the measurements were diverging. Note that the profiles shown for the ACE-FTS are the smoothed profiles, thus the smoothing effect of the 125HR measurement has been taken into consideration. From the plots, it was clear that the sPV along the lines-of-sight was an important comparison criterion, as cases when both measurements were inside or both were outside, or even both measured through the vortex edge typically showed good agreement in the partial columns, while pairs when the sPV was divergent typically had poorer agreement, as would be expected from the different air masses sampled. Temperature served as an additional important criterion, as within the polar vortex, chemical processing is highly dependent on temperature. As such, significant differences in temperature along the lines-of-sight for the two profiles, even when the sPV is similar, can indicate large differences in the sampled air masses.

Using the information gained by the plots, more rigorous coincidence criteria were developed to better identify comparable measurement pairs. While the temporal criteria of 12 hours remained, the spatial coincidence criteria was tightened, requiring the distance between the measurement points at each of the DMP altitudes (rather than solely for the ACE 30-km tangent point to PEARL) to be within 1000 km. Differences in sPV between the two measurements at each altitude along the line-of-sight were restricted to less than $0.3 \times 10^{-4}\,\mathrm{s^{-1}}$, ensuring that the air masses relative to the polar vortex edge were similar for both measurements. Finally, the maximum temperature difference at each altitude point was set to 10 K. The values of these criteria were selected to limit the likelihood of the measurements sampling different air masses, while ensuring that there were sufficient pairs of measurements remaining for a meaningful comparison.

Figure 6.5 shows the comparison between those measurements remaining after the new criteria were applied, with the mean percentage differences, standard deviations, and standard errors shown in Table 6.3. It can be seen that these stringent comparison requirements have significantly reduced the number of pairs contributing to the comparisons, particularly in 2007

when measurements made at Eureka were frequently near the edge of the polar vortex. However, both the mean differences and standard deviations between the two measurements have typically been reduced, and we are confident that these measurement pairs are highly comparable. The bias is seen to be zero within the standard error for O_3, $ClONO_2$ and HNO_3 in 2007, with ACE showing a slight high bias of approximately 5% in HCl and HF, which is comparable with that seen in previous ACE comparisons [*Mahieu et al.,* 2008]. In 2008, the HCl and HF biases are non-significant (within standard error), however negative biases are seen in the other gases. The greater standard deviation in $ClONO_2$ reflects the difficulty of this retrieval, particularly when the column of $ClONO_2$ is low (common outside the polar vortex, thus dominant in the 2008 comparison). This was previously demonstrated in *Wolff et al.* [2008], who described large standard deviations and found a wide range of biases between ACE-FTS and ground-based FTIR measurements around the globe, with no discernible trend. A slight negative bias in ACE HNO_3 was also reported in that study [*Wolff et al,* 2008], comparable in magnitude to that obtained here.

Table 6.3. As for Table 6.2 but for pairs remaining after applying rigorous co-location criteria.

	2007				2008			
	Mean (%)	Standard deviation (%)	Standard error (%)	*n*	Mean (%)	Standard deviation (%)	Standard error (%)	*n*
O_3	1.11	6.57	2.08	10	-1.51	4.30	1.15	14
HCl	4.86	8.05	2.01	16	-0.23	5.38	1.12	23
$ClONO_2$	-2.86	14.24	3.56	16	-15.33	22.62	3.72	37
HNO_3	1.09	8.36	2.03	17	-4.77	6.97	1.23	32
HF	5.23	8.88	2.37	14	1.14	16.81	14.34	15

Using the new coincidence criteria, the retrievals for the following spring campaigns 2009 and 2010 were compared. The results are shown in Figure 6.6 and Table 6.4. In 2009, the HCl and HF biases are non-significant (within standard error), however negative biases are seen in the other gases. The bias is seen to be zero within the standard error for HNO_3 in 2010, with ACE showing slight high bias of 2% in HCl and approximately 3% in HF, and negative bias of -2.6% in O_3 and -8.6% in $ClONO_2$.
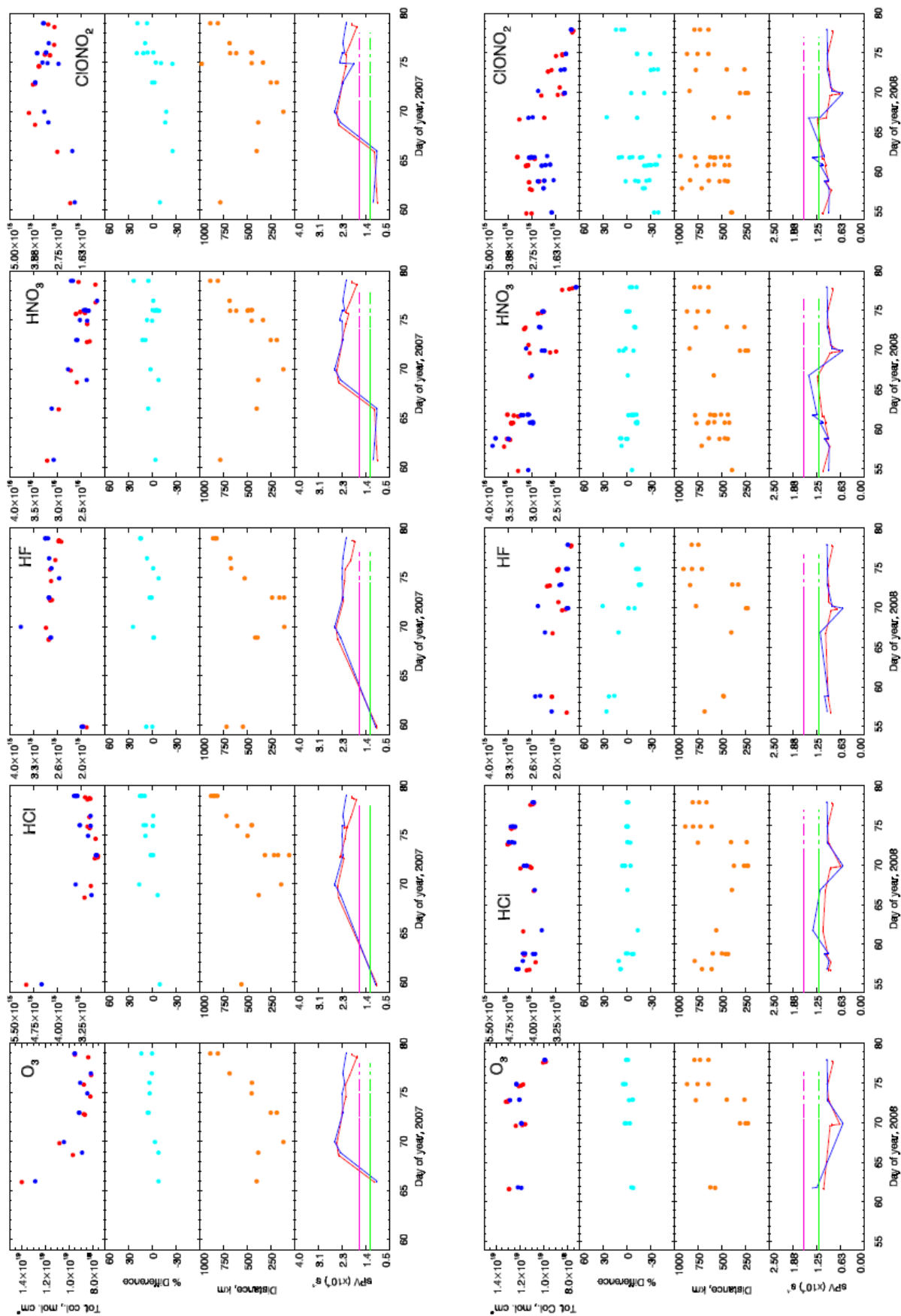
Figure 6.5. As for Fig. 6.1, but with those comparison pairs remaining after tightened criteria have been applied. Note that the distances shown in this plot are now the distance between the measurements along the lines-of-sight at 18 km, as described in the text.
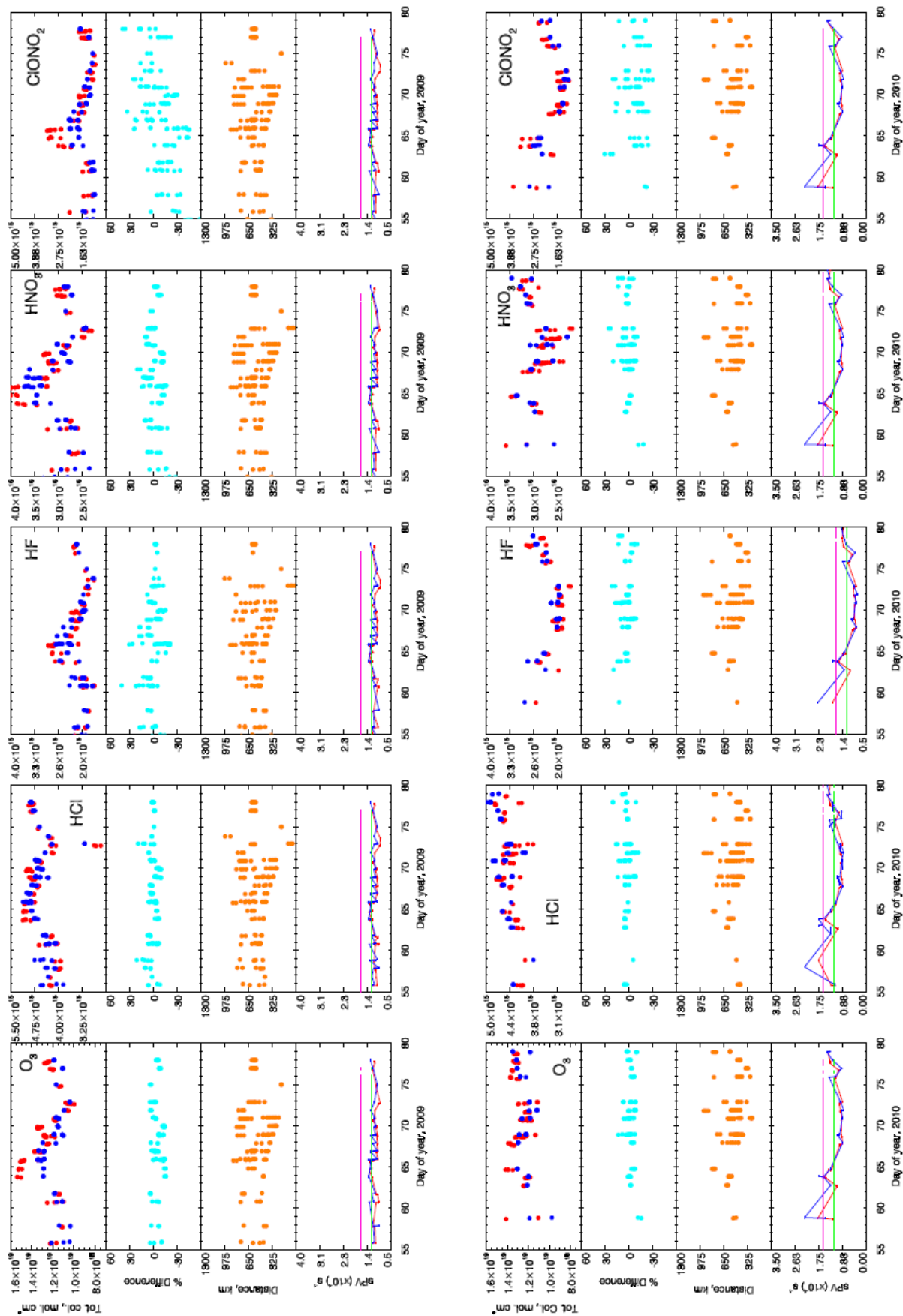
Figure 6.6. As for Fig. 6.5 but for the 2009 and 2010 Canadian Arctic ACE Validation Campaigns.

Table 6.4. Same as Table 6.3 but for the 2009 and 2010 Canadian Arctic ACE Validation Campaigns.

	2009				2010			
	Mean (%)	Standard deviation (%)	Standard error (%)	n	Mean (%)	Standard deviation (%)	Standard error (%)	n
O_3	-5.61	5.87	0.55	115	-2.57	4.64	0.49	90
HCl	0.07	5.59	0.48	134	2.04	5.70	0.56	105
$ClONO_2$	-10.36	19.46	1.65	140	-8.57	12.94	1.40	85
HNO_3	-2.97	8.96	0.74	147	0.53	7.18	0.75	91
HF	-0.34	10.71	1.00	115	3.22	6.73	0.71	91

6.6 Conclusions

The 2007 to 2010 Canadian Arctic ACE Validation Campaigns at Eureka, Nunavut, provided an excellent opportunity to compare ACE-FTS measurements with those made by the 125HR during the highly-variable Arctic polar sunrise period. Validation of the ACE-FTS v2.2 (with O_3, and N_2O_5 updates) results from this period was carried out. Strict coincidence criteria for use around the polar vortex were determined, utilizing DMP data along the lines-of-sight of both instruments. These criteria were: measurement times less than 12 h; distance between measurement points at multiple altitudes within the partial column less than 1000 km; differences in sPV between measurements at multiple altitudes within the partial column less than 0.3×10^{-4} s^{-1}; and temperature differences at each altitude less than 10 K. After applying these criteria, the mean biases between the ACE-FTS and 125HR for 2007 to 2010 were 1.1 to -5.6%, 4.9 to -0.2%, -2.9 to -15.3%, 1.1 to -4.8% and 5.2 to -0.3% for O_3, HCl, $ClONO_2$, HNO_3, and HF respectively. These values were generally insignificant within the standard error, though show positive biases in HCl and HF in 2007 and 2010, and negative biases in HNO_3 and O3 in 2008, 2009, and 2009. The negative bias in $ClONO_2$ is larger than the standard error, except for 2007.

The typical fitting errors for the ACE retrievals are 2%, 5%, 7%, 2.2%, and 7% for O_3, HCl, $ClONO_2$, HNO_3, and HF, respectively. Added in quadrature with the corresponding 125HR error listed in Table 6.1 give the total error for the 125HR/ACE-FTS comparison: 4.3%, 6%, 8%, 8.4%, and 9%, respectively. The O_3 mean differences are within the total error except for 2009. HCl, HNO_3, and HF mean differences are within the total error for all cases, except for HF in 2008. For $ClONO_2$ the mean differences exceed the total error each year, except for 2007.

To conclude, having applied the stringent coincidence criteria, the differences between the two instruments are generally small and are in good agreement with previous ground-based FTIR/ACE-FTS comparisons of these five gases [*Dupuy et al.,* 2009; *Mahieu et al.,* 2008; *Wolff et al.,* 2008]. Clear negative bias is seen for $ClONO_2$ from year-to-year, while for O_3, negative bias is seen for three out of four years. For HCl and HF positive bias is seen for two years and no bias for the other two years. For HNO_3, negative bias is seen for two years and no bias for the other two years. With these results, we can confidently say that the ACE-FTS shows good agreement with the 125HR and that satellite validation can be conducted with ground-based measurements made around the polar vortex edge, provided that comparison criteria are enhanced to account for vortex conditions along the lines-of-sight.

Chapter 7

A Study of the NO_y Budget above Eureka

7.1 Reactive Nitrogen

Reactive nitrogen species play an important role in the chemistry of the stratosphere. Nitrogen oxides ($NO_x = NO + NO_2$) are responsible for significant ozone destruction in the middle stratosphere and furthermore influence the partitioning of the hydrogen, chlorine, and bromine species in the lower stratosphere, thereby affecting ozone loss rates also in this region as discussed in Chapter 1. *Total reactive nitrogen* (NO_y) is defined as

$$NO_y = NO + NO_2 + NO_3 + HNO_3 + 2xN_2O_5 + ClONO_2 + BrONO_2 + HO_2NO_2 . \qquad (7.1)$$

Approximately 97% of the NO_y budget can be accounted for by NO, NO_2, HNO_3, $ClONO_2$, and N_2O_5 [*Brohede et al.*, 2008]. Figure 7.1 shows the contribution of these five species to the NO_y budget at Eureka as simulated by SLIMCAT for various seasons. The noon profiles were averaged by season from August 2006 to March 2010: (a) November-December-January (NDJ) corresponding to polar night, (b) February-March-April (FMA) corresponding to polar sunrise (days of varying length from completely dark to completely light), (c) May-June-July (MJJ) corresponding to 24 h sunlight, and (d) August-September-October (ASO) corresponding to polar sunset (as per FMA, reversed). Throughout the rest of the chapter, we refer to the sum of these five nitrogen species as 5-NO_y.

N_2O is the main source of stratospheric NO_y, producing NO through oxidation

$$\begin{aligned} O(^1D) + N_2O &\rightarrow N_2 + O_2 \\ &\rightarrow 2NO \end{aligned}, \qquad (7.2)$$
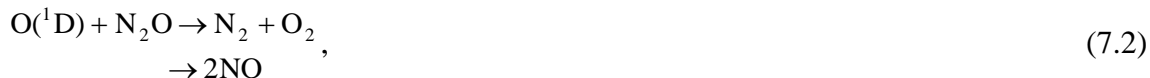
where the $O(^1D)$ oxygen atoms arise primarily from the photodissociation of ozone in the 200-310 nm wavelength region (Hartley band and Herzberg continuum). Nitric oxide is rapidly oxidized to NO_2 by reacting with ozone. Nitrogen dioxide, in turn, is subject to photolysis, regenerating NO. The reaction sequence leaves the sum $NO_x = NO + NO_2$ unaffected:

$$\begin{aligned} NO_2 + h\nu &\rightarrow NO + O \\ O + O_2 + M &\rightarrow O_3 + M \\ NO + O_3 &\rightarrow NO_2 + O_2 . \end{aligned} \qquad (7.3)$$
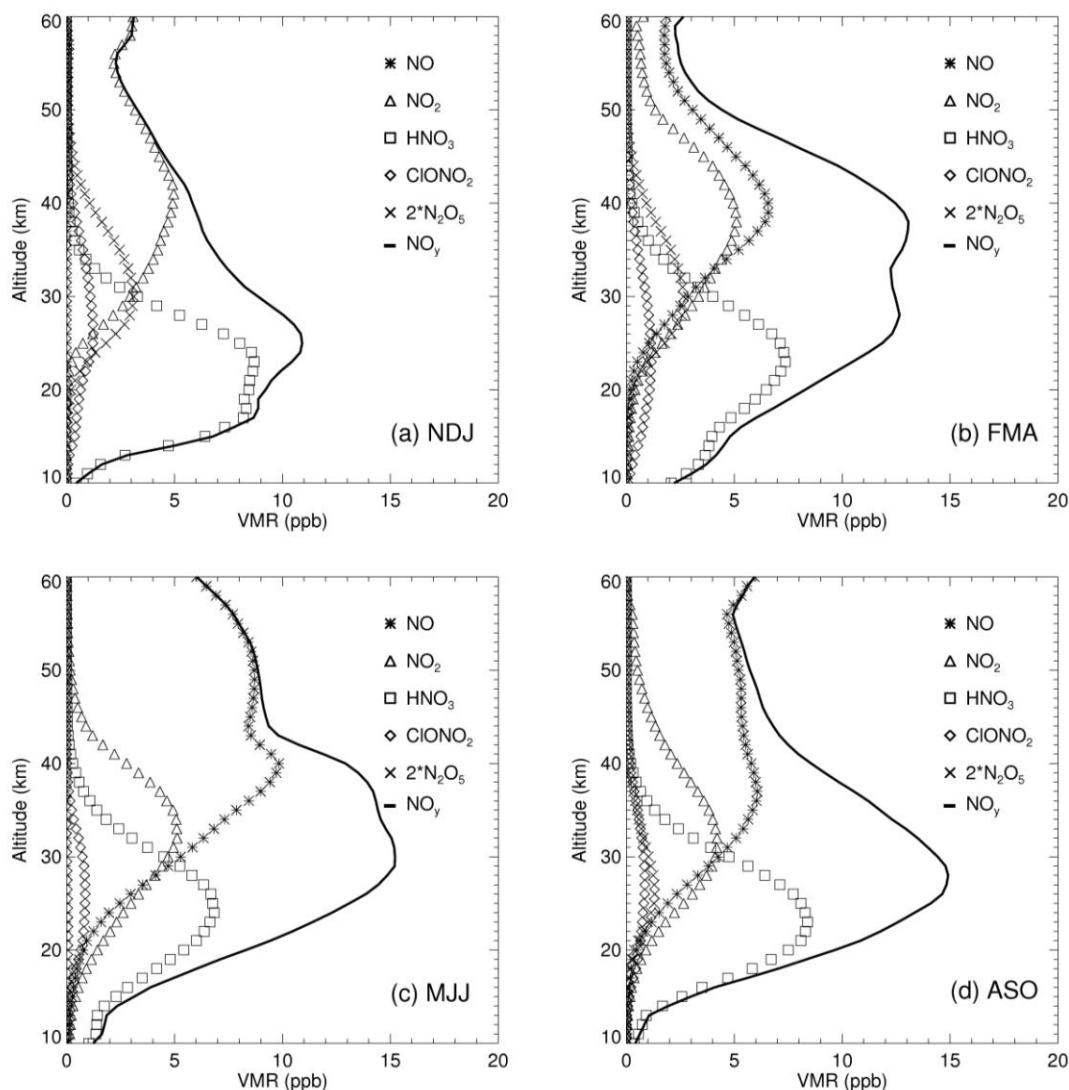
Figure 7.1. Contribution of the five primary species to the NO$_y$ budget at Eureka calculated using SLIMCAT for August 2006 to March 2010. The profiles are averaged by season: (a) NDJ corresponding to the polar night season, (b) FMA corresponding to polar sunrise (days of varying length from completely dark to completely light), (c) MJJ corresponding to 24 h sunlight, and (d) ASO corresponding to polar sunset (as per FMA, reversed).

In the upper stratosphere (~40 km), where the timescale of exchange between NO and NO$_2$ is less than 100 s, a quasi-steady state is quickly established. NO and NO$_2$ have strong diurnal variability. As the sun sets, NO concentrations decrease, while the NO$_2$ concentrations increase. At sunrise, the process is reversed (Equation 7.3). Photochemical box models describe very well the diurnal variation of nitrogen species [*e.g., McLinden et al.,* 2000; *Brohede et al.,* 2007] while measurements (ground-based, *in situ*, and satellite) contribute to studying their vertical distribution.

A smaller and sporadic source of NO$_y$ is the precipitation of energetic particles that form NO in the mesosphere and lower thermosphere, which can be transported downward into the stratosphere [*e.g. Randall et al.,* 2005, 2007, 2009]. This contribution constitutes approximately 2% of the total global budget of NO$_y$, but can be higher in the polar regions.

The sinks of stratospheric NO$_y$ include transport into the troposphere and photolysis in the upper stratosphere (usually above 40 km). During the polar night and early spring, HNO$_3$ may be removed from the gas phase and trapped in polar stratospheric clouds (PSCs) through heterogeneous reactions. If these particles grow sufficiently large, they undergo sedimentation, resulting in NO$_y$ being permanently removed from the stratosphere. This process is referred to as denitrification [*Fahey et al.,* 1989; *Jin et al.,* 2006; *Santee et al.,* 2008]. Evaporation of these particles at lower altitudes can release HNO$_3$, renitrifying the lower atmosphere [*Dibb et al.,* 2006; *Grossel et al.,* 2010]

Recent studies have shown that N$_2$O is increasing at a rate of 2.6% per decade [*Forster et al.*, 2007] and it has been described as the most important anthropogenic ozone-depleting substance emitted today [*Ravishankara et al.*, 2009]. On the other hand, the stratospheric effects of climate change are predicted to reduce the NO$_y$/N$_2$O ratio [*Plummer et al.*, 2010], so the future evolution of NO$_y$ is unclear. This makes measurements of long-term changes in NO$_y$ of particular scientific interest.

Efforts have been made to measure NO$_y$ since 1978, when the Limb Infrared Monitor of the Stratosphere (LIMS) satellite instrument was launched onboard Nimbus-7 and measured HNO$_3$ and NO$_2$ [*Gille and Russell,* 1984]. Later, NO and NO$_2$ measurements made by the Halogen Occultation Experiment (HALOE) were combined with HNO$_3$ and ClONO$_2$ measurements made by the Cryogenic Limb Array Etalon Spectrometer (CLAES) to determine NO$_y$ for 1992-1994 [*Danilin et al.,* 1999]. The Michelson Interferometer for Passive Atmospheric Sounding (MIPAS) launched in 2002 onboard the European Environmental Satellite (Envisat) was the first satellite instrument to measure all five primary NO$_y$ species [*Mengistu Tsidu et al.,* 2005]. The ACE-FTS measures the five primary NO$_y$ species and HNO$_4$, from which a global NO$_y$ climatology has recently been derived [*Jones et al.,* 2011].

Stratospheric reactive nitrogen has been also measured by other techniques using balloon-borne instruments [*Ridley et al.,* 1984; *Kondo et al.,* 1994] and *in situ* lower stratospheric aircraft sampling [*e.g.*, *Kawa et al.*, 1992]. During the spring and summer of 1997, a coordinated campaign of balloon, aircraft, and ground-based measurements of the atmospheric composition

was conducted from Fairbanks, Alaska (65ºN, 148ºW), to gain a more direct and quantitative understanding of the reasons for ozone loss observed during the high-latitude summer [*Toon et al.,* 1999]. As part of the Photochemistry of Ozone Loss in the Arctic Region in Summer (POLARIS) campaign, the Jet Propulsion Laboratory (JPL) MklV interferometer performed two balloon flights from Fairbanks and also performed ground-based FTIR column observations. These captured the temporal evolution of the column abundances of the NO$_x$ to NO$_y$ ratio, and were compared with similar ground-based measurements performed at Ny Ålesund, Spitzbergen (79ºN, 12ºE). NO$_y$ was obtained by summing the individual column abundances of $NO + NO_2 + HNO_3 + ClONO_2$, without considering N_2O_5. FTIR measurements of individual NO$_y$ primary species have been made at other polar stations: Kiruna, Harestua, Ny Ålesund, and Esrange [*Mellqvist et al.,* 2002], Kiruna [*Griesfeller et al.,* 2006], Eureka and Thule [*Farahani et al.,* 2007], and Arrival Heights [*Wood et al.,* 2004]. No published study, to the best of my knowledge, has previously presented an NO$_y$ product derived from the five primary species using a ground-based FTIR.

The goals of this study are to derive an NO$_y$ partial column data product from ground-based FTIR measurements at Eureka that includes the five primary NO$_y$ species, to use the resulting four-year time series to assess seasonal and interannual variability, and to compare the results with three atmospheric models and ACE-FTS satellite data. This work has been published in *Lindenmaier et al.* [2011a].

7.2 Instruments

7.2.1 CANDAC Bruker IFS 125HR

The retrieval method used for this comparison was described in Chapter 3. The microwindows used for each primary species are the original Eureka microwindows. The *ad hoc* SNRs used for determining the measurement covariance were selected for each gas using the trade-off curve method described in Section 3.3. A summary of the spectral fitting microwindows that have been used for each gas, the DOFS, and an estimated error in the partial column is given in Table 7.1. The estimated error (determined using a set of "representative spectra") contains the measurement error, forward model parameter errors and interference errors, all added in quadrature. The smoothing error is not included, as all comparison data was smoothed by the 125HR averaging kernels (the error budget calculation was made using Equation 3.31 and excluding the smoothing error S_s).

Partial column densities of NO, NO$_2$, HNO$_3$, and ClONO$_2$ for the 15 to 40 km range have been retrieved from the recorded spectra. This altitude range was chosen based on the averaging kernels and sensitivity for each of these four species. Figure 7.2 shows an example of layer averaging kernels for spectra acquired on March 6, 2009. The dashed line shows the sensitivity for each case, being mostly above 50% for the chosen altitude range and meaning that 50% from the information comes from the measurement rather from the *a priori*. The DOFS are also shown. Figure 7.3 shows the 15-40 km partial column averaging kernels (red dashed lines), and for comparison, the 0.61-100 km total column averaging kernels (black continuous lines) for the same spectra.

Table 7.1. Summary of retrieval microwindows (or multi-microwindows), interfering species, DOFS, and estimated total uncertainties for the four NO$_y$ species retrieved from the 125HR spectra. The multi-microwindows are fitted simultaneously. Interfering species are usually scale fitted, profile fitting being indicated by (P). DOFS was calculated as trace of **A,** the averaging kernel matrix, and a mean value is given below (the spectra used for DOFS calculations are the same used for the error calculation). The total uncertainty was calculated as described in the text, with individual uncertainties resulting from measurement, model parameter errors, and interference added in quadrature.

	Microwindow(s) (cm^{-1})	Interfering species	DOFS	Total measurement error (%)
NO	1875.645-1875.840	H$_2$O	2.3	6.9
	1899.850-1900.150	N$_2$O, CO$_2$, H$_2$O		
	1900.450-1900.550	CO$_2$,H$_2$O		
	1903.070-1903.180	CO$_2$,H$_2$O		
	1906.100-1906.200	CO$_2$,H$_2$O, N$_2$O		
NO$_2$	2914.590-2914.707	CH$_4$, CH$_3$D	1.85	14.5
	2918.100-2918.350	CH$_4$, CH$_3$D		
	2919-400-2919.650	CH$_4$, CH$_3$D,H$_2$O		
	2922.360-2922.750	CH$_4$, H$_2$O, HDO		
	2924.750-2924.925	CH$_4$, H$_2$O, HDO, OCS		
HNO$_3$	867.500-870.000	H$_2$O, OCS, NH$_3$	2.1	13.3
ClONO$_2$	779.850-780.450	O$_3$ (P), CO$_2$ (P), HNO$_3$	0.8	22.5*
	782.550-782.870	O$_3$ (P), CO$_2$ (P), H$_2$O, HNO$_3$		
	938.300-939.300	CO$_2$ (P)		

* In the case of ClONO$_2$, total uncertainties are much lower during the sunrise period, ~ 4%, and higher during summer, ~50%.
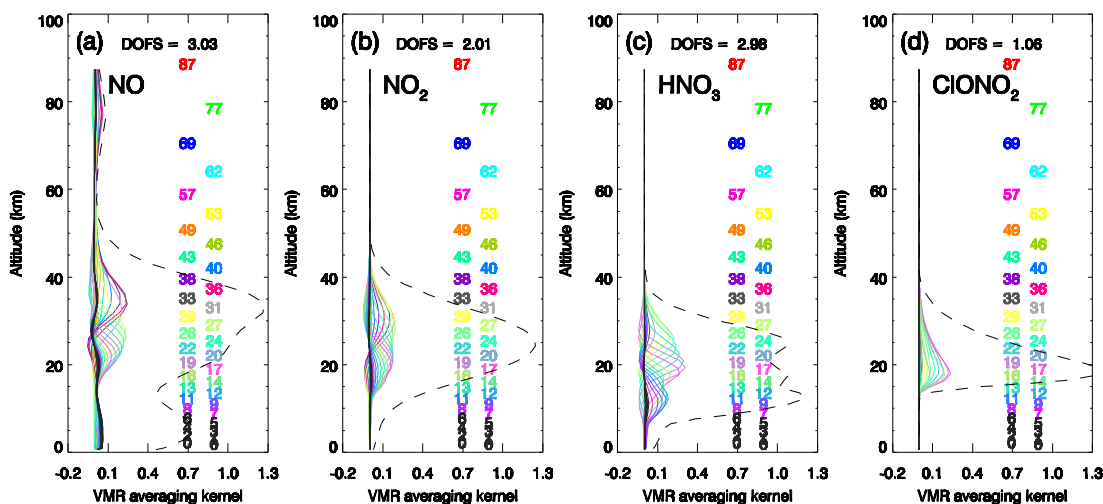
Figure 7.2. Typical 125HR VMR averaging kernels for March 6, 2009 for: (a) NO, (b) NO$_2$, (c) HNO$_3$, and (d) ClONO$_2$. The dashed line represents the sensitivity, or the amount of information coming from the measurement rather than the *a priori*. The numbers on the right indicate the altitudes. The DOFS are also included.
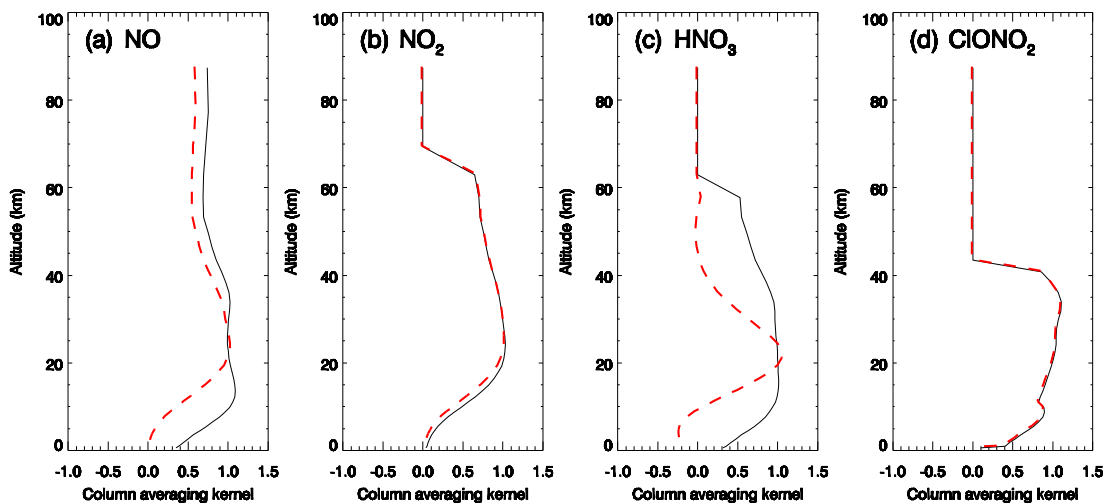
Figure 7.3. Typical 125HR column averaging kernels for March 6, 2009 for: (a) NO, (b) NO$_2$, (c) HNO$_3$, and (d) ClONO$_2$. The dashed red lines represent the 15-40 km partial column averaging kernels, the black line correspond to the total column averaging kernels.

7.2.2 ACE-FTS

The ACE-FTS was described in Section 6.2. The NO$_y$ species currently retrieved from the ACE-FTS measurements include NO, NO$_2$, N$_2$O$_5$, HNO$_3$, ClONO$_2$. HNO$_4$ is also retrieved for research purposes. V2.2 plus N$_2$O$_5$ updates was used in this study.

7.3 Models

7.3.1 CMAM-DAS

The Canadian Middle Atmosphere Model (CMAM) is an upward extension of the Canadian Centre for Climate Modelling and Analysis (CCCma) third-generation atmospheric general circulation model (AGCM3). The middle atmosphere component includes comprehensive interactive treatments of stratospheric chemistry, radiative processes and wave-driven dynamics. Detailed descriptions are given by *de Grandpré et al.* [2000] and *Scinocca et al.* [2008]. The chemical module includes all the relevant catalytic ozone loss cycles and heterogeneous reactions on sulphate aerosols and PSCs. It includes parameterizations for type Ib PSCs (super-cooled ternary solutions, STS) and type II PSCs (water ice), while there is no treatment for type Ia PSCs (nitric acid trihydrate, NAT particles). Sedimentation of particles is not implemented and thus the model does not simulate denitrification, *i.e.*, the permanent removal of NO$_y$ through the sedimentation of PSC particles in the stratospheric winter polar vortex.

In this work, data are taken from the data assimilation version of the model, CMAM-DAS, and in particular from its recent International Polar Year (IPY) simulation, covering the period February 2007 to August 2009. As opposed to the climate version of the model, CMAM-DAS assimilates the observed day-to-day variations in meteorology, enabling direct comparisons of the simulated chemical species distribution with observations for specific years. CMAM-DAS runs at T47 spectral horizontal resolution (corresponding to roughly 3.75º x 3.75º grid spacing) and employs 71 levels in the vertical, with a resolution that varies from several hundred meters in the lower troposphere to ~1.5 km near 20 km, and ~2.5 km from 60 km to the model lid near 100 km. It uses a 3-D variational assimilation scheme to assimilate observations from surface stations, radiosondes, aircrafts, cloud drift winds and AMSU-A brightness temperatures from the NOAA-15 and NOAA-16 satellites [*Polavarapu et al.*, 2005; *Ren et al.,* 2011].

7.3.2 GEM-BACH

The GEM-BACH model consists of the Canadian Global Environmental Multiscale (GEM) model in combination with the Belgium Atmospheric CHemistry module (BACH). A detailed description of the model is given by *de Grandpré et al.* [2009]. The model is based on the stratospheric version (GEM-Strato) of the Canadian GEM model [*Côté et al.,* 1998] which has been coupled online with a comprehensive module of stratospheric chemistry developed at

the Belgium Institute of Space Aeronomy. The model has 80 levels, including 27 in the stratosphere, and runs at a horizontal resolution of 1.5° with a lid at 0.1 hPa. It uses semi-implicit and semi-Lagrangian numerical techniques optimized to handle a large number of advection equations for the transport of species. Radiative processes are computed according to the correlated-k distribution approach [*Li and Barker,* 2005], which has the accuracy of a line-by-line code.

The Belgium Atmospheric Chemistry module is the foundation of the Belgian Assimilation System of Chemical Observations from the Environmental satellite (Envisat) chemical transport model (BASCOE CTM [*Daerden et al.,* 2007]) and assimilation system [*Errera et al.,* 2008; *Viscardy et al.,* 2010]. It includes 57 species that interact through 143 gas-phase, 48 photolysis, and 9 heterogeneous reactions. We use here a long run of GEM-BACH realized specifically for the IPY and covering the period from March 2007 to February 2009. In this version, the chemical and photodissociation rates follow the Jet Propulsion Laboratory compilation by *Sander et al.* [2003]. While heterogeneous reactions on the surface of PSCs particles are explicitly taken into account, the surface area available for these reactions is parameterized in a crude manner. Type 2 PSCs (water ice) are set to appear at temperatures below 186 K with a surface area density of 5×10^{-9} cm^2/cm^3. Between 186 K and 194 K, they are replaced by Type Ia (NAT) PSCs with the same surface area density. In this temperature range, the sedimentation of NAT PSCs is represented by an exponential loss of HNO$_3$ with a characteristic time of 100 days.

7.3.3 SLIMCAT

The updated Single-Layer Isentropic Model of Chemistry and Transport (SLIMCAT) is a three-dimensional (3D) off-line chemical transport model (CTM) [*Chipperfield*, 2006]. It differs from a general circulation model in that the chemistry component is not integrated into the dynamical model, but is off-line and performed separately for each dynamical time-step. This model has been used for many studies of ozone and ozone related gases in the polar regions [*e.g.*, *Chipperfield and Jones,* 1999; *Solomon et al.*, 2002; *Manney et al.*, 2009]. The model uses winds and temperatures from meteorological analyses of the European Centre for Medium-Range Weather Forecasts (ECMWF) to specify the atmospheric transport and temperatures, and calculates the abundances of chemical species in the troposphere and stratosphere. With hybrid σ-θ vertical coordinate levels (terrain-following sigma coordinates combined with isentropic

levels in the stratosphere) and a sophisticated radiation scheme (a Delta-Eddington approximation-based radiation scheme [*Joseph et al.*, 1976; *Briegleb*, 1992]), it produces realistic representations of tracer transport.

The simulation analyzed here has 2.8º×2.8º horizontal resolution, with 50 levels from the surface to 3000 K (~60 km), using purely isentropic surfaces above 350 K. The model uses a limited number of chemical families containing species which are in rapid photochemical equilibrium, in order to reduce the number of gases that must be advected. Reactions are generally computed using the photochemical data of *Sander et al.* [2003], with photolysis rates calculated using a scheme based on *Lary and Pyle* [1991]. Reactions occurring on the surface of NAT, liquid STS, and ice PSC particles are included in the SLIMCAT model. Denitrification and dehydration are treated using a simple sedimentation scheme.

7.4 Model Comparisons

7.4.1 Methodology

In order to facilitate a consistent comparison between the 125HR and the models, 125HR VMR profiles of NO, NO_2, and $ClONO_2$, which exhibit strong diurnal variations, were scaled to a corresponding noon profile using a photochemical box model [*McLinden et al.*, 2000]. The box model was initialized with monthly-mean climatologies of temperature, ozone, NO_y and other long-lived species. A default albedo of 0.7 was assumed. When these assumed values do not correspond to the actual atmospheric values, there will be an error in the scaling. Furthermore, there is a degree of uncertainty associated with all input photochemical rate constants and absorption coefficients.

In order to estimate the error from the scaling to local noon, we considered the worst case – scaling from a SZA of 90º to local noon – since this represents the largest scaling. This was done for several days throughout the year (days 60-240 in 30-day increments). For polar day, the maximum SZA was used instead of 90º. Each model parameter was varied by a measure of its uncertainty, and the scaling factors were recalculated and compared with the standard values used in the analysis. A list of these parameters and the amount by which they were varied are as follows: temperature: 10 K, ozone: 10%, NO_y: 20%, albedo: 0.5, rate constant $NO+O_3$: 40%, rate constant NO_2+O: 14%, rate constant HNO_3+OH: 20%, photolysis rate constants $jHNO_3$: 10%, jNO_2: 10%, and jN_2O_5: 10%.

The resultant error for each of these terms was added in quadrature for each NO$_y$ species measured by the 125HR. The total relative error in NO$_x$ or NO$_y$ was then constructed by weighting the total uncertainty for each species by its total column (as simulated in the box model). As both morning and afternoon observations were used, and their scaling factors and uncertainties are not the same, the larger of the two was taken to represent the uncertainty for the day in question. The results are shown in Table 7.2.

The largest errors occur in NO$_2$, and to a lesser extent NO and N$_2$O$_5$, with the largest contributions from the uncertainty in surface albedo and the photochemical reactions NO+O$_3$ and NO$_2$+O. The large uncertainty assigned to albedo stems from the variability in snow and/or cloud cover. The behaviour of the overall error in NO$_y$ is a result of two main factors: (i) the fraction of the total NO$_y$ column present as HNO$_3$, which is least sensitive to errors in the input parameters, and which varies with time of year and (ii) the amount by which the scaling factor departs from unity – an indicator of the difference in SZA between 90° and local noon. That is, when local noon occurs at larger SZAs, the scaling is closer to unity and thus not as sensitive to uncertainties in the input parameters. Likewise, when the maximum SZA is smaller than 90°, the required scaling is also closer to unity. The error in NO$_x$ is an overestimate as the error sources that affect the partitioning between NO and NO$_2$ will largely cancel in their sum. No scaling to noon was performed for HNO$_3$, whose diurnal variation is negligible compared to the other species. Partial columns were then calculated for each gas, followed by a "daily mean" partial column calculation.

Table 7.2 Box model percentage errors from scaling to local noon, estimated as described above.

Day	NO (%)	NO$_2$ (%)	HNO$_3$ (%)	N$_2$O$_5$ (%)	ClONO$_2$ (%)	5-NO$_y$ (%)	4-NO$_y$ (%)	NO$_x$ (%)
60	3.1	7.7	0.0	4.1	1.2	0.2	0.2	5.0
90	5.1	16.4	0.1	22.8	3.4	2.0	1.9	10.9
120	6.6	9.6	0.1	7.7	2.4	2.2	2.1	8.2
150	6.5	8.6	0.1	9.7	2.6	2.5	2.5	7.6
180	6.3	8.8	0.1	11.2	3.0	2.7	2.7	7.6
210	6.3	9.9	0.1	11.1	3.4	2.9	2.9	8.0
240	5.4	16.6	0.1	12.6	4.3	3.3	3.3	10.3

For each model, the VMR profiles were chosen for the model grid point closest to Eureka. For CMAM-DAS and GEM-BACH, the model output at 18:00 UT (corresponding to approximately 1 PM local time) was used, while SLIMCAT provided profiles at local noon. The midday model VMR profiles were interpolated on to the 125HR retrieval grid and smoothed by

the 125HR averaging kernels and *a priori* VMR profiles according to the method of *Rodgers and Connor* [2003]:

$$\mathbf{x}_s = \mathbf{x}_a + \mathbf{A}(\mathbf{x}_m - \mathbf{x}_a) \tag{7.4}$$

where $\mathbf{x}_s$ is the smoothed profile, $\mathbf{x}_a$ is the 125HR *a priori* profile, $\mathbf{A}$ is the 125HR averaging kernel matrix, and $\mathbf{x}_m$ is the model VMR profile. The smoothing accounts for the lower vertical resolution and *a priori* profile of the 125HR measurements when comparing to other measurements or model calculations having higher vertical resolution. Partial columns were then calculated from each smoothed profile, using atmospheric densities provided with each model. An example of smoothed versus unsmoothed partial columns for CMAM-DAS is shown in Figure 7.4. For the stratospheric species considered in this study, smoothing typically increases the partial columns, since the averaging kernels are weighted to the stratosphere.
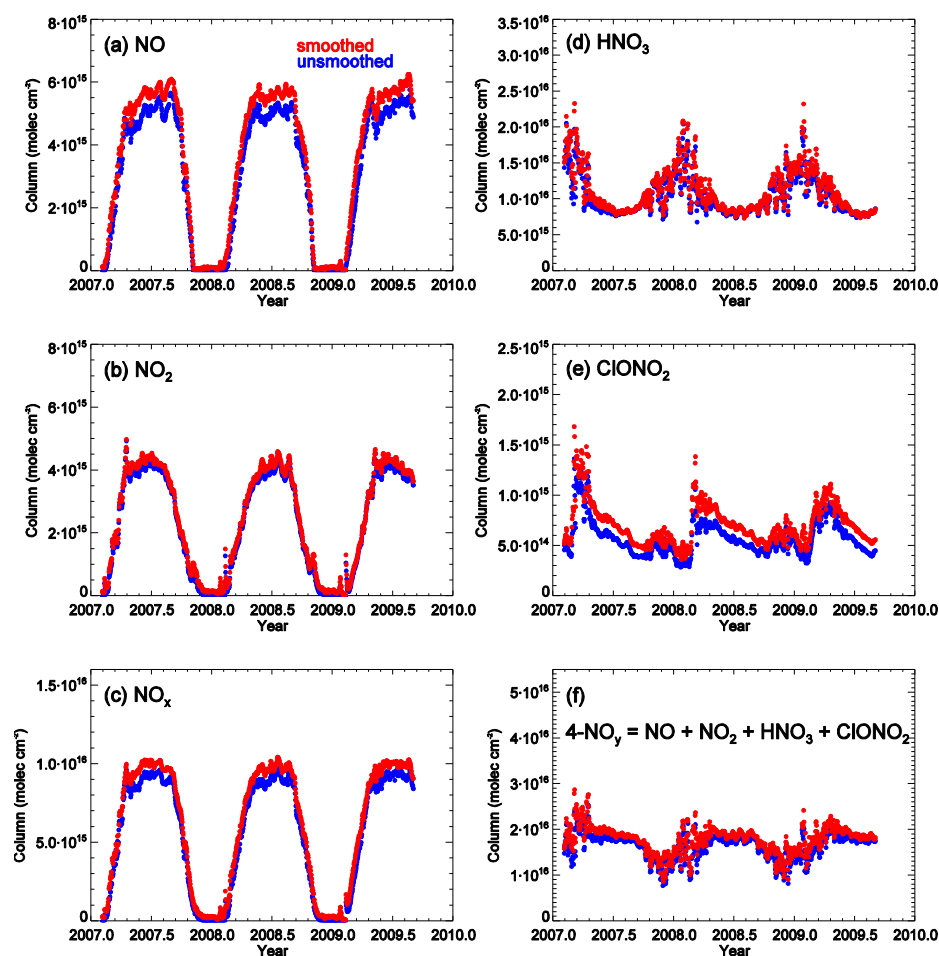
Figure 7.4. Smoothed (red) versus unsmoothed (blue) partial columns for CMAM-DAS. Partial columns were calculated for the 15 to 40 km altitude range. Panels (a) to (f) correspond to NO, NO$_2$, NO$_x$, HNO$_3$, ClONO$_2$, and 4-NO$_y$, respectively.

7.4.2 Results and Discussion

The resulting time series for the smoothed partial columns from the three models were compared with the 125HR measurements. Figure 7.5 shows the comparisons with CMAM-DAS for NO, NO_2, HNO_3, and $ClONO_2$. The CMAM-DAS NO partial columns match the 125HR columns in early spring but become larger, on average by 16%, during late spring and summer.

The CMAM-DAS NO_2 partial columns are consistently larger on average by 8% throughout each year, the difference being more pronounced in the spring of 2007. The CMAM-DAS HNO_3 and $ClONO_2$ partial columns are smaller than the 125HR columns, with the largest differences occurring during summer for HNO_3 and during the spring for $ClONO_2$. The $ClONO_2$ bias is due to a known issue in CMAM-DAS with the partitioning of chlorine reservoir species in the polar vortex, resulting in overestimated HCl mixing ratios and underestimated $ClONO_2$ mixing ratios. The HNO_3 bias is currently not well understood. In a recent comparison of NO_y-N_2O correlations between a variety of coupled chemistry-climate models and data from MIPAS night-time observations and the NASA ER-2 aircraft (see Fig. 6.14 of *SPARC CCMVal*, [2010]) CMAM showed good agreement with the observations. (Note that HNO_3 constitutes the largest fraction of NO_y). This discrepancy between the *SPARC CCMVal* [2010] study and the results presented here needs further analysis.
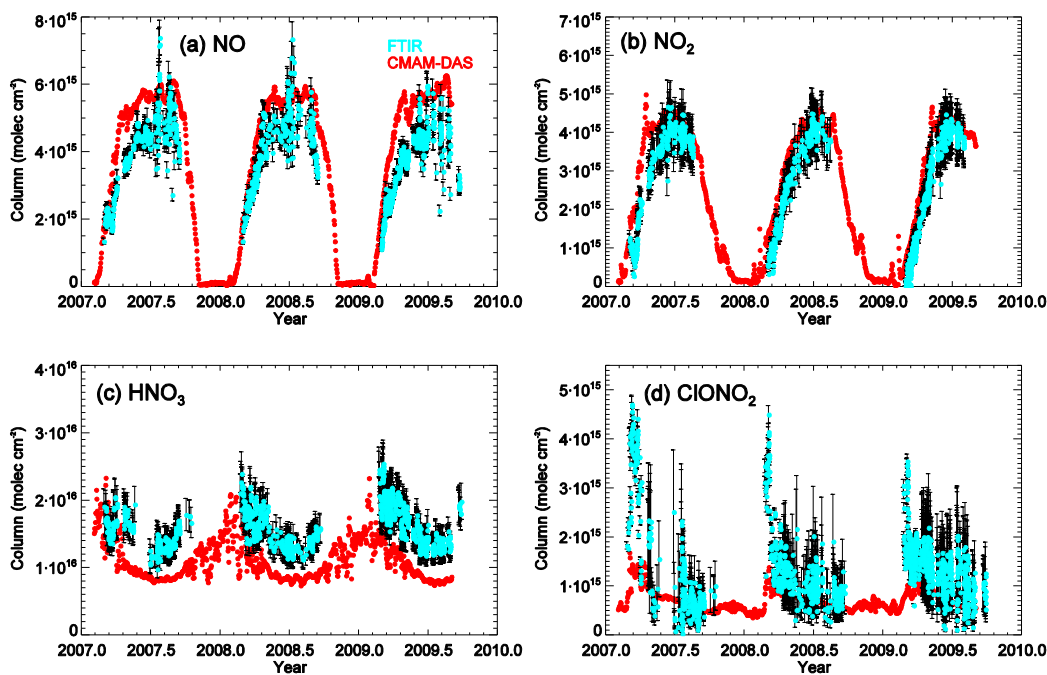
Figure 7.5. Bruker 125HR (cyan) and smoothed CMAM-DAS (red) 15-40 km partial columns for (a) NO, (b) NO_2, (c) HNO_3, and (d) $ClONO_2$. The error bars correspond to the errors in Table 7.1.

Similar plots are shown in Figure 7.6 for GEM-BACH. For NO and NO_2, GEM-BACH has consistently larger partial columns (on average by 18% and 20%, respectively), especially during the summer. The GEM-BACH HNO_3 partial columns match the 125HR well during the spring of 2007, but are slightly smaller than the 125HR for the rest of the comparison period (by approximately 10%). This shows the shortcoming of the GEM-BACH parameterization of denitrification, *i.e.*, irreversible loss of HNO_3 as soon as NAT PSCs appear. For $ClONO_2$, GEM-BACH consistently delivers significantly larger partial columns than observed by the 125HR. This is most probably due to the model neglecting type Ib PSCs (supercooled ternary solutions), while they play an important role in the springtime heterogeneous loss of $ClONO_2$ in the Arctic [e.g. *Hanisco et al.,* 2002]. It should be noted that the PSC parameterization in GEM-BACH (see Section 7.3.2) was adjusted for ozone depletion processes above the Antarctic and was not checked previously against Arctic observations.
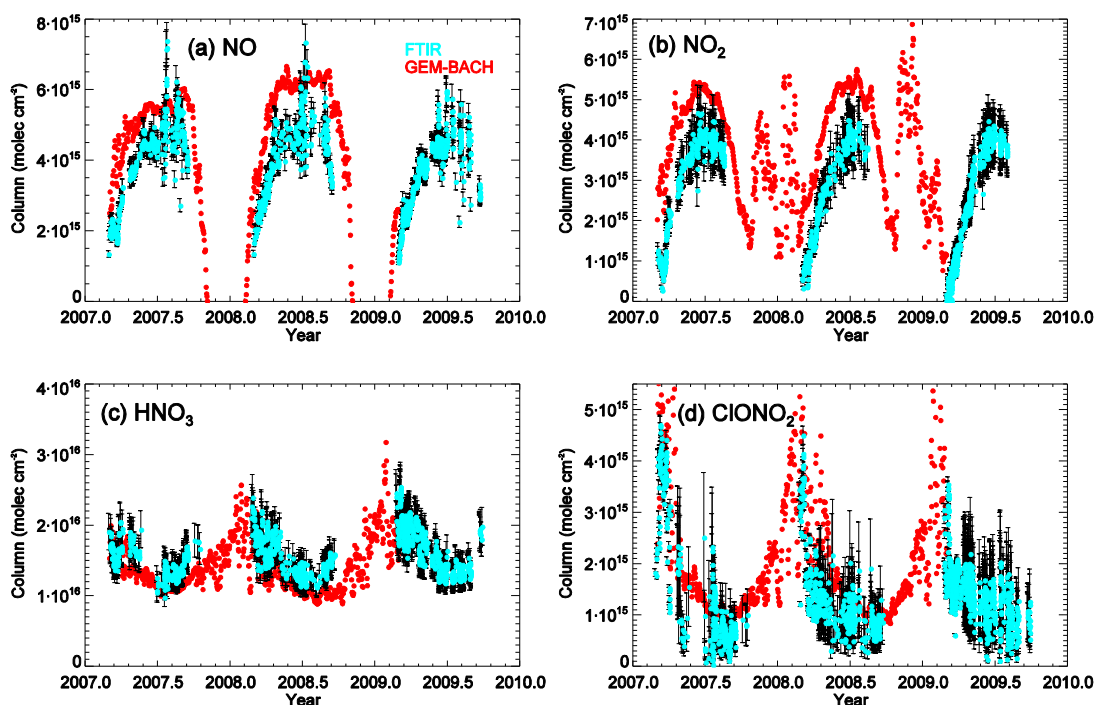
Figure 7.6. Same as Figure 7.5, but for the Bruker 125HR versus smoothed GEM-BACH.

SLIMCAT partial columns show the best agreement with the 125HR data, as seen in Figure 7.7. For NO, SLIMCAT matches the measured partial columns very closely, with the exception of some enhanced columns measured in summer. The SLIMCAT NO_2 partial columns are larger than the measurements, by approximately 5% for the entire comparison interval. For HNO_3, the SLIMCAT partial columns are in good agreement with the measured partial columns (within

approximately 2%) except during the early springs, when they peak earlier than the 125HR. ClONO$_2$ partial columns are in good agreement during all four spring seasons (within approximately 2%) but during the summer-fall periods, SLIMCAT partial columns are larger than the measurement. Model comparisons are extremely difficult around the polar vortex edge due to the resolution of the models, and this may be contributing to the difficulty all the models have in capturing the observations at this time of year.
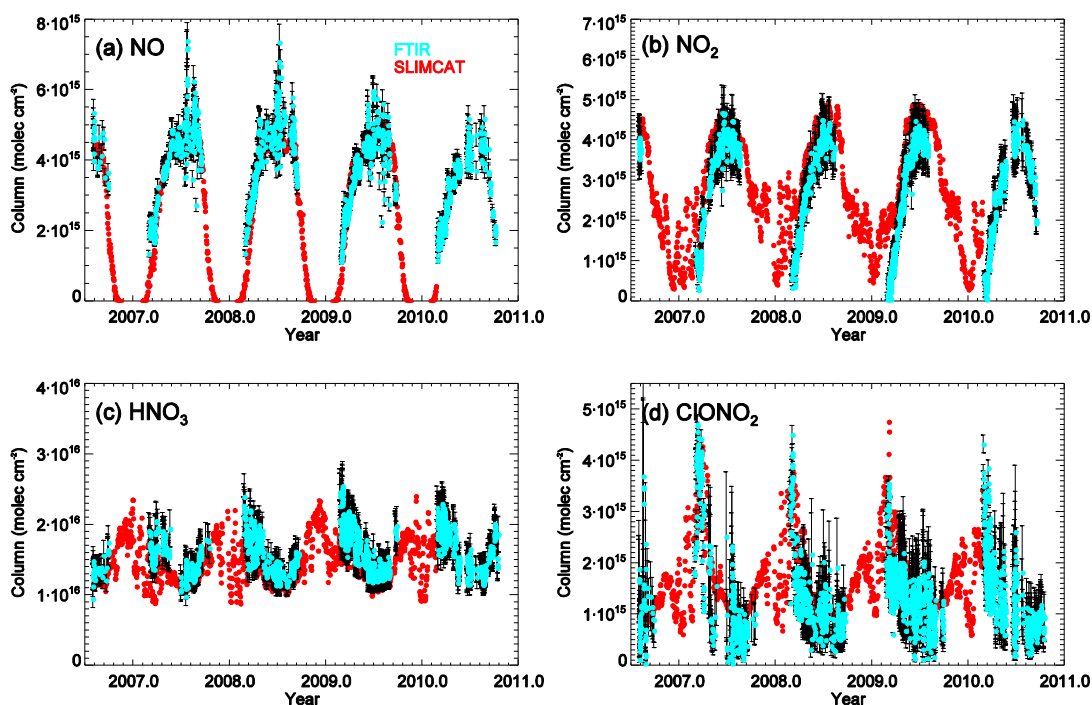
Figure 7.7. Same as Figure 7.5, but for the Bruker 125HR versus smoothed SLIMCAT.

Before continuing, we analyze the partial columns obtained from the measurements with the 125HR. For NO and NO$_2$ the pattern is very similar. After the long polar night, during which NO and NO$_2$ were converted to reservoir forms N$_2$O$_5$ and HNO$_3$, the NO and NO$_2$ partial column amounts increase as the days become longer. These columns peak during 24-hour sunlight period, decreasing again as the sun starts to set in August. The partial columns become close to zero as the sun sets for the last time in late October. During July and August, we notice random enhancements in the NO partial column (clearly seen in Figure 7.8), larger in 2007 and 2008, and smaller in 2009. Since the NO$_2$ partial columns do not show any lower values during these enhanced NO periods, the large NO values may be due to Energetic Particle Precipitation (EPP) events [*Randall et al.,* 2005, 2007, 2009]. This hypothesis is supported by information on the

geomagnetic activity from the Space Weather Prediction Center at NOAA (http://www.swpc. noaa.gov/alerts/archive/). The geomagnetic field activity increased on July 3, 2007 and an isolated major storm was reported at high latitudes midday on July 4. The geomagnetic activity was again at unsettled and minor storm levels on July 11, 18-20, and 31. In 2008, the geomagnetic field activity was at unsettled and active levels during July 11-13, with minor storm levels on July 12. Minor storm conditions were again reported on July 14 at high latitudes and the Advanced Composition Explorer spacecraft solar wind data indicated Earth was under the influence of a warning recurrent coronal hole high-speed stream.

The 125HR HNO$_3$ and ClONO$_2$ partial columns (Figure 7.7) are high in early spring since they were built up during the winter as a consequence of the Brewer-Dobson circulation. During spring and summer, the partial columns decay slowly and start to increase again during the fall, following an annual cycle. In the spring, we see perturbations in the slowly decreasing pattern due to a more dynamically and chemically active atmosphere.
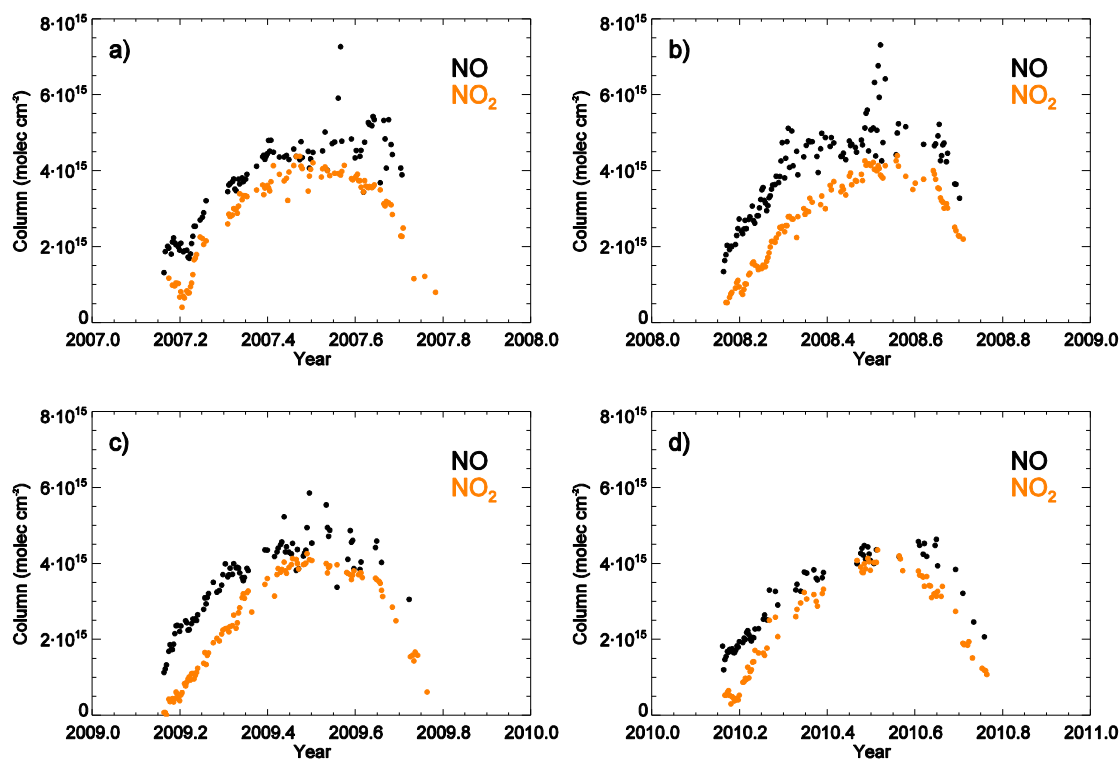
Figure 7.8. Mean values of daily 15-40 km NO (black) and NO$_2$ (orange) partial column per year: (a) 2007, (b) 2008, (c) 2009, and (d) 2010.

To obtain an estimate of the NO$_y$ partial columns, the partial columns for NO, NO$_2$, HNO$_3$, and ClONO$_2$ were added for the 125HR and the three models. This product is henceforth called 4-NO$_y$. The results are shown in Figure 7.9. The mean percentage difference between each model and the 125HR measurements was calculated as:

$$\Delta\% = \frac{100}{N} \sum_{i=1}^{N} \left[\left(MODEL_{PC}^{(i)} - FTIR_{PC}^{(i)} \right) / FTIR_{PC}^{(i)} \right] \tag{7.5}$$

where $FTIR_{PC}^{(i)}$ is the partial column calculated for the 125HR and $MODEL_{PC}^{(i)}$ is the partial column simulated by the model, for day i.

Figure 7.9(a) compares CMAM-DAS 4-NO$_y$ with the 125HR and shows that the model partial columns generally are smaller than those measured by the 125HR. During the 2007 spring, the partial columns match well, but throughout rest of the period, the model partial columns are consistently smaller than the 125HR columns. Figure 7.9(b) shows the mean percentage difference for the compared pairs, (-17.7±0.5)%, where the given error here and henceforth through the paper, is the standard error on the mean. The standard error on the mean relative difference between the model and the 125HR partial column (*sem*, in percent) has been evaluated as $sd/\sqrt{N}$, in which sd is the statistical 1-sigma (1σ) standard deviation of the observed differences, and N is the number of coincidences. The *sem* provides a measure of the significance of an observed bias [*De Mazière et al.,* 2008]. The standard deviation about the mean, 7.6%, is also shown. For this comparison, the negative bias is a consequence of the low bias in the CMAM-DAS HNO$_3$ partial columns (Figure 7.5), as HNO$_3$ dominates the NO$_y$ budget.

For the GEM-BACH comparison seen in Figure 7.9(c), the agreement with the 125HR is good. There is a slight positive bias of (5.0 ±0.8)% (Figure 7.9(d)), indicating that the model partial columns are slightly larger. The standard deviation in this case is 9.7%. For the SLIMCAT comparison (Figure 7.9(e)), the model partial columns are smaller than those measured by the 125HR during the spring of each year, and better match the measurements during the summer. The mean bias in this case is negative, (-6.3±0.5)%, as shown in Figure7.9(f), with a standard deviation of 8.4%. For the 4-NO$_y$ data product, the mean percentage differences relative to the measurements for SLIMCAT and GEM-BACH are similar, being within the mean total (measurement + scaling) error of 9.5%. For CMAM-DAS, the mean difference is larger than the mean total error.
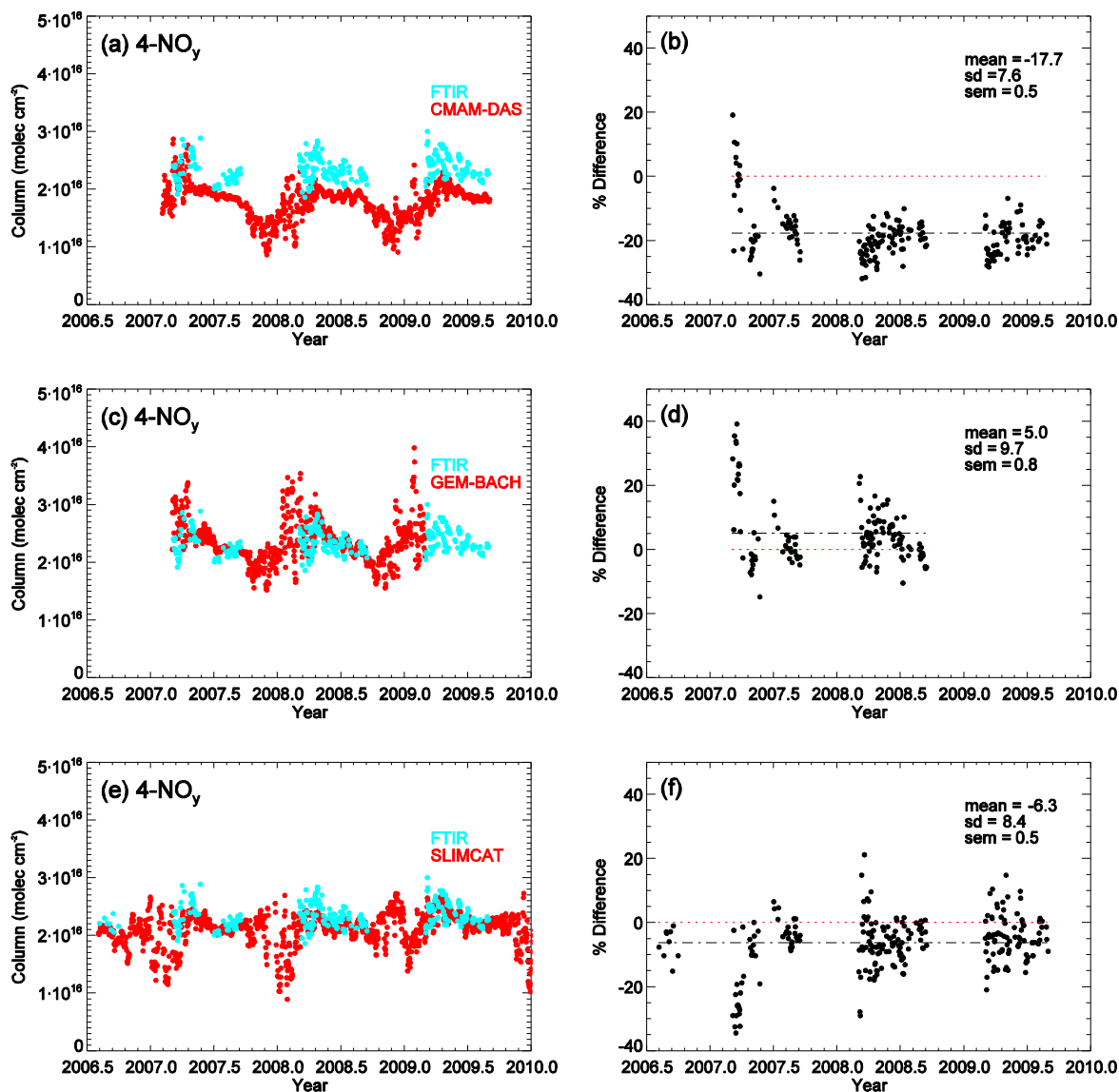
Figure 7.9. 4-NOy partial column Bruker 125HR (cyan) and smoothed model (red) 15-40 km partial columns for (a) CMAM-DAS, (c) for GEM-BACH, and (e) for SLIMCAT. The differences for each coincidence is shown on the right, (b) for CMAM-DAS, (d) for GEM-BACH, and (f) for SLIMCAT, along with the mean percentage difference and the standard deviation. The red dotted line shows the zero line, while the black dot-dash line shows the mean percentage difference.

We note large differences among the models during the first two months of 2008 and 2009. During these wintertime periods, GEM-BACH delivers notably higher values than the two other models. This is due to the simplistic PSC parameterization in GEM-BACH, which does not allow any segregation between gas-phase and condensed HNO_3. Hence the HNO_3 abundances

used for this model are total abundances, including both the gaseous and condensed phase, while for the other two models, gas-phase HNO$_3$ are used.

The 125HR measures four of the five NO$_y$ primary species: NO, NO$_2$, HNO$_3$, and ClONO$_2$. Since N$_2$O$_5$ also contributes significantly to the Arctic NO$_y$ budget, as shown in Figure 7.1, we used the simulated N$_2$O$_5$/NO$_x$ partial column ratios from the models discussed above to calculate N$_2$O$_5$. The resulting NO$_y$ product, including all five primary NO$_y$ species (henceforth called 5-NO$_y$), was derived as follows:

$$5\text{-}NO_y^{FTIR} = NO^{FTIR} + NO_2^{FTIR} + HNO_3^{FTIR} + ClONO_2^{FTIR} + 2 \times (N_2O_5^{model}/NO_x^{model}) \times NO_x^{FTIR} \qquad (7.6)$$

where $N_2O_5^{model}/NO_x^{model}$ is the model ratio, and NO_x^{FTIR} is the measured NO$_x$ partial column. Figure 7.10 shows these ratios for each model. For all three models, the summer ratios are near zero due to 24-hour daylight and hence very similar, however differences are seen for early spring and fall-winter, with CMAM-DAS ratios significantly higher than those from GEM-BACH and SLIMCAT. This discrepancy is most likely due to the less detailed transport scheme in CMAM-DAS as compared to the other models. While GEM-BACH transports every species separately and SLIMCAT transports all nitrogen species separately except NO$_x$ (NO + NO$_2$), in CMAM-DAS four of the shorter-lived nitrogen species (NO + NO$_2$ + NO$_3$ + 2xN$_2$O$_5$) are transported together. Bulk-transport by chemical family is done generally to minimize the computational cost of a transport scheme and to avoid strong gradients in advected fields. This means that after each transport step in the model, the advected family is split apart into its individual family members using the partitioning ratios saved on the grid during the previous time step. The partitioning between NO and NO$_2$ is very fast and completely dependent on sunlight, so the NO concentration goes to zero in the night in all three models. But the partitioning between NO$_x$ and the longer-lived species, *e.g.*, N$_2$O$_5$ and HNO$_3$, is slower. Both GEM-BACH and SLIMCAT see substantial values of NO$_2$ in the polar night, which is evidence of air masses that have recently been exposed to sunlight. Since in CMAM-DAS the partitioning is locked down on to the model grid, nitrogen oxides from lower latitudes can be advected into the polar night but when the advected quantity is split apart into the separate species, the partitioning will be that of an air mass that has been in the dark for a long time, which explains why CMAM-DAS displays near-zero NO$_2$ (Figure 7.5) and an anomalous N$_2$O$_5$/NO$_x$ ratio throughout the winter (Figure 7.10).

The adjusted 125HR results (5-NO$_y$) are shown in Figure 7.11, along with the 5-NO$_y$ partial columns obtained from the three models. The CMAM-DAS, GEM-BACH, and SLIMCAT results for 5-NO$_y$ are similar to those for 4-NO$_y$, with mean differences of (-16.0±0.6)%, (5.5±1.0)%, and (-5.8±0.4)%, and standard deviations of 9.4%, 12.0%, and 7.6% respectively, as seen in Figure 7.11(b), (d), and (f). Again, the mean percentage differences relative to the measurements for GEM-BACH and SLIMCAT are within the mean total error (measurement + scaling) of 9.6%, while those for CMAM-DAS are larger.
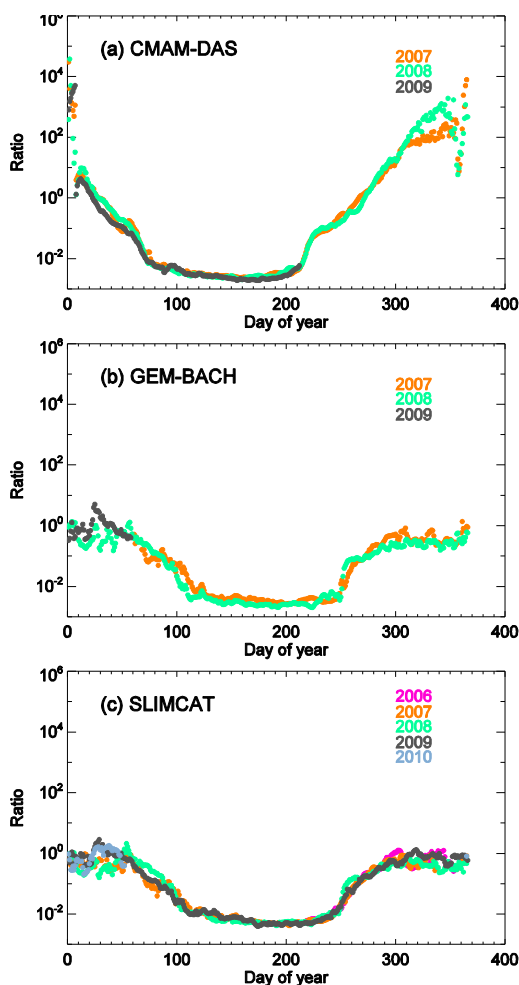
Figure 7.10. N$_2$O$_5$/NO$_x$ ratios for (a) CMAM-DAS, (b) GEM-BACH, and (c) SLIMCAT. The colours correspond to different years as shown in the legend.

7.5 ACE-FTS comparisons

7.5.1 Methodology

The methodology for comparing ACE-FTS data with the 125HR was described in the previous chapter. In brief, the following filtering criteria were applied to the VMR profiles: a

time difference of less than ±12h, a spatial difference of ≤1000 km and a maximum temperature difference of <10 K between the sampled air masses at each altitude along the line-of-sight between 15 and 40 km. In addition, the scaled potential vorticity (sPV) differences between the 125HR and ACE-FTS at each altitude along the line-of-sight were restricted to less than $0.3 \times 10^{-4}\,s^{-1}$, ensuring that the sampled air masses were similar for both measurements relative to the polar vortex edge. sPV was derived for both ACE-FTS and 125HR at locations along the line-of-sight using the GEOS Version 5.0.1 (GEOS-5) analyses [*Reinecker et al.,* 2008].
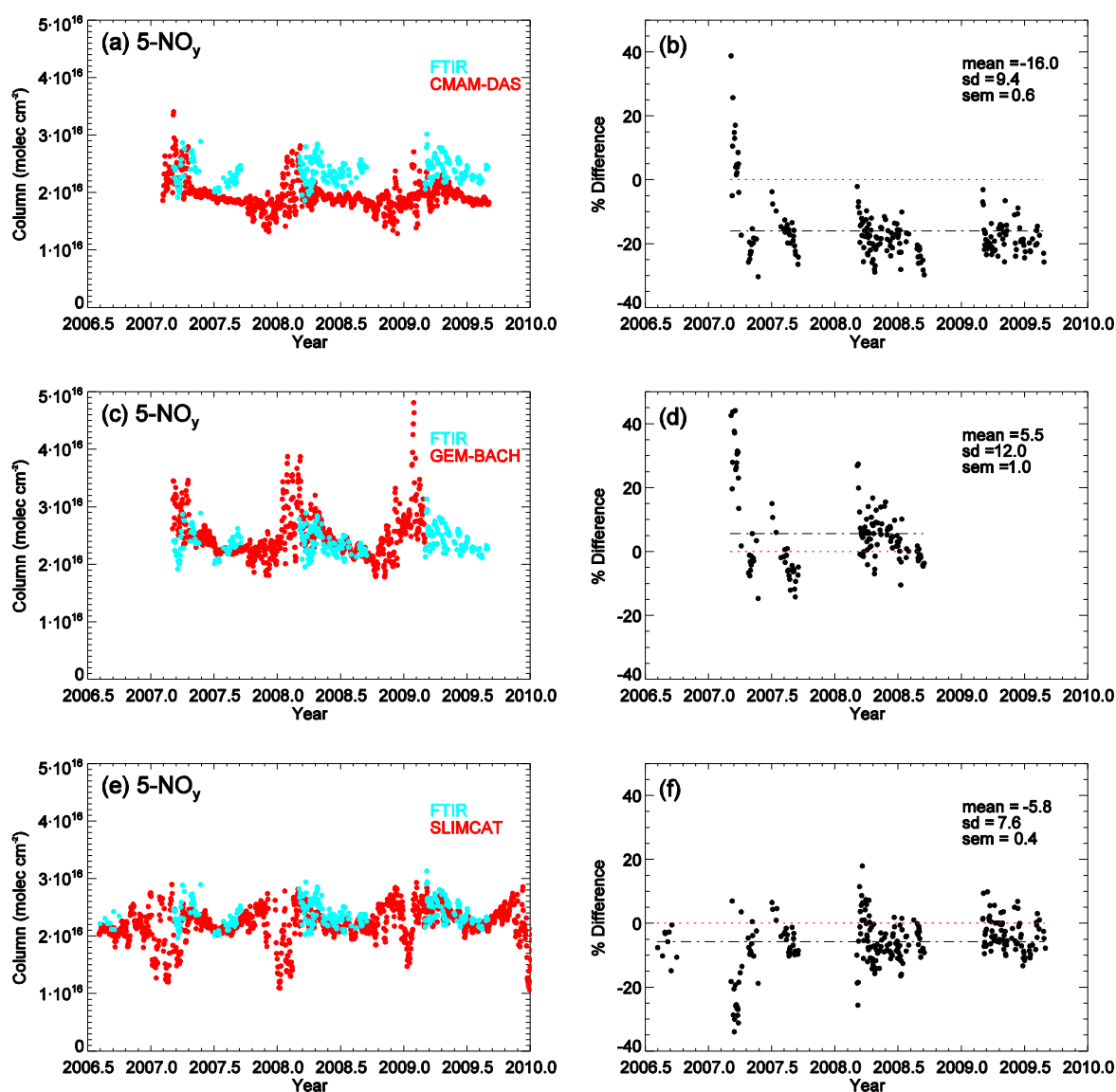
Figure 7.11. Same as Figure 7.9 but for 5-NOy.

For all coincident ACE-FTS NO, NO$_2$, and ClONO$_2$ profiles, a scaling to noon was also performed, to account for the diurnal variation of these species. The ACE-FTS profiles were then

interpolated on to the 125HR retrieval grid and smoothed by the 125HR averaging kernels and *a priori* profiles, using Equation 6.1. Partial columns were calculated for the altitude range 15-40 km to match the 125HR partial columns, and finally, the "daily mean" partial columns were derived for those cases when more than one ACE-FTS measurement was found for a particular day. The 4-NO$_y$ and 5-NO$_y$ were then calculated for both the 125HR and ACE-FTS. To calculate 5-NO$_y$ for the 125HR, the ACE-FTS N$_2$O$_5$/NO$_x$ ratios were used, applying Equation 7.6, where the model ratio was replaced by the ACE-FTS ratio.

7.5.2 Results and Discussion

The quality of the ACE-FTS measurements has been demonstrated by previous studies. *Kerzenmacher et al.* [2008] provide an assessment of ACE-FTS v2.2 NO and NO$_2$. A companion paper by *Wolff et al.* [2008] provides an assessment of the quality of ACE-FTS v2.2 HNO$_3$, ClONO$_2$, and the ACE-FTS v2.2 N$_2$O$_5$ update. Both studies included comparisons with globally distributed ground-based FTIR spectrometers affiliated with the NDACC. For the comparisons of ACE-FTS NO partial columns with six ground-based FTIRs, the mean differences (ACE-FTS – FTIRs) were between -14.5% and -67.5%, becoming more negative from South to North [*Kerzenmacher et al.,* 2008]. Partial column comparisons for NO$_2$ showed a mean difference of +7.3% between the ACE-FTS instrument and the same six ground-based FTIR spectrometers.

For HNO$_3$, the comparison with nine ground-based FTIRs showed an agreement within the range -12.6% to +6.0% [*Wolff et al.,* 2008]. For ClONO$_2$, the same study showed an agreement within the range -8.8% to +8.9%. For N$_2$O$_5$, there are no comparisons with ground-based FTIRs, but the comparison with MIPAS on ENVISAT using the Institut für Meteorologie und Klimaforschung and Instituto de Astrofísica de Andalucía (IMK-IAA) data processor showed a low bias of the ACE-FTS relative to MIPAS IMK-IAA of -0.25 ppbv at an altitude of 30 km (the altitude of maximum N$_2$O$_5$). The mean absolute differences at lower altitudes (16-27 km) were found to be typically −0.05 ppbv for MIPAS nighttime and ±0.02 ppbv for MIPAS daytime measurements [*Wolff et al.,* 2008].

For the 5-NO$_y$ product, approximately two years of overlap between Odin and ACE permitted the comparison of Odin NO$_y$ climatology [*Brohede et al.,* 2008] with an ACE-FTS climatology [*Jones et al.,* 2011]. The comparison was made for pressure surfaces up to 1 hPa and gave absolute differences better than 2 ppbv, equivalent to relative differences less than 20%.

Figure 7.12(a) shows the comparison between ACE-FTS and the 125HR 5-NO_y partial columns using all coincidences between 2007 and 2010. Figure 7.12(b) shows the percentage differences between the two instruments (ACE-FTS − 125HR)/125HR. There were fewer coincidences for 2007 and 2008 than for 2009 and 2010. This is a consequence of the number of 125HR spectra acquired during each spring campaign, which is influenced by the local meteorological conditions at Eureka. The break-down of the ACE-FTS and the 125HR 5-NO_y partial column comparison per year is shown in Figure 7.13, while Table 7.2 gives the mean percentage differences, standard deviations, and standard errors on the mean by year. 2007 was a year when most of the 125HR measurements sampled air inside the vortex. For these coincidences, the ACE-FTS measurements were consistently larger than those of the 125HR, as shown in Figure 7.12(b). During the following years, the 125HR sampled most of the time through the vortex edge and the comparisons show both positive and negative differences. Overall, there is a positive mean bias for all years, with ACE-FTS higher than the 125HR. Results for 4-NO_y and 5-NO_y are similar, except for 2008, for which the 5-NO_y difference (0.8%) is much smaller than that for 4-NO_y (9.1%). Over the entire comparison period, the mean percentage difference for 5-NO_y is (5.6±2.3)%, with a standard deviation of 12.2%. This agreement between the ACE-FTS and the 125HR provides confidence in the NO_y product derived from ground-based FTIR measurements at Eureka.
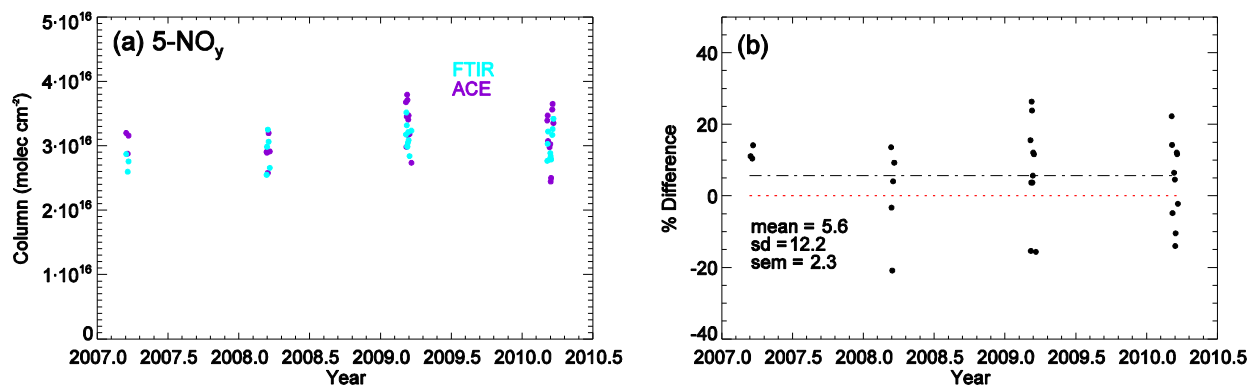
Figure 7.12. (a) 5-NOy Bruker 125 HR (cyan) and smoothed ACE-FTS (purple) 15-40 km partial columns, (b) differences calculated for each coincidence. The mean percentage difference and the standard deviation are also shown. The red dotted line shows the zero line, while the black dot-dash line shows the mean percentage difference.
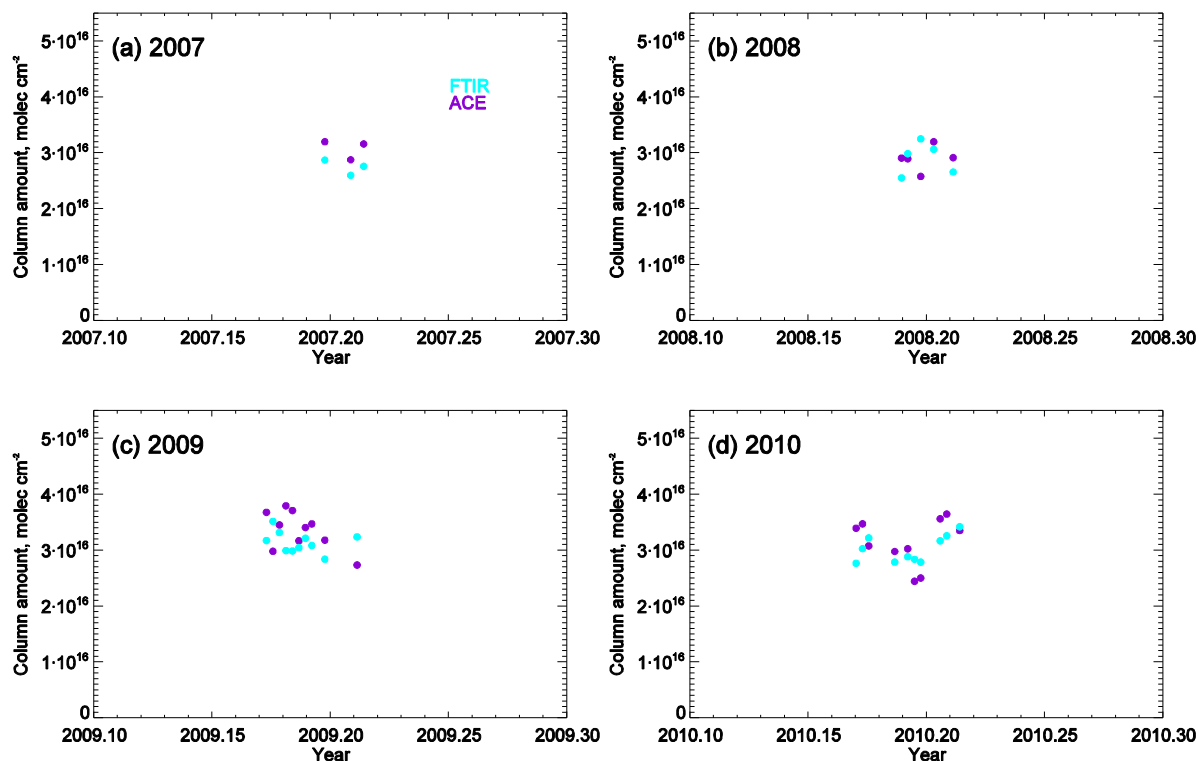
Figure 7.13. 5-NOy Bruker 125 HR (cyan) and smoothed ACE-FTS (purple) 15-40 km partial columns, for (a) 2007, (b) 2008, (c) 2009, and (d) 2010.

Table 7.3. Break-down by year of the ACE-FTS versus Bruker 125HR mean percentage difference ((ACE-FTS – 125HR)/125HR), standard deviation, standard error on mean, and number of coincidences.

	4-NO$_y$			5-NO$_y$			
	Mean % difference	Standard deviation (%)	Standard error on mean (%)	Mean % difference	Standard deviation (%)	Standard error on mean (%)	n
2007	13.6	2.8	1.6	12.2	2.0	1.1	3
2008	9.1	9.1	4.1	0.8	13.5	6.0	5
2009	6.9	7.1	2.2	7.4	14.2	4.5	10
2010	6.8	3.1	1.0	4.2	11.6	3.7	10
TOTAL	8.0	6.1	1.2	5.6	12.3	2.3	28

7.6 Seasonal and Interannual Variability of NO$_y$

To assess the seasonal and interannual variability of NO$_y$ above Eureka, we used the 5-NO$_y$ calculated using the SLIMCAT N$_2$O$_5$/NO$_x$ ratio. The motivation for this choice was that SLIMCAT provided the longest model data set, with a ratio that was consistent with GEM-BACH. Figure 7.14 shows the 125HR time series of the 5-NO$_y$ partial columns for each year, beginning August 2006 and ending October 2010. Variability is greatest during the spring, decreasing in summer and fall. Considering the period up to day 140, we find a mean partial column ($\pm 1\sigma$) of $(2.5\pm 0.2)\times 10^{16}$ molec cm^{-2}, while for all days after 140, we find a mean partial column of $(2.3\pm 0.1)\times 10^{16}$ molec cm^{-2}. This shows that the spring mean is higher by approximately 8%, while the spring variability, indicated by the standard deviation, is twice that of the summer and fall. The more scattered partial columns can be explained by more dynamically-active meteorological conditions during spring compared to the summer, with the higher partial column values driven by the subsidence of NO$_y$-rich air from above the partial column range into the column inside the polar vortex.
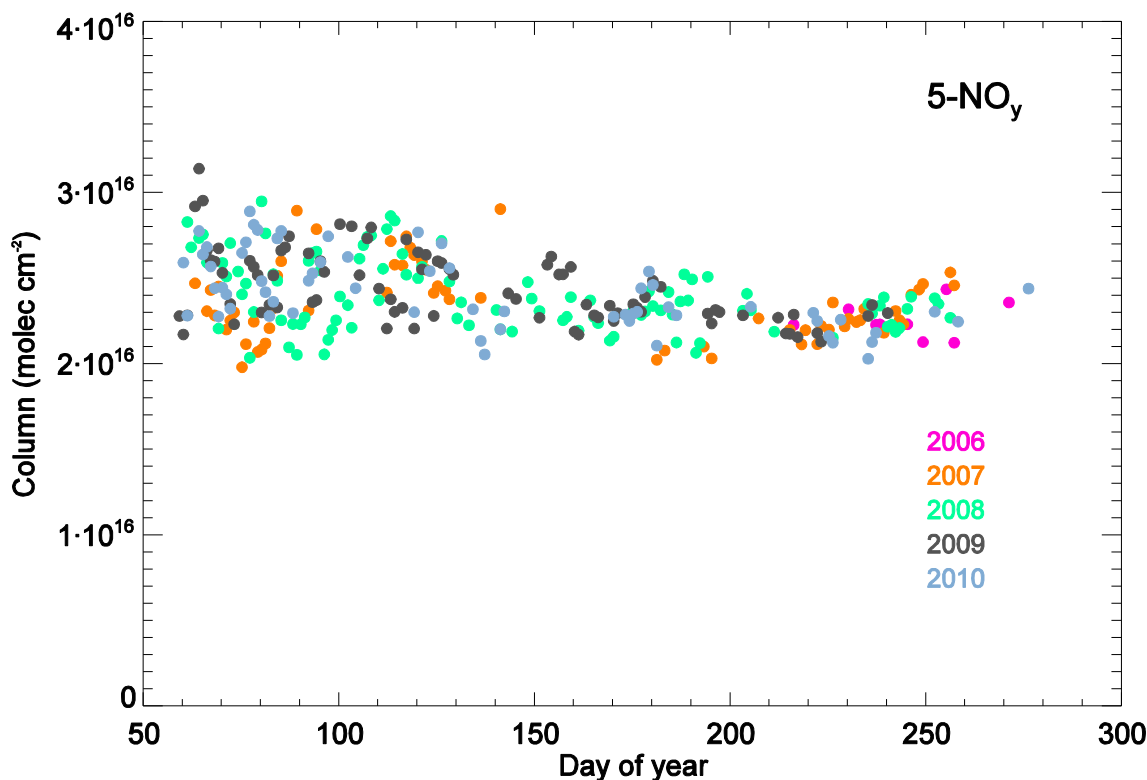
Figure 7.14. 125HR 5-NO$_y$ 15-40 km partial columns for the years shown in the legend.

To estimate the number of years necessary to detect a trend in the NO$_y$ data product at Eureka, Equation 3 from *Weatherhead et al.* [1998] was used:

$$n* = \left[\frac{3.3\sigma_N}{|\omega_0|} \sqrt{\frac{1+\phi}{1-\phi}} \right]^{2/3},$$
(7.7)

where $n*$ represents the number of years of data required to detect a trend of specified magnitude $|\omega_0|$, σ_N is the standard deviation of the mean calculated for N data points, and ϕ is the autocorrelation in the data. Further description of the terms and of the way they were derived can be also found in *Tiao et al.* [1990]. The value 3.3 in Equation 7.7 is used for the degree of certainty of 90% (this number would be larger (smaller) if we require a higher (lower) degree of certainty than 90%). Considering the four-year 5-NO$_y$ timeseries above, values of $\sigma_N = 8.29\%$ and $\phi = 0.59$ were calculated. The number of years of data required to detect an NO$_y$ trend of 0.2% per year (estimated from the *SPARC CCMVal* [2010] study) is 41.7 years. This result is in accordance with Table 1 of *Weatherhead et al.* [1998], which shows that long period of time is necessary to detect such a small trend. Note that for a trend of magnitude $|\omega_0| = 0.3\%$ per year, the number of years of data required for trend detection becomes $n* = 31.8$ years. For a trend of the same magnitude of $|\omega_0| = 0.3\%$, a data noise level of $\sigma_N = 1.46\%$ would be required to detect a trend in 10 years. If we consider only the measurements after day 140 for all four years (for these days the standard deviation is just half of that for the spring, as discussed earlier), $\sigma_N = 5.30\%$ and $\phi = 0.49$. For this case, the number of years required to detect an NO$_y$ trend of magnitude $|\omega_0| = 0.2\%$ per year will be $n* = 28.6$ years.

To investigate the springtime evolution of NO$_y$, Figure 7.15 shows the spring series for 5-NO$_y$ and its constituent species, along with the sPV for 2007 to 2010. The top panel, for each year, shows the NO$_y$ partial columns together with those of HNO$_3$, since its contribution is the largest. For all four years, it is evident that the variability of the 5-NO$_y$ partial columns is dominated by the variability in the HNO$_3$ column. The middle panels show the other four NO$_y$ species. In the bottom panels, the evolution of the sPV is given for the 18, 26, and 36 km altitude levels, corresponding to the lower and middle stratosphere.

The 2006/2007 winter Arctic vortex was particularly strong and cold, resulting in significant destruction of stratospheric ozone [*Rösevall et al.,* 2007; *WMO,* 2011]. After sunrise, occurring on February 20 at Eureka, the 125HR sampled the atmosphere inside the polar vortex
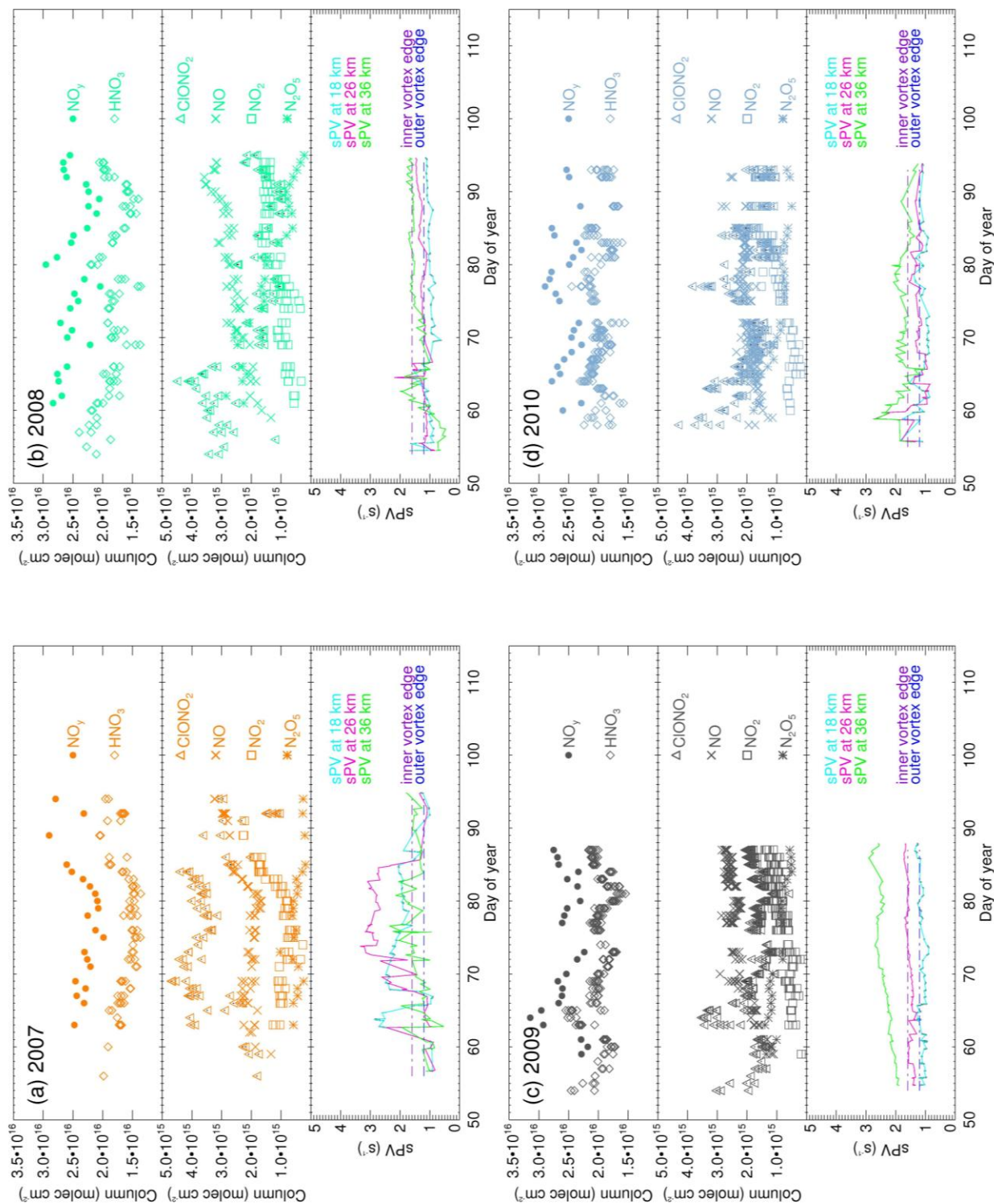
Figure 7.15. 125HR 15 - 40 km partial columns of 5-NO$_y$ and constituent species, measured in the spring (a) 2007, (b) 2008, (c) 2009, and (d) 2010. The colors match those in Figure 7.14. The top panels show the partial columns of 5-NO$_y$ and HNO$_3$, the middle panel shows the partial columns of ClONO$_2$, NO, NO$_2$, and N$_2$O$_5$. The bottom panels show the evolution of sPV for three altitudes: 18 km (cyan), 26 km (pink), and 36 km (green). The dash-dot lines mark the inner (purple) and outer (blue) vortex edge.

for most of the spring, as can be seen from the evolution of sPV. These measurements are consistent with our understanding of the chemical processes that occur in the dynamically-isolated air within the vortex, whereby HNO_3-containing PSCs form during cold winters, chlorine is released from its reservoirs (HCl and $ClONO_2$) to participate in springtime ozone destruction, and the resulting springtime repartitioning of chlorine in the Arctic results in enhanced $ClONO_2$ for some time after PSCs have disappeared [*Dufour et al.,* 2006; *WMO,* 2007; *Santee et al.,* 2008]. High $ClONO_2$ columns were measured inside the vortex during 2007 (Figure 7.15) showing that active chlorine started to return into its reservoirs. This is consistent with the evolution of $ClONO_2$ and HCl measured by *Batchelor et al.* [2010] for this period. Also in the 2007 spring, we see that the HNO_3 partial columns are smaller inside the vortex compared to the vortex edge. Usually, if the vortex is not perturbed by PSC formation, HNO_3 concentrations are large and well correlated with PV [*Santee et al.,* 1999]. In 2007, vortex temperatures (not shown) were favorable for PSC formation, reaching values below the type II PSC threshold in December and January, and below the type I PSC threshold through March 21. However, radiosonde measurements above Eureka never fell below 198 K during our campaign. The low HNO_3 values measured at Eureka are thought to be a consequence of HNO_3 being removed from the gas phase in liquid/solid PSC particles elsewhere in the vortex, with this HNO_3-poor air being transported over Eureka. As the days become longer, more NO and NO_2 form from the nighttime reservoir, N_2O_5, through photolysis, implying that the evolution of the N_2O_5 partial columns is opposite to that of NO and NO_2.

During the following years, the instrument sampled mostly through the edge of, or outside, the polar vortex, as seen in the sPV plots in Figure 7.15 for 2008, 2009, and 2010. 2008 was another cold winter with significant chemical processing [*WMO*, 2011]. 2009 and 2010 were both characterized by a strong and prolonged sudden stratospheric warming in late January, with no chemical processing and Cl deactivated after early February. The evolution of NO$_y$ shows some temporal variability within each of these years, which is mostly a consequence of dynamics. Some peaks in the $ClONO_2$ partial columns coincide with larger sPV values, corresponding to measurements inside the polar vortex. Some examples are day 64 in 2008, and days 58, 59, 77 in 2010. During 2009, enhanced partial columns of HNO_3, $ClONO_2$, and N_2O_5 can be seen near day 63, when the sampled layers were on the vortex edge rather than inside the vortex. This is again a consequence of the build up at the vortex edge region, as discussed above. Similar peaks were also seen in the total columns of O_3, HCl, and HF for those days (not shown

here). Each year, the photolysis of HNO_3 and N_2O_5 to NO and NO_2 is observed, with low NO and NO_2 in early spring, increasing as the days become longer, as shown above.

7.7 Conclusions

A four-year time series of the total reactive nitrogen (NO_y) stratospheric partial columns (15-40 km) above Eureka, Nunavut, has been obtained using measurements made by the 125HR. Four components of the NO_y budget were measured (NO, NO_2, HNO_3, $ClONO_2$), while N_2O_5 was derived using model ratios of N_2O_5/NO_x for the closest grid point to Eureka. For the four individual NO_y species, the SLIMCAT model results showed the best agreement with the 125HR measurements. Comparisons of 5-NO_y (NO + NO_2 + HNO_3 + $ClONO_2$ + 2 x N_2O_5) with three atmospheric models were also made. The comparison showed that the CMAM-DAS 5-NO_y partial columns were smaller than the FTIR partial columns, the mean percentage difference [100 x (model − 125HR) / 125HR] being (-16.0±0.6)% (where the uncertainty represents the standard error of the mean). GEM-BACH 5-NO_y showed an agreement of (5.5±1.0)%, with the model partial columns being slightly larger than the 125HR columns. For the SLIMCAT chemical transport model, the 5-NO_y partial columns were slightly smaller than the 125HR columns, the mean percentage difference being (-5.8±0.4)%. For GEM-BACH and SLIMCAT, the differences were found to be within the mean total (measurement + scaling) error of 9.6%, while the CMAM-DAS difference was larger than the mean total error estimated for the 5-NO_y.

The 125HR measurements were further compared with ACE-FTS springtime measurements, a period when ACE has overpasses above Eureka. Data from four Canadian Arctic ACE Validation Campaigns at Eureka were compared using strict coincidence criteria to constrain time, distance, temperature, and sPV at altitudes along the lines-of-sight for both instruments for the compared air masses. For 5-NO_y, a mean percentage difference of (5.6±2.3)% was found, indicating that the ACE-FTS partial columns are slightly larger than the 125HR columns. The small difference shows that the two instruments are in good agreement, despite their different viewing geometries and the high variability of the springtime Arctic stratosphere.

The seasonal and interannual variability of 5-NO_y above Eureka was also investigated. The 5-NO_y partial column was approximately constant through the sunlit part of the year, from mid-February to mid-October, with greater variability during the spring. The mean partial column averaged for the spring period (up to day 140) was (2.5±0.2)x10^{16} molec cm^{-2}, while for

the period after day 140, it was $(2.3\pm0.1)\times10^{16}$ molec cm^{-2}. In the longer term, this data product can be also used for trend studies. A 41.7 years time frame was derived to be necessary to detect an NO$_y$ trend of 0.2% per year.

The springtime evolution of 5-NO$_y$ and its constituent nitrogen species, along with sPV, was examined for 2007 to 2010. The variability of the 5-NO$_y$ partial column was seen to be dominated by that of HNO$_3$. The evolution of the individual nitrogen species was found to be consistent with the current understanding of the chemical and dynamical processes that occur in the polar stratosphere.

Chapter 8

Unusually low O_3, HCl, and HNO_3 Total Columns Measured at Eureka in Spring, 2011

8.1 Introduction

As discussed in Chapter 1, during polar winter, heterogeneous reactions on the surfaces of stratospheric particles at cold temperatures convert the chlorine reservoir species HCl and $ClONO_2$ to active chlorine that participates in springtime ozone destruction [*Solomon et al.,* 1986]. The northern hemisphere winter polar vortex typically forms in the lower stratosphere early in November, is strongest in mid-January and typically dissipates in late March or early April [*WMO,* 2011]. In winter 2010/2011, a cold and strong Arctic vortex formed and was located above our research site, Eureka, for much of the time until late March [*Manney et al.,* 2011]. This chapter reports unusually low O_3, HCl, and HNO_3 column measurements at Eureka, compared to measurements from previous years. The measurements were made with the Bruker 125HR during the 2011 spring Canadian Arctic ACE Validation Campaign, which took place from February 23 to April 6. This work has been submitted for publication [*Lindenmaier et al.,* 2011b].

8.2 Measurements
8.2.1 CANDAC Bruker IFS 125HR

For this analysis, the retrieval method described in Chapter 3 was used. The spectral fitting microwindows that have been used for each gas and the input parameters are those in Table 3.1. Figure 8.1 shows typical column averaging kernels for O_3, HCl, HNO_3, $ClONO_2$, and HF for the 125HR along with the sensitivity and the DOFS The retrieval for each gas has good sensitivity in the lower stratosphere, with DOFS varying from 1.06 for $ClONO_2$ to 6.64 for O_3. Total columns from 0.61 to 100 km were calculated from 2007 to 2011 and used in this work. The error calculations are based on the methodology of *Rodgers* [1976, 1990], as discussed in Section 3.5 (S_{TOTAL} calculated using Equation 3.31 and a set of representative spectra), and are shown in Table 8.1.
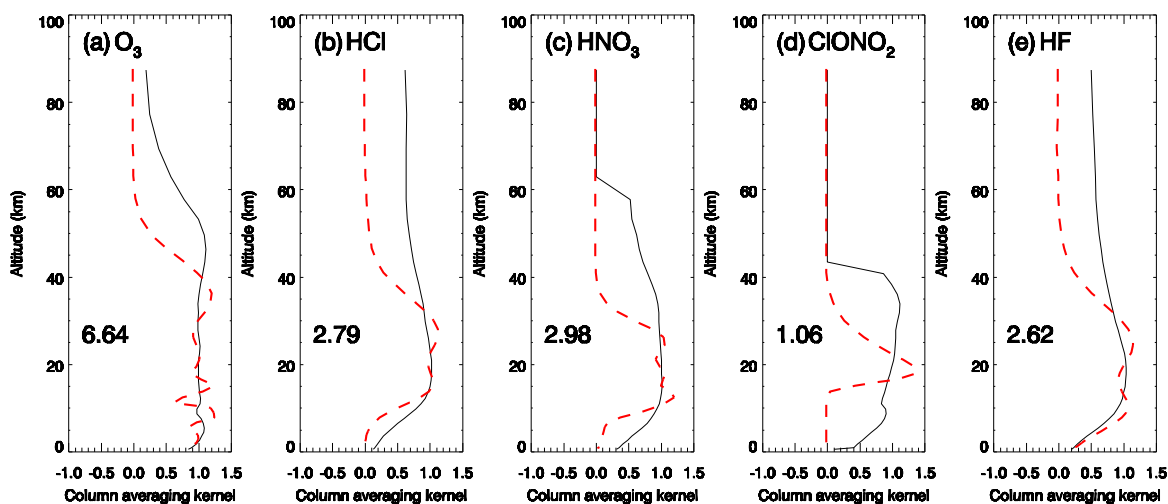
Figure 8.1. Typical column averaging kernels (black solid line) and sensitivities (red dashed line) for the Bruker 125HR springtime measurements (March 6, 2009 at solar zenith angle of 85.58º). The numbers represent typical springtime DOFS for each gas.

Table 8.1. Springtime total errors for O$_3$, HCl, HNO$_3$, ClONO$_2$, and HF total columns retrieved from the FTIR spectra. The total error was calculated as described in Sections 8.2.1 and 8.2.2, respectively.

	Total error (%)	
	125HR	**DA8**
O$_3$	4.5	11.3
HCl	3.7	12.3
HNO$_3$	13.5	16.9
ClONO$_2$	4.5	18.2
HF	4.7	13.2

8.2.2 Environment Canada ABB Bomem DA8

The Environment Canada ABB Bomem DA8 FTIR spectrometer (henceforth the DA8) was installed at Eureka in 1993 and has acquired solar absorption spectra each spring through to 2008 [*Donovan et al.,* 1997; *Farahani et al.,* 2007; *Paton-Walsh et al.,* 2008; *Fu et al.,* 2011; *Fast et al.,* 2011]. The DA8 spectrometer is a vertically aligned Michelson interferometer that,

similarly to the Bruker 125HR, records high-resolution solar absorption spectra over the spectral range from 700 to 5000 cm^{-1}. The spectra were analyzed using the SFIT1 spectral fitting routine [*Rinsland et al.,* 1982, 1988], using the line parameters in the HITRAN 1992 compilation [*Rothman et al.,* 1992] plus updates. Scaling factors derived from the fits were applied to the *a priori* VMR profiles at all altitude layers to obtain the final scaled profiles. These profiles were convolved with the density-weighted pressure and temperature profiles to generate the column profiles, which were integrated to derive the column densities. In this work, these DA8 total columns were scaled prior to comparison with the Bruker 125HR total columns to account for the bias induced by the use of a different retrieval algorithm and line list. The biases in the DA8 measurements relative to those retrieved with the HITRAN 2004 compilation and SFIT2 are -3.9% for O$_3$, -0.4% for HCl, -14.3% for HNO$_3$, +15.6% for ClONO$_2$, and 0.0% for HF as shown by *Fast et al.* [2011]. The same paper also describes the error budget calculation for the errors presented in Table 8.1. Here, we present DA8 results for 10 years from 1997 to 2006, to provide a 15-year record for the trace gas comparisons.

8.2.3 CANDAC Rayleigh-Mie-Raman Lidar

The CANDAC Rayleigh-Mie-Raman Lidar (CRL) is a ground-based lidar system installed at the Zero Altitude PEARL Auxiliary Laboratory in Eureka. The CRL transmits at 532 nm and 355 nm using two Nd:YAG lasers with repetition rates of 10 Hz. The CRL has eight detection channels: vibrational and pure-rotational Raman channels for the measurement of tropospheric molecular nitrogen, water vapor and temperature profiles, along with two elastic backscatter channels. The 532 nm and 355 nm elastic channels can be used for PSC detection and for characterization and determination of aerosol/cloud backscatter ratio. The depolarization ratio can also be calculated at 532 nm allowing for the discrimination between liquid and solid phase cloud particles. For a complete description of the instrument see *Nott et al.* [2011].

8.2.4 Radiosondes

Balloon-borne radiosondes measure profiles of atmospheric temperature, pressure and humidity. Radiosonde observations are taken year round at Eureka twice daily, at 6 AM and 6 PM (corresponding to 11 AM and 11 PM Universal Time) using Vaisala RS92 GPS radiosondes. These have an accuracy of ±0.5 hPa for pressure, ±0.5 K for temperature, and ±3.5% for relative humidity [*Vömel et al.,* 2007; *Steinbrecht et al.,* 2008]. The data from the balloon are transmitted

continuously to the launching station, where they are interpreted and entered into Environment Canada's Upper Air Archive.

8.3 Results and Discussion

8.3.1 Meteorological Conditions

The polar vortex dominates the winter dynamics of the stratosphere and has a profound effect on the distribution of chemical constituents. Before analyzing the evolution of the trace gas columns above Eureka, it is useful to know what the meteorological conditions were during the 2010/2011 winter-spring. Since the northern hemisphere polar vortex can be highly variable on both horizontal and vertical spatial scales throughout its life cycle, it is important to determine the vortex edge evolution on multiple heights in the atmosphere. The vortex edge was determined using the Q-diagnostic and the algorithm developed by *Harvey et al.* [2002], an algorithm widely used to characterize the polar vortex [*Chshyolkova et al.,* 2007; *Manson et al.,* 2008; *Xu et al.,* 2009]. The scalar quantity Q is a measure of the relative contribution of strain and rotation in the wind field, derived from the Met Office (MetO) analyses [*Swinbank and O'Neill,* 1994]. To identify the vortex edge, Q was integrated along the stream function contours. A detailed description of the Q-diagnostic method can be found in *Fairlie* [1995] and *Harvey et al.* [2002] and references therein.

Figure 8.2 shows the vortex edge on isentropic surfaces corresponding to potential temperatures from 450 K to 1000 K (~18 to 35 km, coinciding with the levels that contribute significantly to the 125HR column measurements) for three days of our measurement campaign. The first panel corresponds to day 54 (February 23), the day when the ACE validation campaign started. We see that the vortex has a shear with height towards the south, being above Eureka at all altitudes. The second panel corresponds to day 69 (March 10), a day when the vortex core was centered above Eureka and the vortex edges at each altitude were almost aligned. The last panel corresponds to day 84 (March 25), when the vortex edges displayed significant shear with altitude. The vortex edge had then moved over Eureka, with the lower part of the vortex elongated relative to the upper region. A movie showing the evolution of the vortex above Eureka can be found at http://www.usask.ca/physics/ isas/vtex11jfm.gif, and is included as supplementary material in *Lindenmaier et al.* [2011b].
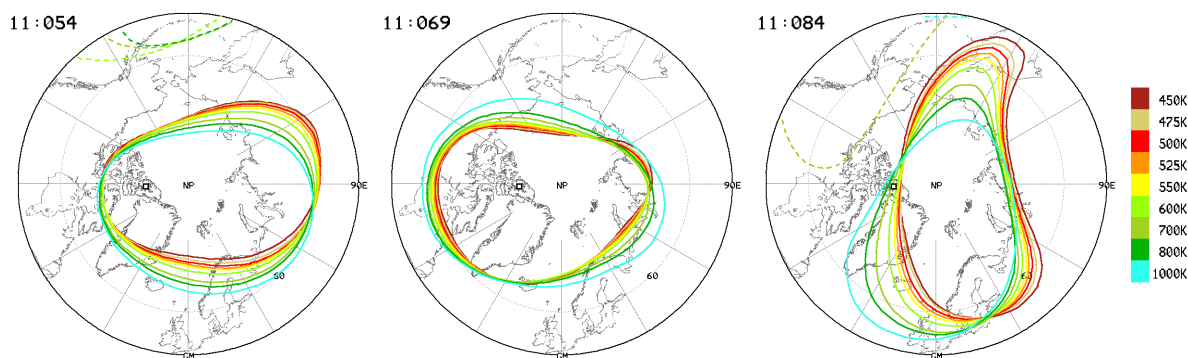
Figure 8.2. MetO vortex edges calculated using the Q-diagnostic for potential temperature surfaces from 450 to 1000 K. Solid colored lines show the cyclonic, dashed lines the anti-cyclonic, contours for these levels. On the left upper side of each map, the day of the year (2011) is specified. The black square indicates the location of Eureka. The southern boundary is at 50ºN. (Figure courtesy of Chris Meek and Alan Manson, University of Saskatchewan)

On day 37 (February 6), the vortex moved above Eureka and stayed above our site until day 83 (March 24). Figure 8.3 shows the temperatures on the 525-K isentropic surface (~21 km altitude) with a 5-K contour interval, and the black solid line gives the edge of the vortex for the same level. The first panel corresponds to day 54 (February 23), the first day of the 125HR measurements. The following panels have a 5-day time step, and the last panel corresponds to day 96 (April 6), the last day of the campaign. A second movie showing the full evolution of the temperatures during winter-spring can be found at http://www.usask.ca/physics/isas/ tk10-11.gif, and is also included as supplementary material in *Lindenmaier et al.* [2011b].

The minimum temperatures during the winter/spring 2010/2011 were persistently cold, staying below the PSC formation threshold for more than 100 days [*Manney et al.,* 2011]. On the 525-K level, temperatures within the vortex first dropped below the type I PSC threshold (195 K, essentially the same for STS and NAT) on day 330 of 2010 (November 27) and continued to decrease (as shown in the movie). It dropped below 190 K (the precision is limited by the temperature step of 5 K in the plots) on day 353 (December 20) staying low until January 11. On day 21 in 2011 (January 21), the temperature again fell below 190 K until day 60 (March 1) except on days 17, 18, and 31-35 (January 17, 18 and January 31-February 4). The temperature continued to oscillate between 190 and 195 K from day 60 (March 1) to day 90 (March 31), when the temperatures increased above 195 K, and remained above this threshold for the remainder of the spring [*Manney et al.,* 2011].
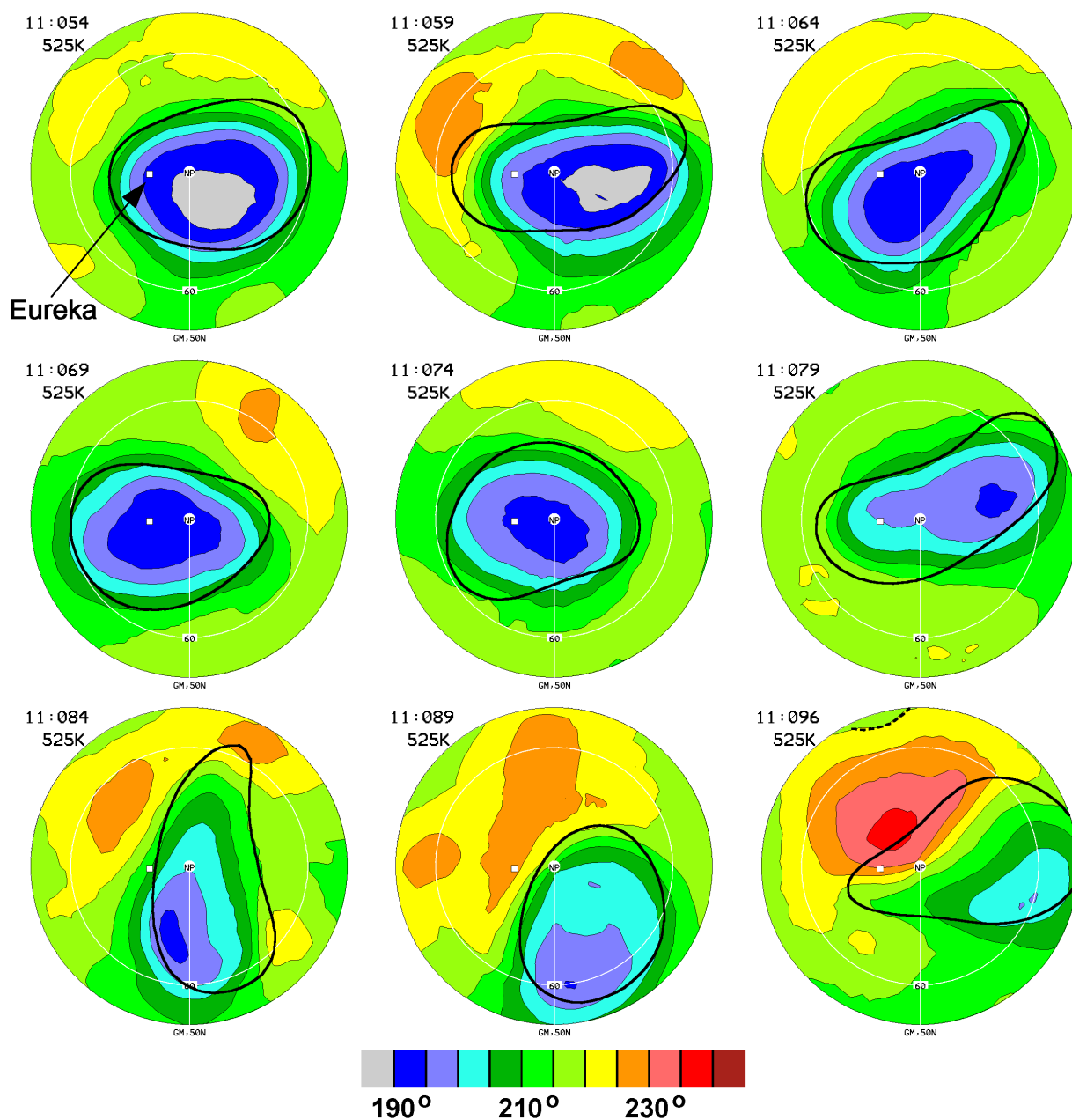
Figure 8.3. MetO 5-K temperature contours for the 525-K potential temperature level (color-coded as shown in the legend), with overlaid vortex edge for the same level (black solid line). These contours correspond to the days shown on the top left side of each map. The white square indicates the location of Eureka, while the white circle indicates the 60ºN latitude. The southern boundary is at 50ºN. (Figure courtesy of Chris Meek and Alan Manson, University of Saskatchewan).

8.3.2 Temperature and PSC Observations

Since the vortex was above Eureka for much of the winter, the evolution of the temperatures on the 525-K isentropic surface above our site was similar to the description above. Figure 8.4 shows the evolution of the temperature on the 525-K isentropic surface obtained from the MetO analyses for Eureka (green squares), along with the temperatures at 21 km measured by radiosondes launched at Eureka (black circles). Just prior to our measurement campaign, the vortex moved above Eureka on day 38 (February 7) and the temperature dropped below 195 K. It reached 188 K for seven consecutive days, 41-47 (February 10-16), then varied, but generally remained below 195 K until day 77 (March 18). This persistence of temperatures below typical PSC thresholds into late March conditioned the atmosphere for chemical O$_3$ loss [*Manney et al.,* 2011].
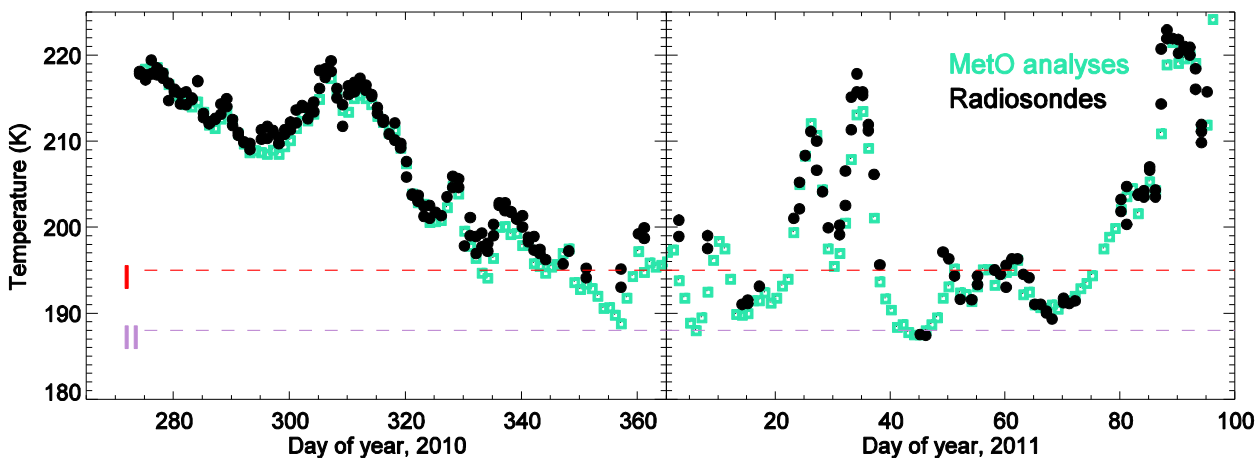
Figure 8.4. The temperature over Eureka on the 525-K isentropic surface derived from the MetO analyses (green squares) and from the radiosondes at 21 km, launched twice a day (black circles). The two dashed horizontal lines correspond to the threshold temperature values for the formation of PSC type I (red) and type II (purple).

The Eureka radiosonde temperature profiles, presented in Figure 8.5, show the evolution of temperature at each altitude during February (top panels) and March (bottom panels). For each month, these are split into three periods for clarity. The type I and II PSC threshold temperatures are also shown. From February 7 to the end of the month, the temperature dropped below the type I PSC threshold at altitudes of ~17 to 24 km, reaching the type II PSC threshold from 20 to 23 km on February 14 and 15. NASA's Cloud-Aerosol Lidar and Infrared Pathfinder Satellite Observation (CALIPSO) showed the presence of PSCs near Eureka between February 11 and 17

between 18 and 23 km (not shown, images can be found at: http://www-calipso.larc.nasa.gov/ products/lidar/browse _images/show_calendar.php).

The CRL was not operational at that time (it started operation on February 20), but indicated the presence of PSCs above Eureka during March (Figure 8.6). The backscatter ratios at 532 nm for March 8-12 show that the cloud has two dominant layers centered at 15 and 18 km. The mean backscatter ratio of the background aerosol at 11-13 km, where the temperatures were greater than 200 K was 1.13 ± 0.1. This was taken as the background aerosol backscatter ratio for comparison with the clouds, whose backscatter ratio varied between 1.3 and 2.3. The clouds had a depolarization ratio of approximately 10% and this, along with the enhanced backscatter ratio, indicates mixed-phase type I PSCs during this period [*Pitts et al.,* 2009]. As can be seen in Figure 8.5, the temperatures from 15 to 24 km during this period were below the threshold for type I PSC formation but above that for type II clouds. PSCs were observed by the CRL as late as March 18 (not shown), much later into the season than PSCs are usually seen in the Arctic [*Langematz and Kunze,* 2006].

8.3.3 Total Column Measurements

In 2011, the 125HR began acquiring data on February 23 and results are reported here through April 6, the end of an intensive period of measurements that were made as part of the Canadian Arctic ACE Validation Campaign. There are some gaps in the data, particularly in late March, due to cloudy and unsettled weather. From these measurements, O$_3$, HCl, HF, HNO$_3$, and ClONO$_2$ vertical profiles were retrieved, and total columns were calculated. The results are discussed and compared with total columns from previous years.

Figure 8.7 shows the evolution of the scaled potential vorticity at Eureka for each year. For 1997-2006 (years with daily average DA8 measurements), sPV was calculated daily at 12 UT using MERRA (Modern Era Retrospective-analysis for Research and Applications) analyses [*Reinecker et al.,* 2011] for the 21-km altitude above Eureka. For 2007-2011 (years with 125HR measurements), sPV was calculated at 21 km along the 125HR line-of-sight using the GEOS version 5.2.0 (GEOS-5) analyses [*Reinecker et al.,* 2008] and is only shown for days with 125HR measurements. An sPV of 1.2×10^{-4} s^{-1} was used as proxy for the outer edge of the polar vortex and sPV of 1.6×10^{-4} s^{-1} was used for the inner edge [*Manney et al.,* 2007]. While during some years, the instruments sampled mostly inside the polar vortex (*e.g.,* 1997, 2000, 2004,

2005, 2007, 2011), for other years they measured mostly outside the vortex (*e.g.,* 1999, 2001, 2008, 2009, 2010).
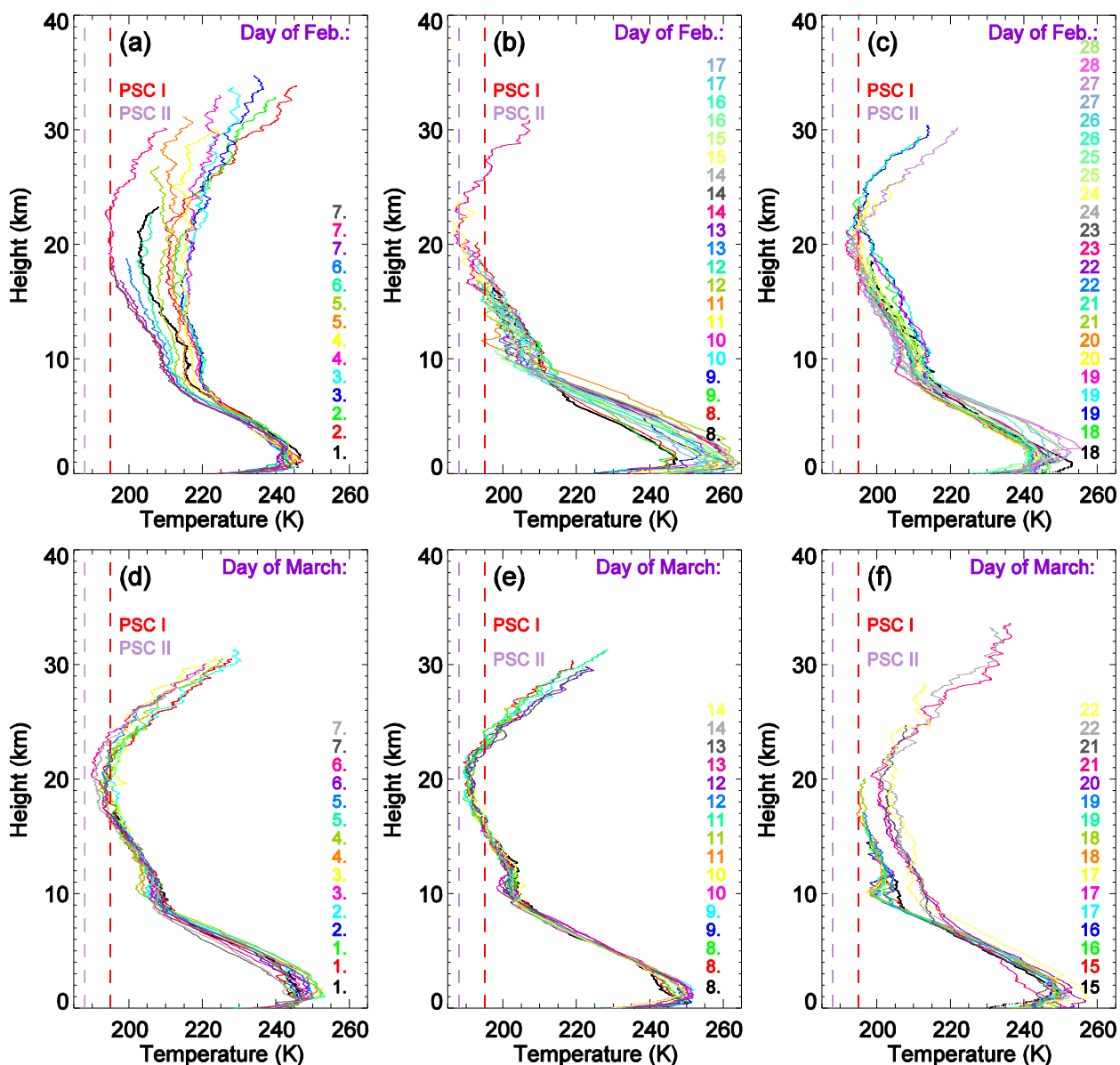
Figure 8.5. Radiosonde temperature profiles for February 1 to 28 (panels (a)-(c)) and March 1 to 22 (panels (d)-(f)). The day is shown on the right side of each panel, color coded. The two dashed vertical lines correspond to the threshold temperature values for the formation of type I (red) and type II (purple) PSCs at a water vapor pressure of (3-5)x10^{-4} hPa, corresponding to approximately 16 km [*Jacob*, 1999]. The division of days per plot was chosen to make the temperature drop below PSC type I or PSC type II thresholds more visible.
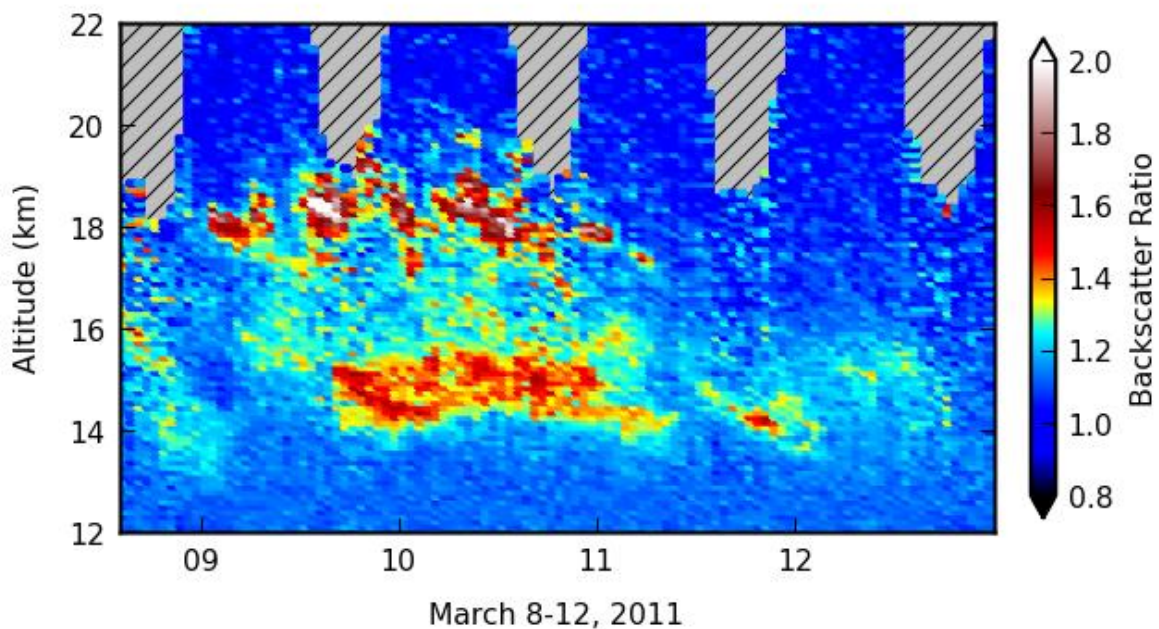
Figure 8.6. Backscatter ratio at 532 nm as measured by the CRL for March 8 to 12. The hashed areas represent data that were considered to be noise. (Figure courtesy of Chris Perro, Graeme Nott, and Tom Duck, Dalhousie University)

Figure 8.8 shows total columns of the gases mentioned above, along with the evolution of the sPV on measurement days in 2011, derived at locations along the 125HR line-of-sight for the 18, 20, 22, and 26 km altitude levels spanning the lower stratosphere. For all these levels, we find that in 2011 our sampled air masses were well inside the vortex from the start of the measurements until day 78 (March 19). For the remainder of the campaign, the 125HR sampled through the edge of the vortex or outside, except on day 86 (March 27) and days 95 and 96 (April 5 and 6). The gray shading highlights the days in 2011 when the instrument sampled air masses on the edge or outside the vortex. Note that the daily sequence of MetO images that shows the vortex edge (Q-diagnostic) for days 50 to 100 on the 525-K surface (Figure 8.3) agrees very well with the combination of GEOS-5/sPV used in the remainder of the analyses shown in this chapter. For days 53 to 84 and 88 to 93, both vortex-edge methods agree in showing Eureka inside and outside the vortex, respectively. The only mild disagreement occurs on day 87, when the combination of GEOS-5 with sPV contours indicated Eureka inside the
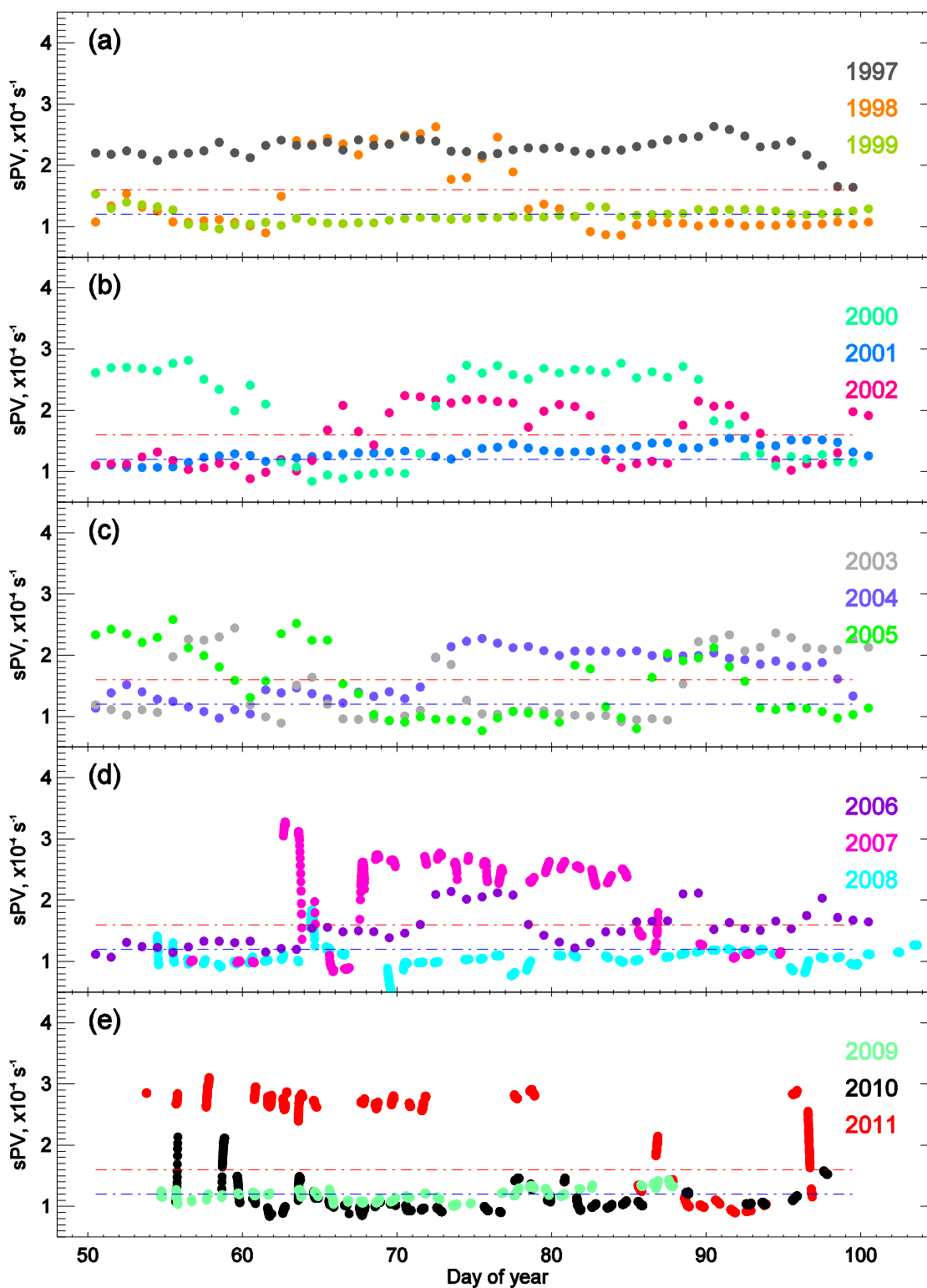
Figure 8.7. Scaled potential vorticity at 21 km above Eureka for 1997 to 2011 as described in the text. The red and blue dot-dash lines show the inner (red) and the outer (blue) vortex edge, respectively.
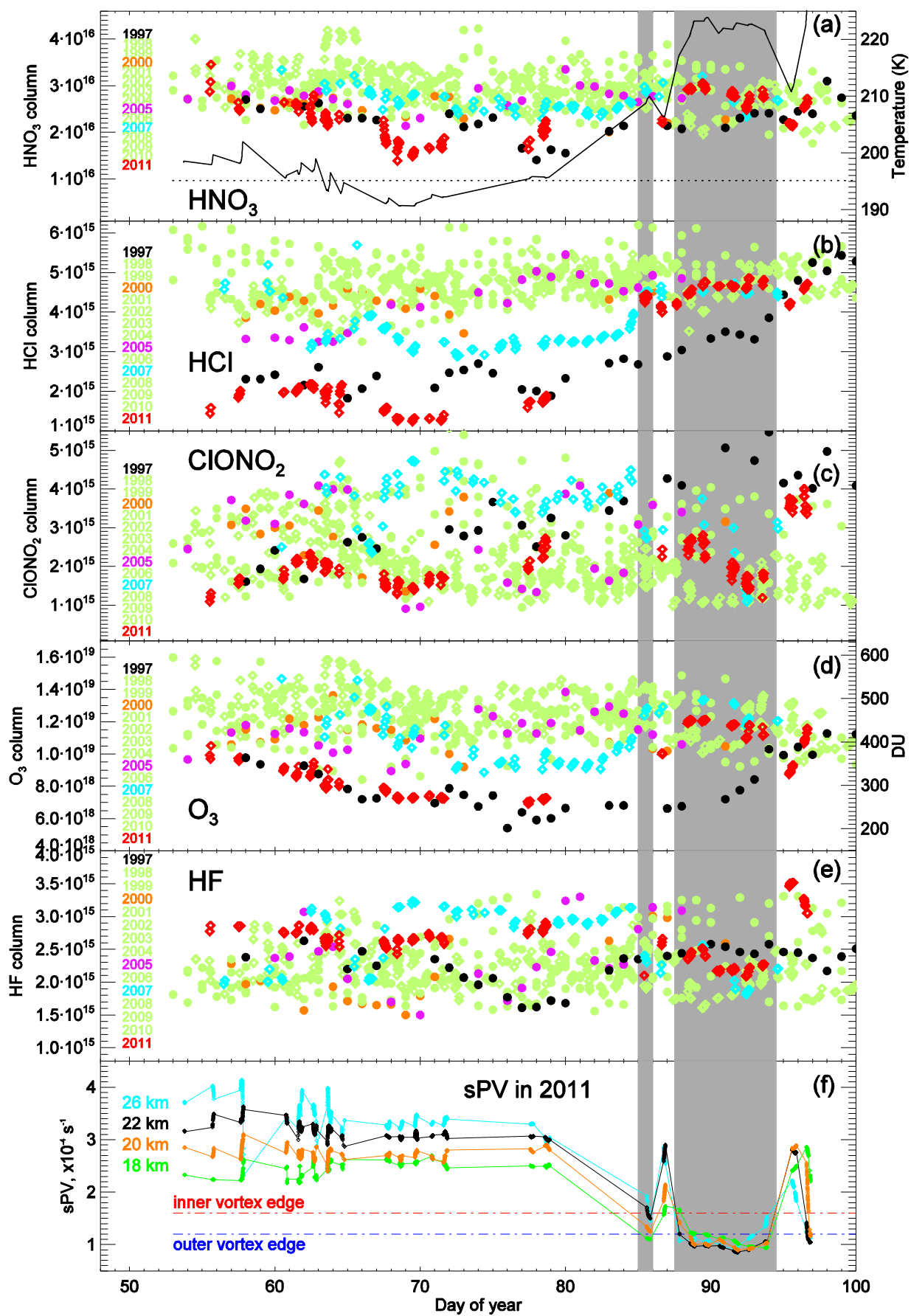
Figure 8.8. From (a) to (e) spring time series of HNO$_3$, HCl, ClONO$_2$, O$_3$, and HF total columns (molec cm^{-2}) from 1997 to 2011. Filled circles represent DA8 measurements and open diamonds represent 125HR measurements. The colors correspond to different years as shown in the legend. For O$_3$, panel (d), the left y-axis gives the column amounts in molec cm^{-2}, while the right y-axis gives the column amounts in Dobson units (DU). Panel (a) also shows the evolution of the temperature at 21 km along the line-of-site for the 2011 measurements at Eureka (black solid line) and the threshold temperature value for the formation of type I PSCs (black dotted line). Panel (f) shows the evolution of the sPV along the line-of-sight for the 18, 20, 22, and 26 km altitude levels, color-coded as shown in the legend. These values correspond to our measurements only; sPV values for days when measurements were not acquired are not shown. The red and blue dot-dash lines show the inner (red) and the outer (blue) vortex edge, respectively. The gray shading highlights the days when the instrument sampled air masses on the edge or outside the vortex.

vortex or on the edge depending upon the height (Figure 8.8), while both GEOS-5 and MetO using the Q-diagnostic at 525 K (~21 km) showed Eureka on the edge.

The 2011 gas-phase HNO$_3$ total columns, Figure 8.8(a) red diamonds, decrease slowly until day 64 (March 5), followed by a sharp decrease with a minimum on day 68 (March 9) and low values until day 77 (March 18). The instrument sampled air inside the vortex through all these days. The solid black line represents the temperature along the line-of-sight at 21 km. The minimum HNO$_3$ column occurs at the time when the temperature was well below the type I PSC temperature threshold, indicating that HNO$_3$ had been taken up onto the surfaces of (liquid or solid) PSC particles. The minimum HNO$_3$ total column is 1.39×10^{16} molec/cm^2, approximately the same as the 1997 (black circles) minimum seen on day 78 (March 19). The minima measured during these two years stand out from the HNO$_3$ total column values measured during the 15 years. 2000, 2005 and 2007 are also highlighted as these three years were cold and characterized by chemical ozone depletion [*Jin et al.,* 2006; *Rösevall et al.,* 2007, 2008; *WMO,* 2007, 2011].

The evolution of the chlorine reservoir HCl is shown in Figure 8.8(b). The 2011 total columns are persistently lower than all previous years for days 55-78 (February 24-March 19). The 2011 HCl total columns reached minima of ~1.2×10^{15} molec/cm^2 on days 68-71 (March 9-12), indicating chlorine activation, and then gradually increased. Beginning on day 77, the chlorine slowly converted back into its reservoir form, as shown by the recovery of HCl inside the vortex. This recovery continued until the last day of measurements. For comparison, in 1997 the maximum reduction in HCl occurred on day 64 (March 5). For the other years, no extreme

values were observed, although some low values can be seen for days 58 (February 27) to 65 (March 6) and 68 (March 9) to 83 (March 24) in 2005 and 2007, respectively.

Total columns of the second chlorine reservoir, $ClONO_2$, are shown in Figure 8.8(c). The minima seen for 2005 correspond to measurements outside the vortex, as shown in Figure 8.7(c). The 2011 values are in the lower range of columns measured over the past 15 years. At the beginning of the campaign, the $ClONO_2$ total columns are close to the values measured in 1997. After day 59 (February 28) the 1997 total columns increase, while the 2011 ones remain low, increasing on day 77 (March 18). Note that during days 68-71, there is a small decrease in the $ClONO_2$ column, which coincides with the HCl decrease and suggests that chlorine activation is occurring. The increase on day 77 that persisted inside the vortex until the end of the campaign shows the conversion of active chlorine to its reservoir form. When PSCs can no longer form and the active chlorine reverts to its reservoir species, the resulting repartitioning of the chlorine in the Arctic typically results in enhanced $ClONO_2$ and sustained low values of HCl for some time after PSCs have disappeared [*Santee et al.,* 2008]. The enhancement in $ClONO_2$ is due to the reaction of NO_2 with ClO, which is more rapid than the competing reaction of active chlorine to form HCl, and is followed by a slow repartitioning between $ClONO_2$ and HCl over the coming weeks. However, in 2011, the conversion of active chlorine back into these reservoirs was simultaneous, differing from the usual repartitioning (resembling the Antarctic). This suggests that the NO_2 necessary for $ClONO_2$ to form was less abundant than in previous years, possibly due to permanent removal through PSC sedimentation [*Manney et al.,* 2011].

Figure 8.8(d) shows the evolution of O₃ total columns. The columns slowly decrease, with the lowest O₃ column seen on day 77, being 6.9×10^{18} molec/cm^2 (257 DU). This minimum follows after the chlorine activation and is consistent with chemical ozone destruction. However, the unusually persistent cold in 2011 would have resulted in lower column ozone than in most previous Arctic winters even in the absence of chemical loss [*Petzoldt,* 1999; *Manney et al.,* 2011]. The evolution of column ozone in 1997 was dominated by dynamical effects [*Petzoldt,* 1999] and the chemical ozone loss was modest in that year. The 1997 O₃ total columns slowly decrease in the first half of the interval, followed by the ozone minimum on day 76 (March 17) and then by a gradual recovery. For 1997, the minimum value is 5.4×10^{18} molec/cm^2 (201 DU). Low O₃ was also seen in 2007, when the 125HR sampled inside the vortex for approximately two weeks (as shown in Figure 8.7(d)), but those total column values are ~100 DU larger than the 2011 total columns. For the other years, both day-to-day and interannual variability are

observed (being in agreement with the evolution of the vortex above Eureka shown in Figure 8.7 for each year), but none of the minima are as pronounced as those in 1997 and 2011.

HF is a long-lived tracer of vertical motion in the stratosphere [*Mankin et al.,* 1990; *Toon et al.,* 1992]. It is produced in the stratosphere through photodissociation and is chemically unreactive. If an air column is displaced downward, with replacement at the top by air from neighbouring columns, then the total column abundance of HF will increase. Since the air inside the vortex is isolated from that at midlatitudes and undergoes descent, for all air masses sampled inside the vortex we expect the HF total columns to be larger than those outside the vortex. During 2011, HF total columns (Figure 8.8(e)) are large and relatively constant through days 55-83 (February 24-March 24) when the instrument sampled air masses inside the vortex, decreasing and then increasing after day 84 (March 25) as the instrument sampled air outside and then inside the vortex, respectively.

8.3.4 Normalizing with HF

Because dynamical effects usually dominate the evolution of the column ozone in the Arctic, in order to assess the degree to which changes in the total columns of ozone, HCl, HNO_3, and $ClONO_2$ are due to chemical processing, we normalized the measured total columns of these species with the HF columns. HF is a good dynamic tracer; the VMR profiles of O_3, HCl, HNO_3, and $ClONO_2$ correlate well with the HF profile in the lower stratosphere, where most of their column abundances reside, so that vertical transport will change their vertical column abundances proportionally. Another important advantage is that there is very little tropospheric contribution to the HF total column, which could otherwise mask variations due to stratospheric transport.   Thus, the normalization with HF removes many of the dynamical effects, such as diabatic descent and tropopause height changes [*Toon et al.,* 1999; *Mellqvist et al.,* 2002].

Figure 8.9 shows the normalized total columns of HNO_3, HCl, $ClONO_2$, and O_3. The shaded area highlights the days of 2011 when the instrument sampled the air on the edge or outside the vortex (as in Figure 8.8). We assume that if the normalized value for any of these gases decreases inside the vortex, this is due mainly to chemical processes.

For 2011, the HNO_3/HF ratios (Figure 8.9(a)) have the same evolution as the HNO_3 total columns in Figure 8.8(a). The slow decrease in the normalized HNO_3 values from the beginning of the measurements to day 64, followed by the sharp decrease on day 68, is of microphysical origin and confirms that HNO_3 was taken up onto the surfaces of PSC particles. For 2000, the

low normalized HNO₃ total columns between days 80 and 90 correspond to days when the instrument sampled inside the vortex. The same is true for 2005, days 81-82, and 2007, days 68 to 83, but none of these low values are as pronounced as those seen in 2011.
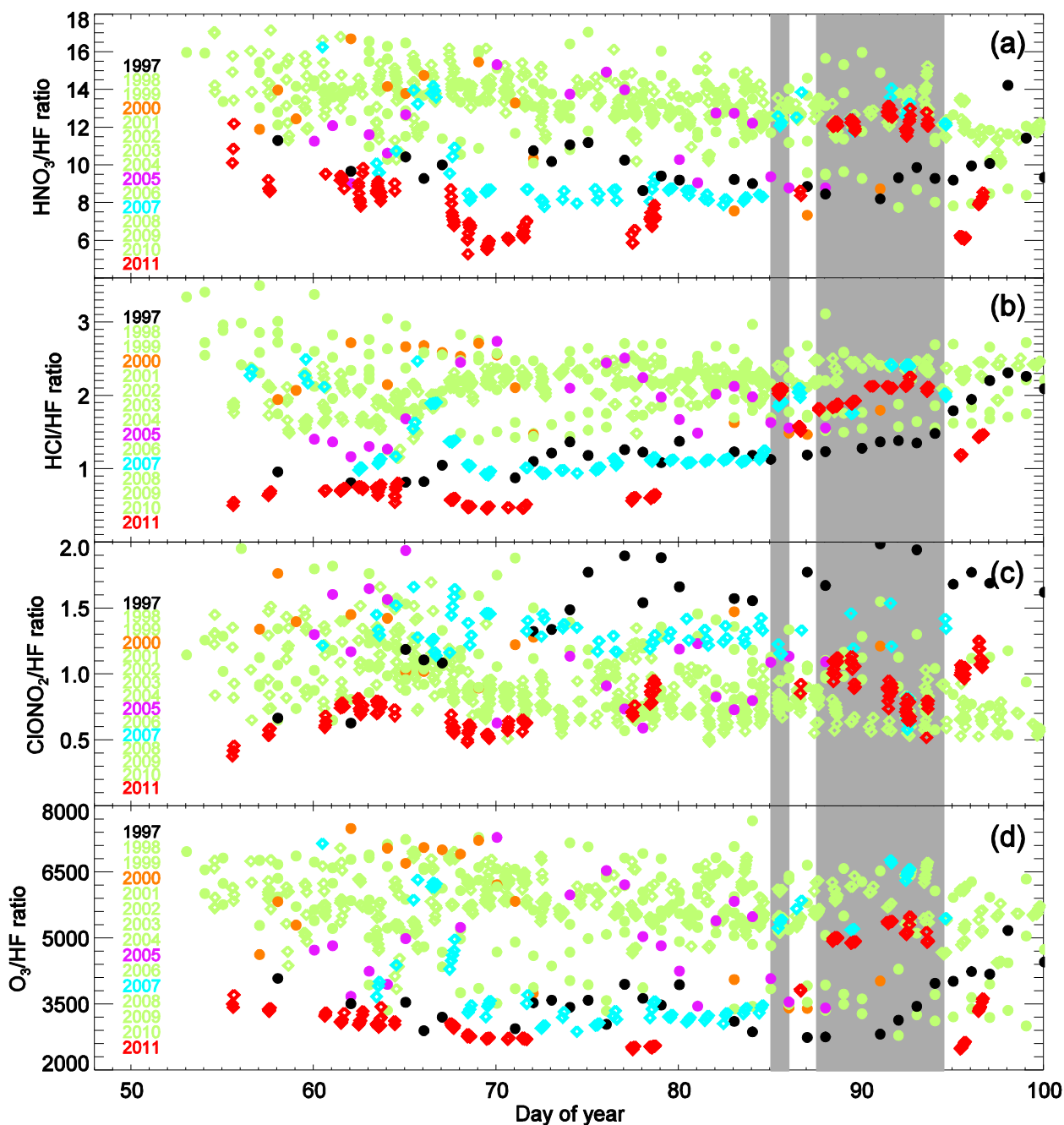
Figure 8.9. Spring time series of (a) HNO₃, (b) HCl, (c) ClONO₂, and (d) O₃, normalized by HF total columns, from 1997 to 2011. Filled circles represent DA8 ratios and open diamonds represent 125HR ratios. The colors correspond to different years as shown in the legend. The gray shading has the same meaning as in Figure 8.8.

The HCl/HF and ClONO$_2$/HF 2011 ratios (Figure 8.9(b) and (c), respectively), exhibit behavior similar to the total columns shown in Figure 8.8 (b) and (c). Low values are again seen for days 68-71 (March 9-12), and are evidence of chemical activation on the surfaces of PSC particles. After day 77, the normalized values slowly increase, as the active chlorine returns into the reservoir species HCl and ClONO$_2$. In 1997 and 2007, for measurements within the vortex, the HCl/HF ratios are lower (except for 2011) while the ClONO$_2$/HF ratios are higher than during other years. These show the overshoot of ClONO$_2$ when the active chlorine returns into this reservoir.

The O$_3$/HF ratio maintains its very low values, being consistently below 4000 for days 55-78 (February 24-March 19), and much lower than most of the normalized O$_3$ values from previous years. These low values are evidence of chemical O$_3$ depletion given the meteorological conditions and all observations presented above. The minimum normalized value is 2489 and occurs on day 77 (March 18), right after the period when we see the chlorine activation. Ozone inside the vortex remains low, the normalized O$_3$ value on day 95 (April 5) when the instrument again sampled vortex air masses, is as low as 2503. The ratios are much higher for the measurements performed outside the vortex, as highlighted by the shaded region. For the other cold years, the normalized ozone values are also low within the vortex, with 1997 and 2007 values being close to those in 2011 for some days, but none of them smaller than those seen in 2011.

To conclude, normalizing with HF reduced the dynamical effects, thus highlighting interannual differences due to chemistry. The low values of normalized HNO$_3$, HCl, and ClONO$_2$ that occurred on days 68-71 followed by the minimum in normalized O$_3$ that occurred on day 77 are indicative of chlorine activation on cold aerosol particles followed by chemical ozone destruction. Since the 125HR is a sun-dependent instrument, we do not have measurements inside the vortex from times without chemical loss (late in the fall and during the polar night), and so we are not able to define a baseline for quantifying chemical loss using only measurements. Therefore we chose to use the model passive subtraction method.

8.4 Comparisons with a Chemical Transport Model

SLIMCAT [*Chipperfield,* 2006] is a three-dimensional off-line chemical transport model. It differs from a general circulation model in that the chemistry component is not integrated into the dynamical model, but is off-line and performed separately for each time-step. This model has

been used for many studies of ozone and ozone-related gases in the polar regions [*e.g.*, *Chipperfield and Jones,* 1999; *Solomon et al.,* 2002; *Feng et al.,* 2007; *Manney et al.,* 2009a; *Feng et al.,* 2011]. The model uses winds and temperatures from meteorological analyses of the European Centre for Medium-Range Weather Forecasts (ECMWF) to specify the atmospheric transport, and calculates the abundances of chemical species in the troposphere and stratosphere.

Figure 8.10 shows, from top to bottom, the SLIMCAT (blue triangles) and the 125HR (red diamonds) total columns of O_3, HCl, HNO_3, $ClONO_2$, and HF, along with the corresponding percentage differences. SLIMCAT simulations are compared with 125HR measurements for days 55 to 96 (February 24-April 6). Good agreement can be seen for O_3 (panel (a)) except on days 86-93 (March 27-April 3), when the model total columns are slightly larger than the 125HR total columns likely due to model resolution smoothing over the vortex edge. The mean difference was calculated as

$$\Delta\% = \frac{100}{N} \sum_{i=1}^{N} \left[\left(MODEL_{TC}^{(i)} - 125HR_{TC}^{(i)} \right) / 125HR_{TC}^{(i)} \right] \qquad (8.1)$$

where $125HR_{TC}^{(i)}$ is the total column measured by the 125HR and $MODEL_{TC}^{(i)}$ is the total column simulated by the model, for day i, N is the number of coincidences. For O_3, we found a mean percentage difference of 7.8±0.3%, where the given error is the standard error of the mean, which provides a measure of the significance of an observed bias [*De Mazière et al.,* 2008].

For HCl, the agreement between SLIMCAT and the 125HR total columns is good for the entire period, the mean percentage difference being 1.9±0.04%. The modeled HNO_3 total columns show a negative bias -23.8±0.1% compared to the measurements, more pronounced at the beginning of the measurement period. This may indicate a limited treatment of the PSCs in the model. For $ClONO_2$, we have good agreement except on days 86-93 (March 27-April 3) as in the case of ozone. For these days, SLIMCAT total columns are larger than those for the 125HR. The mean percentage difference calculated for all the data is 10.4±0.2%.

The HF total columns for the 125HR and for the model exhibit similar evolution from days 55 to 96 (February 24 to April 6), but there is a positive bias in the simulated values, SLIMCAT total columns being larger by 19.5±0.1%. SLIMCAT overestimates the total column abundance of HF in the lowermost stratosphere, the result being a positive bias compared to the measurements. A similar result, 22.54±6.55% (here ±1σ), was found by *Duchatelet et al.* [2010], who compared SLIMCAT HF total columns with mid-latitude ground-based FTIR total columns, for the 1984-2009 period.
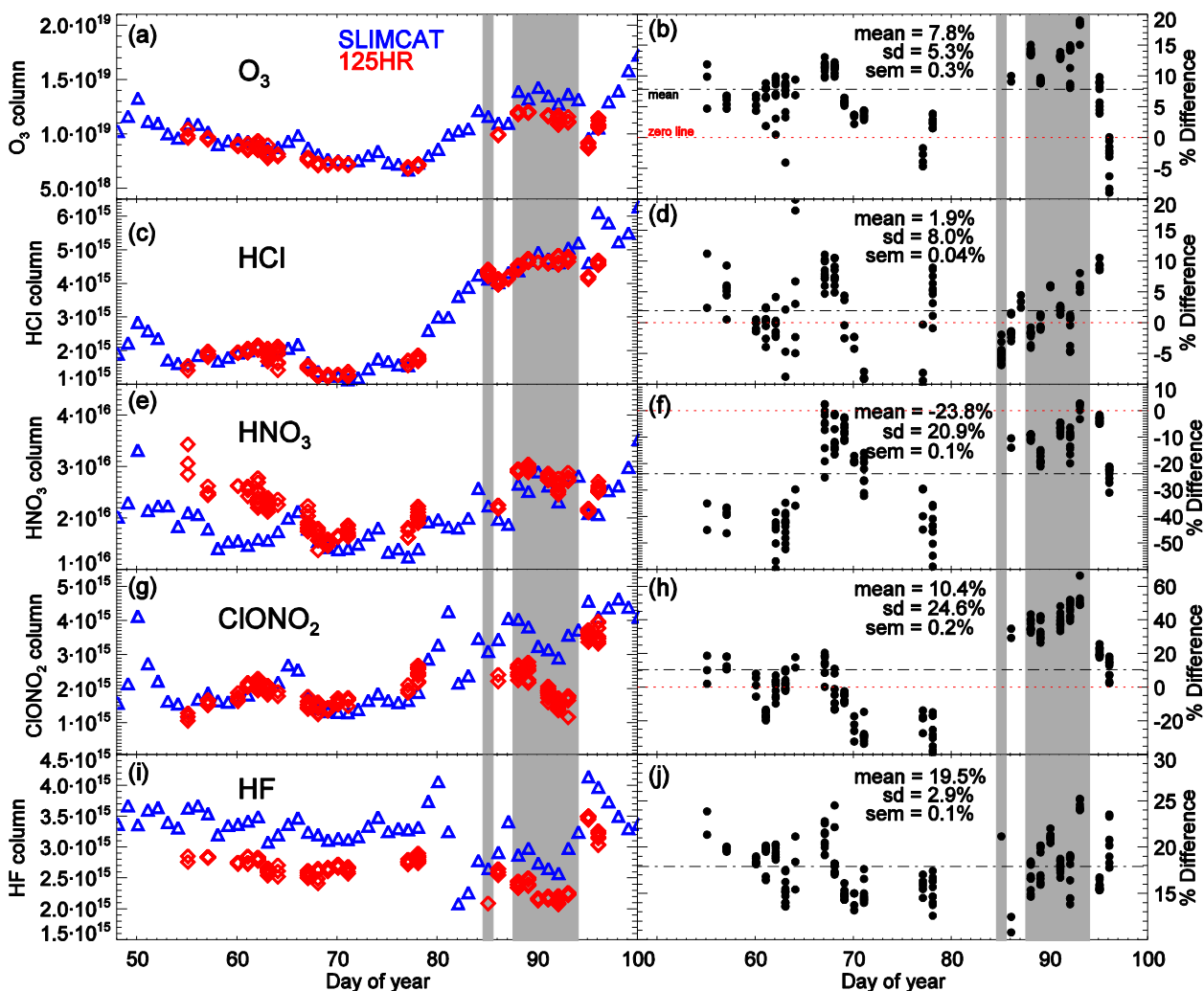
Figure 8.10. 125HR (red diamonds) and SLIMCAT (blue triangles) total column comparisons for O₃, HCl, HNO₃, ClONO₂, and HF. In the panels on the left side, the total columns for each gas are shown for the measurements and the model, while in the panels on the right side the corresponding percentage differences are shown. The mean percentage difference, the standard deviation, and the standard error of the mean are also given. These were calculated as shown in the text. The gray shading has the same meaning as in Figure 8.8.

To quantify chemical ozone loss, we used SLIMCAT and the passive subtraction method. SLIMCAT can be run in two modes: one with full chemistry and dynamics (the "active" run) and one in which ozone is treated as a passive dynamical tracer with no chemistry (the "passive" run). In this method, differences between the measured ozone total columns and those from the passive model runs are assumed to be due to chemistry [*Manney et al,* 1995; *Goutail et al.,* 1999; *Feng et al.,* 2005].

The SLIMCAT active O_3 total columns are shown together with the passive O_3 total columns in Figure 8.11(a). While at the beginning of January there is no significant difference between the two time series, they begin to diverge in mid-January, reaching a maximum difference on day 80 (March 21). The differences vary from day 81 (March 22) to the end of the period, with a second maximum difference on day 95 (April 5). The evolution of the differences between the passive and active SLIMCAT O_3 (blue squares) can be seen in Figure 8.11(b). The maximum difference of 266 DU was reached on day 95 (April 5). The difference between the 125HR measured total columns and the SLIMCAT passive O_3 are shown with red circles. These differences are slightly higher than the passive-active SLIMCAT differences. The maximum difference in this case was reached on the same day, day 95, being 276 DU and 3.6% higher than the model maximum.

The corresponding percentage difference between the passive and active SLIMCAT O_3 is shown in panel (c). To quantify the ozone loss inside the vortex, we calculated the mean percentage difference, excluding the days when the instrument sampled out of the vortex. The mean percentage difference which represents the chemical ozone depletion above Eureka from February 23 to April 6 is then 35%.

8.5 Conclusions

As a consequence of dynamically variable meteorological conditions, springtime Arctic ozone levels exhibit significant interannual variability in the lower stratosphere. Meteorological conditions during winter/spring 2011 were particularly favorable to the formation of a strong vortex that lasted into April. Temperatures above Eureka were persistently low, and below the type I PSC threshold in the lower stratosphere for an extended period. PSCs were observed over Eureka by CALIPSO and by the CRL between February 11 and 17 and between March 8 and 12, respectively.

The spring 2011 O_3, HCl, HNO_3, $ClONO_2$, and HF total column measurements made at Eureka using the Bruker 125HR FTIR are consistent with the occurrence of significant chemical ozone depletion. Unusually low ozone columns were measured from mid-February to late March compared to the previous 14 years. The normalized O_3/HF, HCl/HF, and HNO_3/HF ratios, for which the effects of dynamics are reduced, also showed record minima over this period. The normalized HNO_3 columns decreased during the period when temperatures were below the PSC type I formation threshold. The normalized HCl and $ClONO_2$ columns also decreased during the

same period, indicating chlorine activation. The normalized ozone columns showed minima immediately after the chlorine activation period, confirming the occurrence of ozone chemical processing.
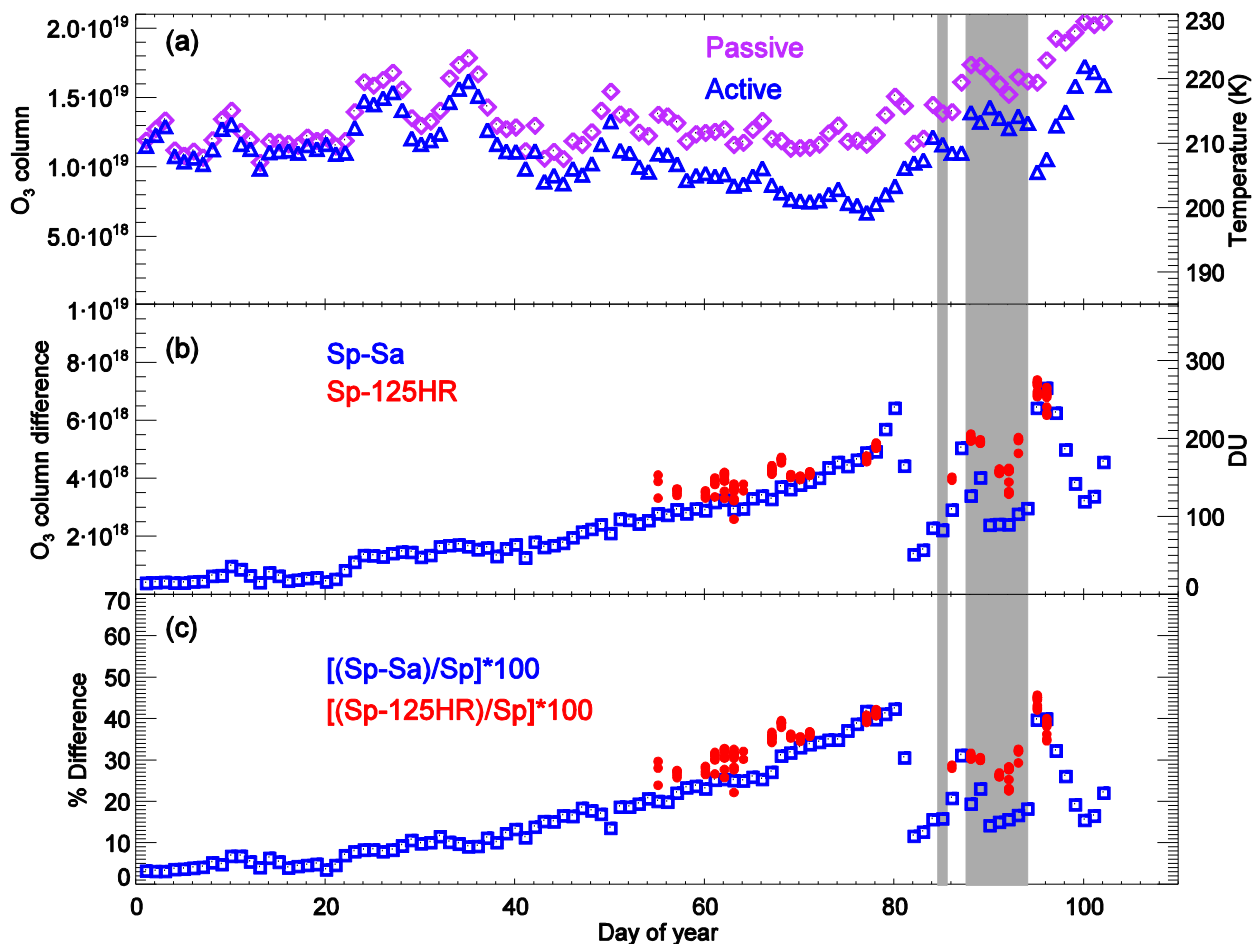
Figure 8.11. (a) Passive (purple) and active (blue) SLIMCAT O$_3$ total columns. (b) The difference between the passive (Sp) and active (Sa) SLIMCAT O$_3$ columns (blue squares) and the differences between the passive (Sp) SLIMCAT O$_3$ and the measured (125HR) total columns (red circles). Panel (c) is similar to panel (b), but for the percentage differences calculated for the two cases. The gray shading has the same meaning as in Figure 8.8.

The SLIMCAT and 125HR total columns showed good agreement for O$_3$, HCl, and ClONO$_2$, with large differences for HNO$_3$ and HF. SLIMCAT was used to quantify chemical ozone loss using the passive subtraction method. Chemical ozone depletion inside the vortex above Eureka was estimated to be 35%.

Chapter 9

General Conclusions and Perspectives

This chapter summarizes the results presented in this thesis and describes how they contribute to our scientific knowledge. In addition, ideas for how to further extend this study are proposed.

9.1 Research Summary

Ground-based FTIR spectroscopy is a powerful technique for the study of the lower atmosphere, allowing the retrieval of the abundances of more than 30 different trace gases. The new CANDAC high-resolution Fourier transform spectrometer, the Bruker 125HR, installed at PEARL at Eureka in July 2006, expanded our measurement capabilities for studies of Arctic atmospheric composition throughout the sunlit part of the year, replacing the old Bomem DA8 FTIR spectrometer. The location of Eureka is of particular importance to the global NDACC FTIR network as it provides measurements in the High Arctic, and complements the satellite data. After a formal certification process, the 125HR was approved in January 2009 as the new NDACC instrument at Eureka.

The SFIT2 v3.92c retrieval algorithm was implemented to combine the information contained in the recorded spectra with the best *a priori* knowledge to produce vertical profiles and total and partial columns of O_3, HCl, HNO_3, HF, $ClONO_2$, HCN, C_2H_6, CO, N_2O, CH_4, NO, and NO_2. The vertical profiles and total and partial columns were used to study springtime ozone depletion, to monitor the seasonal and interannual variability of these gases, and to validate satellite instruments and atmospheric models.

Chapter 1 presented a short history of ozone-related trace gas measurements in the polar regions. While the Antarctic ozone depletion mechanism is well understood, in the Arctic meteorological conditions are very variable and are a strong modulator of chemical ozone depletion. Chapter 2 introduced the location of Eureka and the instrument, while Chapter 3 described the retrieval tools: the Inverse Method and the retrieval algorithm, SFIT2, along with details on the input parameters and the error analysis implemented for the 125HR. The retrieval microwindows for Eureka were first developed by former graduate students (Elham Farahani, Dejian Fu) and the *a priori* profiles, S_a covariance matrices and ILC were compiled by former post-doctoral fellow Keeyoon Sung for the Bomem DA8 analyses. These were the starting points

for my research. After the 125HR was installed at Eureka, I focused on implementing the SFIT2 retrieval algorithm and the error analysis. This was done in collaboration with Dr. Rebecca Batchelor.

Subsequent chapters describe my research and contributions to science. Chapter 4 described the way in which ozone retrievals at Eureka were optimized. 22 microwindows were selected along with their corresponding interfering species based on simulations, and then compared. The microwindow providing the highest sensitivity in both the troposphere and stratosphere, and the smallest total error, was found to be in the spectral region from 1000 to 1005 cm^{-1}. Based on the analysis of the 16-year ozonesonde record at Eureka (1993-2009), the elements of the $\mathbf{S_a}$ covariance matrix were also selected (based on the 1σ) for each altitude, improving on the previously used constant 70% value.

This work was continued in collaboration with the NDACC IRWG through the harmonization initiative, as discussed in Chapter 5, for HCl, HNO_3, HF, $ClONO_2$, HCN, C_2H_6, CO, N_2O, and CH_4. The Eureka microwindows and retrieval parameters were compared with those recommended by the NDACC IRWG, with the goal of harmonizing the retrievals among all NDACC sites. The microwindow comparisons showed that while for C_2H_6 and HNO_3 the recommended microwindows were more suitable for retrievals at Eureka, for $ClONO_2$ the recommended microwindow gave worse results. For HCN and HF, the results were similar for the two sets of microwindows, while for O_3, CO, N_2O, and CH_4 the recommended microwindows were already in use at Eureka. New WACCM *a priori* profiles and covariance matrices were also provided for Eureka and they were compared during the harmonization exercise with the original Eureka parameters. The results showed that not all recommended parameters worked well for Eureka; for O_3, $ClONO_2$, and C_2H_6, the original Eureka parameters worked better than the recommended ones. For HF and HCN, the evaluation is waiting for WACCM input parameters and improved microwindows. CH_4 and C_2H_6 also need final decisions on the microwindow choice and improved linelist, respectively.

One of the objectives of the ACE satellite mission is to study ozone depletion in the Arctic. Previous validation exercises have identified the highly variable polar conditions of the spring period to be a challenge for validation efforts. In Chapter 6, comparisons between the 125HR and ACE-FTS were used to develop strict criteria that allow the ground and satellite-based instruments to be confidently compared. In brief, a time difference of less than ±12h, a spatial difference of ≤1000 km and a maximum temperature difference of <10 K between the

sampled air masses at each altitude between 15 and 40 km were the new restrictions applied. In addition, the scaled potential vorticity differences between the 125HR and ACE-FTS at each altitude along the line-of-sight were restricted to less than $0.3 \times 10^{-4}\,s^{-1}$, ensuring that the sampled air masses were similar for both measurements relative to the polar vortex edge. When these criteria were taken into consideration, the mean differences between the ACE-FTS and the 125HR were significantly reduced for most comparisons. After applying the new criteria, the mean biases between the ACE-FTS and 125HR partial columns for 2007-2010 were -5.61 to 1.11%, -0.23 to 4.86%, -15.33 to -2.86%, -4.77 to 1.09%, and -0.34 to 5.23% for O_3, HCl, $ClONO_2$, HNO_3, and HF respectively.

N_2O, the main source of stratospheric NO_y, has been described as the most important anthropogenic ozone-depleting substance emitted today, whose concentration in the atmosphere is continuously increasing. On the other hand, the stratospheric effects of climate change are predicted to reduce the NO_y/N_2O ratio, so the future evolution of NO_y is unclear. This makes measurements of long-term changes in NO_y of particular scientific interest. Chapter 7 describes a method that was developed to calculate an NO_y data product for Eureka, using the 125HR measurements. This product contains the five primary NO_y species NO, NO_2, HNO_3, N_2O_5, and $ClONO_2$, and its four-year 15 to 40 km partial column time series was used to study the NO_y seasonal and interannual variability. The mean partial column averaged for the spring period (up to day 140) was found to be $(2.5 \pm 0.2) \times 10^{16}$ molec cm^{-2}, while for the period after day 140, it was $(2.3 \pm 0.1) \times 10^{16}$ molec cm^{-2}. The springtime evolution of 5-NO_y and its constituent nitrogen species, along with sPV, was also examined for 2007 to 2010. The variability of the 5-NO_y partial columns was seen to be dominated by that of HNO_3 and the evolution of the individual nitrogen species was found to be consistent with the current understanding of the chemical and dynamical processes that occur in the polar stratosphere.

The NO_y data product obtained for Eureka was compared to three atmospheric models and the ACE-FTS. The comparison showed that the CMAM-DAS 5-NO_y partial columns were smaller than the FTIR partial columns, the mean percentage difference [100 x (model − 125HR) / 125HR] being (-16.0 ± 0.6)% (where the uncertainty represents the standard error of the mean). GEM-BACH 5-NO_y showed an agreement of (5.5 ± 1.0)%, with the model partial columns being slightly larger than the 125HR columns. For the SLIMCAT chemical transport model, the 5-NO_y partial columns were slightly smaller than the 125HR columns, the mean percentage difference being (-5.8 ± 0.4)%. For GEM-BACH and SLIMCAT, the differences were found to be within the

mean total error of 9.6%, while the CMAM-DAS difference was larger than the mean total error estimated for the 5-NO_y. For the ACE-FTS comparison, a mean percentage difference of $(5.6\pm2.3)\%$ was found, indicating that the ACE-FTS partial columns are slightly larger than the 125HR columns.

As a consequence of dynamically variable meteorological conditions, springtime Arctic O_3 levels exhibit significant interannual variability in the lower stratosphere. In the winter of 2011, the polar vortex was strong and cold for an unusually long time. The 125HR measurements from February 23 to April 6 during the Canadian Arctic ACE Validation Campaign showed unusually low O_3, HCl, and HNO_3 total column values. In Chapter 8, these measurements were compared to total columns from the previous 14 years measured by the 125HR and the Bomem DA8. To reduce dynamical effects, these total columns were normalized by the HF total column. The normalized values of the O_3, HCl, and HNO_3 total columns were smaller than those from previous years, and confirmed the occurrence of chlorine activation and chemical ozone depletion. SLIMCAT and the passive subtraction method were used to quantify the chemical ozone depletion, which was calculated as the mean percentage difference between the SLIMCAT passive ozone and the measured ozone, and was found to be 35%.

To conclude, this work has made several contributions to scientific knowledge:

- The installation of a new state-of-the-art FTIR spectrometer at PEARL with the goal of long-term measurements of stratospheric and tropospheric composition. Being semi-automated, this instrument enabled measurements of species such as O_3, NO, NO_2, HNO_3, $ClONO_2$, HCl, HF, N_2O, CH_4, C_2H_6, CO, HCN, and other gases having absorption features in the infrared domain that were not measured by other instruments at PEARL, during the sunlit part of the year (late February to late October). Long-term measurements provide a valuable data set for trend analyses (building on the previous DA8 dataset) and also for model intercomparisons and satellite validation.

- Implementation of retrievals at Eureka within the framework of NDACC.

- Submission of scientific data from August 2006 to October 2011 to the NDACC archive for public use. These data have been used in five publications in addition to the five led by Lindenmaier and Batchelor.

- Improvement of the microwindows and retrieval parameters for O_3.

- Assessment of the retrieval parameters for ten trace gases at Eureka coordinated with the IRWG as part of the harmonization initiative.

- Improvement of the comparison method for ground and satellite-based instruments, allowing for a more confident comparison under variable Arctic conditions.

- First published NO_y climatology from ground-based FTIR spectroscopy based on the five primary species of NO_y: NO, NO_2, HNO_3, $ClONO_2$, and N_2O_5. This was used for studying the seasonal and interannual variability of NO_y and an estimate of the number of years necessary for trend detection was also made.

- Comparisons of individual NO_y primary species measured by the PEARL FTIR spectrometer and of the NO_y data product with three atmospheric models and the ACE-FTS. These comparisons provided useful feedback to the modeling groups and for ACE-FTS validation.

- A case study of unusual chemical ozone depletion at Eureka in 2011, complementing the results published by *Manney et al.* [2011]. The 2011 spring total columns of O_3, HCl, HF, HNO_3, and $ClONO_2$ at Eureka were compared with the previous 14-year Eureka FTIR time series of total columns of these gases, and the chemical ozone depletion was quantified.

9.2 Recommendations for Future Work

In July 2011, the PEARL 125HR celebrated its five-year anniversary at Eureka. During these years, it operated at a high standard, providing valuable spectra. The following recommendations are meant to keep the instrument running at the same level and also give some ideas of how to improve the instrument operations and the retrieval technique.

Instrument and Measurements

1. Make regular low pressure HBr and HCl gas cell measurements for maintaining a proper alignment of the instrument.

2. Maintain the optics in clean condition, and the KBr beamsplitter under vacuum or in the jar with proper desiccant, to preserve its quality.

3. Perform regular maintenance operations, including the chiller and the scroll pump, to avoid damage of the parts and ensure optimal operation.

4. Replace the solar tracker with a good quality active/passive tracker, to reduce the need for operator intervention.

5. Automate the process of filling the InSb and HgCdTe detectors with liquid nitrogen.

6. Maintain a dynamic, real-time data transfer to the Toronto Cube station and sufficient space on the Bruker computer for data acquisition.

7. Extend the measurements by performing lunar measurements whenever possible, especially during the polar night, to fill the gaps between the sunlit periods through the years.

8. Winterize the instrument properly each year until lunar measurements are made on a regular basis, and carefully protect the external optical components.

9. Build a protective tube around the input 45º mirror and window, up to the solar tracker, so measurements are not perturbed on the mezzanine or laboratory level and falling objects do not break the input optics.

Retrievals

1. Finish the WACCM comparison exercise for all ten species:

    - For HCN a seven-microwindow approach should be studied along with the reduced microwindow set adapted by Vigouroux (personal communication); the second part of the exercise should be also evaluated with an improved WACCM HCN product.

    - Using the final microwindow and HITRAN line list recommended for CH_4 (expected in the near future), the second part of the harmonization exercise should be repeated to confirm that WACCM parameters work well.

    - Using the *a priori* profiles that the IRWG will recommend for HF, perform the second part of the harmonization exercise.

    - Pseudolines will be provided by the IRWG for C_2H_6 retrievals. These should be assessed for Eureka retrievals.

    - The ILC should be investigated for N_2O to confirm that the 7-km value is correct.

    - A detailed error analysis is recommended before the final decision is made for each gas regarding the retrieval parameters that will be used in the future.

2. Explore in more detail the results obtained during the comparison exercise for those species for which the new parameters gave significant improvements (*e.g.,* CO) and use them for further projects.

3. Reprocess all acquired data with the SFIT2 v3.4 algorithm, the new parameters, and the HITRAN 2008 line list.

4. Build trends using the 125HR measurements and the data acquired by the Bomem DA8.

5. Expand the list of regularly retrieved gases for Eureka (*e.g.*, H_2O, OCS, COF_2, CH_2O, C_2H_2, C_2H_4, CH_3OH, CHOOH, CFCs).

Interpretation of Retrievals

1. Continue ongoing satellite validation activities. The comparisons with ACE-FTS measurements should be redone for the new v.3 data product of ACE, and compared with the results obtained for the older version v2.2 with the purpose of validating the new version.

2. Continue the model validation, especially for those models and gases for which large differences occurred (*e.g.*, CMAM-DAS for most species compared, SLIMCAT for HF and early spring HNO_3, all species close to the polar vortex edge).

3. Combine the 125HR measurements with measurements from other instruments at PEARL to better understand the processes that occur during the polar winter/spring (descent, PSC formation, chlorine activation, chemical ozone depletion, EPP events) and throughout the year (transport of pollutants, biomass burning products, and gases resulting from volcanic eruptions).

4. Combine the Eureka 125HR measurements with similar measurements from the other NDACC Arctic sites to provide a larger picture of the evolution of species of interest (NO_y, O_3, chlorine species, *etc.*).

Appendix A

NDACC IRWG Harmonization Exercise

In addition to the plots shown in Chapter 5, example of spectral fits, averaging kernels, *a priori* profiles, retrieved profiles, and total column time series with differences are presented below for the two steps of the IRWG harmonization initiative.

A.1 HCl
A.1.1 Step I
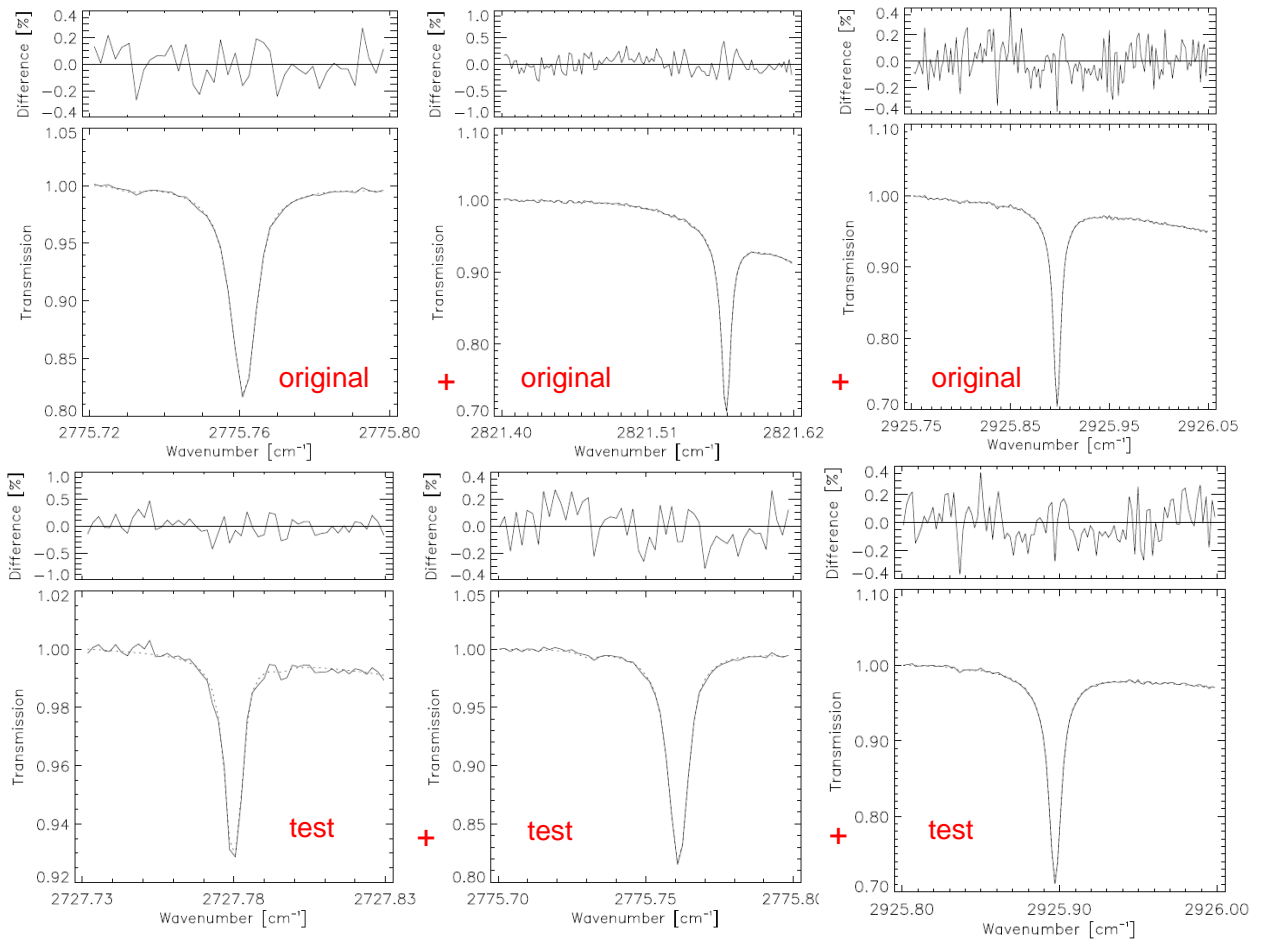
Figure A.1. Example of fits for spectrum 080622F3.S2 using the original Eureka microwindows (upper panels) and the recommended test microwindows (bottom panels). For this spectrum, SZA=59.48º, DOFS$_{orig}$=1.17, DOFS$_{test}$=1.94, RMS$_{orig}$=0.144, RMS$_{test}$=0.152.
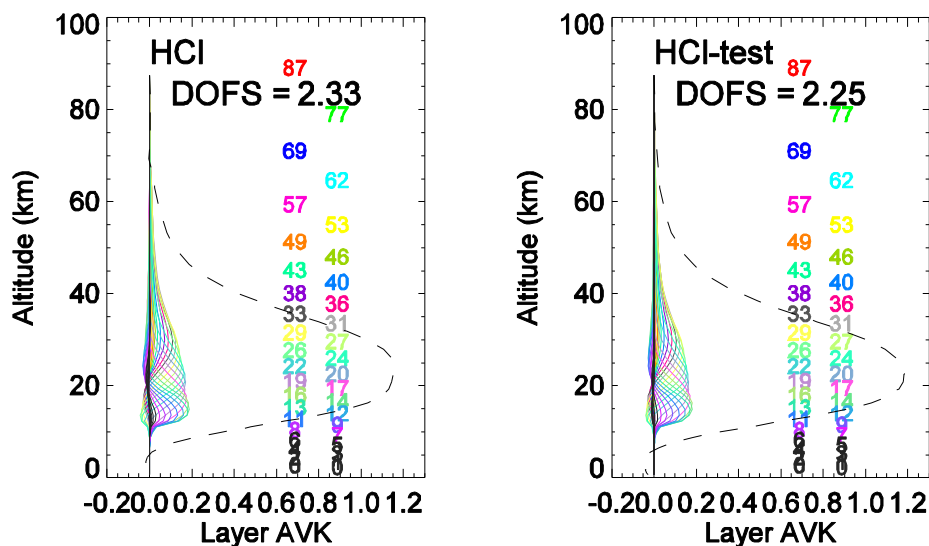
Figure A.2. Example of layer averaging kernels for spectrum 070830F3.S2 for the original Eureka microwindows and the test microwindows. The dashed line shows the sensitivity at each altitude.

Figure A.3. HCl total columns (a), percentage differences (b) calculated using Equation 5.1, DOFS (c), and RMS fitting residual (d) for the microwindow comparison. The mean percentage difference and the standard deviation are also specified along with the number of spectra compared. The test results are shown in red.

A.1.2 Step II
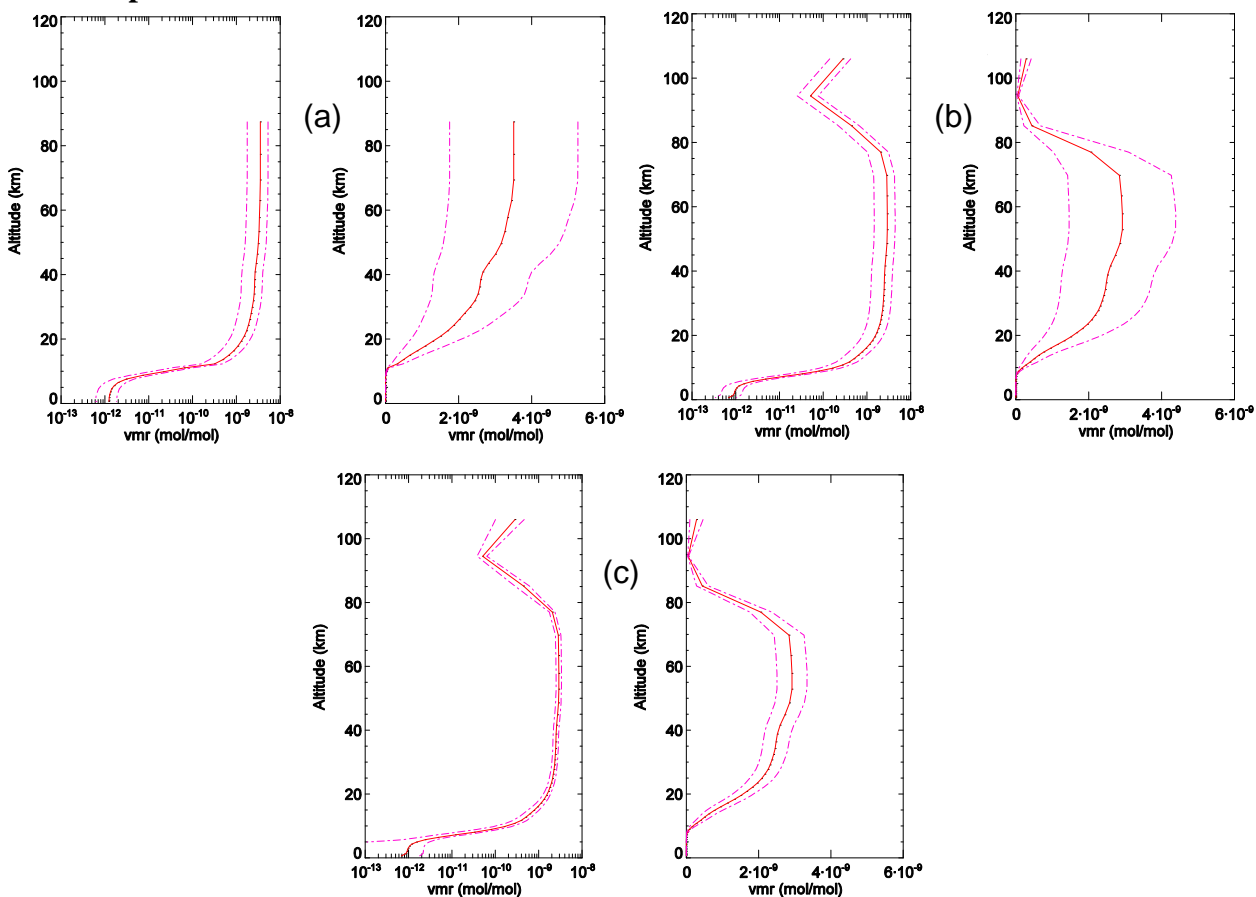
Figure A.4. The *a priori* profiles (solid line) used in the second part of the IRWG harmonization exercise for HCl. The dashed lines indicate the *a priori* profile variability given by $\mathbf{S_a}$ for each altitude. Panels (a), (b), and (c) correspond to cases 1, 2, and 3, respectively, as specified in Table 5.3. The profiles are plotted on both log (left panels) and linear (right panels) scales to show the structures at small VMR.
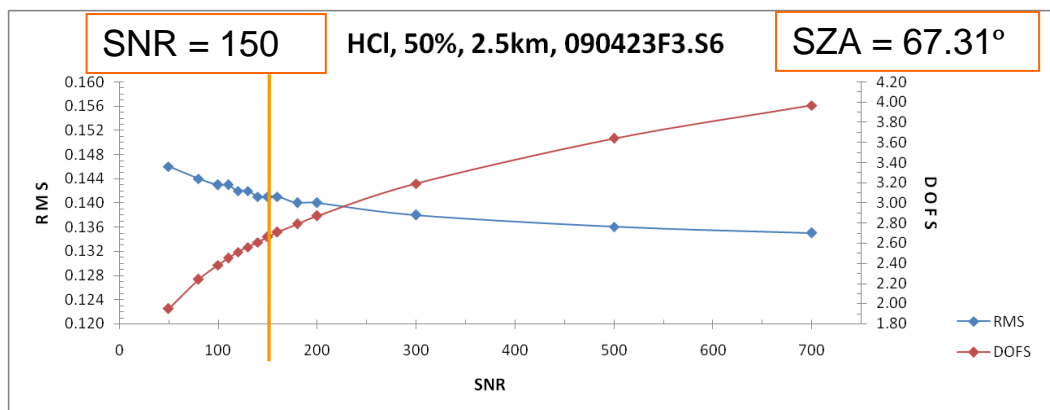
Figure A.5. The trade-off-curve for HCl, for case 2 from Table 5.3 corresponding to a Gaussian ILC of 2.5 km.
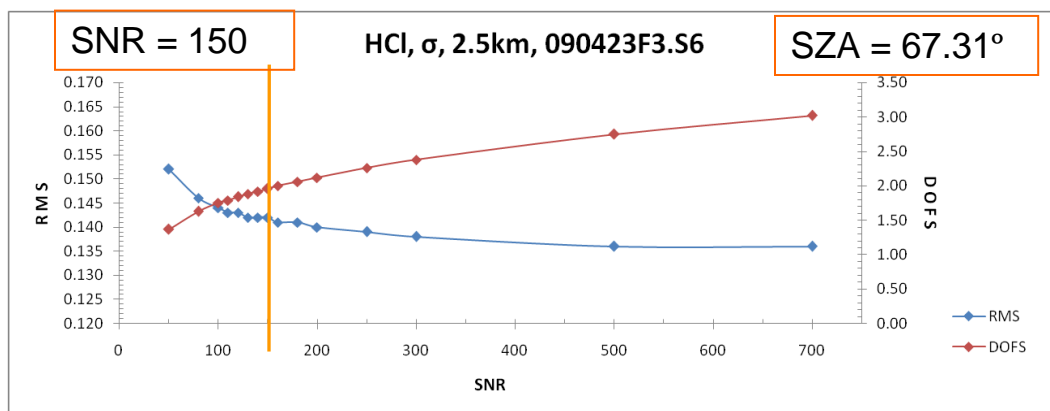
Figure A.6. The trade-off-curve for HCl, for case 3 from Table 5.3 corresponding to a Gaussian ILC of 2.5 km.
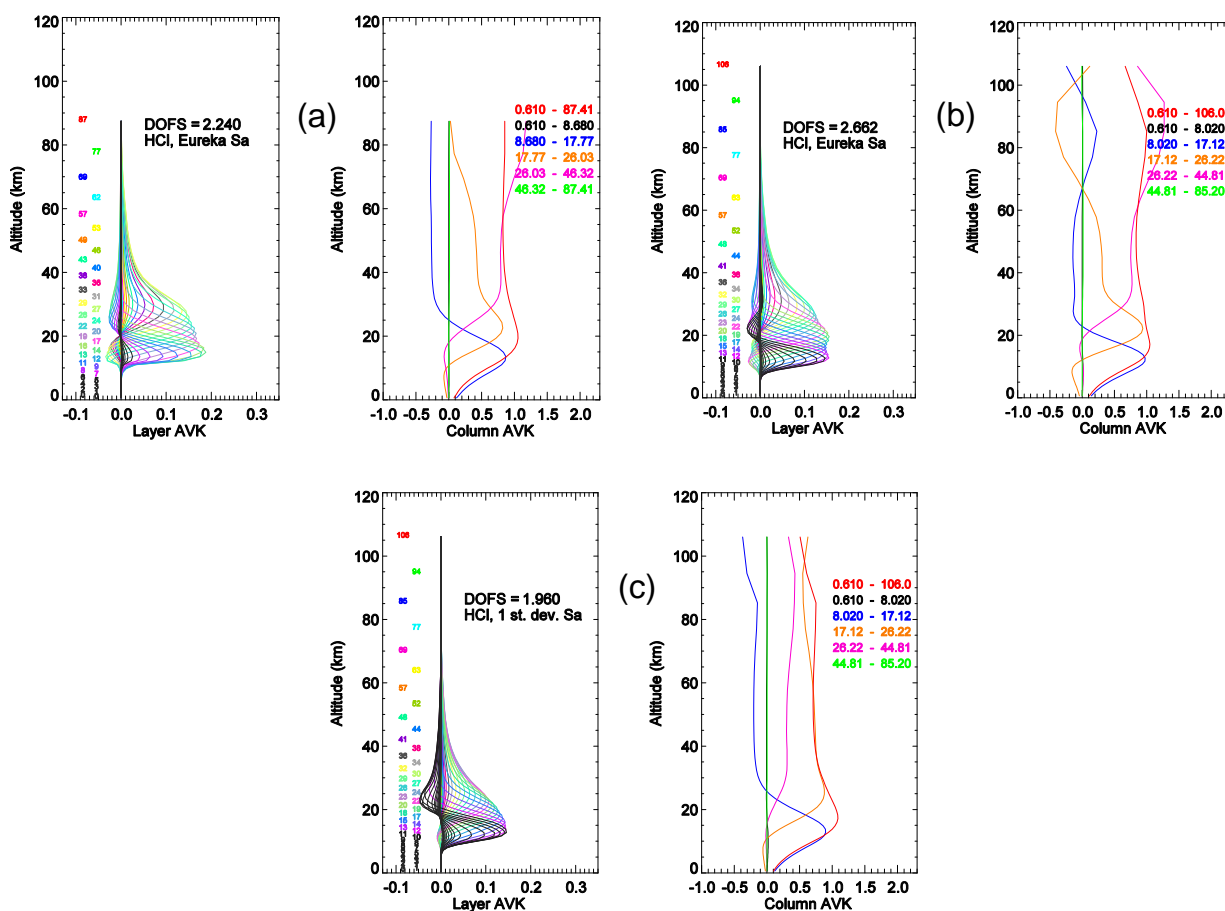
Figure A.7. HCl layer averaging kernels (left panels) and column averaging kernels (right panels) for: (a) case 1, (b) case 2, and (c) case 3, for spectrum 090423F3.S6, SZA=67.31°. For the layer AVKs, the height of the layer is specified on the left with numbers (height given in km) colored as the corresponding kernel. The column AVKs are colored according to the partial column range shown in the legend.
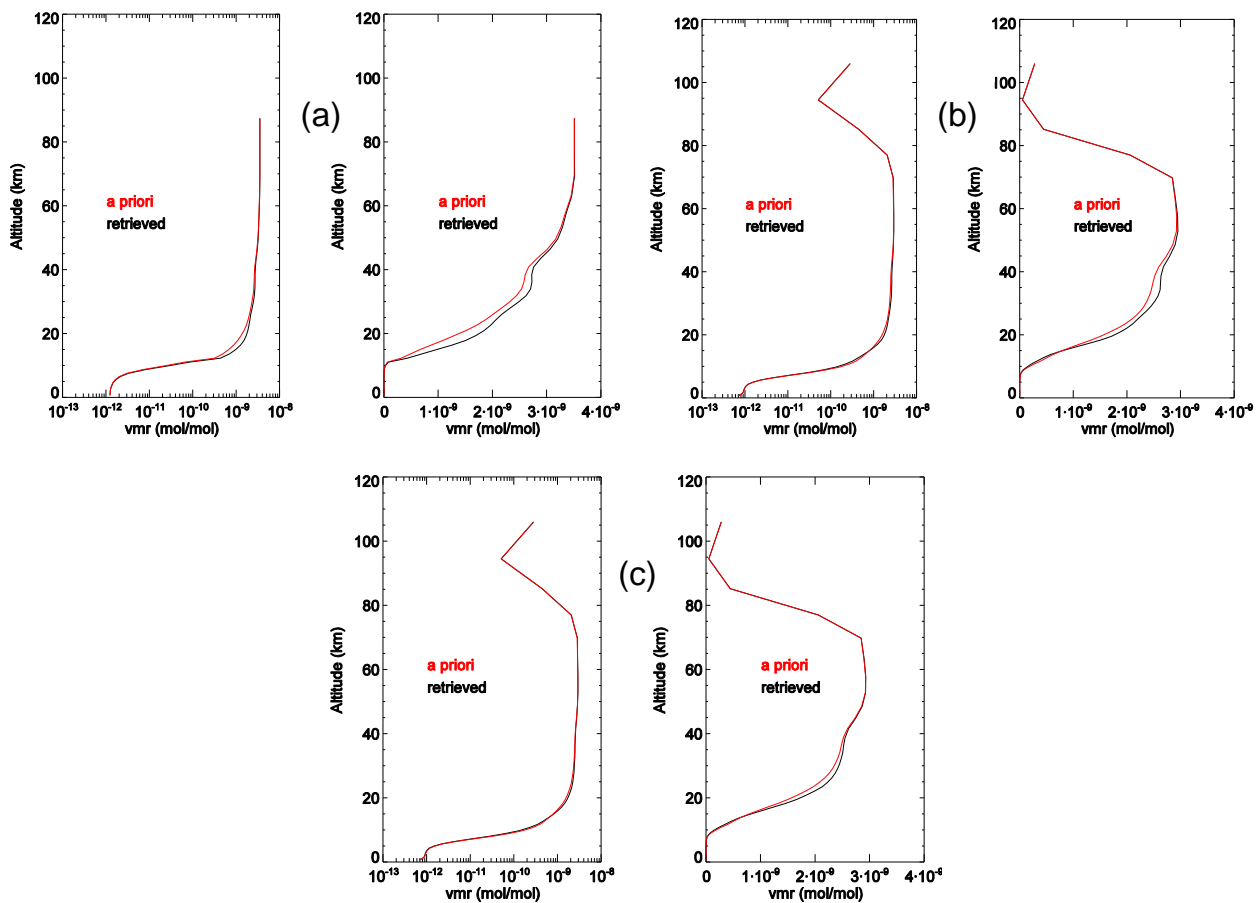
Figure A.8. HCl Retrieved profiles (black) for (a) case 1, (b) case 2, and (c) case 3 for spectrum 090423F3.S6, SZA=67.31°. The *a priori* profiles are shown in red. The profiles are plotted on both log scale (left panels) and linear scale (right panels).

A.2 HNO₃
A.2.1 Step I
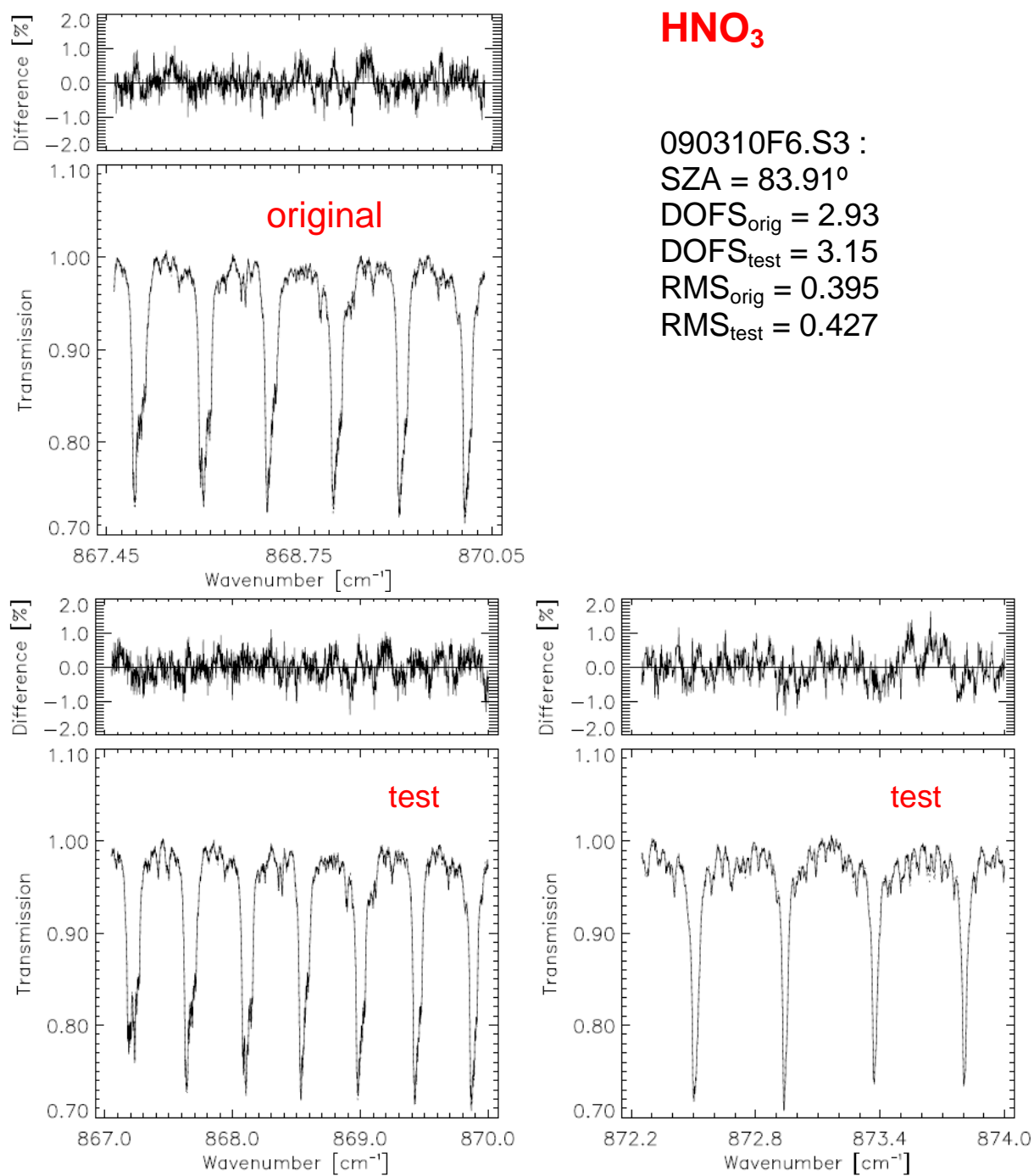
Figure A.9. Example of fits for HNO₃ retrievals for spectrum 090310F6.S3 using the original Eureka microwindow (upper panels) and the recommended test microwindows (bottom panels).
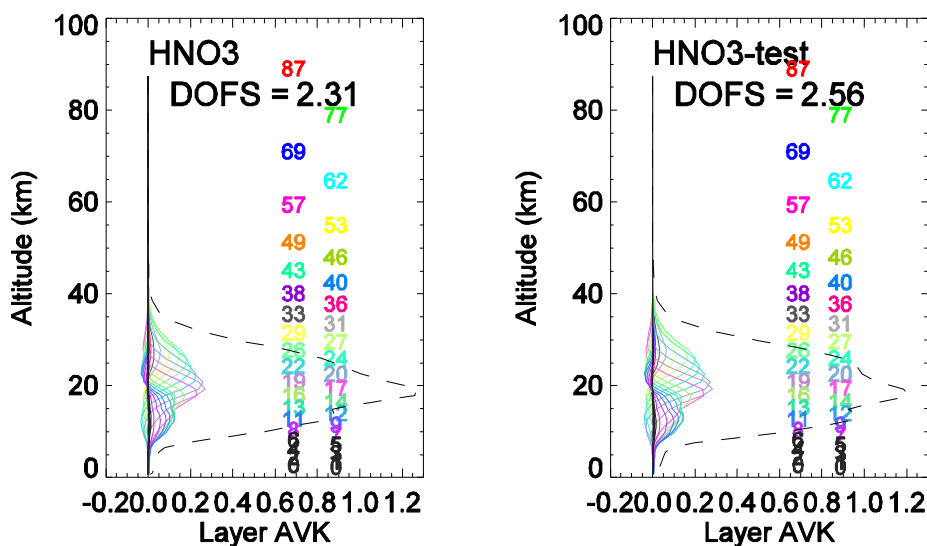
Figure A.10. Example of averaging kernels for spectrum 070830F6.S2 for the original Eureka microwindow and the test microwindows.
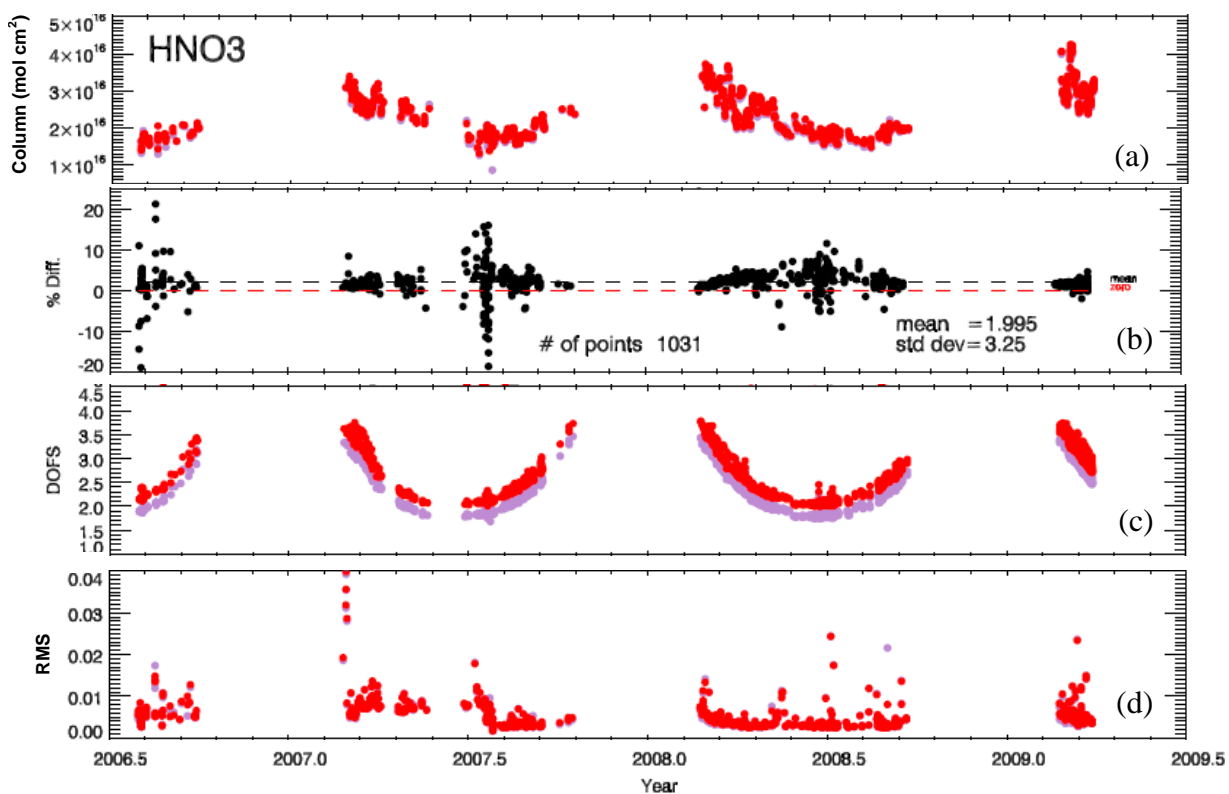
Figure A.11. HNO$_3$ total columns (a), percentage differences (b) calculated using Equation 5.1, DOFS (c), and RMS fitting residual (d) for the microwindow comparison. The mean percentage difference and the standard deviation are also specified along with the number of spectra compared. The test results are shown in red.

A.2.2 Step II
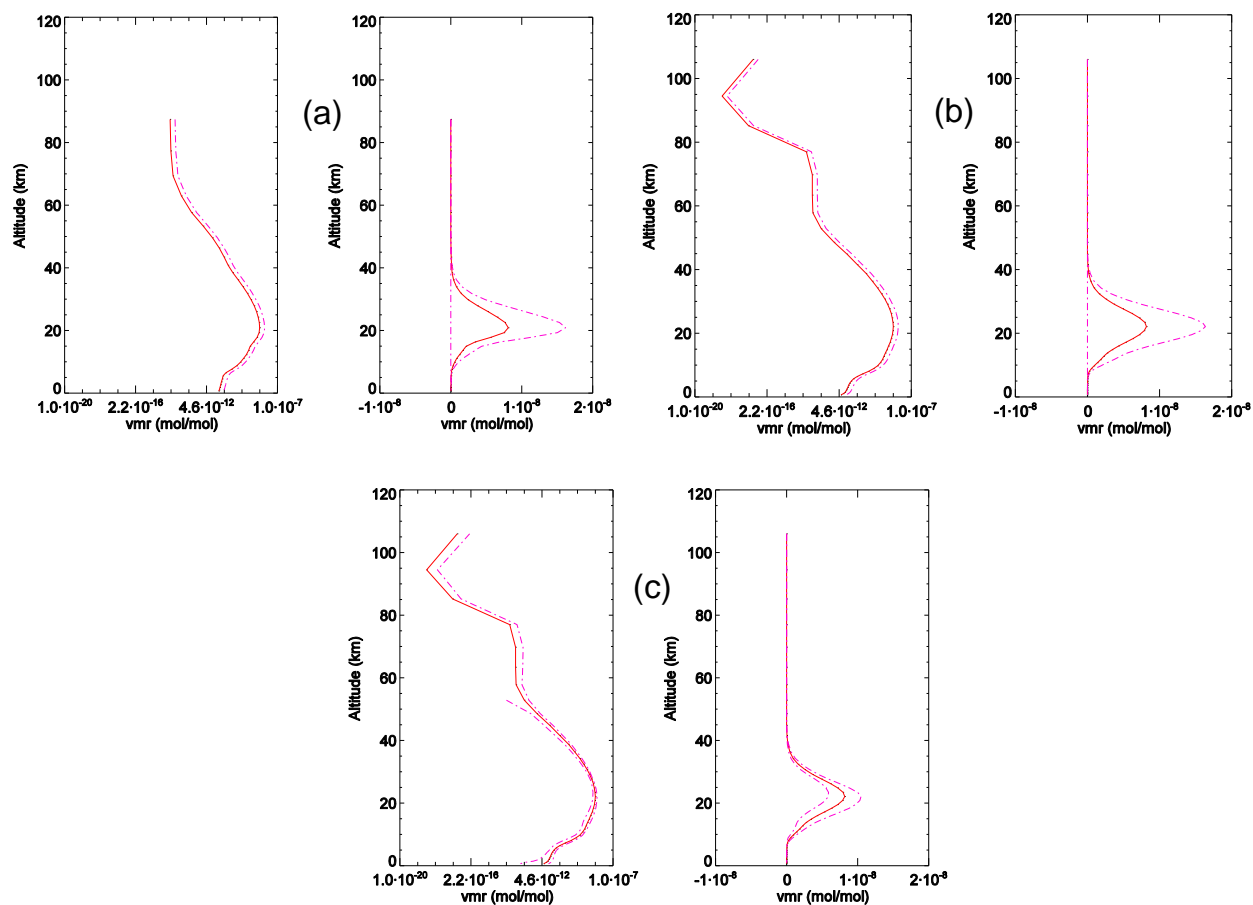
Figure A.12. The *a priori* profiles (solid line) used in the second part of the IRWG harmonization exercise for HNO₃. The dashed lines indicate the *a priori* profile variability given by $\mathbf{S}_a$ for each altitude. Panels (a), (b), and (c) correspond to cases 1, 2, and 3, respectively, as specified in Table 5.3. The profiles are plotted on both log scale (left panels) and linear scale (right panels) to show the structures at small VMR.
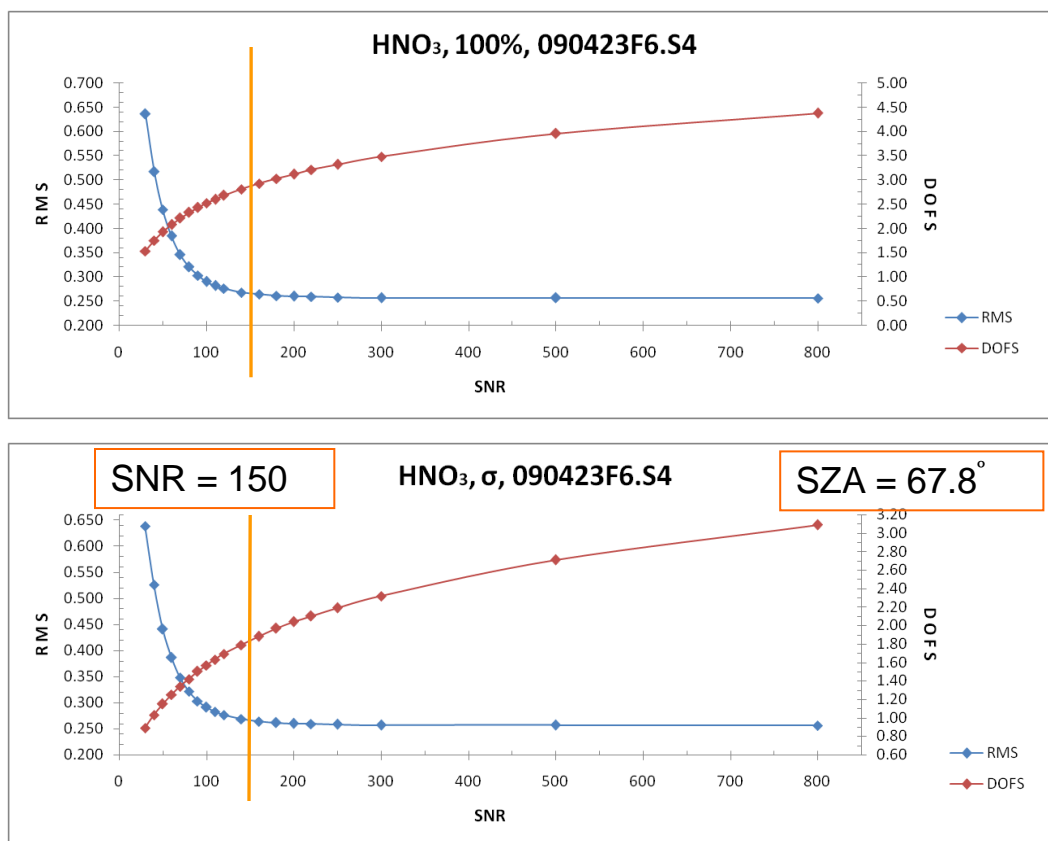
Figure A.13. HNO$_3$ RMS fitting residual trade-off curves for cases 2 (top panel) and 3 (bottom panel), for spectrum 090423F6.S4.
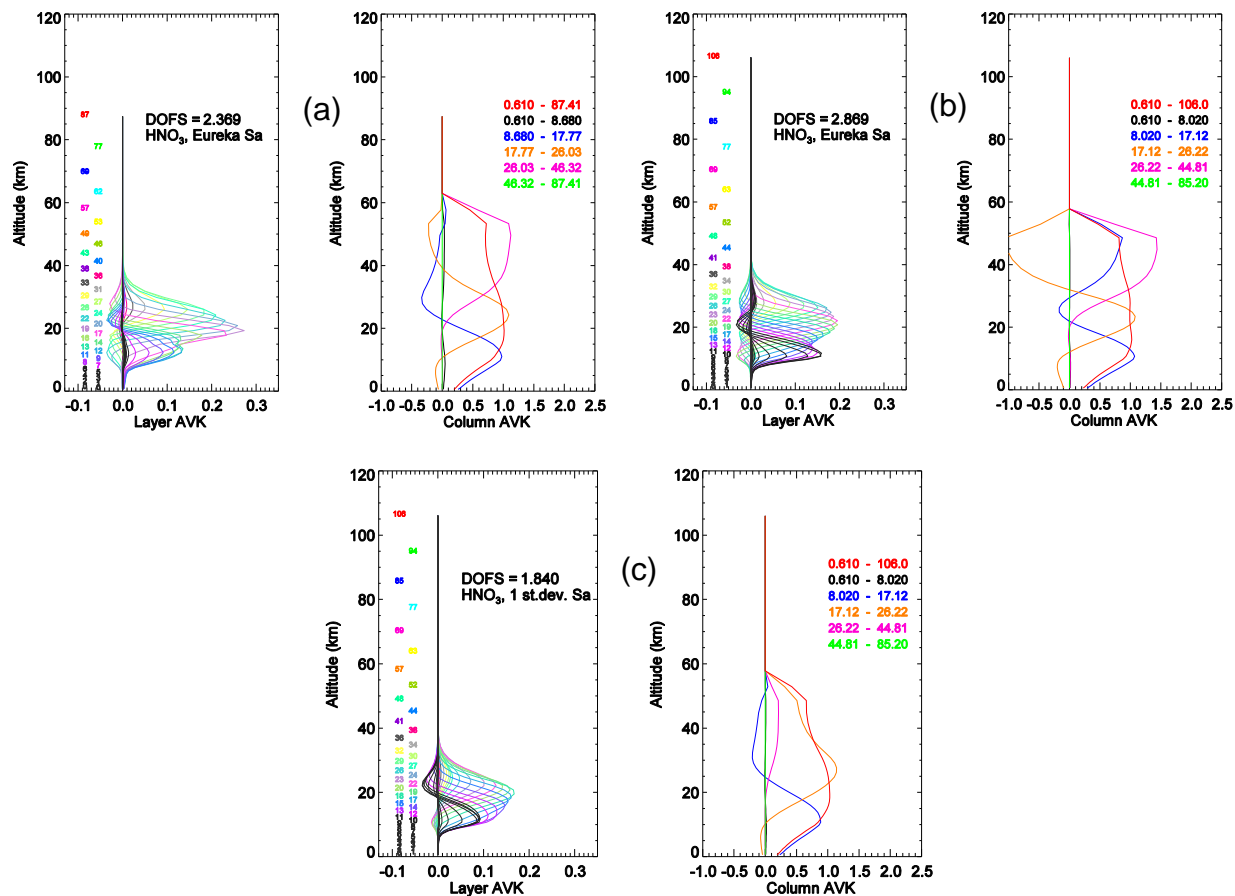
Figure A.14. HNO$_3$ layer averaging kernels (left panels) and column averaging kernels (right panels) for: (a) case 1, (b) case 2, and (c) case 3, for spectrum 090423F6.S4, SZA=67.8°. For the layer AVKs, the height of the layer is specified on the left with numbers (height given in km) colored as the corresponding kernel. The column AVKs are colored according to the partial column range shown in the legend.

Figure A.15. HNO$_3$ retrieved profiles (black) using the set-up from: (a) case 1, (b) case 2, and (c) case 3, for spectrum 090423F6.S4, SZA=67.8°. The a priori profiles are shown in red. The profiles are plotted on both log (left panels) and linear (right panels) scales.

A.3 HF

HF

080622F1.S2 :
SZA = 59.73⁰
$DOFS_{orig}$ = 0.45
$DOFS_{test}$ = 2.91
RMS_{orig} = 0.146
RMS_{test} = 0.269

Figure A.16. Example of HF fits for spectrum 080622F1.S2 using the original Eureka microwindow (upper panels) and the test microwindows (bottom panels).
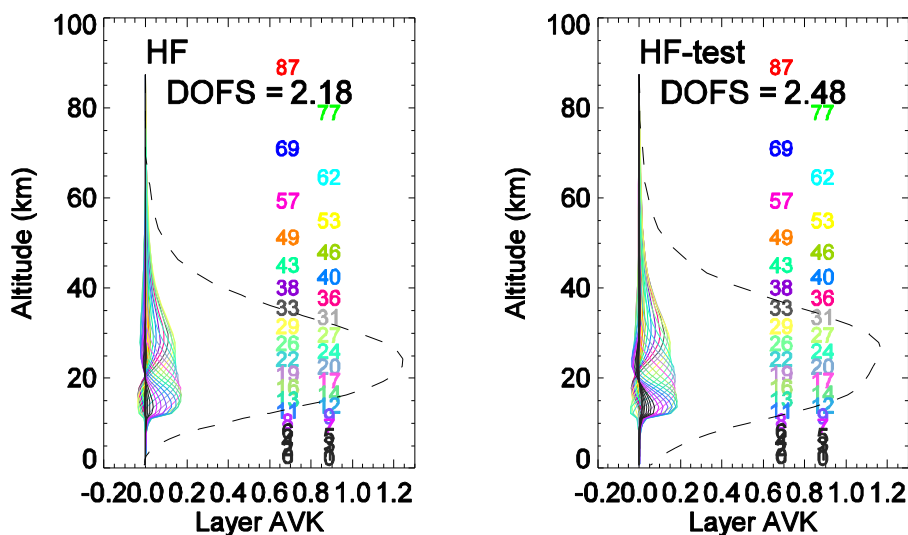
Figure A.17. Example of HF layer averaging kernels for spectrum 070830F1.S2 for the original Eureka microwindow and the test microwindows.
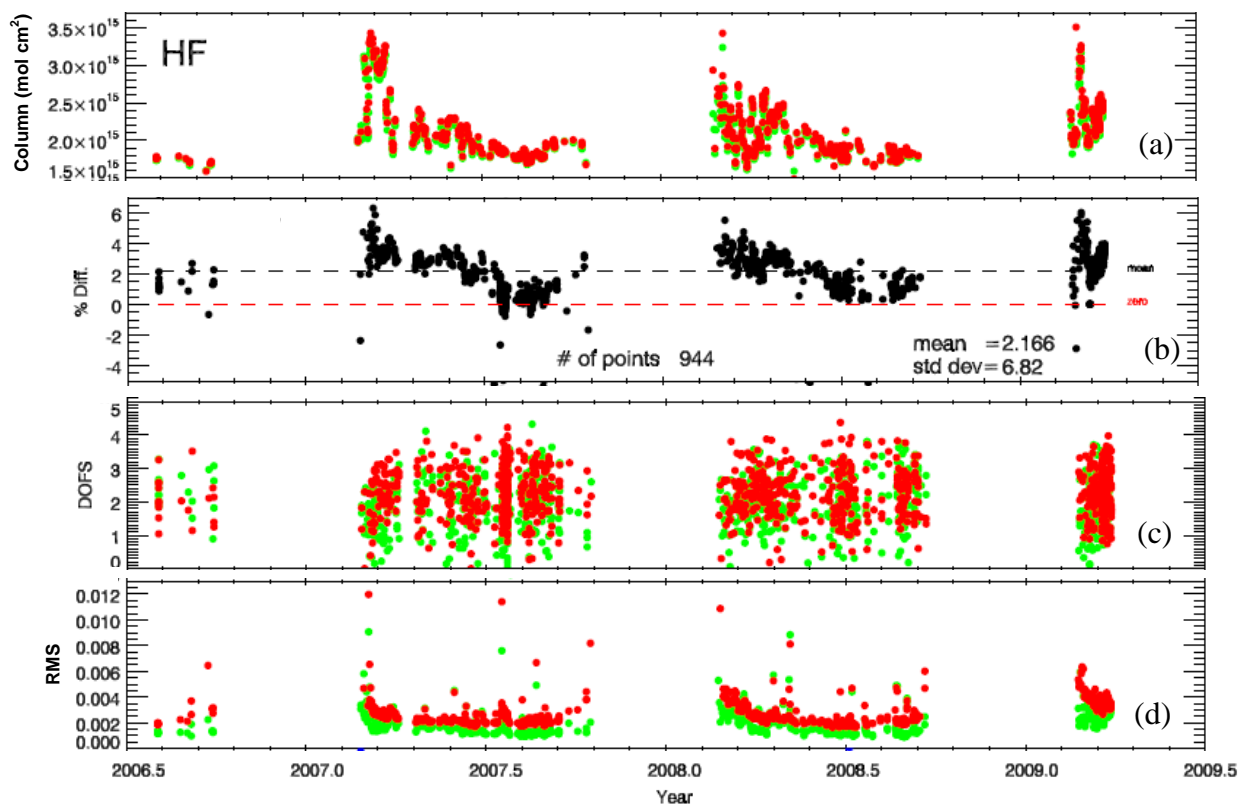
Figure A.18. HF total columns (a), percentage differences (b) calculated using Equation 5.1, DOFS (c), and RMS fitting residual (d) for the microwindow comparison. The mean percentage difference and the standard deviation are also specified along with the number of spectra compared. The test results are shown in red.

A.4 ClONO₂
A.4.1 Step I

ClONO₂

090310F6.S3 :
SZA = 83.91º
$DOFS_{orig}$ = 1.04
$DOFS_{test}$ = 0.92
RMS_{orig} = 0.369
RMS_{test} = 0.387
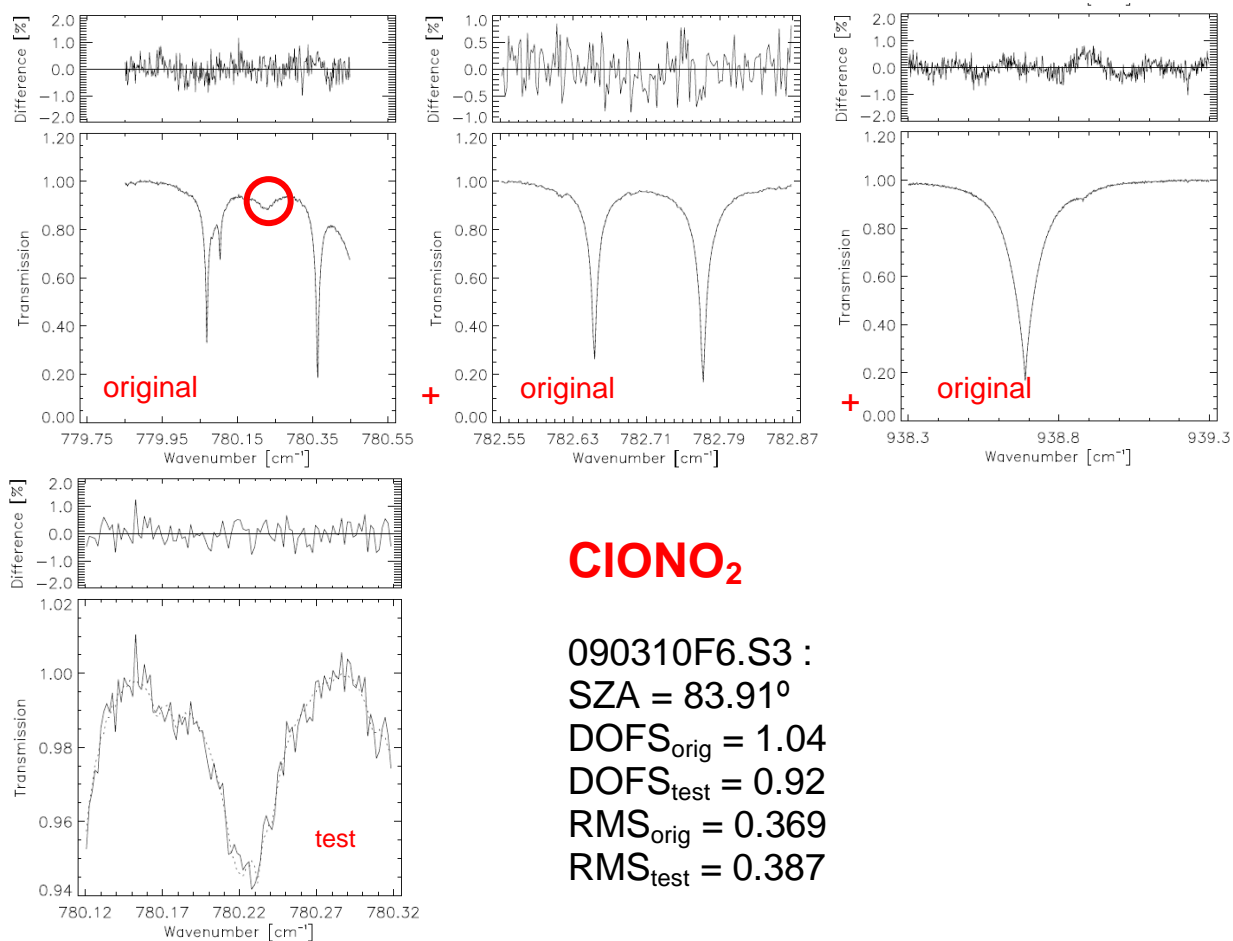
Figure A.19. Example of $ClONO_2$ fits for spectrum 090310F6.S3 using the original Eureka microwindows (upper panels) and the test microwindow (bottom panels).
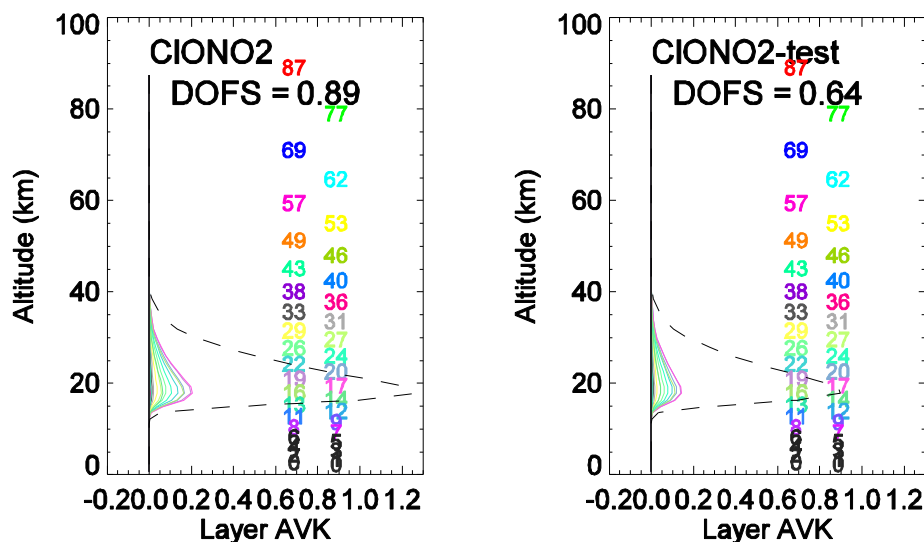
Figure A.20. Example of ClONO$_2$ layer averaging kernels for spectrum 070830F3.S2 for the original Eureka microwindows and the test microwindow.
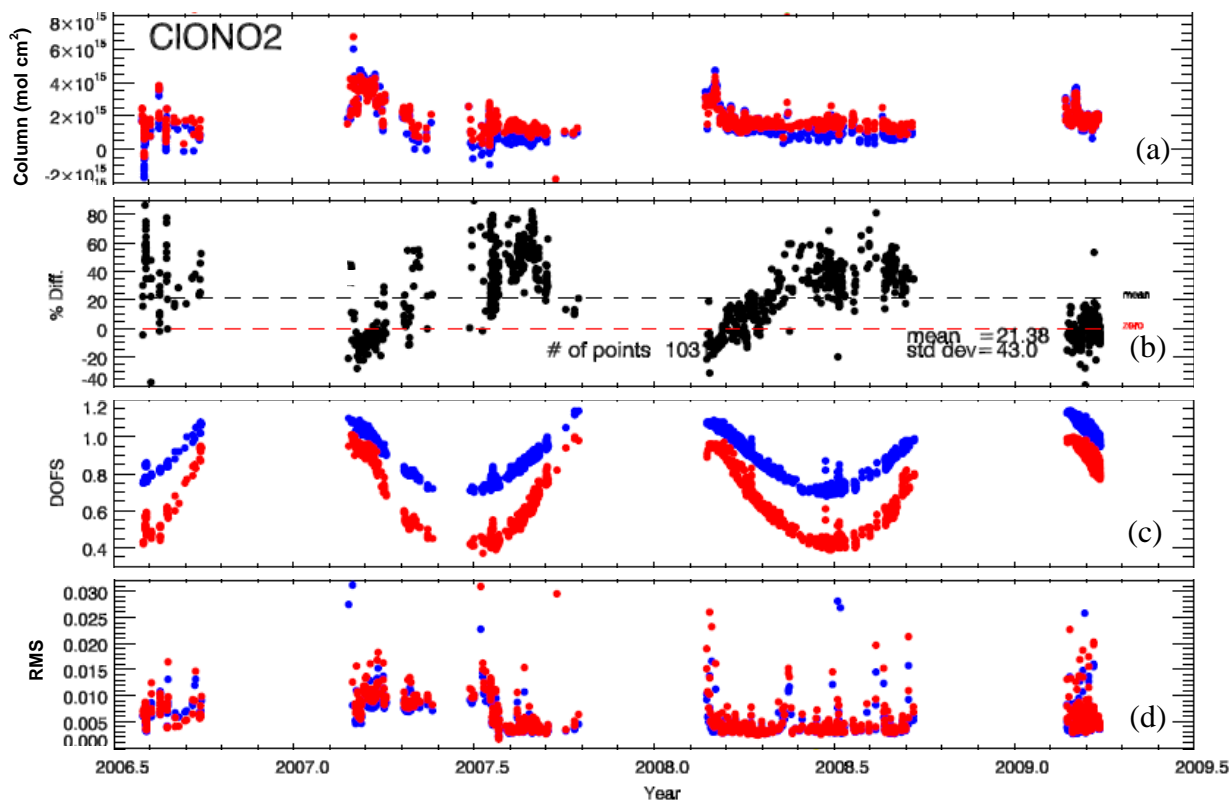
Figure A.21. ClONO$_2$ total columns (a), percentage differences (b) calculated using Equation 5.1, DOFS (c), and RMS fitting residual (d) for the microwindow comparison. The mean percentage difference and the standard deviation are also specified along with the number of spectra compared. The test results are shown in red.

A.4.2 Step II
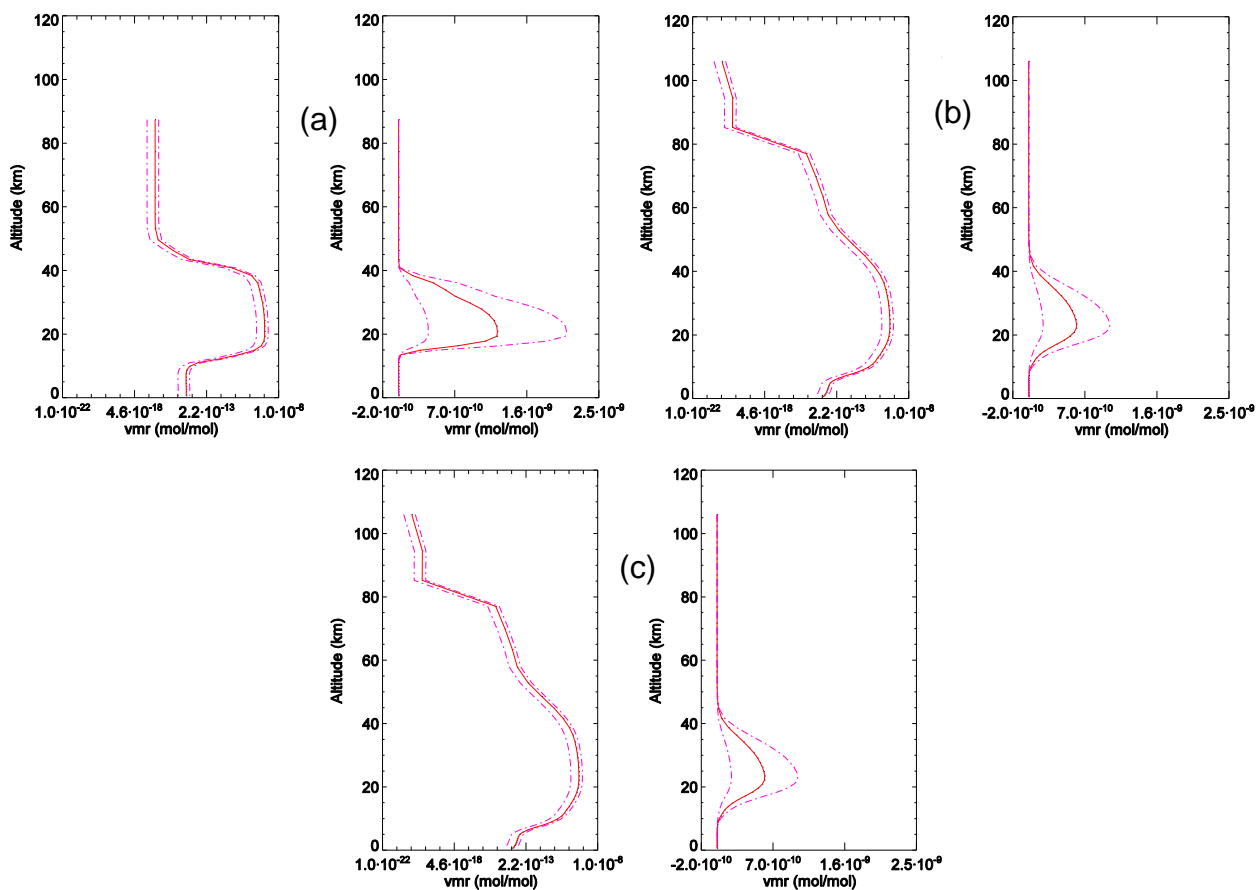
Figure A.22. The *a priori* profiles (solid line) used in the second part of the IRWG harmonization exercise for ClONO$_2$. The dashed lines indicate the *a priori* profile variability given by $\mathbf{S_a}$ for each altitude. Panels (a), (b), and (c) correspond to cases 1, 2, and 3, respectively, as specified in Table 5.3. The profiles are plotted on both log (left panels) and linear (right panels) scales.
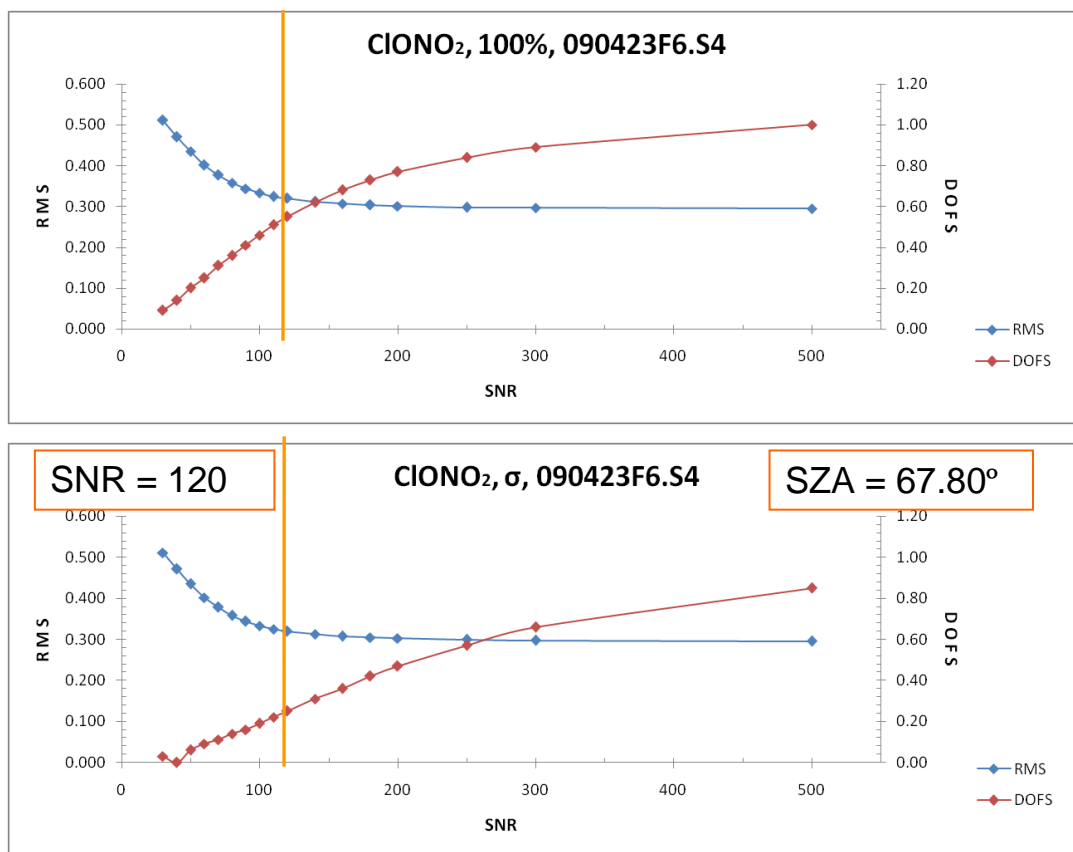
Figure A.23. ClONO$_2$ RMS fitting residual trade-off curves for cases 2 (top panel) and 3 (bottom panel), for spectrum 090423F6.S4.
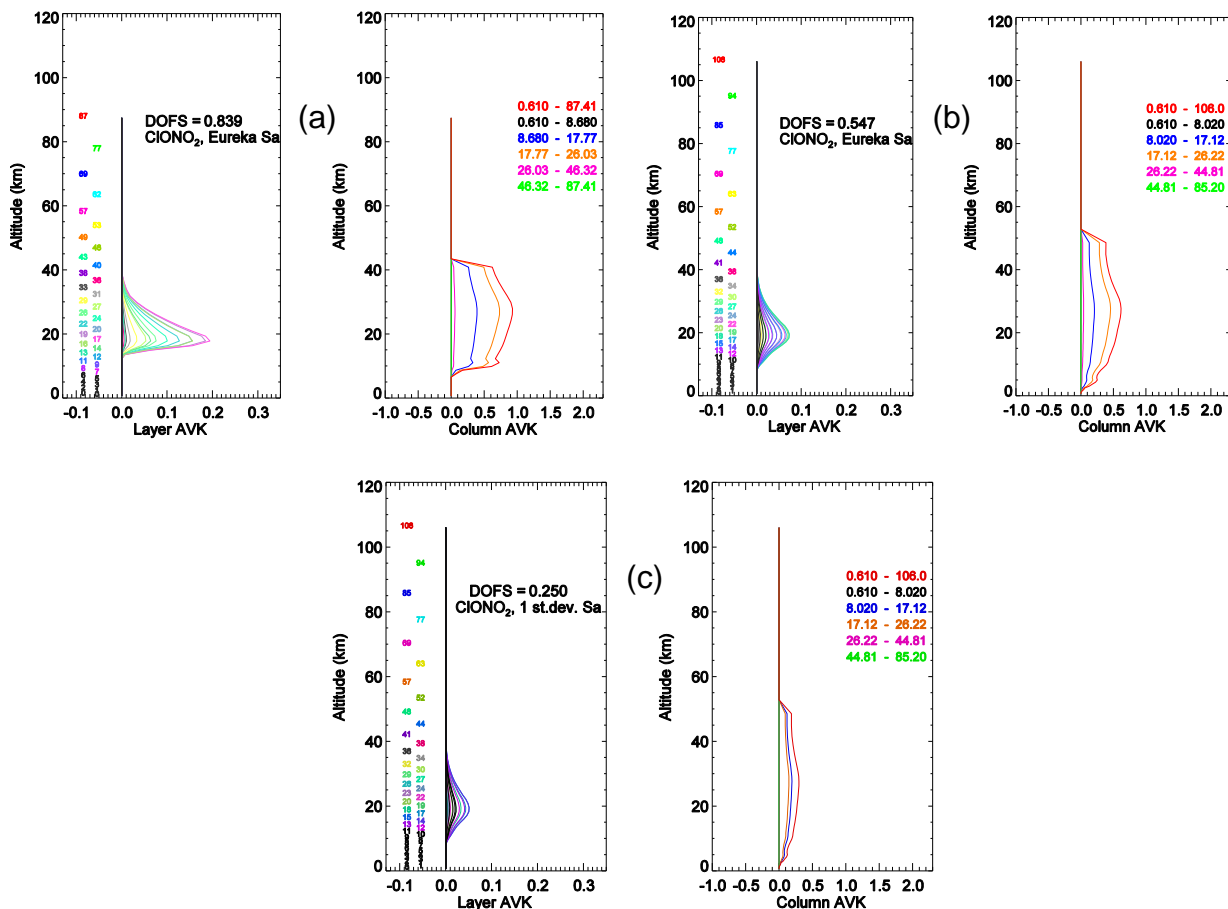
Figure A.24. ClONO$_2$ layer averaging kernels (left panels) and column averaging kernels (right panels) for: (a) case 1, (b) case 2, and (c) case 3, for 090423F6.S4, SZA=67.8°. For the layer AVKs the height of the layer is specified on the left with numbers (height given in km) colored as the corresponding kernel. The column AVKs are colored according to the partial column range shown in the legend.
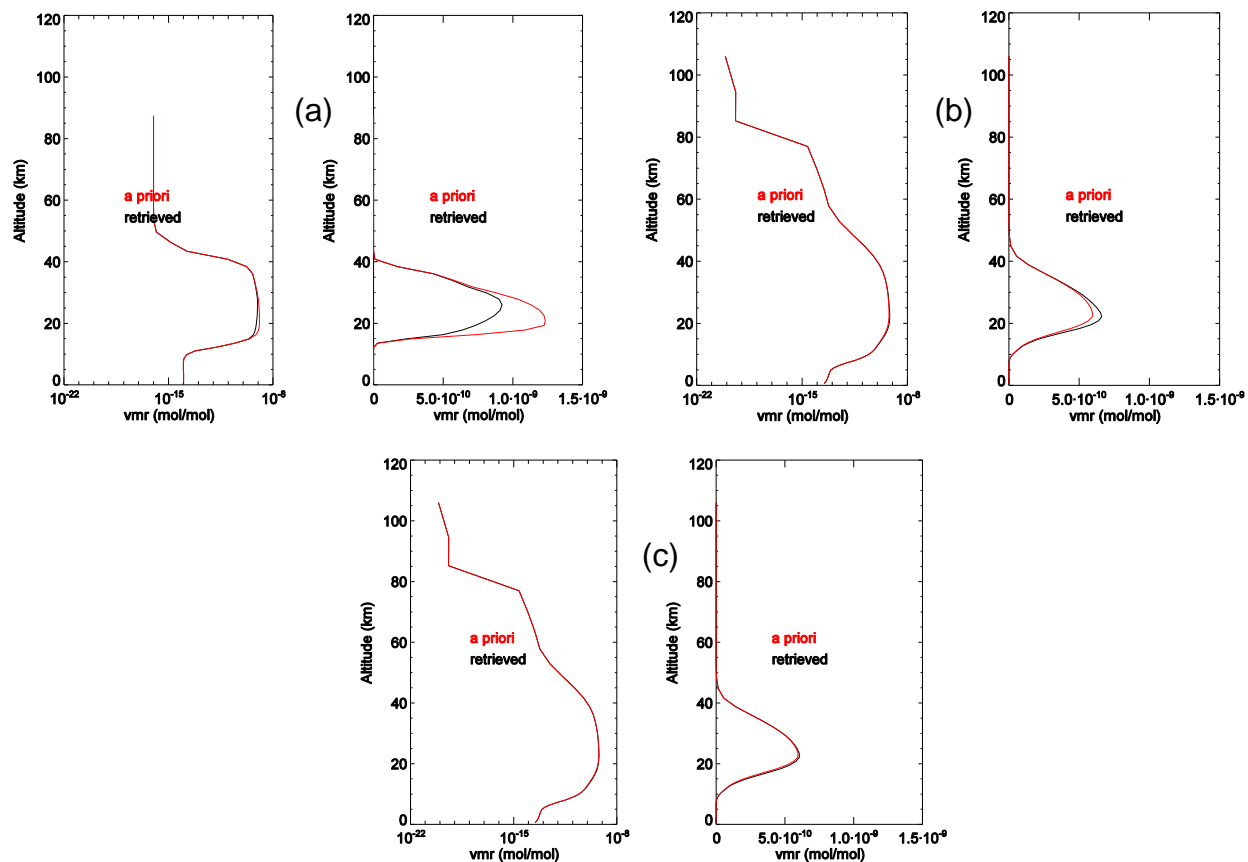
Figure A.25. ClONO$_2$ retrieved profiles (black) for: (a) case 1, (b) case 2, and (c) case 3, for spectrum 090423F6.S4, SZA=67.80º. The *a priori* profiles are shown in red. The profiles are plotted on both log (left panels) and linear (right panels) scales.

A.5 HCN

HCN

090310F2.S3 :
SZA = 83.92°
$DOFS_{orig}$ = 2.23
$DOFS_{test}$ = 2.23
RMS_{orig} = 0.115
RMS_{test} = 0.121
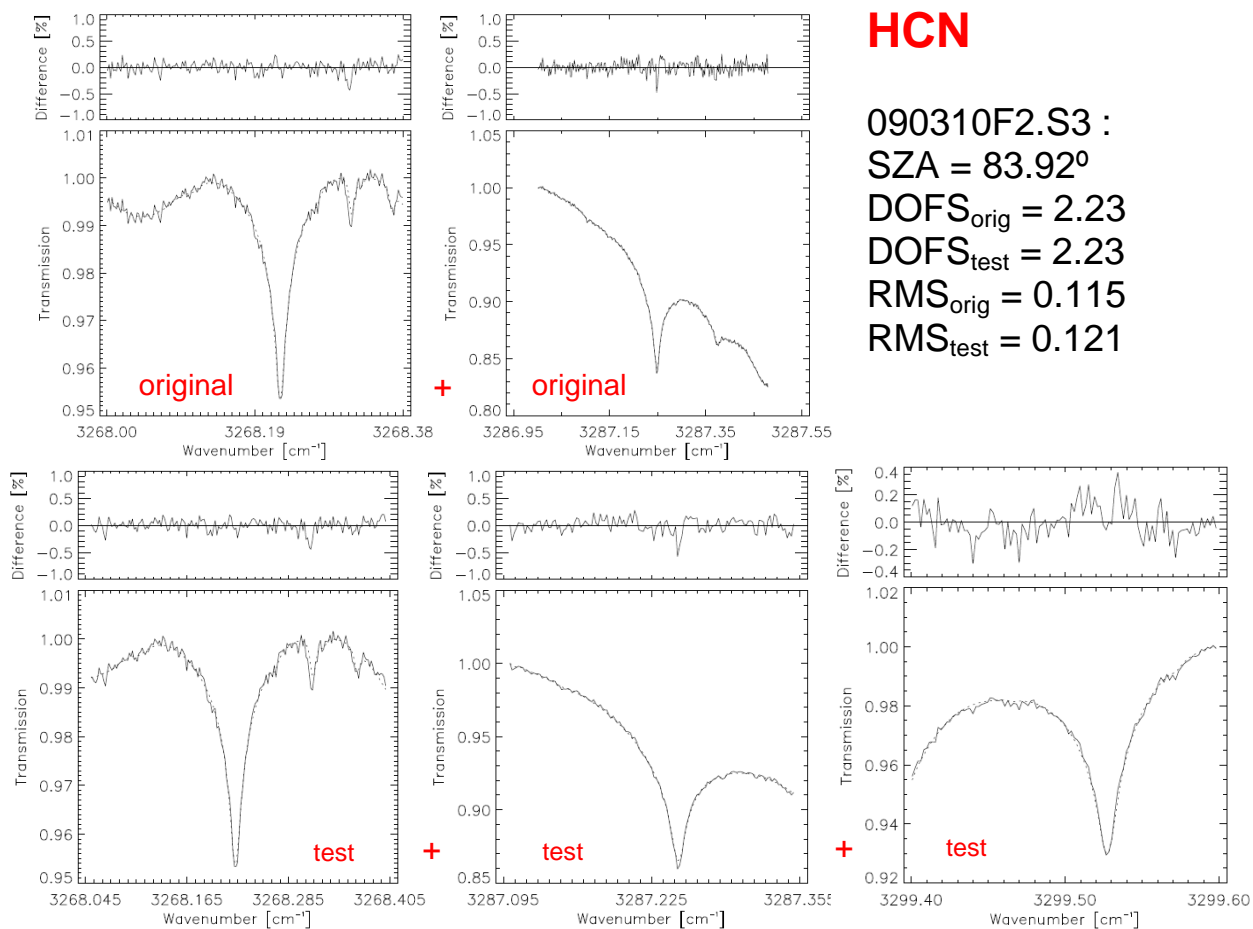
Figure A.26. Example of HCN fits for spectrum 090310F2.S3 for the original Eureka microwindows (upper panels) and the test microwindows (bottom panels).
.
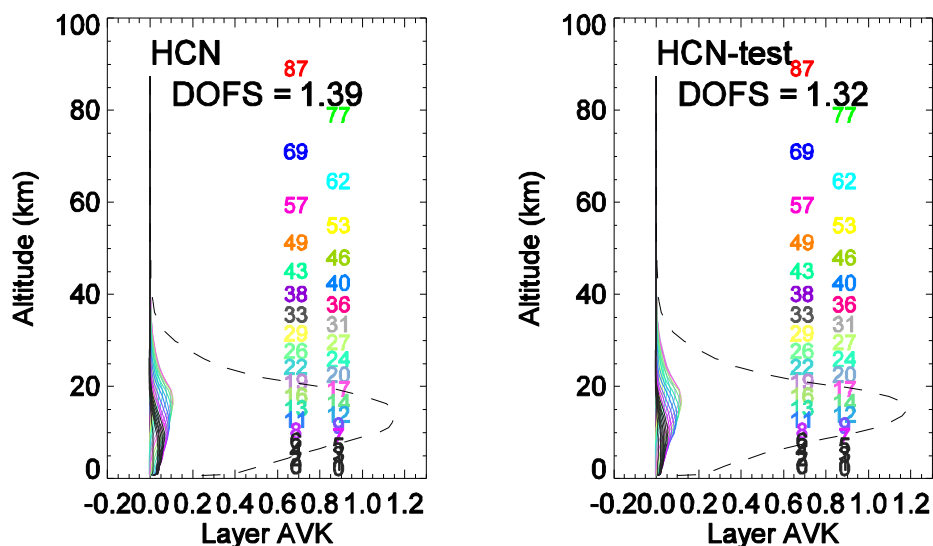
Figure A.27. Example of HCN layer averaging kernels for spectrum 070831F1.S2, SZA=72.39°
for the original Eureka microwindows and the test microwindows.
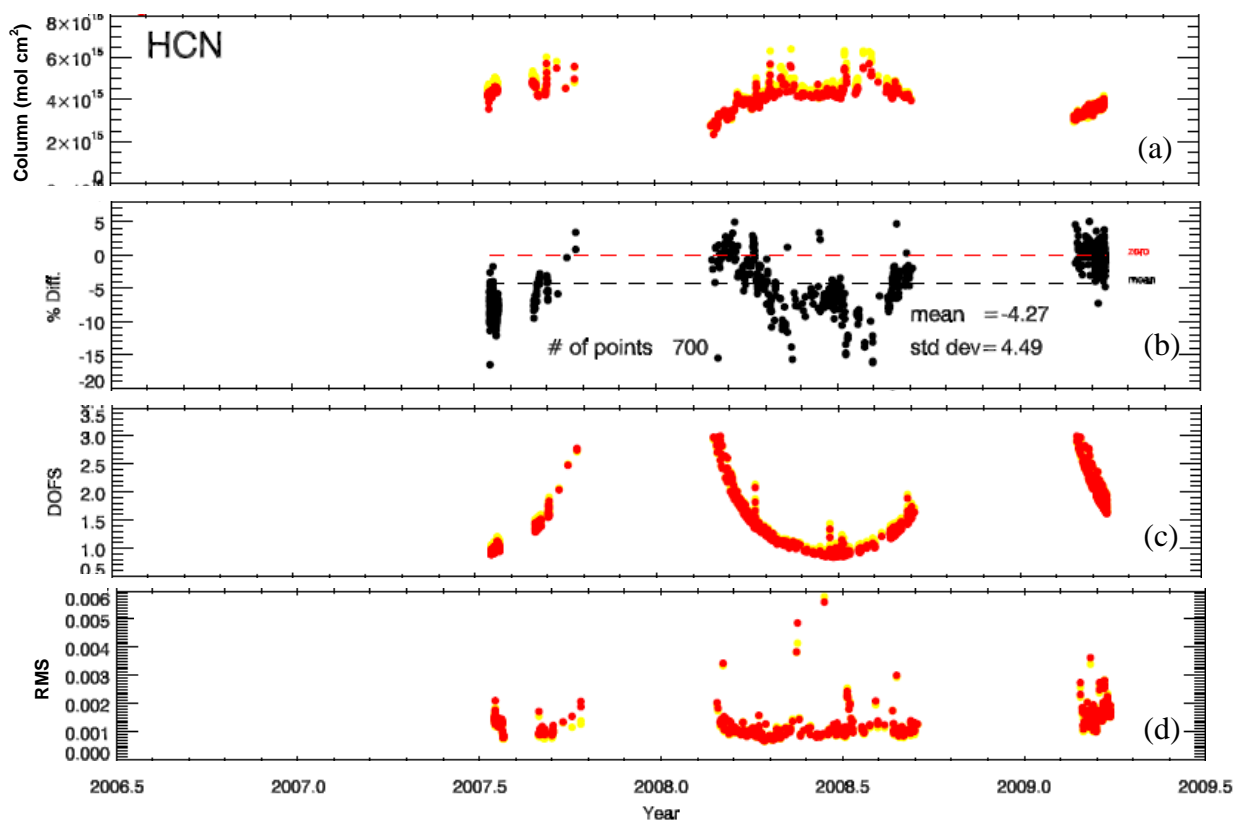
Figure A.28. HCN total columns (a), percentage differences (b) calculated using Equation 5.1,
DOFS (c), and RMS fitting residuals (d) for the microwindow comparison. The mean percentage
difference and the standard deviation are also specified along with the number of spectra
compared. The test results are shown in red.

A.6 C$_2$H$_6$
A.6.1 Step I

C$_2$H$_6$

080426F3.S1 :
SZA = 67.03^0
DOFS$_{orig}$ = 1.21
DOFS$_{test}$ = 1.68
RMS$_{orig}$ = 0.173
RMS$_{test}$ = 0.348
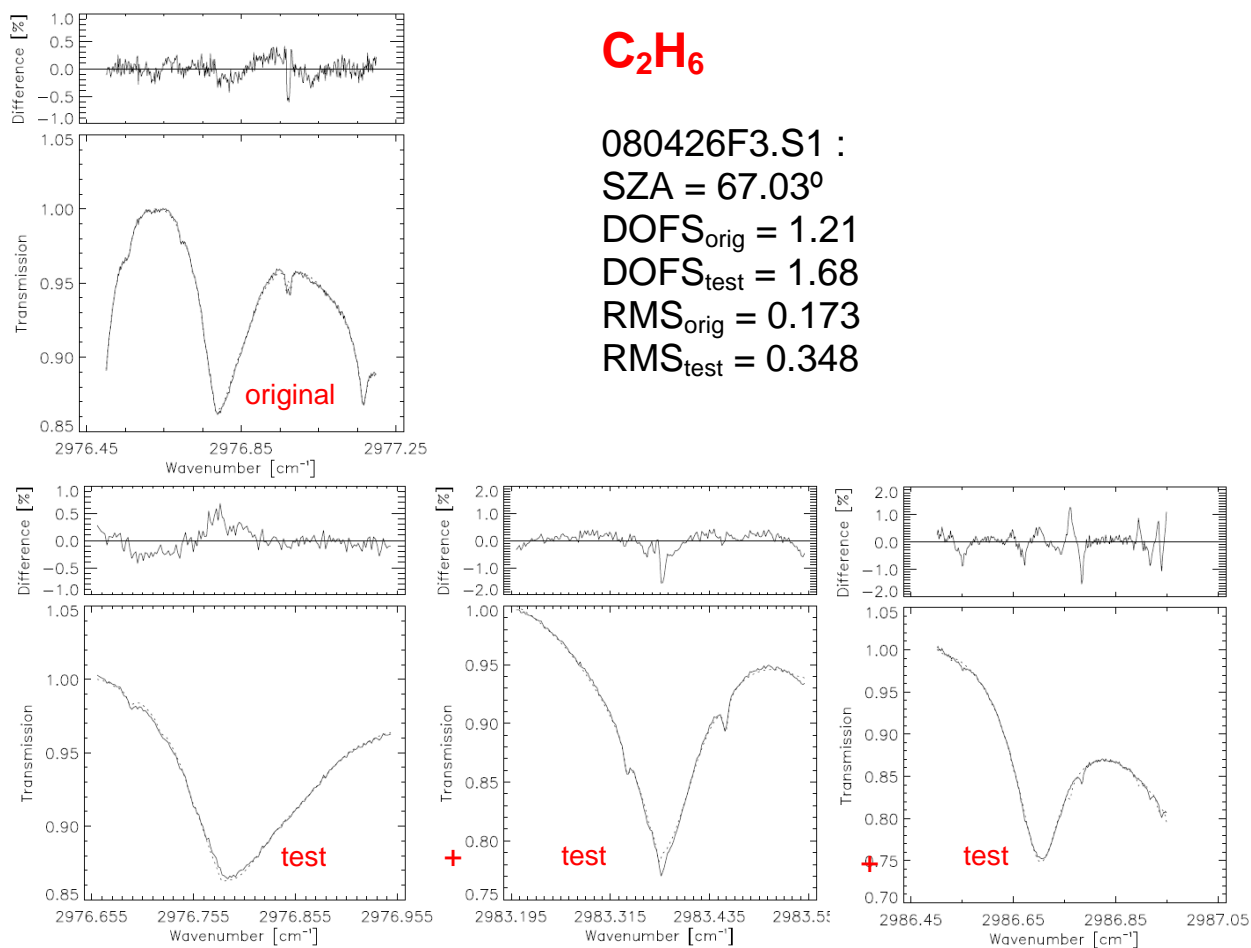
Figure A.29. Example of C$_2$H$_6$ fits for 080426F3.S1 using the original Eureka microwindow (upper panels) and the IRWG test microwindows (bottom panels).
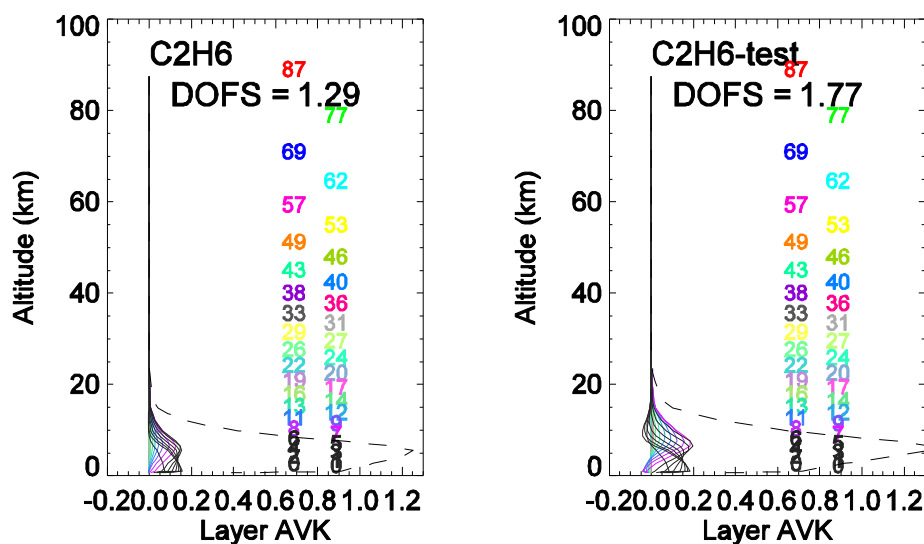
Figure A.30. Example of C_2H_6 layer averaging kernels for spectrum 070830F3.S2, SZA=71.78º for the original Eureka microwindow and the IRWG test microwindows.
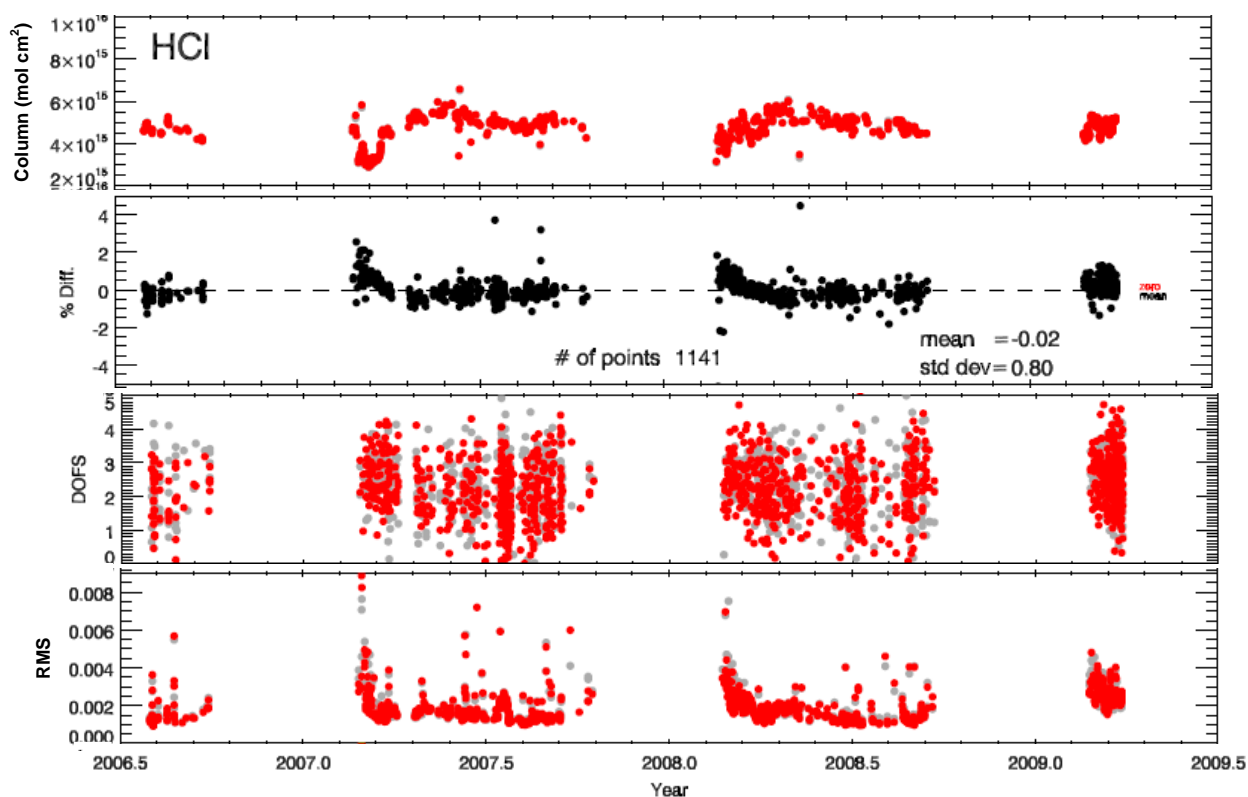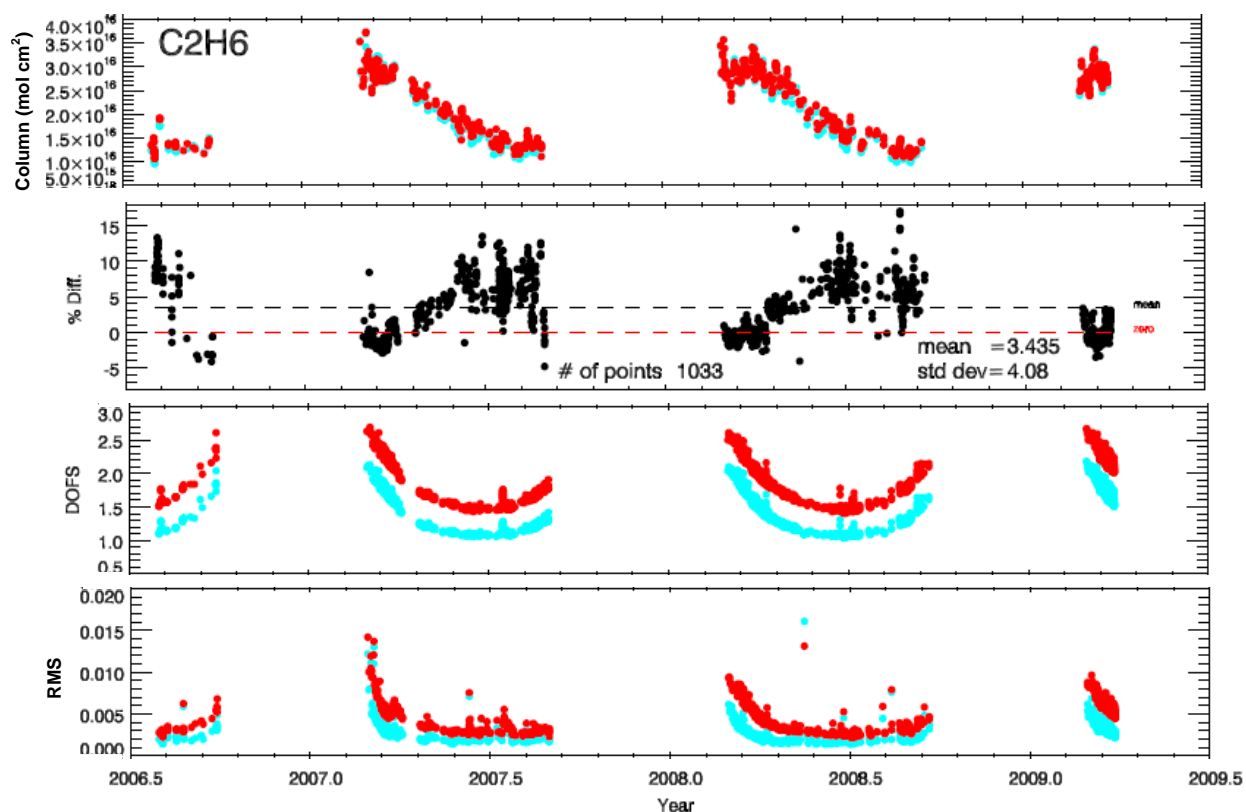

Figure A.31. C_2H_6 total columns (a), percentage differences (b) calculated using Equation 5.1, DOFS (c), and RMS fitting residuals (d) for the microwindow comparison. The mean percentage difference and the standard deviation are also specified along with the number of spectra compared. The test results are shown in red.

A.6.2 Step II
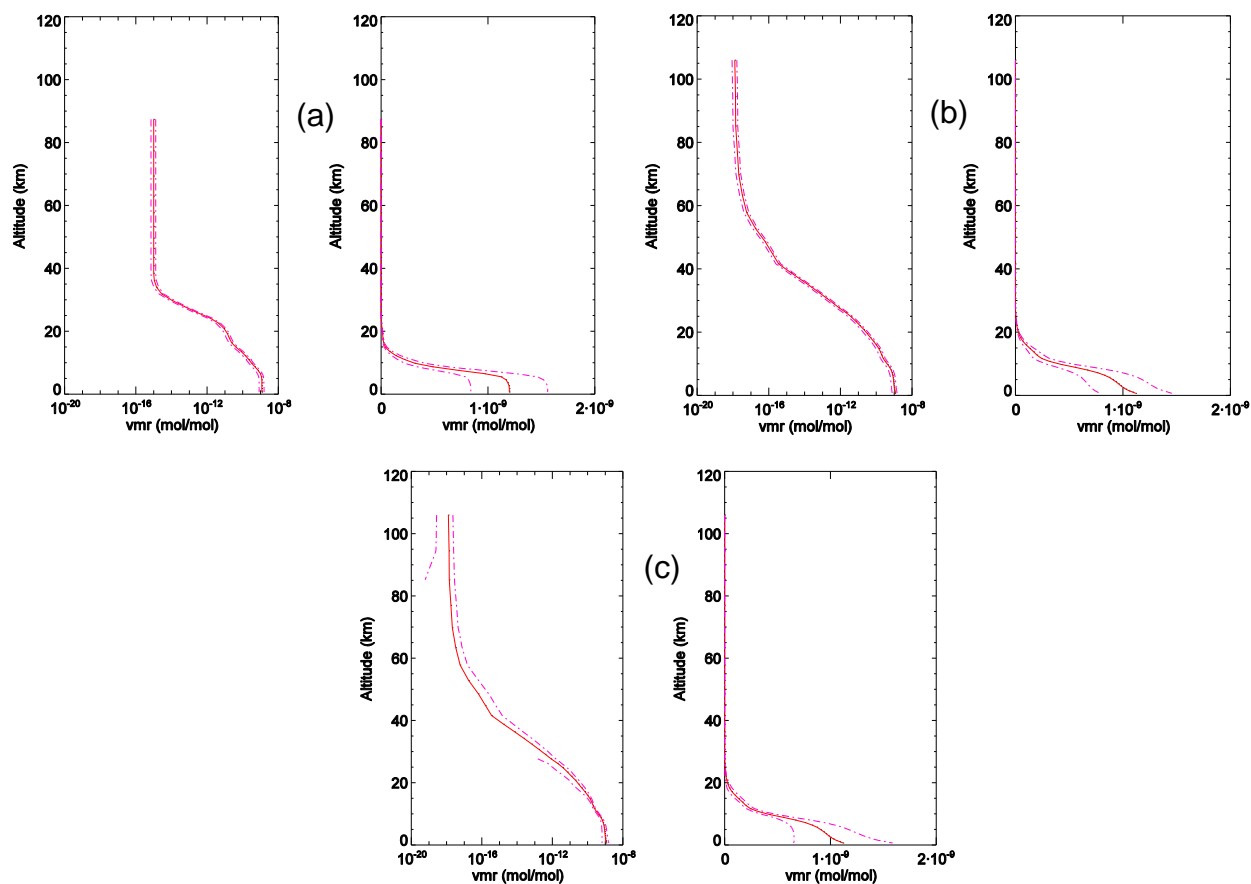
Figure A.32. The *a priori* profiles (solid line) used in the second part of the IRWG harmonization exercise for C_2H_6. The dashed lines indicate the *a priori* profile variability given by $\mathbf{S_a}$ for each altitude. Panels (a), (b), and (c) correspond to cases 1, 2, and 3, respectively, as specified in Table 5.3. The profiles are plotted on both log (left panels) and linear (right panels) scales to show the structures at small VMR.
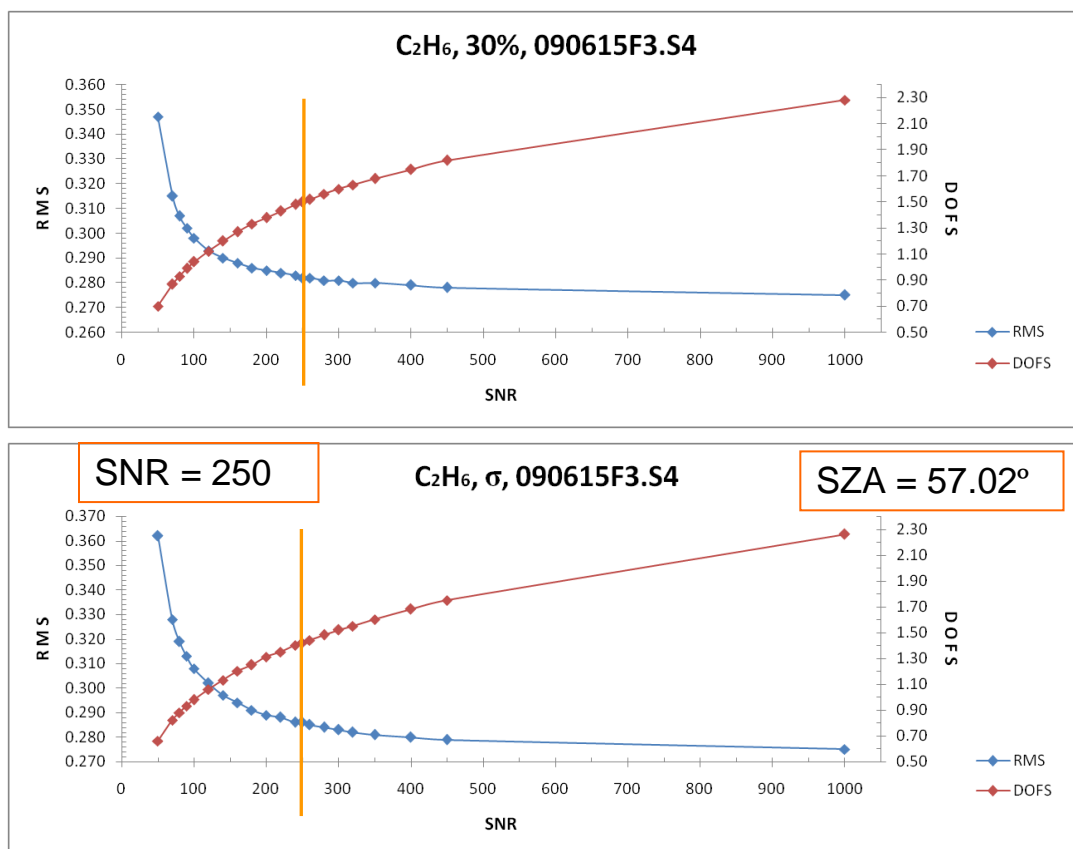
Figure A.33. C_2H_6 RMS fitting residual trade-off curves for cases 2 (top panel) and 3 (bottom panel), for spectrum 090615F3.S4.
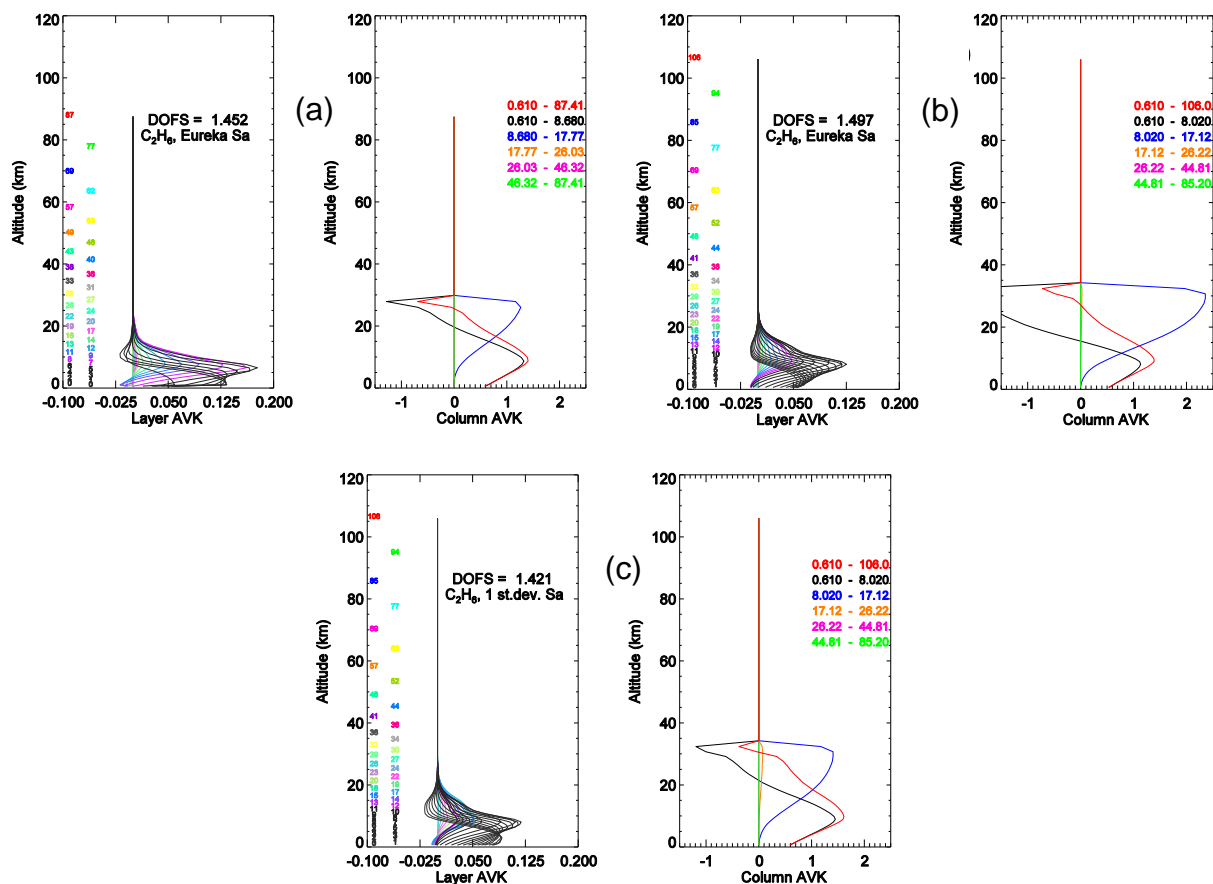
Figure A.34. C_2H_6 layer averaging kernels (left panels) and column averaging kernels (right panels) for: (a) case 1, (b) case 2, and (c) case 3, for spectrum 090615F3.S4, SZA=57.02°. For the layer AVKs the height of the layer is specified on the left with numbers (height given in km) colored as the corresponding kernel. The column AVKs are colored according to the partial column range shown in the legend.
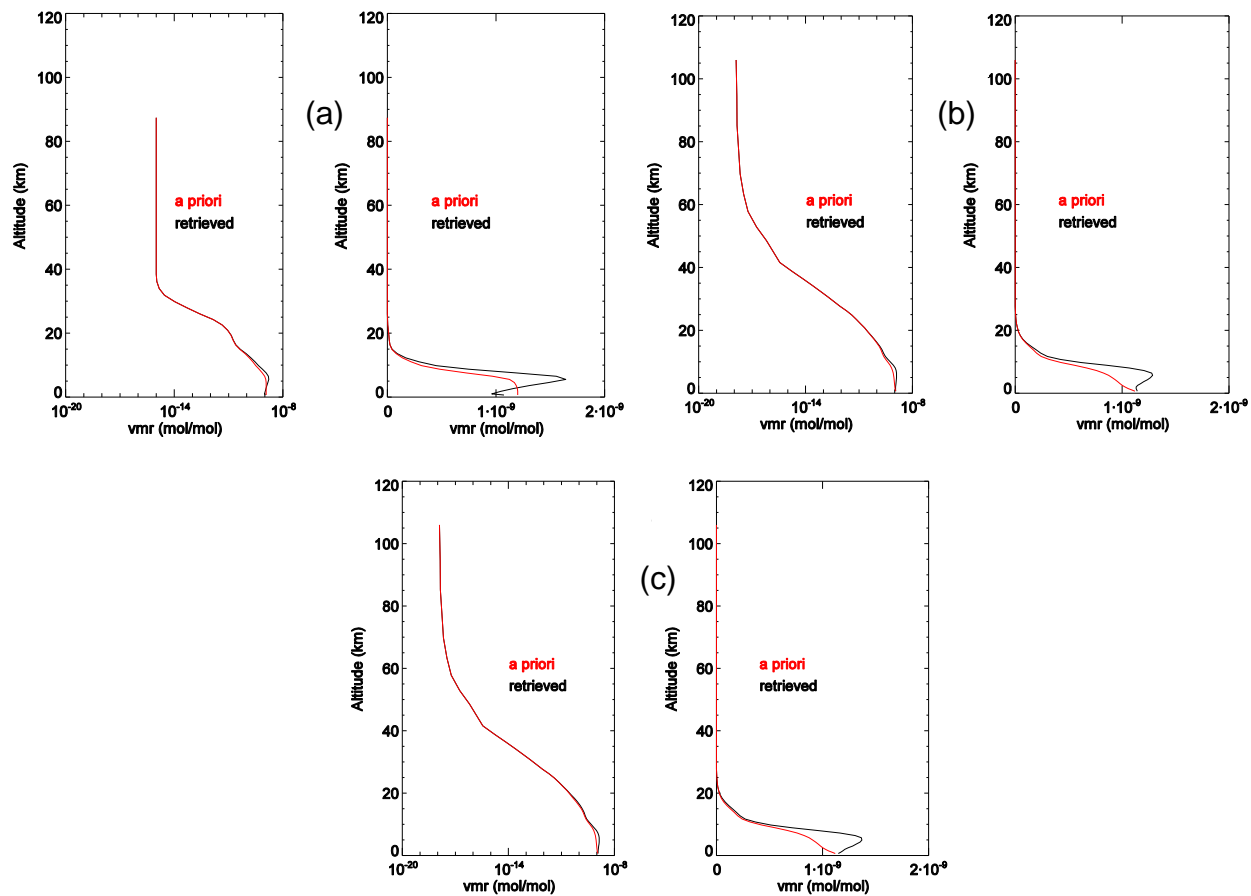
Figure A.35. C_2H_6 retrieved profiles (black) for: (a) case 1, (b) case 2, and (c) case 3, for spectrum 090615F3.S4, SZA=57.02º. The *a priori* profiles are shown in red. The profiles are plotted on both log (left panels) and linear (right panels) scales.

A.7 CO
A.7.1 Step I
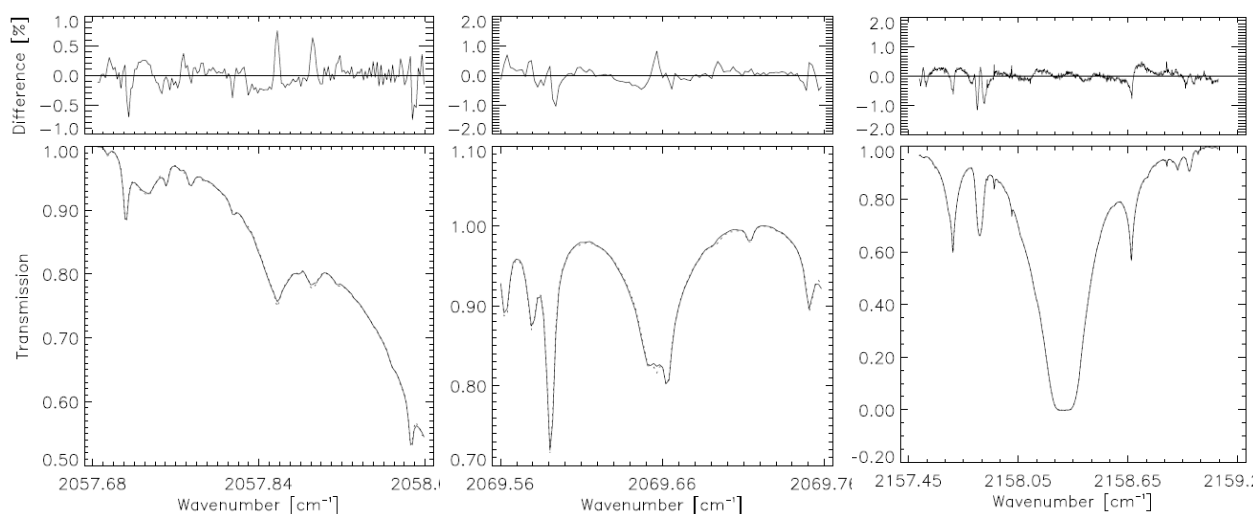
Figure A.36. Example of fits for CO retrievals for spectrum 080622F5.S2, SZA=60.78º, DOFS=2.57, and RMS=0.294. Note that for CO the original microwindows are the same as the IRWG-recommended microwindows.
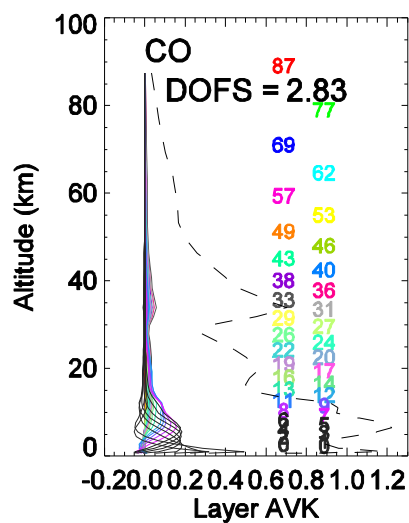
Figure A.37. Layer averaging kernels for the spectrum in Figure A.36.
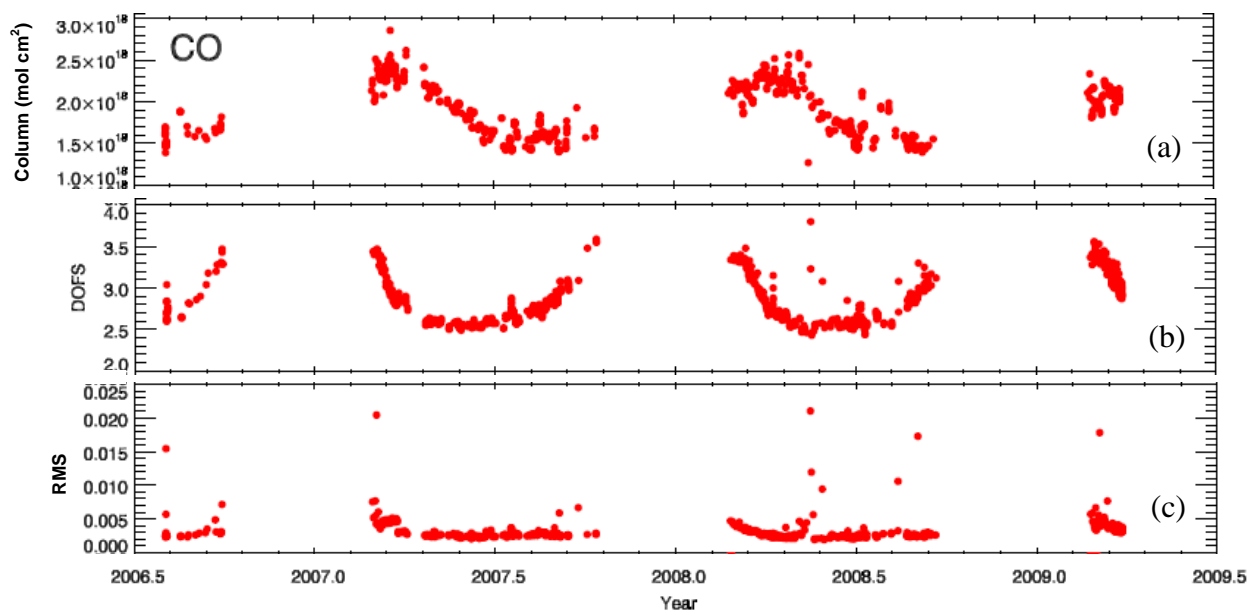
Figure A.38. (a) CO total columns for August 2006 to May 2009, (b) DOFS, and (c) RMS fitting residual for the same time interval.

A.7.2 Step II
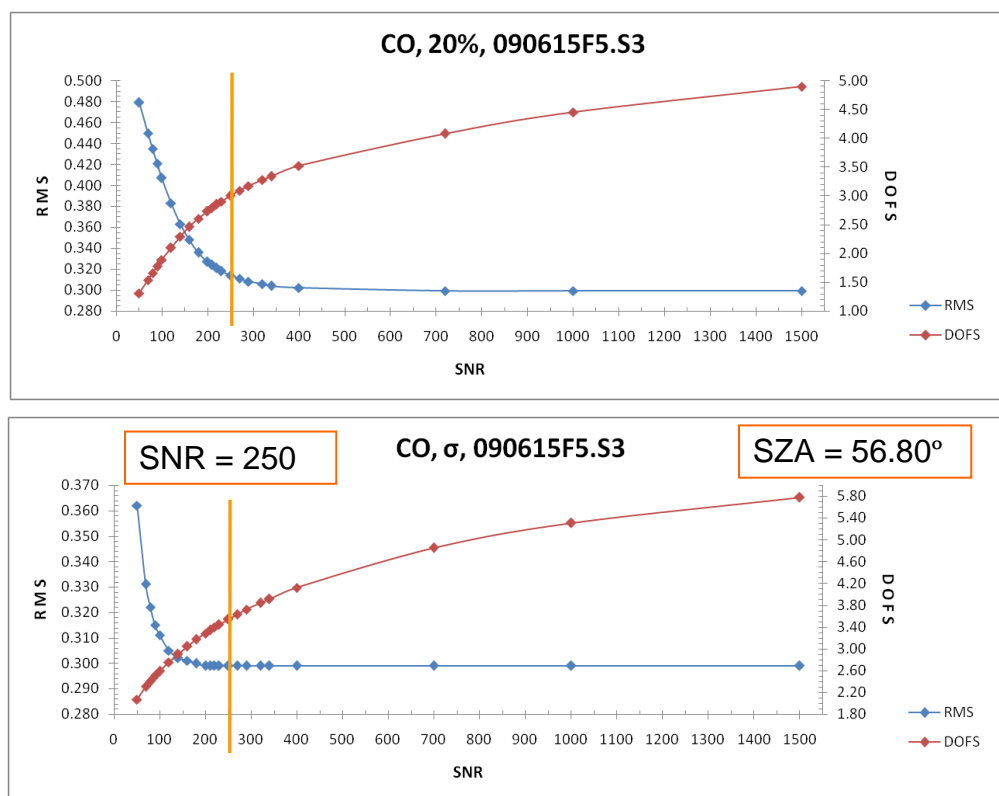
Figure A.39. CO RMS fitting residual trade-off curves for cases 2 (top panel) and 3 (bottom panel), for spectrum 090615F5.S3.

A.8 N₂O
A.8.1 Step I

N₂O

080622F3.S2 :
SZA = 59.48⁰
DOFS = 3.88
RMS = 0.191
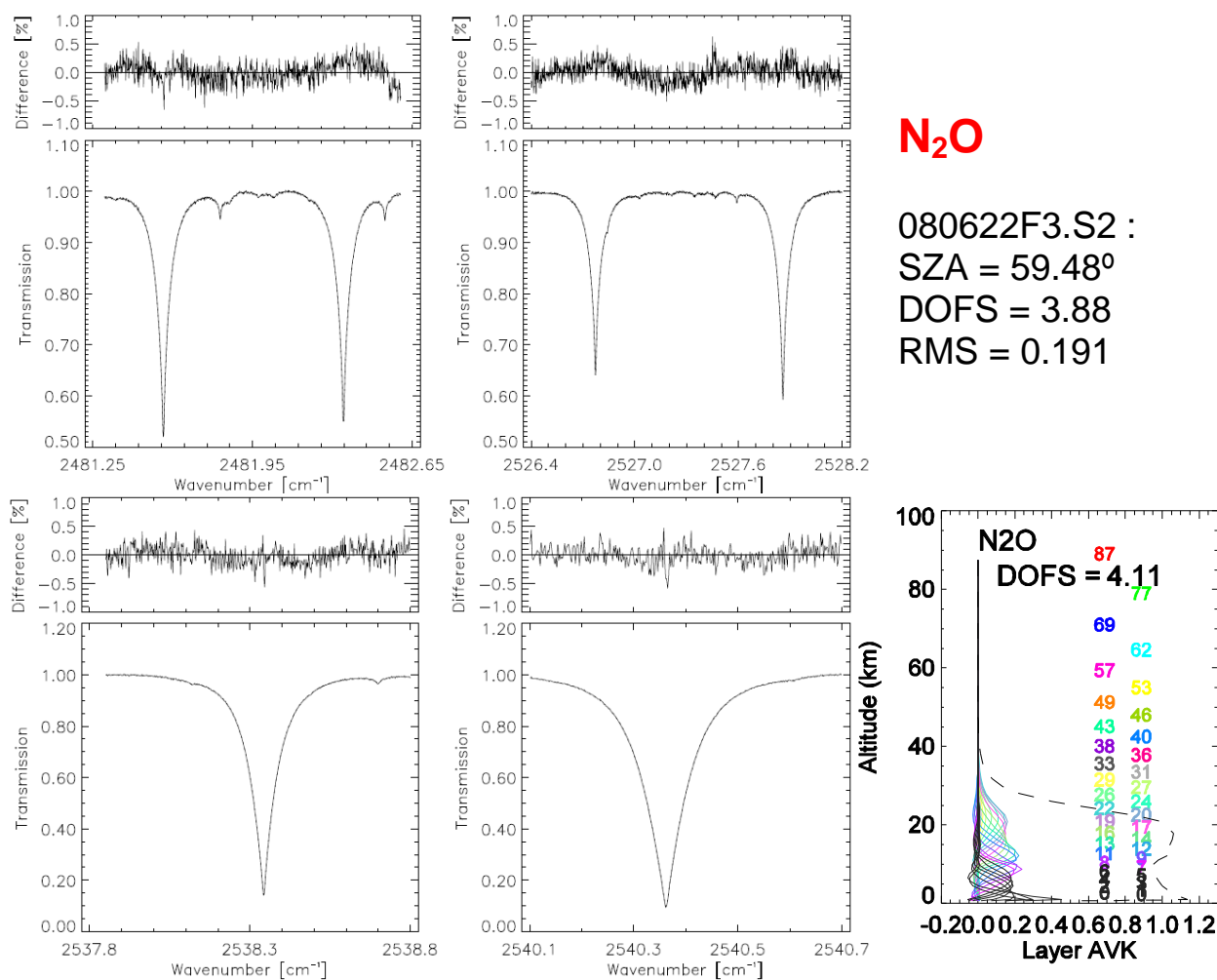
Figure A.40. Example of fits for N₂O retrievals for spectrum 080622F3.S2. The kernels are also shown for spectrum 070830F3.S2, SZA=71.78°. For this spectrum the DOFS is larger as the SZA becomes larger in late summer. Note that the original microwindows are the same as the IRWG-recommended microwindows.
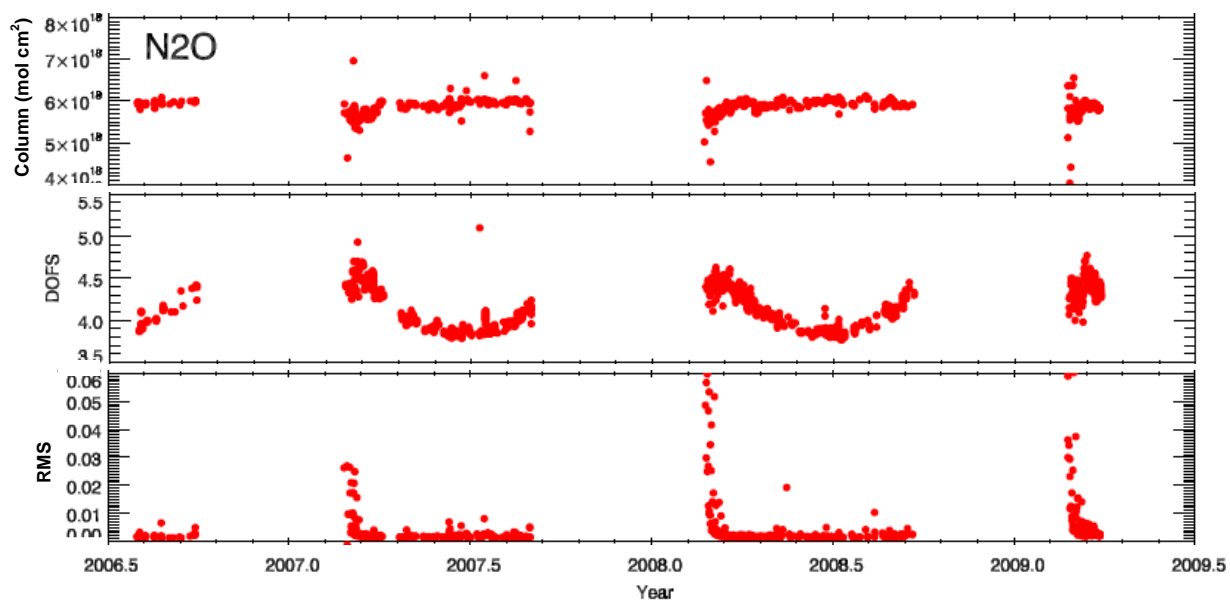
Figure A.41. (a) N$_2$O total columns for August 2006 to May 2009, (b) DOFS, and (c) RMS fitting residuals for the same time interval.

A.8.2 Step II
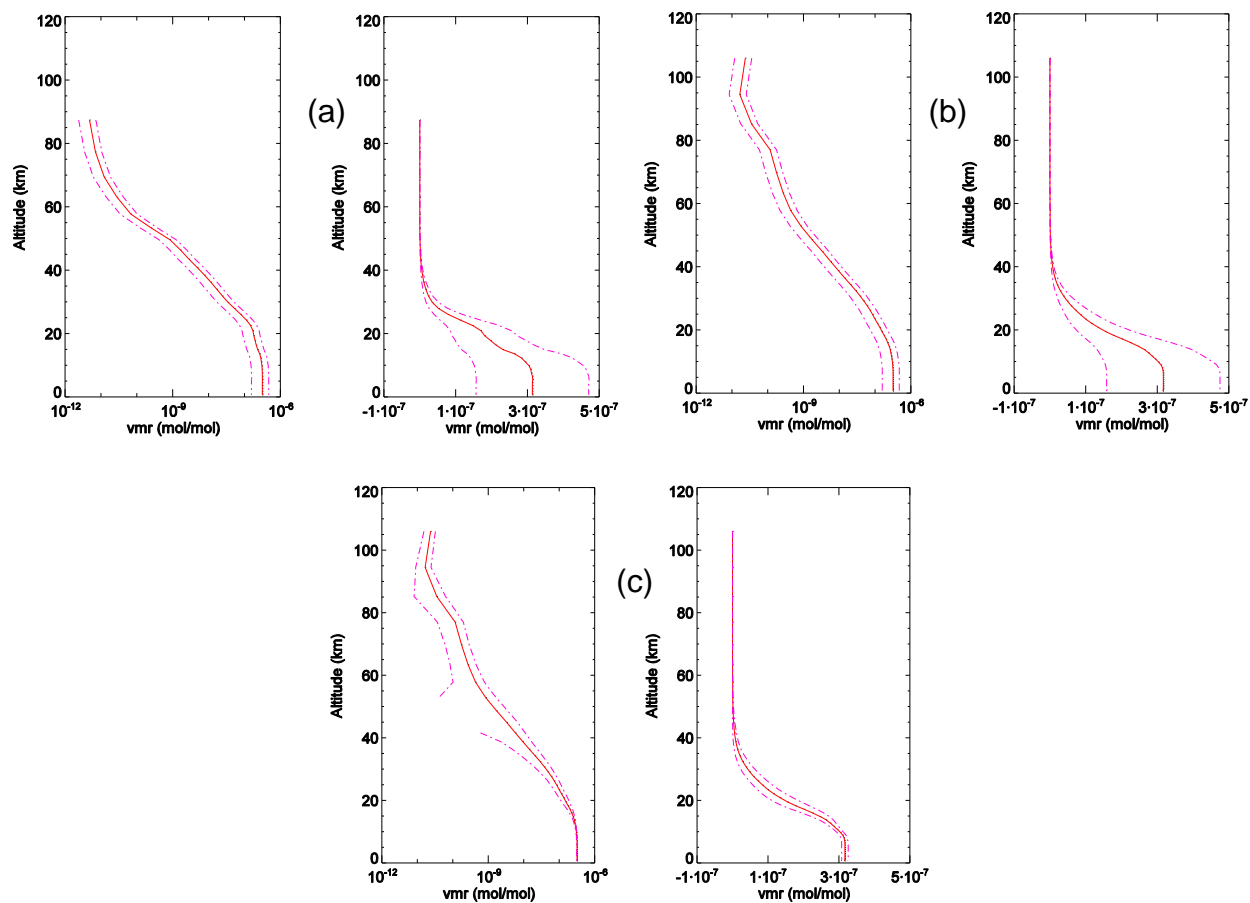
Figure A.42. The *a priori* profiles (solid line) used in the second part of the IRWG harmonization exercise for N_2O. The dashed lines indicate the *a priori* profile variability given by $\mathbf{S_a}$ for each altitude. Panels (a), (b), and (c) correspond to cases 1, 2, and 3, respectively, as specified in Table 5.3. The profiles are plotted on both log (left panels) and linear (right panels) scales.
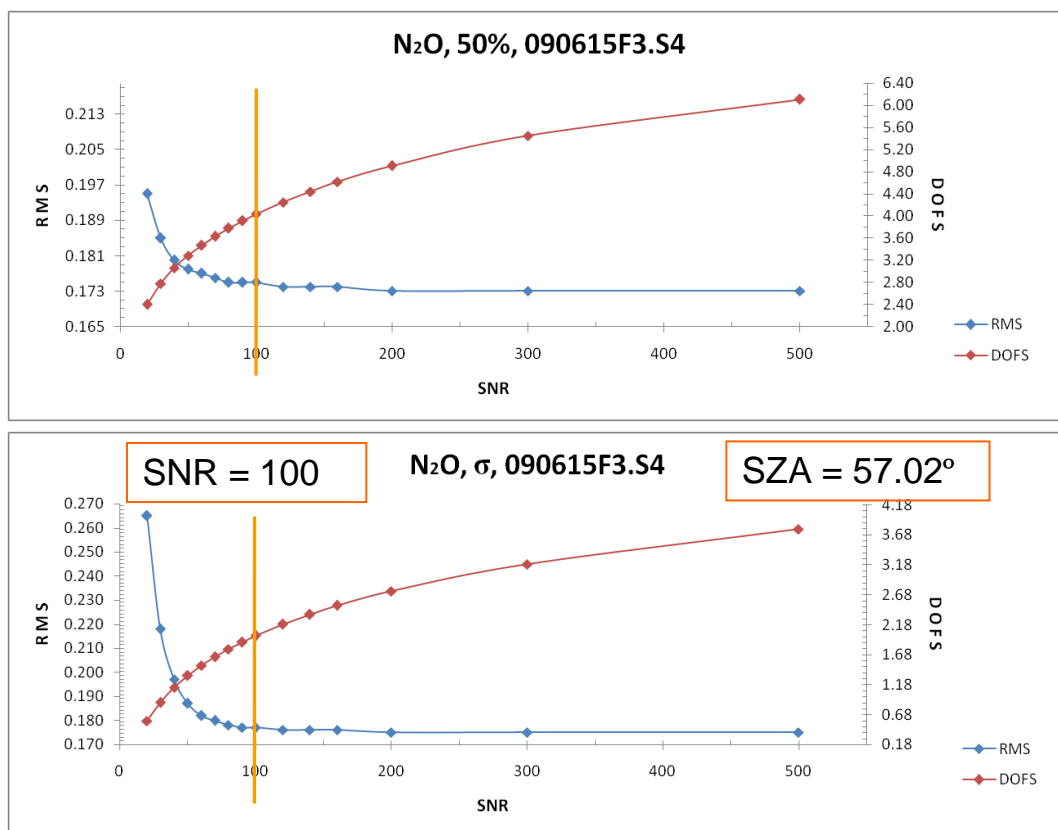
Figure A.43. N_2O RMS fitting residual trade-off curves for cases 2 (top panel) and 3 (bottom panel), for spectrum 090615F3.S4.
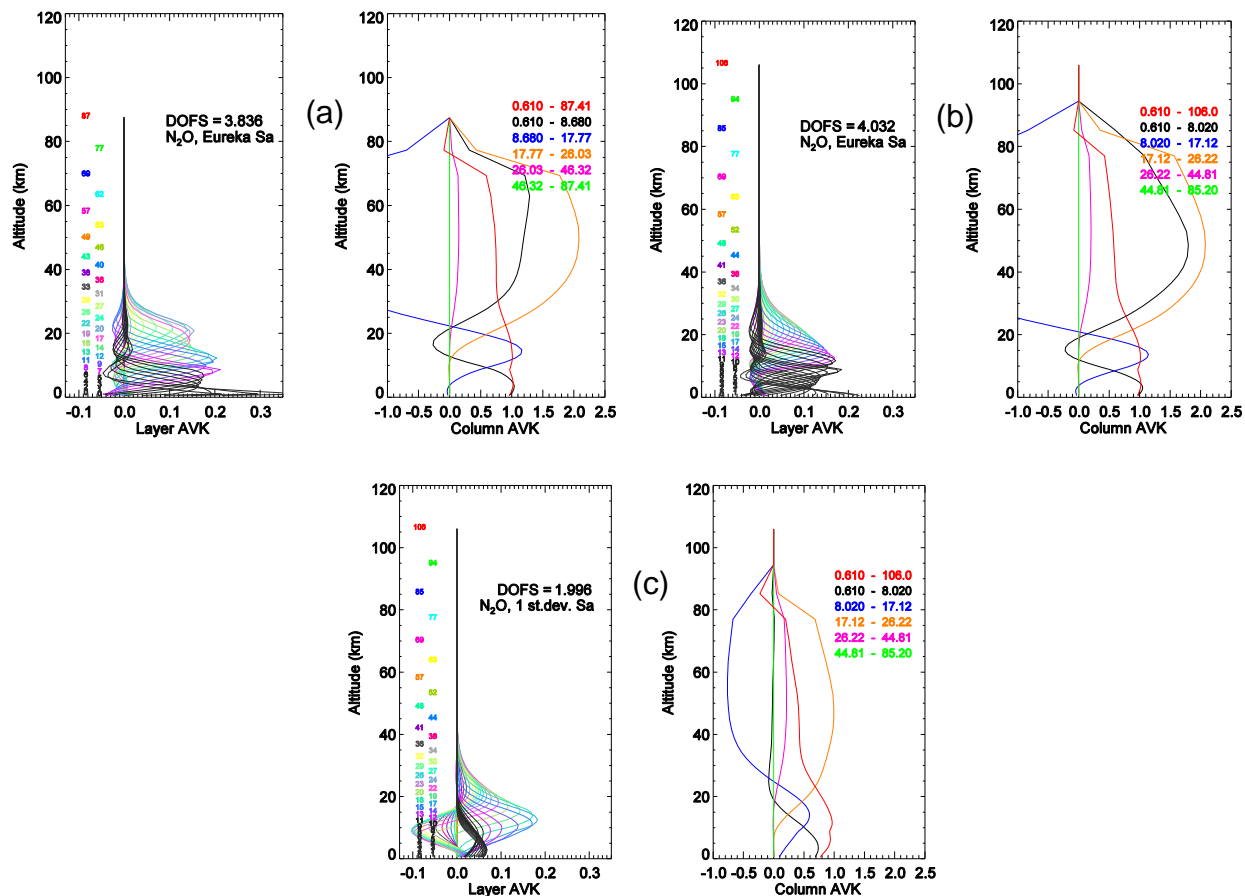
Figure A.44. N$_2$O layer averaging kernels (left panels) and column averaging kernels (right panels) for: (a) case 1, (b) case 2, and (c) case 3, for spectrum 090615F3.S4, SZA=57.02º. For the layer AVKs the height of the layer is specified on the left with numbers (height given in km) colored as the corresponding kernel. The column AVKs are colored according to the partial column range shown in the legend.
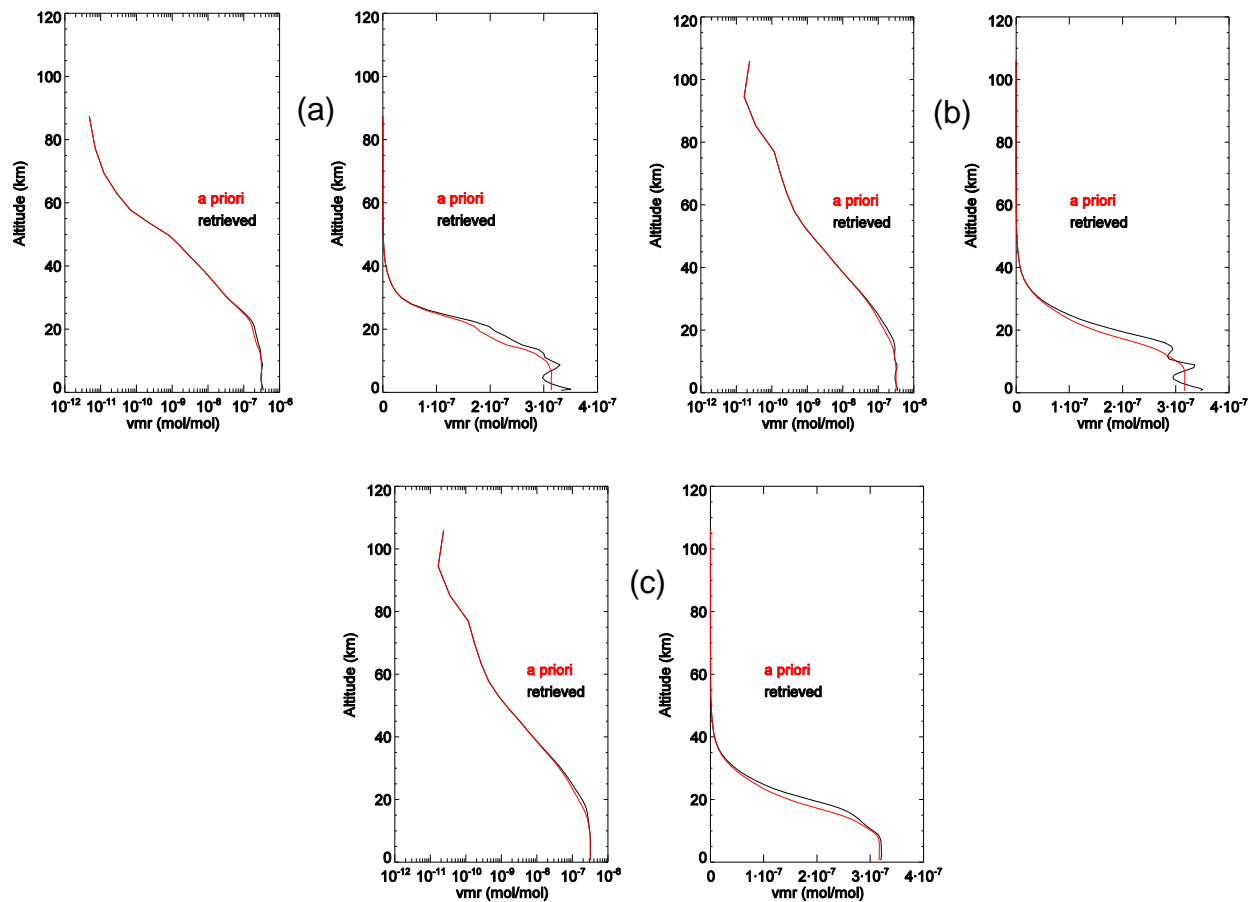
Figure A.45. N$_2$O retrieved profiles (black) for (a) case 1, (b) case 2, and (c) case 3 for spectrum 090615F3.S4, SZA=57.02º. The *a priori* profiles are shown in red. The profiles are plotted on both log (left panels) and linear (right panels) scales.

A.9 CH$_4$
A.9.1 Step I
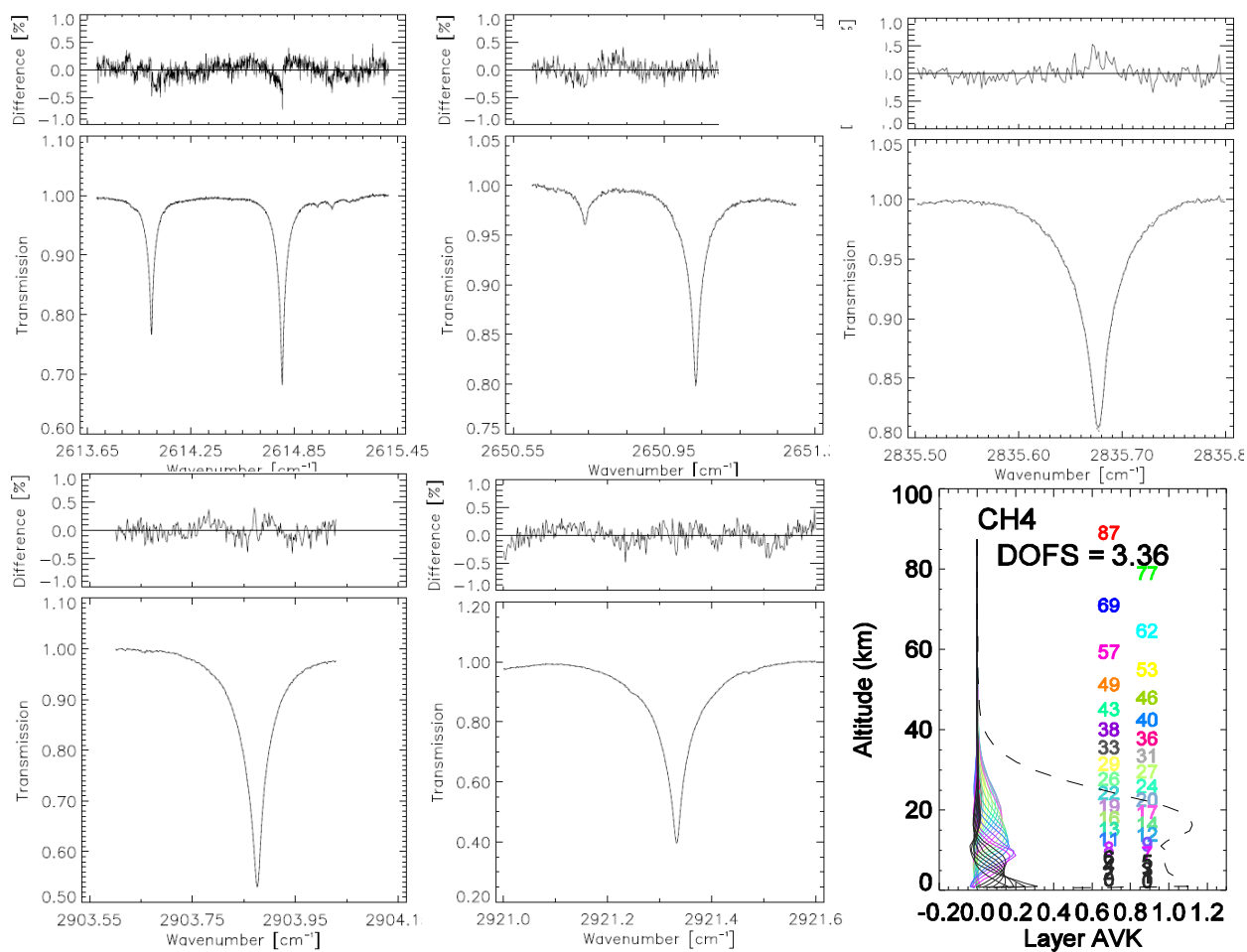
Figure A.46. Example of fits for CH$_4$ retrievals for spectrum 080622F3.S2, SZA=59.48º, DOFS=3.02, and RMS=0.153. The kernels are also shown for spectrum 070830F3.S2, SZA=71.78º. For this spectrum, the DOFS is larger as the SZA becomes larger in late summer. Note that the original microwindows are the same as the IRWG recommended microwindows.

Figure A.47. (a) CH$_4$ total columns for August 2006 to May 2009, (b) DOFS, and (c) RMS fitting residuals for the same time interval.

A.9.2 Step II
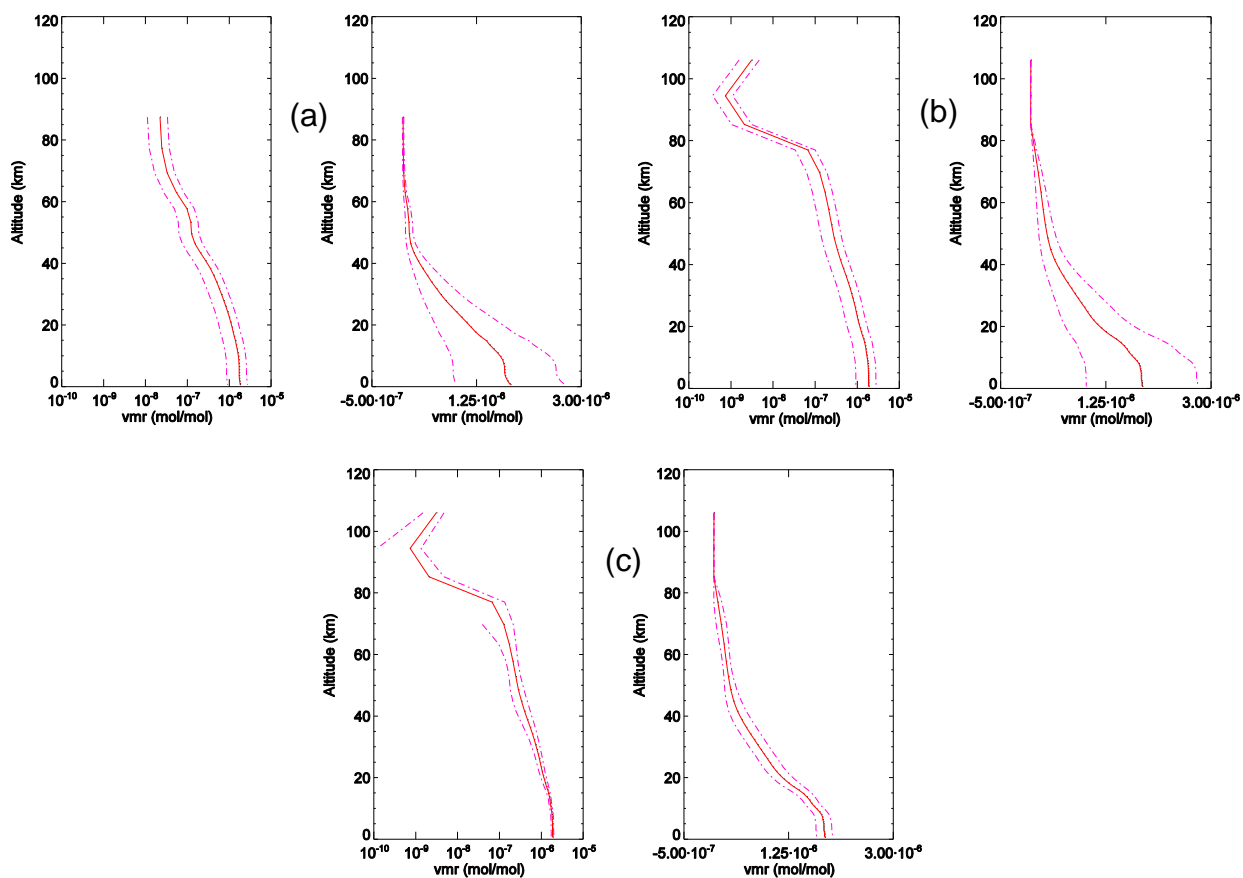
Figure A.48. The *a priori* profiles (solid line) used in the second part of the IRWG harmonization exercise for CH_4. The dashed lines indicate the *a priori* profile variability given by S_a for each altitude. Panels (a), (b), and (c) correspond to cases 1, 2, and 3, respectively, as specified in Table 5.3. The profiles are plotted on both log (left panels) and linear (right panels) scales.
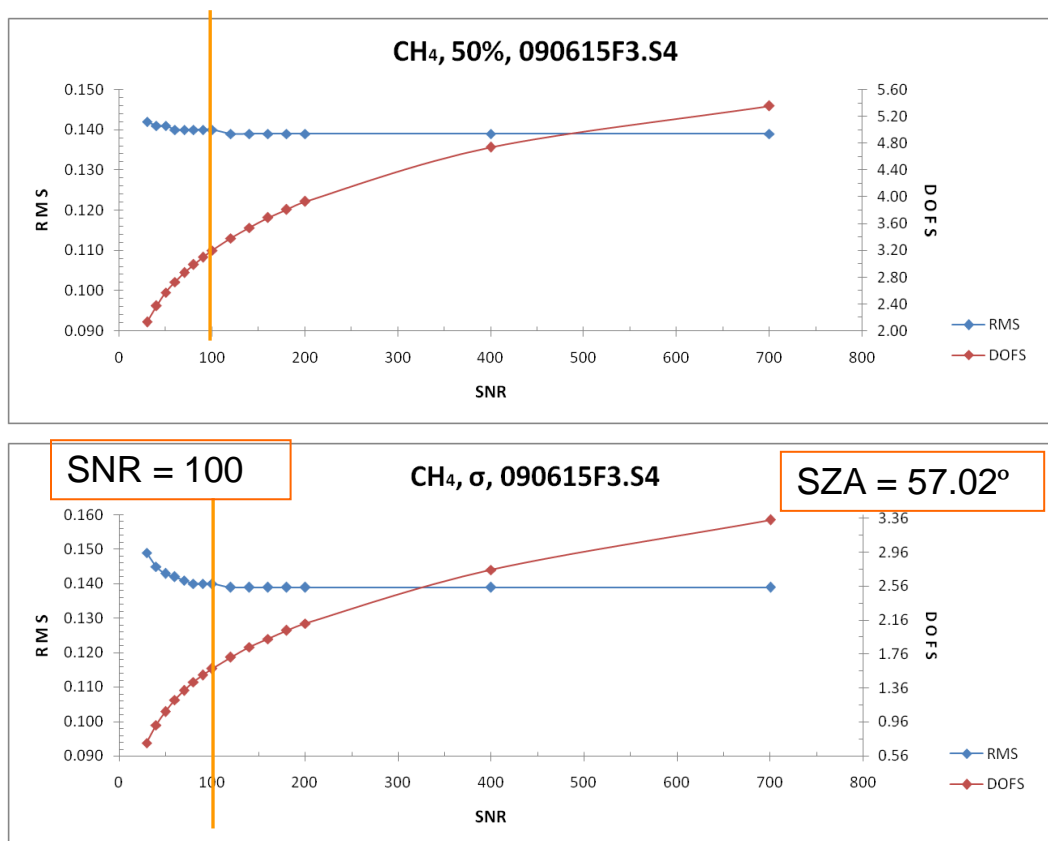
Figure A.49. CH$_4$ RMS fitting residual trade-off curves for cases 2 (top panel) and 3 (bottom panel), for spectrum 090615F3.S4.
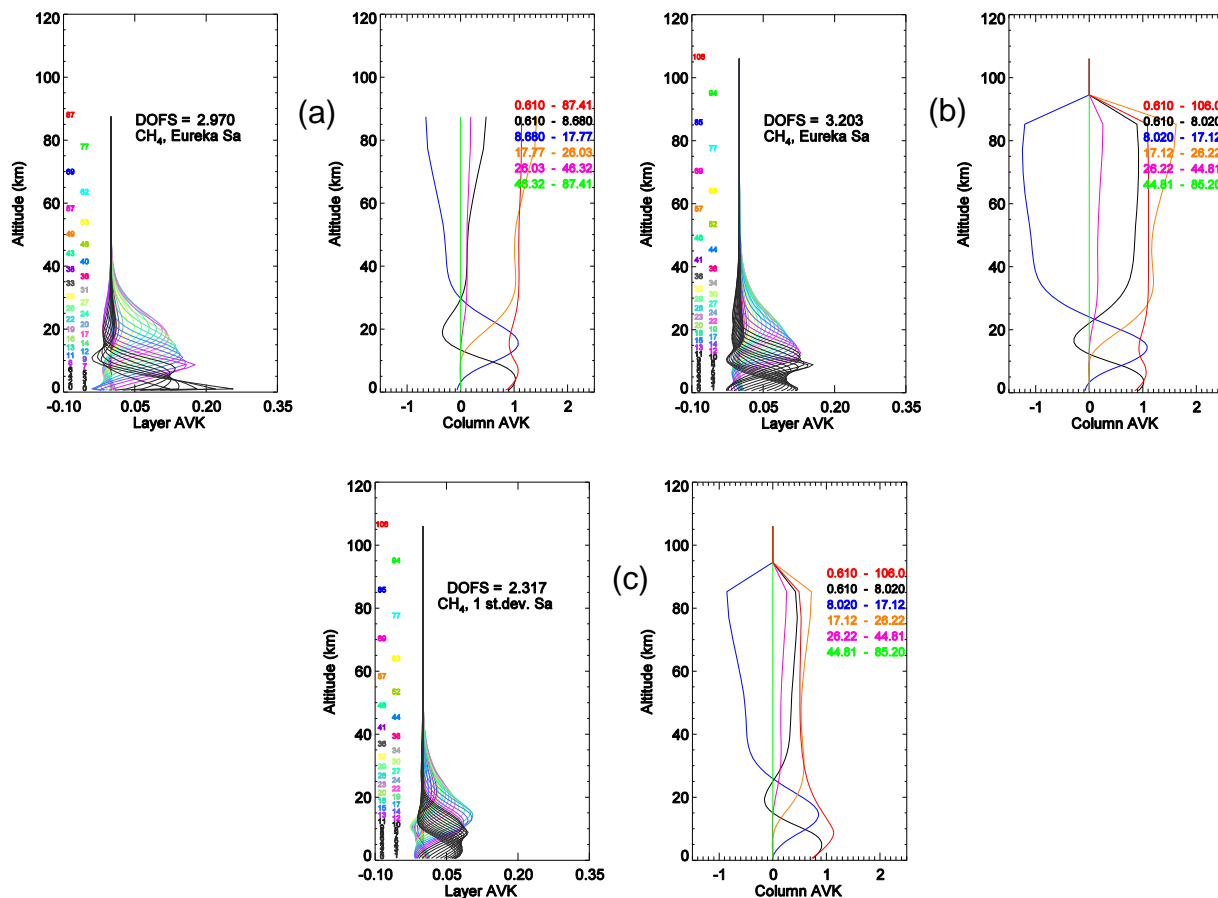
Figure A.50. CH$_4$ layer averaging kernels (left panels) and column averaging kernels (right panels) for: (a) case 1, (b) case 2, and (c) case 3, for spectrum 090615F3.S4, SZA=57.02°. For the layer AVKs, the height of the layer is specified on the left with numbers (height given in km) colored as the corresponding kernel. The column AVKs are colored according to the partial column range shown in the legend.
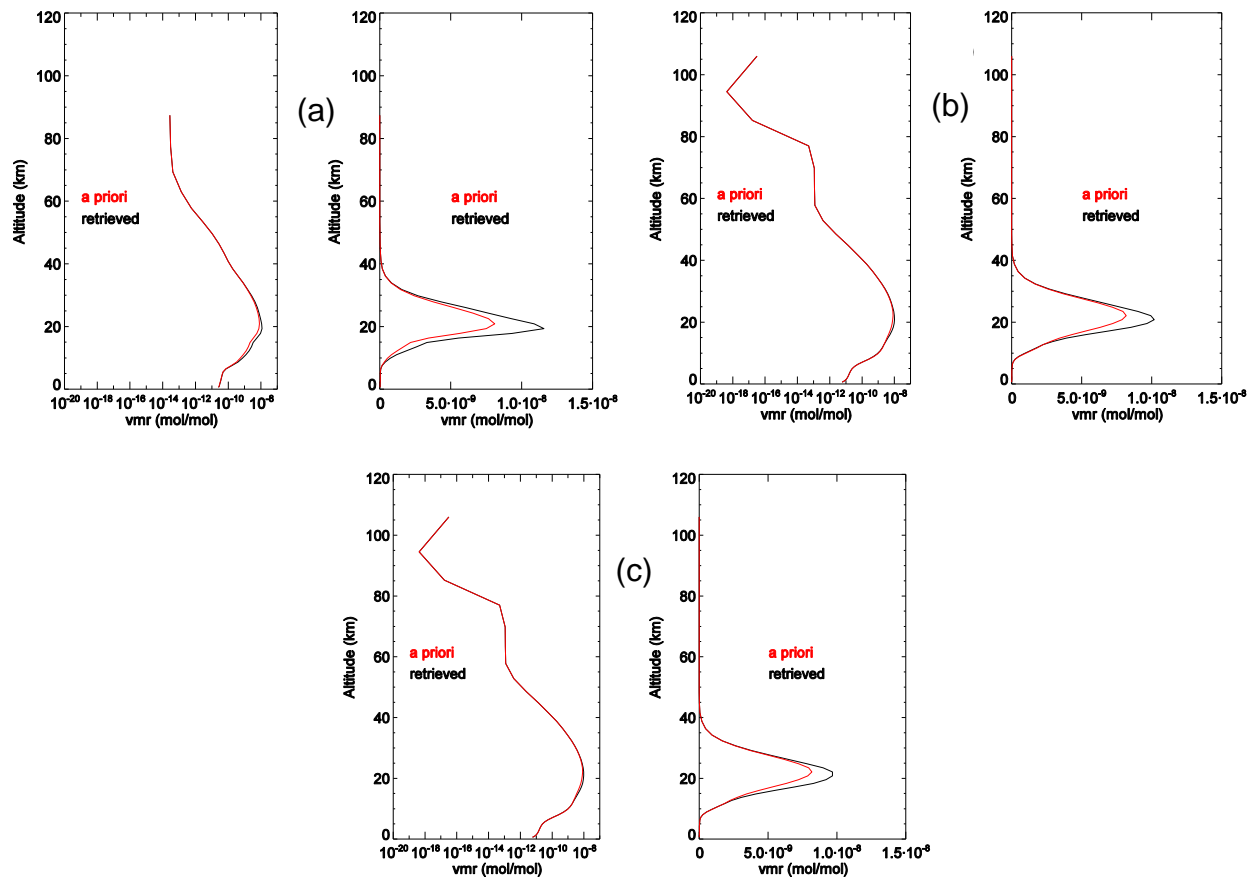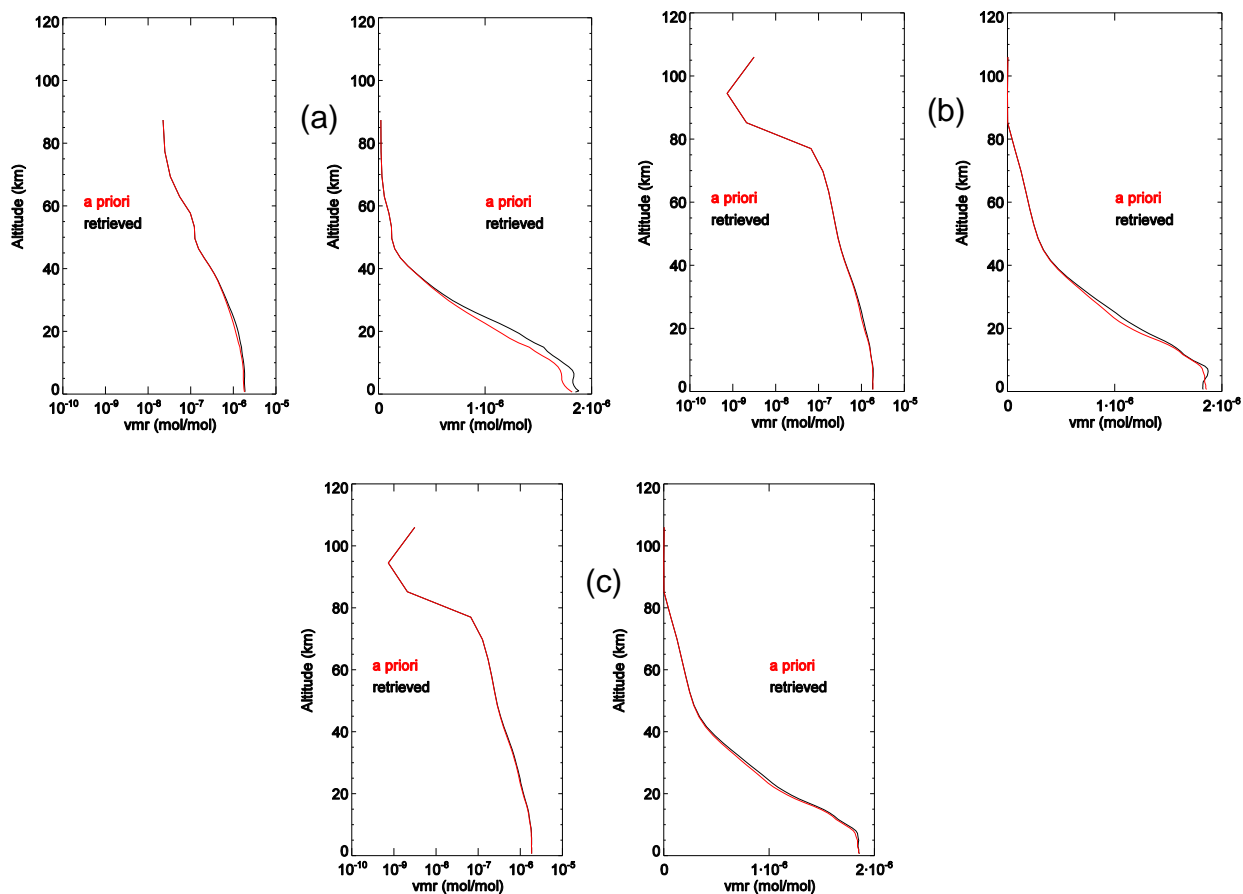
Figure A.51. CH$_4$ Retrieved profiles (black) for (a) case 1, (b) case 2, and (c) case 3, for spectrum 090615F3.S4, SZA=57.02º. The *a priori* profiles are shown in red. The profiles are plotted on both log (left panels) and linear (right panels) scales.
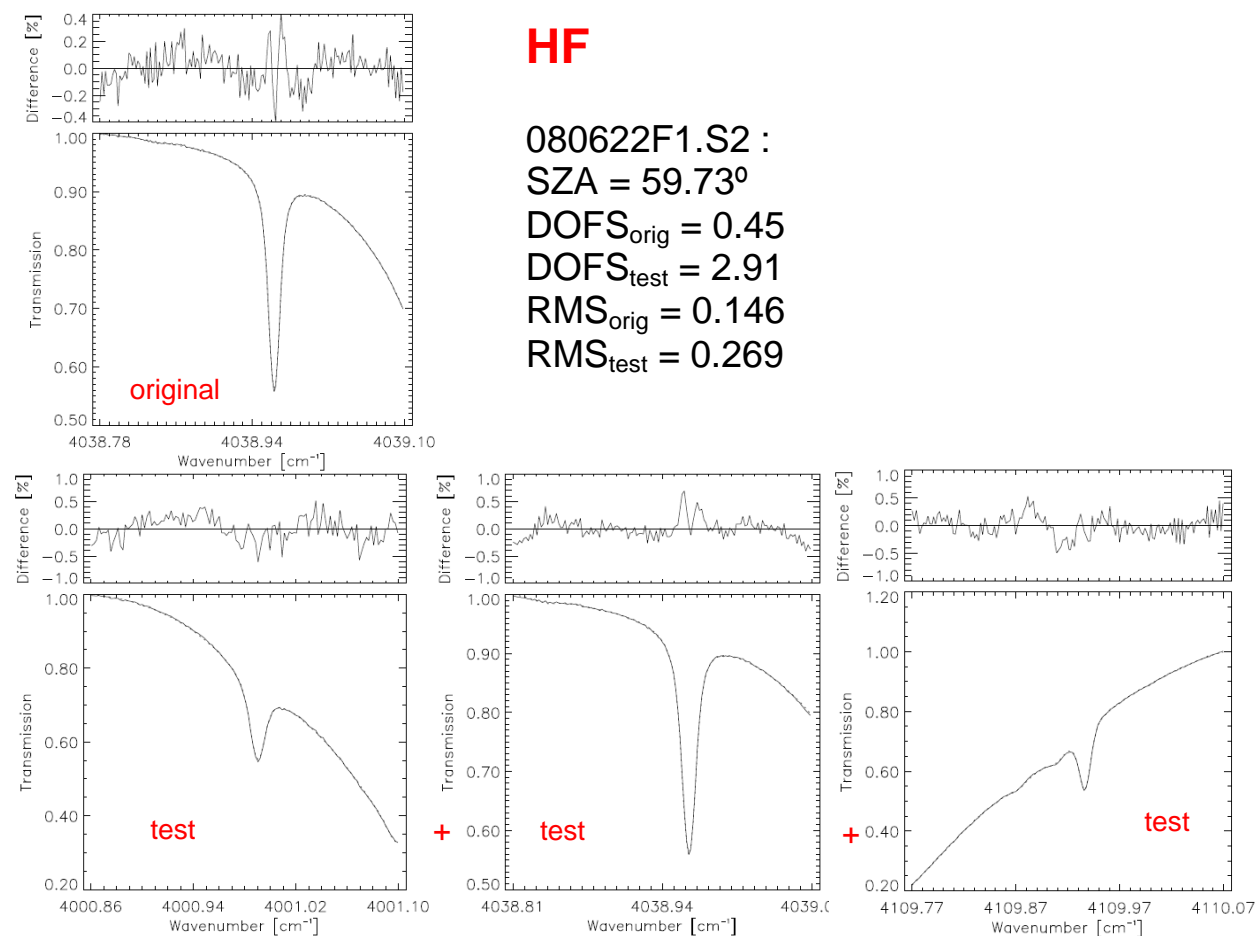
References

Abbatt, J. P., L. T. Molina, and M. J. Molina (1992), Heterogeneous interactions of $ClONO_2$ and HCl on nitric acid trihydrate at 202 K, *J. Phys. Chem.*, *96*, 7674–7679.

Adams, C., K. Strong, R. Batchelor, P. F. Bernath, C. Boone, D. Degenstein , W. H. Daffer, J. R. Drummond, E. Farahani, C. Fayt, A. Fraser, F. Goutail, F. Hendrick, F. Kolonjari, R. Lindenmaier, G. Manney, C. T. McElroy, C. A. McLinden, J. Mendonca, J.-H. Park, B. Pavlovic, A. Pazmino, C. Roth, V. Savastiouk, K.A. Walker, D. Weaver, and X. Zhao, Validation of ACE and OSIRIS ozone and NO_2 measurements using ground-based instruments at 80ºN, *Atmos. Meas. Techniques Discuss.*, 5, 517−588, 2012.

Adrian, G. P., M. Baumann, T. Blumenstock, H. Fischer, A. Friedle, L. Gerhardt, G. Maucher, H. Oelhaf, W. Scheuerpflug, P. Thomas, O. Trieschmann, and A. Wegner, (1994), First results of ground-based FTIR measurements of atmospheric trace gases in north Sweden and Greenland during EASOE, *Geophys. Res. Lett.*, *21*(13), 1343–1346.

Andrews, D. G., J. R. Holton, and C. B. Leovy (1987), *Middle Atmosphere Dynamics*, Academic Press, San Diego.

Arnold, F., and S. Spreng (1994), Balloon-borne mass spectrometer measurements of HCl and HF in the winter Arctic stratosphere, *Geophys. Res. Lett., 21(13),* 1255–1258.

Arnold, F., V. Burger, K. Gollinger, M. Roncossek, J. Schneider, and S. Spreng (1998), Observations of nitric acid perturbations in the winter Arctic stratosphere: Evidence for PSC-sedimentation, *J. Atmos. Chem, 30,* 49–59.

Austin, J., N. Butchart, and K. P. Shine (1992), Possibility of an Arctic ozone hole in a doubled-CO_2 climate, *Nature*, *360*, 221–225.

Barath, F., M. C. Chavez, R. E. Cofield, D. A. Flower, M. A. Frerking, M. B. Gram, W. M. Harris, J. R. Holden, R. F. Jarnot, W. G. Kloezeman, G. J. Klose, G. K. Lau, M. S. Loo, B. J. Maddison, R. J. Mattauch, R. P. McKlnney, G. E. Peckham, H. M. Pickett, G. Siebes, F. S.

Soltis, R. A. Suttie, J. A. Tarsala, J. W. Waters, and W. J. Wilson (1993), The Upper Atmosphere Research Satellite Microwave Limb Sounder Experiment, *J. Geophys. Res., 98*(D6)*,* 10751–10762.

Barret, B., M. De Mazière, and P. Demoulin (2002), Retrieval and characterization of ozone profiles from solar infrared spectra at the Jungfraujoch, *J. Geophys. Res., 107*, 4788−4803.

Batchelor, R.L., K. Strong, R. Lindenmaier, R. Mittermeier, H. Fast, J. R. Drummond, P. F. Fogal (2009), A new Bruker IFS 125HR FTIR spectrometer for the Polar Environment Atmospheric Research Laboratory at Eureka, Canada- measurements and comparison with the existing Bomem DA8 spectrometer, *J. Atmos. Oceanic Technol., 26*(7), 1328-1340.

Batchelor, R.L., F. Kolonjari, R. Lindenmaier, R.L. Mittermeier, W. Daffer, H. Fast, G. Manney, K. Strong, K. A. Walker (2010), Four Fourier Transform Spectrometers and the Arctic Polar Vortex: Instrument intercomparison and ACE-FTS validation at Eureka during the IPY springs of 2007 and 2008, *Atmos. Meas. Techniques*, *3*, 51–66.

Bates, D. R., and M. Nicolet (1950), Atmospheric hydrogen, *Publ. Astron. Soc. Pac*., *62*, 106–110.

Bell, R. J. (1972), *Introductory Fourier Transform Spectroscopy*, Academic Press, New York.

Bell, W., N. A. Martin, T. D. Gardiner, N. R. Swann, P. T. Woods, P. F. Fogal, and J. W. Waters (1994), Column measurements of stratospheric trace species over Åre, Sweden, in the winter of 1991−1992, *Geophys. Res. Lett*., *21*(13), 1347−1350.

Bernath, P. F., C. T. McElroy, M. C. Abrams, C. D. Boone, M. Butler, C. Camy-Peyret, M. Carleer, C. Clerbaux, P.-F. Coheur, R. Colin, P. DeCola, M. DeMaziere, J. R. Drummond, D. Dufour, W. F. J. Evans, H. Fast, D. Fussen, K. Gilbert, D. E. Jennings, E. J. Llewellyn, R. P. Lowe, E. Mahieu, J. C. McConnell, M. McHugh, S. D. McLeod, R. Michaud, C. Midwinter, R. Nassar, F. Nichitiu, C. Nowlan, C. P. Rinsland, Y. J. Rochon, N. Rowlands, K. Semeniuk, P. Simon, R. Skelton, J. J. Sloan, M.-A. Soucy, K. Strong, P. Tremblay, D. Turnbull, K. A.

Walker, I. Walkty, D. A. Wardle, V. Wehrle, R. Zander, and J Zou (2005), Atmospheric Chemistry Experiment (ACE): Mission Overview, *Geophys. Res. Lett., 32,* L15S01, doi:10.1029/2005GL022386.

Beyerle, G., R. Neuber, O. Schrems, F. Wittrock, and B. Knudsen (1994), Multiwavelength lidar measurements of stratospheric aerosols above Spitsbergen during winter 1992/93, *Geophys. Res. Lett., 21*(1)*,* 57–60.

Blom, C., H. Fischer, N. Glatthor, T. Gulde, and M. Hopfner (1994), Airborne measurements during the European Arctic Stratospheric Ozone Experiment: column amounts of HNO_3 and O_3 derived from FTIR emission sounding, *Geophys. Res. Lett., 21*(13), 1351–1354.

Boone, C. D., R. Nassar, K. A. Walker, Y. Rochon, S. D. McLeod, C. P. Rinsland, and P. F. Bernath (2005), Retrievals for the Atmospheric Chemistry Experiment Fourier Transform Spectrometer, *Appl. Opt., 44,* 7218–7231.

Brasseur, G., and M. H. Hitchman (1988), Stratospheric response to trace gas perturbations: Changes in ozone and temperature distributions, *Science*, *240*, 634–637.

Brasseur, G. P., X. X. Tie, P. J. Rasch, and F. Lefevre (1997), A three-dimensional simulation of the Antarctic ozone hole: Impact of anthropogenic chlorine on the lower stratosphere and upper troposphere, *J. Geophys. Res*., *102*(D7), 8909–8930.

Brasseur, G. and E. Remsberg (1999), *Summary of the MMII Intercomparisons for Chemistry, in: Models and Measurements Intercomparison II,* edited by J. H. Park, M. K. W. Ko, C. H. Jackman, R. A. Plumb, J. A. Kaye, and K. H. Sage, pp 190–306, NASA Langley Research Center.

Brewer, A. W. (1949), Evidence for a world circulation provided by the measurements of helium and water vapour distribution in the stratosphere, *Quart. J. Roy. Meteor. Soc, 75,* 351–363.

Brewer, A., and J. Milford (1960), The Oxford-Kew Ozonesonde, *Proc. Roy. Soc. London,* A256, 470–495.

Briegleb, B. P. (1992), Delta-Eddington approximation for solar radiation in the NCAR Community Climate Model, *J. Geophys. Res., 97*(D7), 7603–7612.

Brohede, S., C. A. McLinden, G. Berthet, C. S. Haley, D. Murtagh, and C. Sioris (2007), A stratospheric NO$_2$ climatology from Odin/OSIRIS limb-scatter measurements, *Can. J. Phys.,* 1253-1274, doi:10.1139/P07–141.

Brohede, S., C. A. McLinden, J. Urban, C. S. Haley, A. I. Jonsson, and D. Murtagh (2008), Odin stratospheric proxy NOy measurements and climatology, *Atmos. Chem. Phys., 8,* 5731–5754.

Bronnimann, S., J. Staehelin, S. F. G. Farmer, J. C. Cain, T. Swendby, T. Svenoe (2003), Total ozone observations prior to the IGY. I: A history, *Q. J. R. Meteorol. Soc., 129*, 2797–2817.

Browell, E. V., C. F. Butler, S. Ismail, P. A. Robinette, A. F. Carter, N. S. Higdon, O. B. Toon, M. R. Schoeberl, and A. F. Tuck (1990), Airborne lidar observations in the wintertime Arctic stratosphere: Polar Stratospheric Clouds, *Geophys. Res. Lett., 17*(4), 385–388.

Brühl. C., S. R. Drayson, J. M. Russell III, P. J. Crutzen, J. M. McInerney, P. N. Purcell, H. Claude, H. Gernandt, T. J. McGee, I. S. McDermid, and M. R. Gunson (1996), Halogen Occultation Experiment ozone channel validation, *J. Geophys. Res., 101*(D6)*, 10217–10240.

Brühl, C., B. Steil, G. Stiller, B. Funke, and P. Jöckel (2007), Nitrogen compounds and ozone in the stratosphere: comparison of MIPAS satellite data with the chemistry climate model ECHAM5/MESSy1, *Atmos. Chem. Phys., 7*(21), 5585–5598.

Bruker Optics User Manual, 1st edition, Bruker Optik GmbH, 2006.

Brune, W. H., D. W. Toohey, J. G. Anderson, and K. R. Chan, (1990), In situ observations of ClO in the Arctic stratosphere: ER-2 aircraft results from 59ºN to 80ºN latitude, *Geophys. Res. Lett*., *17*(4), 505–508.

Brune, W. H., J. G. Anderson, D. W. Toohey, D. W. Fahey, S. R. Kawa, R. L. Jones, D. S. McKenna, and L. R. Poole (1991), The potential for ozone depletion in the Arctic polar stratosphere, *Science*, *252*, 1260–1266.

Cariolle, D., A. Lasserre-Bigorry, and J.-F. Royer (1990), A general circulation model simulation of the springtime Antarctic ozone decrease and its impact on midlatitudes, *J. Geophys. Res*., *95*(D2), 1883–1898.

Carroll, M., R. Sanders, S. Solomon, and A. Schmeltekopf (1989), Visible and near-ultraviolet spectroscopy at McMurdo Station, Antarctica 6. Observations of BrO, *J. Geophys. Res., 94*(D14), 16633–16638.

Carslaw, K. S., Luo, B. P., Clegg, S. L., Peter, T., Brimblecombe, P., Crutzen, P. J. (1994), Stratospheric aerosol growth and HNO_3 gas phase depletion from coupled HNO_3 and water uptake by liquid particles, *Geophys. Res. Lett., 21*(23), 2479–2482.

Carslaw, K. S., and T. Peter (1997), Uncertainties in reactive uptake coefficients for solid stratospheric particles, 1, Surface chemistry, *Geophys. Res. Lett*., *24*(14), 1743–1746.

Chapman, S. (1930), On ozone and atomic oxygen in the upper atmosphere, *Philos. Mag*., *10*, 369–383.

Chipperfield, M. P., and J. A. Pyle (1988), Two-dimensional modeling of the Antarctic lower stratosphere, *Geophys. Res. Lett*., *15*(8), 875–878.

Chipperfield, M. P., and R. L. Jones (1999), Relative influences of atmospheric chemistry and transport on Arctic ozone trends, *Nature, 400*, 551–554.

Chipperfield, M. P. (2006), New version of the TOMCAT/SLIMCAT off-line chemical transport model: Intercomparison of stratospheric traces experiments, *Q. J. R. Meteorol. Soc., 132,* 1179–1203.

Chshyolkova, T., A.H. Manson, C.E. Meek, T. Aso, S.K. Avery, C.M. Hall, W. Hocking, K. Igarashi, C. Jacobi, N. Makarov, N. Mitchell, Y. Murayama, W. Singer, D. Thorsen, M. Tsutsumi (2007), Polar Vortex Evolution during Northern Hemispheric Winter 2004/05, *Ann. Geophys., 25,* 1279−1298.

Chubachi, S. (1984), Preliminary result of ozone observations at Syowa Station from February, 1982 to January, 1983, *Mem. Natl. Inst. Polar Res. Jpn. Spec. Issue*, *34*, 13–20.

Coffey, M. T., A. Goldman, J. W. Hannigan, W. G. Mankin, W. G. Schoenfeld, C. P. Rinsland, C. Bernardo, and D. W. T. Griffith (1998), Improved vibration-rotation (0-1) HBr line parameters for validating high resolution infrared atmospheric spectra measurements, *J. Quant. Spectrosc. Radiat. Transfer, 60,* 863–867.

Cornu, A. (1879), Observation de la limite ultraviolette du spectre solaire à diverses altitudes, *C. R. Hebd. Seances Acad. Sci*., *89*, 808.

Côté , J., S. Gravel, A. Méthot, A. Patoine, M. Roch, and A. Staniforth (1998), The operational CMC–MRB Global Environmental Multiscale (GEM) model. Part I: Design considerations and formulation. *Mon. Wea. Rev., 126*, 1373–1395.

Cox, R. A., A. R. MacKenzie, R. H. Müller, T. Peter, and P. J Crutzen (1994), Activation of stratospheric chlorine by reactions in liquid sulphuric acid, *Geophys. Res. Lett., 21*(13), 1439–1442.

Crewell, S., K. Künzi, H. Nett, T. Wehr, and P. Hartogh (1994), Aircraft measurements of ClO and HCl during EASOE 1991/92, *Geophys. Res. Lett*., *21*(13), 1267−1270.

Crutzen, P. J. (1970), The influence of nitrogen oxide on the atmospheric ozone content, *Q. J. R. Meteorol. Soc.*, *96*, 320–327.

Crutzen, P. J. (1971), Ozone production rates in an oxygen-hydrogen-nitrogen oxide atmosphere, *J. Geophys. Res.*, *76*(30), 7311–7327.

Daerden, F., N. Larsen, S. Chabrillat, Q. Errera, S. Bonjean, D. Fonteyn, K. Hoppel, and M. Fromm (2007), A 3D CTM with detailed online PSC microphysics: Analysis of the Antarctic winter 2003 by comparison with satellite observations. *Atmos. Chem. Phys., 7*, 1755–1772.

Danilin, M. Y., and J. C. McConnell (1995), Stratospheric effects of bromine activation on/in sulfate aerosol, *J. Geophys. Res.*, *100*(D6), 11237–11243.

Danilin, M. Y. I., M. Koike, G. K. Yue, N. B. Jones, and P. V. Johnston (1999), Nitrogen species in the post-Pinatubo stratosphere: Model analysis utilizing UARS measurements, *J. Geophys. Res., 104*(D7), 8247–8262.

de Grandpré, J., S. R. Beagley, V. I. Fomichev, E. Griffioen, J. C. McConnell, A. S. Medvedev, and T. G. Shepherd (2000), Ozone climatology using interactive chemistry: Results from the Canadian middle atmosphere model. *J. Geophys. Res., 105*(D21)*, 26475–26491.

de Grandpré, J., R. Ménard, Y. J. Rochon, C. Charette, S. Chabrillat, and A. Robichaud (2009), Radiative impact of ozone on temperature predictability in a coupled chemistry-dynamics data assimilation system, *Amer. Meteorol. Soc., 137, 679–692.

De Mazière, M., C. Vigouroux, P. F. Bernath, P. Baron, T. Blumenstock, C. Boone, C. Brogniez, V. Catoire, M. Coffey, P. Duchatelet, D. Griffith, J. Hannigan, Y. Kasai, N. Jones, E. Mahieu, G. L. Manney, C. Piccolo, C. Randall, C. Robert, C. Senten, K. Strong, J. Taylor, C. Tétard, K. A. Walker, and S.Wood (2008), Validation of ACE-FTS v2.2 methane profiles from the upper troposphere to the lower mesosphere, *Atmos. Chem. Phys., 9*, 2421–2435.

Dessler, A. E., M. D. Burrage, J.-U. Grooss, J. R. Holton, J. L. Lean, S. T. Massie, M. R. Schoeberl, A. R. Bouglass, and C. H. Jackman (1998), Selected science highlights from the first 5 years of the Upper Atmosphere Research Satellite (UARS) program, *Rev. Geophys*., *36*, 183–210.

de Zafra, R. L., M. Jaramillo, A. Parrish, P. Solomon, B. Connor, and J. Barnett (1987), High concentrations of chlorine monoxide at low altitudes in the Antarctic spring stratosphere: Diurnal variation, *Nature*, *328*, 408–411.

de Zafra, R. L., M. Jaramillo, J. Barrett, L. K. Emmons, P. M. Solomon, and A. Parrish (1989), New observations of a large concentration of ClO in the springtime lower stratosphere over Antarctica and its implications for ozone-depleting chemistry, *J. Geophys. Res*., *94*(D9), 11423–11428.

de Zafra, R. L., L. K. Emmons, J. M. Reeves, and D. T. Shindell (1994), An overview of millimeter-wave spectroscopic measurements of chlorine monoxide at Thule, Greenland, February–March, 1992: Vertical profiles, diurnal variation, and longer-term trends, *Geophys. Res. Lett*., *21*(13), 1271–1274.

Dibb, J. E., E. Scheuer, M. Avery, J. Plant, and G. Sachse (2006), In situ evidence for renitrification in the Arctic lower stratosphere during the polar aure validation experiment (PAVE), *Geophys. Res. Lett., 33,* L12815, doi:10.1029/2006GL026243.

Dils, B., M. De Mazière, J. F. Müller, T. Blumenstock, M. Buchwitz, R. de Beek, P. Demoulin, P. Duchatelet, H. Fast, C. Frankenberg, A. Gloudemans, D. Griffith, N. Jones, T. Kerzenmacher, I. Kramer, E. Mahieu, J. Mellqvist, R. L. Mittermeier, J. Notholt, C. P. Rinsland, H. Schrijver, D. Smale, A. Strandberg, A. G. Straume, W. Stremme, K. Strong, R. Sussmann, J. Taylor, M. van den Broek, V. Velazco, T. Wagner, T. Warneke, A. Wiacek, and S. Wood (2006), Comparisons between SCIAMACHY and ground-based FTIR data for total columns of CO, CH_4, CO_2 and N_2O, *Atmos. Chem. Phys., 6,* 1953–1976.

Dobson, G. M. B. and D. N. Harrison (1926), Observations of the amount of ozone in the Earth's atmosphere and its relation to other geophysical conditions, *Proc. R. Soc. London, A110,* 660–693.

Dobson, G. M. B. (1968), Forty years' research on atmospheric ozone at Oxford: A history, *Appl. Opt.*, *7*, 387–405.

Donovan, D. P., H. Fast, Y. Makino, J. C. Bird, A. I. Carswell, J. Davies, T. J. Duck, J. W. Kaminski, C. T. McElroy, R. L. Mittermeier, S. R. Pal, V. Savastiouk, D. Velkov, and J. A. Whiteway (1997), Ozone, column ClO, and PSC measurements made at the NDSC Eureka observatory (80ºN, 86ºW) during the spring of 1997, *Geophys. Res. Lett., 24*(22), 2709–2712.

Douglass, A. R., R. S. Stolarski, M. R. Schoeberl, C. H. Jackman, M. L. Gupta, P. A. Newman, J. E. Nielsen, and E. L. Fleming (2008), Relationship of loss, mean age of air and the distribution of CFCs to stratospheric circulation and implications for atmospheric lifetimes, *J. Geophys. Res.*, *113*, D14309, doi: 10.1029/2007JD009575.

Drdla, K. and Schoeberl, M. R. (2002), Microphysical modeling of the 1999–2000 Arctic winter: 2. Chlorine activation and ozone depletion, *J. Geophys. Res., 108*(D5), 8319−8334.

Duchatelet, P., P. Demoulin, F. Hase, R. Ruhnke, W. Feng, M. P. Chipperfield, P. F. Bernath, C. D. Boone, K. A. Walker, and E. Mahieu (2010), Hydrogen fluoride total and partial column time series above the Jungfraujoch from long-term FTIR measurements: Impact of the line-shape model, characterization of the error budget and seasonal cycle, and comparison with satellite and model data, *J. Geophys. Res., 115,* D22306, doi:10.1029/2010JD014677.

Dufour, G., R. Nassar, C. D. Boone, R. Skelton, K. A. Walker, P. F. Bernath, C. P. Rinsland, K. Semeniuk, J. J. Jin, J. C. McConnell, and G. L. Manney (2006), Partitioning between the inorganic chlorine reservoirs HCl and ClONO2 during the Arctic winter 2005 from the ACE-FTS, *Atmos. Chem. Phys., 6,* 2355–2366.

Dupuy, E., K. A. Walker, J. Kar, C. D. Boone, C. T. McElroy, P. F. Bernath, J. R. Drummond, R. Skelton, S. D. McLeod, R. C. Hughes, C. R. Nowlan, D. G. Dufour, J. Zou, F. Nichitiu, K. Strong, P. Baron, R. M. Bevilacqua, T. Blumenstock, G. E. Bodeker, T. Borsdorff, A. E. Bourassa, H. Bovensmann, I. S. Boyd, A. Bracher, C. Brogniez, J. P. Burrows, V. Catoire, S. Ceccherini, S. Chabrillat, T. Christensen, M. T. Coffey, U. Cortesi, J. Davies, C. De Clercq, D. A. Degenstein, M. De Mazière, P. Demoulin, J. Dodion, B. Firanski, H. Fischer, G. Forbes, L. Froidevaux, D. Fussen, P. Gerard, S. Godin-Beekmann, F. Goutail, J. Granville, D. Griffith, C. S. Haley, J. W. Hannigan, M. Höpfner, J. J. Jin, A. Jones, N. B. Jones, K. Jucks, A. Kagawa, Y. Kasai, T. E. Kerzenmacher, A. Kleinböhl, A. R. Klekociuk, I. Kramer, H. Küllmann, J. Kuttippurath, E. Kyrölä, J.-C. Lambert, N. J. Livesey, E. J. Llewellyn, N. D. Lloyd, E. Mahieu, G. L. Manney, B. T. Marshall, J. C. McConnell, M. P. McCormick, I. S. McDermid, M. McHugh, C. A. McLinden, J. Mellqvist, K. Mizutani, Y. Murayama, D. P. Murtagh, H. Oelhaf, A. Parrish, S. V. Petelina, C. Piccolo, J.-P. Pommereau, C. E. Randall, C. Robert, C. Roth, M. Schneider, C. Senten, T. Steck, A. Strandberg, K. B. Strawbridge, R. Sussmann, D. P. J. Swart, D. W. Tarasick, J. R. Taylor, C. Tétard, L. W. Thomason, A. M. Thompson, M. B. Tully, J. Urban, F. Vanhellemont, C. Vigouroux, T. von Clarmann, P. von der Gathen, C. von Savigny, J. W. Waters, J. C. Witte, M. Wolff, and J. M. Zawodny (2009), Validation of ozone measurements from the Atmospheric Chemistry Experiment (ACE), *Atmos. Chem. Phys., 9,* 287–343.

Emmons, L., J. Reeves, D. Shindell, and R. deZafra (1994), N_2O as an indicator of Arctic vortex dynamics: Correlations with O3 over Thule, Greenland in February and March, 1992, *Geophys. Res. Lett., 21*(13), 1275–1278.

Errera, Q., F. Daerden, S. Chabrillat, J. C. Lambert, W. A. Lahoz, S. Viscardy, S. Bonjean, and D. Fonteyn (2008), 4D-Var assimilation of MIPAS chemical observations: Ozone and nitrogen dioxide analyses. *Atmos. Chem. Phys., 8,* 6169–6187.

Eyring, V., I. Cionni, J. F. Lamarque, H. Akiyoshi, G. E. Bodeker, A. J. Charlton-Perez, S. M. Frith, A. Gettelman, D. E. Kinnison, T. Nakamura, L. D. Oman, S. Pawson, and Y. Yamashita (2010a), Sensitivity of 21st century stratospheric ozone to greenhouse gas scenarios, *Geophys. Res. Lett., 37,* L16807, doi:10.1029/2010GL044443.

Eyring, V., I. Cionni, G. E. Bodeker, A. J. Charlton-Perez, D. E. Kinnison, J. F. Scinocca, D. W. Waugh, H. Akiyoshi, S. Bekki, M. P. Chipperfield, M. Dameris, S. Dhomse, S. M. Frith, H. Garny, A. Gettelman, A. Kubin, U. Langematz, E. Mancini,M. Marchand, T. Nakamura, L. D. Oman, S. Pawson, G. Pitari, D. A. Plummer, E. Rozanov, T. G. Shepherd, K. Shibata, W. Tian, P. Braesicke, S. C. Hardiman, J. F. Lamarque, O. Morgenstern, J. A. Pyle, D. Smale, and Y. Yamashita (2010), Multi-model assessment of stratospheric ozone return dates and ozone recovery in CCMVal-2 models, *Atmos. Chem. Phys., 10,* 9451–9472.

Fabian, P., R. Borchers, and K. Kourtidis (1994), Bromine-containing source gases during EASOE, *Geophys. Res. Lett., 21*(13), 1219–1222.

Fabry, C. and H. Buisson (1913), L'absorption de l'ultraviolet par l'ozone et la limite du spectre solaire, *J. Phys. Rad., 5,*196–206.

Fabry, C. (1950), *L'ozone atmospherique,* Centre Nationale de la Recherche Scientifique, Paris, France.

Fahey, D.W., D. M. Murphy, K. K. Kelly, M. K. W. Ko, M. H. Proffitt, C. S. Eubank, G. V. Ferry, M. Lowenstein, and K. R. Chan (1989a), Measurements of nitric oxide and total reactive nitrogen in the Antarctic stratosphere: Observations and chemical implications, *J. Geophys. Res., 94*(D14), 16665−16681.

Fahey, D. W., K. K. Kelly, G. V. Ferry, L. R. Poole, J. C. Wilson, D. M. Murphy, M. Loewenstein, and K. R. Chan (1989b), In situ measurements of total reactive nitrogen, total water and aerosol in a polar stratospheric cloud in the Antarctic, *J. Geophys. Res*., *94*(D9), 11299 −11315.

Fahey, D. W., S. R. Kawa, and K. R. Chan (1990a), Nitric oxide measurements in the Arctic winter stratosphere, *Geophys. Res. Lett*., *17*(4), 489–492.

Fahey, D. W., K. K. Kelly, S. R. Kawa, A. F. Tuck, M. Loewenstein, K. R. Chan, and L. E. Heidt (1990b), Observations of denitrification and dehydration in the winter polar stratospheres, *Nature*, *344*, 321–324.

Fairbrother, D. H., D. J. D. Sullivan, and H. S. Jonston (1997), Global thermodynamic atmospheric modeling: Search for new heterogeneous reactions, *J. Phys. Chem. A.*, *101*, 7350–7358.

Fairlie, T. D. A. (1995), Three-dimensional transport simulations of the dispersal of volcanic aerosol from Mount Pinatubo, *Quart. J. Roy. Meteorol. Soc., 121*(528), 1943–1980.

Farahani, E. E., H. Fast, R. L. Mittermeier, Y. Makino, K. Strong, C. McLandress,
T. G. Shepherd, M. P. Chipperfield, J. W. Hannigan, M. T. Coffey, S. Mikuteit, F. Hase, T. Blumenstock, and U. Raffalski (2007), Nitric acid measurements at Eureka obtained in winter 2001-2002 using solar and lunar Fourier transform absorption spectroscopy: comparisons with observations at Thule and Kiruna and with results from three-dimensional models, *J. Geophys. Res., 112*, D01305, doi:10.1029/ 2006JD007096.

Farman, J. C., B. G. Gardiner, and J. D. Shanklin (1985), Large losses of total ozone in Antarctica reveal seasonal ClOx/NOx interaction, *Nature*, *315*, 207–210.

Farmer, C. B. (1974), Infrared measurements of stratospheric composition, *Can. J. Chem., 52,* 1544–1559.

Farmer, C., O. Toon, P. Schaper, J.-F. Blavier, and L. Lowes (1987), Stratospheric trace gases in the spring 1986 Antarctic atmosphere, *Nature, 329,* 126–130.

Fast, H., R. L. Mittermeier, and Y. Makino (2011), A ten-year record of Arctic trace gas total column measurements at Eureka, Canada, from 1997 to 2006, *Atmos.-Ocean*, 49(2), 67–94.

Fellgett, P. B. (1951), The Multiplex Advantage. *PhD thesis,* University of Cambridge.

Fellgett, P. B. (1958), A propos de la th´eorie du spectrom`etre interf´erentiel multiplex, *J. Phys. Radium, 19,* 187–191.

Feng, W., M. P. Chipperfield, S. Davies, B. Sen, G. Toon, J. -F. Blavier, C. R. Webster, C. M. Volk, A. Ulanovsky, F. Ravegnani, P. von der Gathen, H. Jost, E. C. Richard, and H. Claude (2005), Three-dimensional model study of the Arctic ozone loss in 2002/2003 and comparison with 1999/2000 and 2003/2004, *Atmos. Chem. Phys., 5*, 139–152.

Fioletov, V. E., J. B. Kerr, D. I. Wardle, J. Davies, E. W. Hare, C. T. McElroy, and D. W. Tarasick, (1997), Long-term ozone decline over the Canadian Arctic to early 1997 from ground-based and balloon observations, *Geophys. Res. Lett., 24*(22), 2705–2708.

Fish, D., R. Jones, R. Freshwater, H. Roscoe, D. Oldham, and J. Harries (1994), Total ozone measured during EASOE by a UV-visible spectrometer which observes stars, *Geophys. Res. Lett., 21*(13), 1387–1390.

Forster, P., V. Ramaswamy, P. Artaxo, T. Berntsen, R. Betts, D. Fahey, J. Haywood, J. Lean, D. Lowe, G. Myhre, J. Nganga, R. Prinn, G. Raga, M. Schulz, and R. V. Dorland (2007), *Changes in Atmospheric Constituents and in Radiative Forcing, in: Climate change 2007: The physical scientific basis, Contribution of Working Group I to the Fourth Assessment Report of the Intergovernmental Panel on Climate Change*, edited by: Solomon, S., Qin, D., Manning, M., Chen, Z., Marquis, M., Averyt, K. B., Tignor, M., and Miller, H., Cambridge University Press, Cambridge, United Kingdom and New York, NY, USA.

Fraser, A., P. F. Bernath, R. D. Blatherwick, J. R. Drummond, P. F. Fogal, D. Fu, F. Goutail, T. E. Kerzenmacher, C. T. McElroy, C. Midwinter, J. R. Olson, K. Strong, K. A. Walker, D. Wunch, and I. J. Young (2007), Intercomparison of ground-based ozone and NO$_2$ measurements during the MANTRA 2004 campaign, *Atmos. Chem. Phys., 7,* 5489–5499.

Fraser, A., F. Goutail, K. Strong, P. F. Bernath, C. Boone, W. H. Daffer, J. R. Drummond, D. G. Dufour, T. E. Kerzenmacher, G. L. Manney, C. T. McElroy, C. Midwinter, C. A. McLinden, F. Nichitiu, C. R. Nowlan, J.Walker, K. A. Walker, H. Wu, and J. Zou (2008),

Intercomparison of UV-visible measurements of ozone and NO2 during the Canadian Arctic ACE validation campaigns: 2004–2006, *Atmos. Chem. Phys., 8,* 1763–1788.

Fu, D., K. A. Walker, K. Sung, C. D. Boone, M. A. Soucy, and P. F. Bernath (2007) The portable atmospheric research interferometric spectrometer for the infrared, PARIS-IR. *J. Quant. Spectrosc. Radiat. Transfer, 103*, 362–370.

Fu, D., K. A.Walker, R. L. Mittermeier, K. Strong, K. Sung, H. Fast, P. F. Bernath, C. D. Boone, W. H. Daffer, P. Fogal, F. Kolonjari, P. Loewen, G. L. Manney, O. Mikhailov, and J. R. Drummond (2011), Simultaneous trace gas measurements using two Fourier transform spectrometers at Eureka, Canada during spring 2006, and comparisons with the ACE-FTS, *Atmos. Chem. Phys., 11,* 5383–5405.

Gallery, W. O., F. X. Kneizys, and S. A. Clough (1983), Air Mass Computer Program for Atmospheric Transmittance/Radiance Calculation: FSCATM, *Environmental Research Papers No. 828* (AFGL-TR-83-0065), Air Force Geophysics Laboratory.

Gandrud, B. W., J. E. Dye, D. Baumgardner, G. V. Ferry, M. Loewenstein, K. R. Chan, L. Sanford, B. Gary, and K. Kelly (1990), The January 30, 1989, Arctic polar stratospheric clouds (PSC) event: Evidence for a mechanism of dehydration, *Geophys. Res. Lett*., *17*(4), 457–460.

Geer, A. J., W. A. Lahoz, S. Bekki, N. Bormann, Q. Errera, H. j. Eskes, D. Fonteyn, D. R. Jackson, M. N. Juckes, S. Massart, V. –H. Peuch, S. Rharmili, and A. Segers (2006), The ASSET intercomparison ozone analyses: Method and first results. *Atmos. Chem. Phys., 6,* 5445–5474.

Geller, M. A., V. Yudin, A. R. Douglass, J. W. Waters, L. S. Elson, A. E. Roche, and J. M. Russell III (1995), UARS PSC, ClONO2, HCl and ClO measurements in early winter: Additional verification of the paradigm for chlorine activation, *Geophys. Res. Lett*., *22*(21), 2937–2940.

Gille, J. C. and J. M. I. Russel (1984), The Limb Infrared Monitor of the Stratosphere: experiment description, performance, and results, *J. Geophys. Res., 89*(D4), 5125–5140.

Gordley, L. L., J. M. Russell III, L. J. Mickley, J. E. Frederick, J. H. Park, K. A. Stone, G. M. Beaver, J. M. Mclnerney, L. E. Deaver, G. Toon, C., F. J. Murcray, R. D. Blatherwick, M. R. Gunson, R. L. Maudin, G. H. Mount, B. Sen, and J. F. Blavier (1996), Validation of nitric oxide and nitrogen dioxide measurements made by the Halogen Occultation Experiment form the UARS platform, *J. Geophys. Res., 101*(D6), 10241–10266.

Goutail, F., J. Pommereau, A. Sarkissian, E. Kyro, and V. Dorokhov (1994), Total nitrogen dioxide at the Arctic polar circle since 1990, *Geophys. Res. Lett., 21*(13), 1371–1374.

Goutail, F., J.-P. Pommereau, C. Phillips, C. Daniel, A. Sarkissian, F. Lefèvre, E. Kyro, M. Rummukainen, P. Ericksen, S. B. Andersen, B.-A. Kaastad-Hoiskar, G. Braathen, V. Dorokhov, and V. U. Khattatov (1999), Depletion of column ozone in the Arctic during the winters 1993–94 and 1994–95, *J. Atmos. Chem., 32,* 1–34.

Griesfeller, A., J. Griesfeller, F. Hase, I. Kramer, P. Loës, S. Mikuteit, U. Raffalski, T. Blumenstock, and H. Nakajima (2006), Comparison of ILAS-II and ground-based FTIR measurements of O_3, HNO_3, N_2O, and CH_4 over Kiruna, Sweden, *J. Geophys. Res., 111,* D11S07, doi:10.1029/2005JD006451.

Griffiths, P. R. (2002), Resolution and instrument line shape, in *Handbook of Vibrational Spectroscopy*, J. M. Chalmers and P. R. Griffiths, Eds., Wiley, Chichester, West Sussex, England, Vol. 1.

Griffiths, P. R. and J. A. de Haseth, *Fourier transform infrared spectrometry*, second edition, Wiley & Sons, 2007. ISBN 978-0-471-19404-0.

Grossel, A., N. Huret, V. Catoire, G. Berthet, J.-B. Renard, C. Robert, and B. Gaubicher (2010), In situ balloon-borne measurements of HNO_3 and HCl stratospheric vertical profiles

influenced by polar stratospheric cloud formation during the 2005-2006 Arctic winter, *J. Geophys. Res., 115,* D21303, doi: 10.1029/2009JD012947.

Haigh, J. D. and J. A. Pyle (1982), Ozone perturbation experiments in a two-dimensional circulation model, *Q. J. R. Meteorol. Soc., 108,* 551–574, doi:10.1002/qj.49710845705.

Hamdouni, A., A. Barbe, P. Demoulin, and R. Zander (1997), Retrieval of ozone vertical column amounts from ground-based high resolution infrared solar spectra, *J. Quant. Spectrosc. Radiat. Transfer,* 57, 11–22.

Hamill, P., O. Toon, and R. Turco (1986), Characteristics of polar stratospheric clouds during the formation of the Antarctic ozone hole, *Geophys. Res. Lett., 13*(12), 1288–1291.

Hampson, J. (1964), Photochemical behavior of the ozone layer, *Tech. Note TN 1627/64*, Can. Armament Res. and Dev. Estab., Valcartier, Que., Canada.

Hanisco, T. F., J. B. Smith, R. M. Stimpfle, D. M. Wilmouth, K. K. Perkins, J. R. Spackman, J. G. Anderson, D. Baumgardner, B. Gandrud, C. R. Webster, S. Dhaniyala, K. A. McKinney, and T. P. Bui (2002), Quantifying the rate of heterogeneous processing in the Arctic polar vortex with in situ observations of OH, *J. Geophys. Res., 107*(D20), 8278−8288.

Hanson, D. R., and K. Mauersberger (1988), The vapor pressures of HNO_3-H_2O solutions, *J. Phys. Chem.*, *92*, 6167–6170.

Hanson, D. R., and A. R. Ravishankara (1993), Reaction of $ClONO_2$ with HCl on NAT, NAD, and frozen sulfuric acid and hydrolysis of N_2O_5 and $ClONO_2$ on frozen sulfuric acid, *J. Geophys. Res.*, *98*(D12), 22931–22936.

Hanson, D. R., and A. R. Ravishankara (1994), Reactive uptake of $ClONO_2$ onto sulfuric acid due to reaction with HCl and H_2O, *J. Phys. Chem.*, *98*, 5728–5735.

Hanson, D. R., and A. R. Ravishankara (1995), Heterogeneous chemistry of bromine species in sulfuric acid under stratospheric conditions, *Geophys. Res. Lett.*, *22*(4), 385–388.

Hartley, W. N. (1880), On the probable absorption of solar radiation by atmospheric ozone, *Chem. News*, *42*, 268.

Harvey, V. L., R. B. Pierce, T. D. Fairlie, M. H. Hitchman (2002), A climatology of stratospheric polar vortices and anticyclones, *J. Geophys. Res., 107* (D20), 4442, doi:10.1029/2001JD001471.

Hase, F., T. Blumenstock, and C. Paton-Walsh (1999), Analysis of the instrumental line shape of high-resolution Fourier transform IR spectrometers with gas cell measurements and new retrieval software, *Appl. Opt., 38,* 3417–3422.

Hegglin, M. I., and T. G. Shepherd (2009), Large climate-induced changes in stratosphere-to-troposphere ozone flux and ultraviolet index, *Nature Geosci., 2*, 687−691.

Hofmann, D. J., J. W. Harder, S. R. Rolf, and J. M. Rosen (1987), Balloon-borne observations of the development and vertical structure of the Antarctic ozone hole in 1986, *Nature*, *326*, 59–62.

Hofmann, D. (1988), Balloon-borne measurements of middle atmosphere aerosols and trace gases in Antarctica, *Rev. Geophys., 26,* 113–130.

Hofmann, D., J. Harder, J. Rosen, J. Hereford, and J. Carpenter (1989), Ozone profile measurements at McMurdo Station, Antarctica, during the spring of 1987, *J. Geophys. Res., 94*(D14), 16527–16536.

Hofmann, D. (1990), Stratospheric cloud microlayers and small-scale temperature variations in the Arctic in 1989, *Geophys. Res. Lett., 17*(4), 369–372.

Höpfner, M., T. von Clarmann, H. Fischer, B. Funke, N. Glatthor, U. Grabowski, S. Kellmann, M. Kiefer, A. Linden, M. Milz, T. Steck, G. P. Stiller, P. Bernath, C. E. Blom, Th. Blumenstock, C. Boone, K. Chance, M. T. Coffey, F. Friedl-Vallon, D. Griffith, J. W. Hannigan, F. Hase, N. Jones, K. W. Jucks, C. Keim, A. Kleinert, W. Kouker, G. Y. Liu, E. Mahieu, J. Mellqvist, S. Mikuteit, J. Notholt, H. Oelhaf, C. Piesch, T. Reddmann, R. Ruhnke, M. Schneider, A. Strandberg, G. Toon, K. A. Walker, T. Warneke, G. Wetzel, S. Wood, and R. Zander (2007), Validation of MIPAS ClONO$_2$ measurements, *Atmos. Chem. Phys. 7,* 257–281.

Isaksen, I. S. A., and F. Stordal (1986), Antarctic ozone depletion: 2-D model studies, *Geophys. Res. Lett.*, *13*(12), 1327–1330.

Jacob, D. J. (1999), *Introduction to Atmospheric Chemistry*, Princeton, Univ. Press.

Jacquinot, P. and C. Dufour (1948), Conditions optiques demploi des cellules photoélectriques dans les spectrographes et les interféromètres. *J. Rech. CNRS* (Paris), 6–91.

Jaramillo, M., R. deZafra, J. Barrett, L. Emmons, P. Solomon, and A. Parrish (1989), Measurements of hydrogen cyanide at McMurdo station Antarctica: Further evidence of winter stratospheric subsidence, *J. Geophys. Res., 94*(D14), 16773–16777.

Jin, J. J., K. Semeniuk, G. L. Manney, A. I. Jonsson, S. R. Beagley, J. C. McConnell, G. Dufour, R. Nassar, C. D. Boone, K. A. Walker, P. F. Bernath, and C. P. Rinsland (2006), Severe Arctic ozone loss in the winter 2004/2005: observations from ACE-FTS, *Geophys. Res. Lett., 33,* L15801, doi:10.1029/2006GL026752.

Johnston, H. S. (1971), Reduction of stratospheric ozone by nitrogen oxide catalysts from supersonic transport exhaust, *Science*, *173*, 517–522.

Johnston, P.V., R. L. McKenzie, J. G. Keys, and W. A. Matthews (1992), Observations of depleted stratospheric NO$_2$ following the Pinatubo volcanic eruption, *Geophys. Res. Lett., 19*(2), 211–213.

Jones, A., G. Qin, K. Strong, K. A. Walker, C. A. McLinden, M. Toohey, T. Kerzenmacher, P. F. Bernath, C. D. Boone (2011), A global inventory of stratospheric NOy from ACE-FTS, *J. Geophys. Res., 116*, D17304, doi:10.1029/2010JD015465.

Jones, R. L., J. Austin, D. S. McKenna, J. G. Anderson, D. W. Fahey, C. B. Farmer, L. E. Heidt, K. K. Kelly, D. M. Murphy, M. H. Proffitt, A. F. Tuck, and J. F. Vedder (1989), Lagrangian photochemical modeling studies of the 1987 Antarctic spring vortex, 1, Comparison with AAOE observations, *J. Geophys. Res.*, *94*(D9), 11529 –11558.

Jones, R. L., D. S. McKenna, L. R. Poole, and S. Solomon (1990), On the influence of polar stratospheric cloud formation on chemical composition during the 1988/89 Arctic winter, *Geophys. Res. Lett.*, *17*(4), 545–548.

Joseph, J. K., W. J. Wiscombe, and J. A. Weinman (1976), The Delta-Eddington approximation for radiative flux transfer, *J. Atmos. Sci., 33,* 2452–2459.

Junge, C. E., C. W. Chagnon, and J. E. Manson (1961), Stratospheric aerosols, *Journal of Meteorology,* 81–108.

Junge, C. E. and J. E. Manson (1961), Stratospheric aerosol studies, *J. Geophys. Res.*, *66*(7), 2163−2182.

Kawa, S. R., D. W. Fahey, L. C. Anderson, M. Loewenstein, and K. R. Chan (1990), Measurements of total reactive nitrogen during the Airborne Arctic Stratospheric Expedition, *Geophys. Res. Lett.*, *17*(4), 485–488.

Kawa, S. R., D. W. Fahey, L. E. Heidt, W. H. Pollock, S. Solomon, D. E. Anderson, M. Loewenstein, M. H. Proffitt, J. J. Margitan, and K. R. Chan (1992), Photochemical partitioning of the reactive nitrogen and chlorine reservoirs in the high-latitude stratosphere, *J. Geophys. Res.*, *97*(D8), 7905–7923.

Kelly, K. K., A. F. Tuck, D. M. Murphy, D. W. Fahey, M. H. Proffitt, R. L. Jones, D. S. Mckenna, M. Loewenstein, J. P. Podolske, S. E. Strahan, G. V. Ferry, K. R. Chan, J. F. Vedder, G. L. Gregory, W. D. Hypes, M. P. McCormick, E. V. Browell, and L. E. Heidt (1989), Dehydration in the lower Antarctic stratosphere during late winter and early spring 1987, *J. Geophys. Res., 94*(D9), 11317–11357.

Kerr, J. B., C. T. McElroy, and R. A. Olafson (1981), *Measurements of ozone with the Brewer spectrophotometer,* In: Proceedings of the Quadrennial International Ozone Symposium. Boulder, CO. 1981. p.74–79.

Kerzenmacher, T. E., K. A. Walker, K. Strong, R. Berman, P. F. Bernath, C. D. Boone, J. R. Drummond, H. Fast, A. Fraser, K. MacQuarrie, C. Midwinter, K. Sung, C. T. McElroy, R. L. Mittermeier, J. Walker, and H. Wu (2005), Measurements of O_3, NO_2 and temperature during the 2004 Canadian Arctic ACE validation campaign, *Geophys. Res. Lett., 32,* L16S07, doi:10.1029/2005GL023032.

Kerzenmacher, T., M. A. Wolff, K. Strong, E. Dupuy, K. A. Walker, L. K. Amekudzi, R. L.Batchelor, P. F. Bernath, G. Berthet, T. Blumenstock, C. D. Boone, K. Bramstedt, C. Brogniez, S. Brohede, J. P. Burrows, V. Catoire, J. Dodion, J. R. Drummond, D. G. Dufour, B. Funke, D. Fussen, F. Goutail, D. W. T. Griffith, C. S. Haley, F. Hendrick, M. Höpfner, N. Huret, N. B. Jones, J. Kar, I. Kramer, E. J. Llewellyn, M. López-Puertas, G. L. Manney, C. T. McElroy, C. A. McLinden, S. Melo, S. Mikuteit, D. P. Murtagh, F. Nichitiu, J. Notholt, C. R. Nowlan, C. Piccolo, J. P. Pommereau, C. E. Randall, A. Richter, M. Schneider, O. Schrems, M. Silicani, G. P. Stiller, J. R. Taylor, C. Tétard, M. Toohey, F. Vanhellemont, T. Warneke, J. M. Zawodny, and J. Zou (2008), Validation of NO_2 and NO from the Atmospheric Chemistry Experiment (ACE) , *Atmos. Chem. Phys., 8*, 5801–5841.

Khattatov, V., V. Yushkov, M. Khaplanov, I. Zaitsev, J. Rosen, and N. Kjome (1994), Some results of water vapor, ozone and aerosol balloon-borne measurements during EASOE, *Geophys. Res. Lett*., *21*(13), 1299–1302.

Kim, Y.-J. and M. Flatau (2010), Hindcasting the January 2009 Arctic sudden stratospheric warming and its influence on the Arctic Oscillation with unified parametrization of orographic drag in NOGAPS. Part I: extended-range stand-alone forecast, *Weather and Forecasting*, *25*(6), 1628–1644.

Kinne, S., O. Toon, G. Toon, C. Farmer, E. Browell, and M. McCormick (1989), Measurements of size and composition of particles in polar stratospheric clouds from infrared solar absorption spectra, *J. Geophys. Res., 94*(D14), 16481–16491.

Ko, M. K. W., J. M. Rodrigues, N. D. Sze, M. H. Proffitt, W. L. Starr, A. Krueger, E. V. Browell, and M. P. McCormick (1989), Implications of AAOE observations for proposed chemical explanations of the seasonal and interannual behavior of Antarctic ozone, *J. Geophys. Res.*, *94*(D14), 16705–16715.

Kohlhepp, R., R. Ruhnke, M. P. Chipperfield, M. De Mazière, J. Notholt, S. Barthlott, R. L. Batchelor, R. D. Blatherwick, Th. Blumenstock, M. T. Coffey, P. Duchatelet, H. Fast, W. Feng, A. Goldman, D. W. T. Griffith, K. Hamann, J. W. Hannigan, F. Hase, N. B. Jones, A. Kagawa, I. Kaiser, Y. Kasai, O. Kirner, W. Kouker, R. Lindenmaier, E. Mahieu, R. L. Mittermeier, B. Monge-Sanz, I. Murata, H. Nakajima, I. Morino, M. Palm, C. Paton-Walsh, Th. Reddmann, M. Rettinger, C. P. Rinsland, E. Rozanov, M. Schneider, C. Senten, B.-M. Sinnhuber, D. Smale, K. Strong, R. Sussmann, J. R. Taylor, G. Vanhaelewyn, T. Warneke, C. Whaley, M. Wiehle, and S.W. Wood (2011), Observed and simulated time evolution of HCl, $ClONO_2$, and HF total column abundances, *Atmosp. Chem. Phys. Discuss., 11,* 32085–32160.

Koike, M., Y. Kondo, W. A. Matthews, P. V. Johnston, and K. Yamazaki (1993), Decrease of stratospheric NO_2 at 44ºN caused by Pinatubo volcanic aerosols, *Geophys. Res. Lett., 20*(18), 1975–1978.

Koike, M., N. B. Jones, W. A. Matthews, P. V. Johnston, R. L. McKenzie, D. Kinnison, and J. Rodriguez (1994), Impact of Pinatubo aerosols on the partitioning between NO_2 and HNO3, *Geophys. Res. Lett., 21*(7), 597–600.

Komhyr, W. D., R. D. Grass, and R. K. Leonard (1986), Total ozone decrease at South Pole, Antarctica, 1964–1985, *Geophys. Res. Lett.*, *13*(12), 1248–1251.

Kondo, Y., U. Schmidt, T. Sugita, P. Aimedieu, M. Koike, H. Ziereis, and Y. Iwasaka (1994), Total reactive nitrogen, N_2O, and ozone in the winter Arctic stratosphere, *Geophys. Res. Lett., 21*(13), 1247–1250.

Kondo, Y., M. Koike, A. Engel, U. Schmidt, M. Mueller, T. Sugita, H. Kanzawa, T. Nakazawa, S. Aoki, H. Irie, N. Toriyama, T. Suzuki, and Y. Sasano (1999), NOy-N_2O correlation observed inside the Arctic vortex in February 1997: dynamical and chemical effects, *J. Geophys. Res., 104*(D7)*,* 8215–8224.

Koop, T., U. M. Biermann, W. Raber, B. P. Luo, P. J. Crutzen, and T. Peter (1995), Do stratospheric aerosols freeze above the ice frost point?, *Geophys. Res. Lett.*, *22*(8), 917–920.

Krueger, A. J., M. R. Schoeberl, and R. S. Stolarski (1987), TOMS observations of total ozone in the 1986 Antarctic spring, *Geophys. Res. Lett.*, *14*(5), 527–530.

Kruger, B. (1990), Observations of polar stratospheric clouds in the Arctic winter 1989 at 79ºN, *Geophys. Res. Lett., 17*(4), 365–268.

Kuester, S., P. Franchois, and M. Fanning (1989), Total ozone, ozone vertical distributions and stratospheric temperatures at South Pole, Antarctica in 1986 and 1987, *J. Geophys. Res., 94*(D9), 11429–11436.

Kurylo, M. J. and S. Solomon (1990), Network for the Detection of Stratospheric Change - A status and implementation report, issued by NASA and NOAA, January 1990.

Kurylo, M. J. and R. Zander (2000), *The NDSC-its status after 10 years of operation*, Proceedings of the XIX quadrennial ozone symposium. Hokkaido University Sapporo, Japan, July 3-8, pp. 167–168.

Kuttippurath, J., S. Godin-Beekmann, F. Lefèvre, and A. Pazmiño (2009), Ozone depletion in the Arctic winter 2007–2008, *Int. J. Remote Sens.*, *30* (15-16), 4071–4082.

Labitzke, K. and collaborators: The Berlin stratospheric data series CD from Meteorological Institute, Freie Universität Berlin, Germany, 2002.

Langematz, U., and M. Kunze (2006), An update on dynamical changes in the Arctic and Antarcticstratospheric polar vortices, *Clim. Dyn., 27*(6), 647–660.

Lary, D. J., and J. A. Pyle (1991), Diffuse radiation, twilight and photochemistry, *J. Atmos. Chem, 13*, 373–392.

Lattanzi, F., C. di Lauro, and J. Vander Auwera (2011), Toward the understanding of the high resolution infrared spectrum of C_2H_6 near 3.3 µm, *J. Mol. Spectrosc., 267,* 71-79.

Leu, M.-T. (1988), Laboratory studies of sticking coefficients and heterogeneous reactions important in the Antarctic stratosphere, *Geophys. Res. Lett.*, *15*(1), 17–20.

Li, J., and H. W. Barker (2005), A radiation algorithm with correlated-k distribution. Part I: Local thermal equilibrium, *J. Atmos. Sci., 62,* 286–309.

Lindenmaier, R., R. L. Batchelor, K. Strong, H. Fast, F. Goutail, F. Kolonjari, C. T. McElroy, R. L. Mittermeier, and K. A. Walker (2010), An evaluation of infrared microwindows for ozone retrievals using the Eureka Bruker 125HR Fourier transform spectrometer, *J. Quant. Spectrosc. Radiat. Transfer, 111*, 569–585.

Lindenmaier, R., K. Strong, R. L. Batchelor, P. F. Bernath, S. Chabrillat, M. P. Chipperfield, W. H. Daffer, J. R. Drummond, W. Feng, A. I. Jonsson, F. Kolonjari, G. L. Manney,C. McLinden, R. Ménard, and K. A. Walker (2011a), A study of the NO_y budget above Eureka, Canada, *J. Geophys. Res., 116,* D23302, doi:10.1029/2011JD016207.

Lindenmaier, R., K. Strong, R. L. Batchelor, M. P. Chipperfield, W. H. Daffer, J. R. Drummond, T. J. Duck, H. Fast, W. Feng, P. F. Fogal, F. Kolonjari, G. L. Manney, A. Manson, C. Meek, R. L. Mittermeier, G. J. Nott, C. Perro, and K. A. Walker (2011b), Unusually low ozone, HCl, and HNO_3 column measurements at Eureka, Canada during winter/spring 2011, *Atmos. Chem. Phys. Discuss., 12,* 1053-1092, 2012.

Lowe, D., and A. R. MacKenzie (2008), Polar stratospheric cloud microphysics and chemistry, *J. Atmos. Solar-Terr. Phys., 70,* 13–40, doi: 10.1016/j.jastp.2007.09.011.

Mankin, W. G., M. T. Coffey, A. Goldman, M. R. Schoeberl, L. R. Lait, and P. A. Newman (1990), Airborne measurements of stratospheric constituents over the Arctic in the winter of 1989, *Geophys. Res. Lett., 17*(4)*,* 473-476.

Manney, G. L., L. Froidevaux, M. L. Santee, R. W. Zurek, and J. W. Waters (1997), MLS observations of Arctic ozone loss in 1996-97, *Geophys. Res. Lett., 24*(22), 2697–2700.

Manney, G. L., W. A. Lahoz, R. Swinbank, A. O'Neill, P. M. Connew, R. W. Zurek (1999), Simulation of the December 1998 stratospheric major warming, *Geophys. Res. Lett., 26*(17), 2773–2736.

Manney, G. L., W. H. Daffer, J. M. Zawodny, P. F. Bernath, K. W. Hoppel, K. A. Walker, B. W. Knosp, C. Boone, E. E. Remsberg, M. L. Santee, V. L. Harvey, S. Pawson, D. R. Jackson, L. Deaver, C. T. McElroy, C. A. McLinden, J. R. Drummond, H. C. Pumphrey, A. Lambert, M. J. Schwartz, L. Froidevaux, S. McLeod, L. L. Takacs, M. J. Suarez, C. R. Trepte, D. C. Cuddy, N. J. Livesey, R. S. Harwood, and J. W. Waters (2007), Solar occultation satellite data and derived meteorological products: Sampling issues and comparisons with Aura Microwave Limb Sounder, *J. Geophys. Res., 112,* D24550, doi:10.1029/2007JD008709.

Manney, G. L., W. H. Daffer, K. B. Strawbridge, K. A. Walker, C. D. Boone, P. F. Bernath, T. Kerzenmacher, M. J. Schwartz, K. Strong, R. J. Sica, K. Krüger, H. C. Pumphrey, A. Lambert, M. L. Santee, N. J. Livesey, E. E. Remsberg, M. G. Mlynczak, and J. R Russell III

(2008), The high Arctic in extreme winters: vortex, temperature, and MLS and ACE-FTS trace gas evolution, *Atmos. Chem. Phys., 8*, 505–522.

Manney, G. L., R. S. Harwood, I. A. MacKenzie, K. Minschwaner, D. R. Allen, M. L. Santee, K. A. Walker, M. I. Hegglin, A. Lambert, H. C. Pumphrey, P. F. Bernath, C. D. Boone, M. J. Schwartz, N. J. Livesey, W. H. Daffer, and R. A. Fuller (2009a), Satellite observations and modeling of transport in the upper troposphere through the lower mesosphere during the 2006 major stratospheric sudden warming, *Atmos. Chem. Phys., 9*, 4775–4795.

Manney, G. L., M. J. Schwartz, K. Krüger, M. L. Santee, S. Pawson, J. N. Lee, W. H. Daffer, R. A. Fuller, and N. J. Livesey (2009b), Aura Microwave Limb Sounder observations of dynamics and transport during the record-breaking 2009 Arctic stratospheric major warming, *Geophys. Res. Lett., 36,* L12815, doi:10.1029/2009 GL038586.

Manney, G. L., M. L. Santee, M. Rex, N. J. Livesey, M. C. Pitts, P. Veefkind, E. R. Nash, I. Wohltmann, R. Lehmann, L. Froidevaux, L. R. Poole, M. R. Schoeberl, D. P. Haffner, J. Davies, V. Dorokhov, H. Gernandt, B. Johnson, R. Kivi, E. Kyrö, N. Larsen, P. F. Levelt, A. Makshtas, C. T. McElroy, H. Nakajima, M. C. Parrondo, D. W. Tarasick, P. von der Gathen, K. A Walker, N. S. Zinoviev (2011), Unprecedented Arctic Ozone Loss in 2011, *Nature*, *478*, 469−475.

Manson, A. H., C.E. Meek and T. Chshyolkova (2008), Regional Stratospheric Warmings in the Pacific-Western Canada (PWC) Sector during Winter 2004/5: Implications for Temperatures, Winds, Chemical Constituents and the Characterization of the Polar Vortex, *Ann. Geophys., 26,* 3597−3622.

McCormick, M. P., H. M. Steele, P. Hamill, W. P. Chu, and T. J. Swissler (1982), Polar stratospheric cloud sightings by SAM II, *J. Atmos. Sci.*, *39*, 1387–1397.

McCormick, M., G. Kent, W. Hunt, M. Osborn, L. Poole, and M. Pitts (1990), Arctic polar stratospheric cloud observations by airborne lidar, *Geophys. Res. Lett., 17*(4), 381–383.

McElroy, M. B., R. J. Salawitch, S. C. Wofsy, and J. A. Logan (1986), Reductions of Antarctic ozone due to synergistic interactions of chlorine and bromine, *Nature*, *321*, 759–762.

McIntyre, M.E., and T.N. Palmer (1983), Breaking planetary waves in the stratosphere, *Nature, 305,* 593–594.

McLinden, C. A., S. C. Olsen, B. Hannegan, O. Wild, M. J. Prather, and J. Sundet (2000), Stratospheric ozone in 3-D models: A simple chemistry and the cross-tropopause flux, *J. Geophys. Res., 105*(D11), 14653–14665.

Meier, A., A. Goldman, P. S. Manning, T. M. Stephen, C. P. Rinsland, N. B. Johnes and S. W. Wood (2004a), Improvements to air mass calculations for ground-based infrared measurements. *J. Quant. Spectrosc. Radiat. Transfer, 83,* 109-113.

Meier, A., G. C. Toon, C. P. Rinsland, A. Goldman, and F. Hase (2004b), *Spectroscopic Atlas of Atmospheric Microwindows in the Middle Infra-Red,* 2nd Edition, IRF Technical Report 048 ISSN 0284-1738, Swedish Institute of Space Physics.

Mellqvist, J., B. Galle, T. Blumenstock, F. Hase, D. Yashcov, J. Notholt, B. Sen, J.-F. Blavier, G. C. Toon, and M. P. Chipperfield (2002), Ground-based FTIR observations of chlorine activation and ozone depletion inside the Arctic vortex during the winter of 1999/2000, *J. Geophys. Res., 107*(D20), 8263−8279.

Mengistu Tsidu, G., G. P. Stiller, T. von Clarmann, B. Funke, M. Höpfner, H. Fischer, N. Glatthor, U. Grabowski, S. Kellmann, M. Kiefen, A. Linden, M. López-Puertas, M. Milz, T. Steck, and D. Y. Wang (2005), NO_y from Michelson Interferometer for Passive Atmospheric Sounding on Environmental Satellite during the Southern Hemisphere polar vortex split in September/October 2002, *J. Geophys. Res., 110*, D11301, doi:10.1029/2004JD005322.

Michelsen, H. A., G. L. Manney, M. R. Gunson, and R. Zander (1998), Correlations of stratospheric abundances of NOy, O_3, N_2O, and CH_4 derived from ATMOS measurements, *J. Geophys. Res., 103*(D21)*,* 28347–28359.

Michelsen, H. A., C. M. Spivakovsky, and S. C. Wofsy (1999), Aerosol-mediated partitioning of stratospheric Cl_y and NO_y at temperatures above 200 K, *Geophys. Res. Lett.*, *26*(3), 299–302.

Molina, M. J., and F. S. Rowland (1974), Stratospheric sink for chlorofluoromethanes: Chlorine atom catalyzed destruction of ozone, *Nature*, *249*, 820–812.

Molina, M. J., T-L. Tso, L. T. Molina, and F. C.-Y. Wang (1987), Antarctic stratospheric chemistry of chlorine nitrate, hydrogen chloride, and ice: Release of active chlorine, *Science*, *238*, 1253–1257.

Mondelain, D., S. Payan, W. Deng, C. Camy-Peyret, D. Hurtmans, and A. W. Mantz (2007), Measurements of the temperature dependence of line mixing and pressure broadening parameters between 296 and 90 K in the v_3 band of $^{12}CH_4$ and their influence on atmospheric methane retrievals, *J. Mol. Spectrosc., 244*, 130-137.

Mount, G., R. Sanders, A. Schmeltekopf, and S. Solomon (1987), Visible spectroscopy at Mc-Murdo Station, Antarctica 1. Overview and daily variations of NO_2 and O_3, austral spring 1986, *J. Geophys. Res., 92*(D7), 8320–8328.

Mount, G., S. Solomon, R. Jakoubek, and A. Schmeltekopf (1988), Observations of stratospheric NO_2 and O_3 at Thule, Greenland, *Science, 242,* 555–558.

Müller, R., S. Tilmes, J.-U. Grooß, D. S. McKenna, M. Müller, U. Schmidt, G. C. Toon, R.A. Stachnik, J. J. Margitan, J. W. Elkins, J. Arvelius, and J. M. Russell III (2003), Chlorine activation and chemical ozone loss deduced from HALOE and balloon measurements in the Arctic during the winter of 1999–2000, *J. Geophys. Res., 108*(D5), 8302−8319.

Murcray, D. G., F. H. Murcray, W. J. Williams, T. G. Kyle, and A. Goldman (1969), Variation of the infrared solar spectrum between 700 cm^{-1} and 2240 cm^{-1} with altitude, *Appl. Opt., 8,* 2519–2536.

Murcray, D. G., D. B. Barker, J. N. Brooks, A. Goldman, and W. J. Williams (1975), Seasonal and latitudinal variation of the stratospheric concentration of HNO_3, *Geophys. Res. Lett.*, *2*(6), 223–225.

Murcray, F., A. Goldman, R. Blatherwick, W. Matthews, and N. Jones (1989), HNO_3 and HCl amounts over McMurdo during the spring of 1987, *J. Geophys. Res., 94*(D14)*, *16615–16618.

Murcray, F., J. Starkey, W. Williams, W. Matthews, U. Schmidt, P. Aimedieu, and C. Camy-Peyret (1994), HNO_3 profiles obtained during the EASOE campaign, *Geophys. Res. Lett., 21*(13), 1223–1226.

Naujokat, B., K. Krüger, K. Matthes, J. Hoffmann, M. Kunze, and K. Labitzke (2002), The early major warming in December 2001 – exceptional?, *Geophys. Res. Lett., 29*(21), 2023, doi:10.1029/2002GL015316.

Network for the Detection of Atmospheric Composition Change (NDACC) Newsletter, Volume 3, January 2008, *http://www.ndsc.ncep.noaa.gov/news/archives/nl2008-1.pdf*

Neuber, R., G. Beyerle, G. Fiocco, A. di Sarra, K.-H. Fricke, B. Knudsen, C. David, S. Godin, L. Stefanutti, and G. Vaughanet (1994), Latitudinal distribution of stratospheric aerosols during the EASOE winter 1991/92, *Geophys. Res. Lett., 21*(13), 1283–1286.

Newman, P. A., J. F. Gleason, R. D. McPeters, and R. S. Stolarski (1997), Anomalously low ozone over the Arctic, *Geophys. Res. Lett., 24*(22), 2689–2692.

Notholt, J., R. Neuber, O. Schrems, and T. V. Clarmann (1993), Stratospheric trace gas concentrations in the Arctic polar night as derived by FTIR-spectroscopy with the moon as IR light source, *Geophys. Res. Lett., 20*(19), 2059–2062.

Notholt, J. (1994), The moon as a light source for FTIR measurements of stratospheric trace gases during the polar night: Application for HNO_3 in the Arctic, *J. Geophys. Res., 99*(D2)*, 3607–3614.

Notholt, J., and O. Schrems (1994), Ground-based FTIR measurements of vertical column densities of several trace gases above Spitsbergen, *Geophys. Res. Lett., 21*(13), 1351–1354.

Notholt, J., and O. Schrems (1995a), Ground-based FTIR spectroscopic absorption measurements of stratospheric trace gases in the Arctic with the sun and the moon as light sources, *J. Mol. Struct., 347,* 407–416.

Notholt, J., P. von der Gathen, and S. Peil (1995b), Heterogeneous conversion of HCl and $ClONO_2$ during the Arctic winter 1992/1993 initiating ozone depletion, *J. Geophys. Res., 100*(D6), 11269–11274.

Notholt, J., G. Toon, R. Lehmann, B. Sen, and J.-F. Blavier (1997a), Comparison of Arctic and Antarctic trace gas column abundances from ground-based Fourier transform infrared spectrometry, *J. Geophys. Res., 102*(D11), 12863–12869.

Notholt, J., G. Toon, F. Stordal, S. Solberg, N. Schmidbauer, E. Becker, A. Meier, and
B. Sen (1997b), Seasonal variations of atmospheric trace gases in the high Arctic at 79ºN, *J. Geophys. Res., 102*(D11), 12855–12861.

Notholt, J., and R. Lehmann (2003), The moon as a light source for atmospheric trace gas observations: measurement technique and analysis method, *J. Quant. Spectrosc. Radiat. Transfer, 76,* 435–445.

Nott, G. J., T. J. Duck, J. G. Doyle, M. E. W. Coffin, C. Perro, C. P. Thackray, J. R. Drummond, P. F. Fogal, E. McCullough, and R. J. Sica, "A remotely-operated lidar for aerosol, temperature, and water vapor profiling in the High Arctic", *J. Atmos. Oceanic Technol.,* Accepted for publication, Manuscript doi:10.1175/JTECH-D-11-00046.1, 2011.
.

Noxon, J. F. (1978), Stratospheric NO_2 in the Antarctic winter, *Geophys. Res. Lett.*, *5*(12), 1021–1022.

Oelhaf, H., T. von Clarmann, H. Fischer, F. Friedl-Vallon, C. Fritzsche, A. Linden, C. Piesch, M. Seefeldner, and W. Völker (1994), Stratospheric $ClONO_2$ and HNO_3 profiles inside the Arctic vortex from MIPAS-B limb emission spectra obtained during EASOE, *Geophys. Res. Lett.*, *21*(13), 1263–1266.

O'Neill, N. T., O. Pancrati, K. Baibakov, E. Eloranta, R. L. Batchelor, J. Freemantle, L. J. B. McArthur, K. Strong, and R. Lindenmaier (2008), Occurrence of weak, sub-micron, tropospheric aerosol events at high Arctic latitudes, *Geophys. Res. Lett., 35,* L14814, doi:10.1029/2008GL033733.

Park, J. H., J. M. Russell III, L. L. Gordley, S. R. Drayson, D. C. Benner, J. M. Mclnerney, M. R. Gunson, G. C. Toon, B. Sen, J. F. Blavier, C. R. Webster, E. C. Zipf, P. Erdman, U. Schmidt, and C. Schiller (1996),Validation of Halogen Occultaiton Experiment CH_4 measurements from the UARS, *J. Geophys. Res., 101*(D6)*,* 10183–10203.

Paton-Walsh, C., R. L. Mittermeier, W. Bell, H. Fast, N. Jones, and A Meier (2008), An intercomparison of ground-based solar FTIR measurements of atmospheric gases at Eureka, Canada, *J. Atmos. Oceanic Technol., 25*, 2028–2036.

Pawson, S., K. Labitzke, S. Leder (1998), Stepwise changes in stratospheric temperature, *Geophys. Res. Lett., 25*(12), 2157–2160.

Pawson, S., and B. Naujokat (1999), The cold winters of the middle 1990s in the northern lower stratosphere, *J. Geophys. Res., 104*(D12), 14209–14222.

Perner, D., A. Roth, and T. Klüpfel, (1994), Groundbased measurements of stratospheric $OClO$, NO_2 and O_3 at Søndre Strømfjord in winter 1991/92, *Geophys. Res. Lett*., *21*(13), 1367–1370.

Peter, T. (1997), Microphysics and heterogeneous chemistry of polar stratospheric clouds, *Annu. Rev. Phys. Chem.*, *48*, 785–822.

Petzoldt, K. (1999), The role of dynamics in total ozone deviations from their long-term mean over the Northern Hemisphere, *Ann. Geophys., 17,* 231–241.

Pfeilsticker, K., and U. Platt (1994), Airborne measurements during the Arctic Stratospheric Experiment: Observations of O_3 and NO_2, *Geophys. Res. Lett*., *21*(13), 1375–1378.

Pitts, M. C., L. R. Poole, and L. W. Thomason (2009), CALIPSO polar stratospheric cloud observations: second-generation detection algorithm and composition discrimination, *Atmos. Chem. Phys., 9*, 7577–7589.

Plumb, R. A., D. W. Waugh, and M. P. Chipperfield (2000), The effects of mixing on tracer relationships in the polar vortices. *J. Geophys. Res., 105*(D8)*,* 10047–10062.

Plumb, R. A. (2002), Stratospheric transport, *J. Meteor. Soc. Japan, 80,* 793–809.

Plummer, D. A., J. F. Scinocca, T. G. Shepherd, M. C. Reader, and A. I. Jonsson (2010), Quantifying the contributions to stratospheric ozone changes from ozone depleting substances and greenhouse gases, *Atmos. Chem. Phys., 10,* 8803–8820.

Polavarapu, S., S. Ren, Y. Rochon, D. Sankey, N. Ek, and coauthors (2005), Data assimilation with the Canadian Middle Atmosphere Model, *Atmos.-Ocean 43*, 77–100.

Pommereau, J. P. and F. Goutail (1988), O_3 and NO_2 ground based measurements by visible spectrometry during Arctic winter and spring 1988, *Geophys. Res. Lett., 15*(8), 891–894.

Pommereau, J-P., and J. Piquard (1994a), Observations of the vertical distribution of stratospheric OClO, *Geophys. Res. Lett., 21*(13)*,* 1231–1234.

Pommereau, J., and J. Piquard (1994b), Ozone and nitrogen dioxide vertical distributions by UV- visible solar occultation from balloons, *Geophys. Res. Lett., 21*(13), 1227–1230.

Poole, L. R., M. P. McCormick (1988), Airborne lidar observations of arctic polar stratospheric clouds: indications of two distinct growth stages, *Geophys. Res. Lett., 15* (1), 21–23.

Portmann, R. W., S. Solomon, R. R. Garcia, L. W. Thomason, L. R. Poole, and M. P. McCormick (1996), Role of aerosol variations in anthropogenic ozone depletion in the polar regions, *J. Geophys. Res., 101*(D17), 22991–23006.

Portmann, R. W., and S. Solomon (2007), Indirect radiative forcing of the ozone layer during the 21st century, *Geophys. Res. Lett.*, *34*, L02813, doi:10.1029/ 2006GL028252.

Pougatchev, N. S., B. J. Connor, and C. P Rinsland (1995), Infrared measurements of the ozone vertical distribution above Kitt Peak, *J. Geophys. Res., 100*(D8), 16689–16697.

Prather, M., M. McElroy, and S. Wofsy (1984), Reductions in ozone at high concentrations of stratospheric halogens, *Nature, 312,* 227–231.

Pyle, J. A., G. Carver, J. L. Grenfell, J. A. Kettleborough, and D. J. Lary (1992), Ozone loss in Antarctica: The implications for global change, *Philos. Trans. R. Soc. London*, *Ser. B*, *338*, 219–226.

Pyle, J. A., N. R. P. Harris, J. C. Farman, F. Arnold, G. Braathen, R. A. Cox, P. Faucon, R. L. Jones, G. Megie, A. O'Neill, U. Platt, J.-P. Pommereau, U. Schmidt, and F. Stordal (1994), An overview of the EASOE Campaign, *Geophys. Res. Lett., 21*(13), 1191–1194.

Ramaswamy, V. (1988), Dehydration mechanism in the Antarctic stratosphere during winter, *Geophys. Res. Lett., 15*(8), 863–866.

Randall, C. E., V. L. Harvey, G. L. Manney, Y. Orsolini, M. Codrescu, C. Sioris, S. Brohede, C. S. Haley, L. L. Gordley, J. M. Zawodny, and J. M. Russell III (2005), Stratospheric effects of energetic particle precipitation in 2003–2004, *Geophys. Res. Lett., 32,* L05802, doi:10.1029/2004GL022003.

Randall, C. E., V. L. Harvey, C. S. Singleton, S. M. Bailey, P. F. Bernath, M. Codrescu, H. Nakajima, and J. M. Russell II (2007), Energetic particle precipitation effects on the Southern Hemisphere stratosphere in 1992–2005, *J. Geophys. Res., 112,* D08308, doi:10.1029/2006JD007696.

Randall, C. E., V. L. Harvey, D. E. Siskind, J. France, P. F. Bernath, C. D. Boone, and K. A.Walker (2009), NO$_x$ descent in the Arctic middle atmosphere in early 2009, *Geophys. Res. Lett., 36,* L18811, doi:10.1029/2009GL039706.

Randel, W., M.–L. Chanin, and C. Michaut (2002), *Intercomparison of Middle Atmosphere Climatologies,* SPARC Report No. 3, WCRP 116, WMO/TD 1142.

Ravishankara, A. R., and D. R. Hanson (1996), Differences in the reactivity of type 1 PSC's depending on their phase, *J. Geophys. Res.*, *101*(D2), 3885–3890.

Ravishankara, A. R., J. S. Daniel, and R. W. Portmann (2009), Nitrous oxide (N$_2$O): the dominant ozone-depleting substance emitted in the 21st century, *Science, 326*, 123–125.

Reber, C., C. Trevathan, R. McNeal, and M. Luther (1993), The Upper Atmosphere Research Satellite (UARS) Mission, *J. Geophys. Res., 98*(D6)*,* 10643–10647.

Reinecker, M. M., M. J. Suarez, R. Todling, J. Bacmeister, L. Takacs, H.-C. Liu, W. Gu, M. Sienkiewicz, R.D. Koster,R. Gelaro, I. Stajner, and J.E. Nielsen (2007), The GEOS-5 Data Assimilation System: A Documentation of GEOS-5.0, Tech. Rep. 104606 V27, NASA.

Reinecker, M. M., M. J. Suarez, R. Todling, J. Bacmeister, L. Takacs, H.-C. Liu, W. Gu, M. Sienkiewicz, R.D. Koster,R. Gelaro, I. Stajner, and J.E. Nielsen (2008), *The GEOS-5 data assimilation system–Documentation of versions 5.0.1, 5.1.0, and 5.2.0*, NASA Tech. Memo., TM–2008–104606, vol. 27, pp 97.

Ren, S., S. Polavarapu, S. Beagley, Y. Nezlin and Y. Rochon (2011), The impact of gravity wave drag on mesospheric analyses of the 2006 stratospheric major warming, *J. Geophys. Res., 116,* D19116, doi:10.1029/2011JD015943.

Rex, M., R. J. Salawitch, G. C. Toon, B. Sen, J. J. Margitan, G. B. Osterman, J.-F. Blavier, R. S. Gao, S. Donnelly, E. Keim, J. Neuman, D. W. Fahey, C. R. Webster, D. C. Scott, R. L. Herman, R. D. May, E. J. Moyer, M. R. Gunson, F. W. Irion, A. Y. Chang, C. P. Rinsland, and T. P. Bui (1999), Subsidence, mixing, and denitrification of Arctic polar vortex air measured during POLARIS, *J. Geophys. Res., 104*(D21), 26611-26623.

Rex, M., R. J. Salawitch, P. von der Gathen, N. R. P. Harris, M. P. Chipperfield, and B. Naujokat (2004), Arctic ozone loss and climate change, *Geophys. Res. Lett., 31,* L04116, doi:10.1029/2003GL018844.

Rex, M., R. J. Salawitch, H. Deckelmann, P. von der Gathen, N. R. P. Harris, M. P. Chipperfield, B. Naujokat, E. Reimer, M. Allaart, S. B. Andersen, R. Bevilacqua, G. O. Braathen, H. Claude, J. Davies, H. De Backer, H. Dier, V. Dorokhov, H. Fast, M. Gerding, S. Godin-Beekmann, K. Hoppel, B. Johnson, E. Kyrö, Z. Litynska, D. Moore, H. Nakane, M.C. Parrondo, A.D. Risley Jr., P. Skrivankova, R. Stübi, P. Viatte, V. Yushkov, and C. Zerefos (2006), Arctic winter 2005: Implications for stratospheric ozone loss and climate change, *Geophys. Res. Lett.*, *33*, L23808, doi: 10.1029/2006GL026731.

Ridley, B. A., H. L. Son, D. R. Hastie, H. I. Schiff, J. C. McConnell, W. F. J. Evans, C. T. McElroy, J. B. Kerr, H. Fast, and R. S. O'Brien (1984), Stratospheric odd nitrogen: measurements of HNO_3, NO, NO_2, and O_3 near 54ºN in winter, *J. Geophys. Res.*, *89*(D3), 4797–4820.

Rinsland, C. P., M. A. H. Smith, P. L. Rinsland, A. Goldman, J. W. Brault, and G. M. Stokes (1982), Ground-based infrared spectroscopic measurements of atmospheric hydrogen cyanide, *J. Geophys. Res., 87*(C13), 11119–11125.

Rinsland, C. P., A. Goldman, F. J. Murcray, F. H. Murcray, R. D. Blatherwick, and D. G. Murcray (1988), Infrared measurements of atmospheric gases above Mauna Loa, Hawaii, in February 1987, *J. Geophys. Res., 91*(D10), 12607–12626.

Rinsland, C. P., M. R. Gunson, R. J. Salawitch, M. J. Newchurch, R. Zander, M. M. Abbas, M. C. Abrams, G. L. Manney, H. A. Michelsen, A. Y. Chang, and A. Goldman (1996), ATMOS measurements of $H_2O + 2CH_4$ and total reactive nitrogen in the November 1994 Antarctic stratosphere: Dehydration and denitrification in the vortex, *Geophys. Res. Lett.*, *23*(17), 2397–2400.

Roche, A., J. Kumer, J. Mergenthaler, G. Ely, W. Uplinger, J. Potter, T. James, and L. Sterritt (1993), The Cryogenic Limb Array Etalon Spectrometer (CLAES) on UARS: Experiment description and performance, *J. Geophys. Res., 98*(D6), 10763–10775.

Roche, A. E., J. B. Kumer, J. L. Mergenthaler, R. W. Nightingale, W. G. Uplinger, G. A. Ely, J. F. Potter, D. J. Wuebbles, P. S. Connell, and D. E. Kinnison (1994), Observations of lower-stratospheric $ClONO_2$, HNO_3, and aerosol by the UARS, CLAES experiment between January 1992 and April 1993, *J. Atmos. Sci.*, *51*, 2877–2902.

Rodgers, C. D. (1976), Retrieval of atmospheric temperature and composition from remote measurements of thermal radiation. *Rev. Geophys.*, *14*(4), 609–624.

Rodgers, C. D. (1990), Characterization and error analysis of profiles retrieved from remote sounding measurements, *J. Geophys. Res.*, *95*(D5), 5587-5595.

Rodgers, C. D. (2000), *Inverse Methods for Atmospheric Sounding: Theory and Practice*, World Scientific Publishing Co. Pte. Ltd, pp. 238.

Rodgers, C. D. and B. J. Connor (2003), Intercomparison of remote sounding instruments, *J. Geophys. Res., 108*(D3), 4116–4130.

Rodriguez, J. M., M. K. W. Ko, N. D. Sze, S. D. Pierce, J. G. Anderson, D. W. Fahey, K. Kelly, C. B. Farmer, G. C. Toon, M. T. Coffey, L. E. Heidt, W. G. Mankin, K. R. Chan, W. L. Starr, J. F. Vedder, and M. P. McCormick (1989), Nitrogen and chlorine species in the spring Antarctic stratosphere: Comparison of models with Airborne Antarctic Ozone Experiment observations, *J. Geophys. Res.*, *94*(D14), 16683–16703.

Rösevall, J. D., D. P. Murtagh, and J. Urban (2007), Ozone depletion in the 2006/2007 Arctic winter, *Geophys. Res. Lett.*, *34,* L21809, doi:10.1029/2007GL030620.

Rösevall, J. D., D. P. Murtagh, J. Urban, W. Feng, P. Eriksson, and S. Brohede (2008), A study of ozone depletion in the 2004/2005 Arctic winter based on data from Odin/SMR and Aura/MLS, *J. Geophys. Res.*, *113,* D13301, doi:10.1029/ 2007JD009560.

Rothman, L. S., R. R. Gamache, R. H. Tipping, C. P. Rinsland, M. A. H. Smith, D. C. Benner, V. M. Devi, J. M. Flaud, C. Camy-Peyret, A. Perrin, A. Goldman, S. T. Massie, L. R. Brown, and R. A. Toth, The HITRAN molecular database: Edition of 1991 and 1992, *J. Quant. Spectrosc. Radiat. Transfer, 48*, 469–507.

Rothman, L. S., A. Barbe, D. Chris Benner, L. R. Brown, C. Camy-Peyret, M. R. Carleer, K. Chance, C. Clerbaux, V. Dana, V. M. Devi, A. Fayt, J.-M. Flaud, R. R. Gamache, A. Goldman, D. Jacquemart, K. W. Jucks, W.J. Lafferty, J.-Y. Mandin, S.T. Massie, V. Nemtchinov, D. A. Newnham, A. Perrin, C. P. Rinsland, J. Schroeder, K. M. Smith, M. A. H. Smith, K. Tang, R. A. Toth, J. Vander Auwera, P. Varanasi, K. Yoshino (2003), The HITRAN molecular spectroscopic database: edition of 2000 including updates through 2001, *J. Quant. Spectrosc. Radiat. Transfer, 82*, 5–44.

Rothman, L. S., D. Jacquemart, A. Barbe, D. Chris Benner, M. Birk, L. R. Brown, M. R. Carleer, C. Chackerian Jr., K. Chance, L. H. Coudert, V. Dana, V. M. Devi, J.-M. Flaud, R. R. Gamache, A. Goldman, J.-M. Hartmann, K. W. Jucks, A. G. Maki, J.-Y. Mandin, S. T. Massie, J. Orphal, A. Perrin, C. P. Rinsland, M. A. H. Smith, J. Tennyson, R. N. Tolchenov, R. A. Toth, J. Vander Auwera, P. Varanasi, and G Wagner (2005), The HITRAN 2004 molecular spectroscopic database, *J. Quant. Spectrosc. Radiat. Transfer, 96*, 139–204.

Rothman, L. S, I. E. Gordon, A. Barbe, D. Chris Benner, P. F. Bernath, M. Birk, V. Boudon, L. R. Brown, A. Campargue, J.-P. Champion, K. Chance, L. H. Coudert, V. Danaj, V. M. Devi, S. Fally, J.-M. Flaud, R. R. Gamache, A. Goldmanm, D. Jacquemart, I. Kleiner, N. Lacome, W. J. Lafferty, J.-Y. Mandin, S. T. Massie, S. N. Mikhailenko, C. E. Miller, N. Moazzen-Ahmadi, O. V. Naumenko, A. V. Nikitin, J. Orphal, V. I. Perevalov, A. Perrin, A. Predoi-Cross, C. P. Rinsland, M. Rotger, M. Šimečková, M. A. H. Smith, K. Sung, S. A. Tashkun, J. Tennyson, R. A. Toth, A. C. Vandaele, J. Vander Auwera (2009), The HITRAN 2008 molecular spectroscopic database, *J. Quant. Spectrosc. Radiat. Transfer, 110*, 533–572.

Rowland, F. S., and M. J. Molina (1975), Chlorofluoromethanes in the environment, *Rev. Geophys.*, *13*, 1–35.

Russell, J. M., III; L. L. Gordley, J. H. Park, S. R. Drayson, W. D. Hesketh, R. J. Cicerone, A. F. Tuck, J. E. Frederick, J. E. Harries, and P. J. Crutzen (1993), The Halogen Occultation Experiment, *J. Geophys. Res., 98*(D6)*, 10777–10797.

Russell III, J. M., L. E. Deaver, M. Z. Luo, J. H. Park, L. L. Gordley, A. F. Tuck, G. C. Toon, M. R. Gunson, W. A. Traub, D. G. Johnson, K. W. Jucks, K. W. Murcray, D. G. Murcray, R. Zander, I. G. Nolt, and C. R. Webster (1996a), Validation of hydrogen chloride measurements made by the Halogen Occultation Experiment form the UARS platform, *J. Geophys. Res., 101*(D6)*, 10151–10162.

Russell III, J. M., L. E. Deaver, M. Z. Luo, R. J. Cicerone, J. H. Park, L. L. Gordley, G. C. Toon, M. R. Gunson, W. A. Traub, D. G. Johnson, K. W. Juck, R. Zander, and I. G. Nolt (1996b), Validation of hydrogen fluoride measurements made by the Halogen Occultation Experiment form the UARS platform, *J. Geophys. Res., 101*(D6)*, 10163–10174.

Salawitch, R. J., G. P. Gobbi, S. C. Wofsy, and M. B. McElroy (1989), Denitrification in the Antarctic stratosphere, *Nature*, *339*, 525–527.

Sander, S. P., d. M. Golden, M. J. Kurylo, C. E. Kolb, M. J. Molina, G. K. Moortgat, B. J. Finlayson-Pitts, A. R. Ravishankara (2003), *Chemical kinetics and photochemical data for*

use in atmospheric studies, JPL Publication 02-25, Evaluation 14, Jet Propulsion Laboratory, pp 334.

Santee, M. L., L. Froidevaux, G. L. Manney, W. G. Read, J. W. Waters, M. P. Chipperfield, A. E. Roche, J. B. Kumer, J. L. Mergenthaler, and J. M. Russell III (1996), Chlorine deactivation in the lower stratospheric polar regions during late winter: Results from UARS, *J. Geophys. Res., 101*(D13), 18835–18859.

Santee, M. L., A. Tabazadeh, G. L. Manney, R. J. Salawitch, L. Froidevaux, W. G. Read, and J. W. Waters (1998), UARS microwave limb sounder HNO3 observations: Implications for Antarctic polar stratospheric clouds, *J. Geophys. Res., 103*(D11), 13285–13313.

Santee, M. L., I. A. MacKenzie, G. L. Manney, M. P. Chipperfield, P. F. Bernath, K. A. Walker, C. D. Boone, L. Froidevaux, N. J. Livesey, and J. W. Waters (2008), A study of stratospheric chlorine partitioning based on new satellite measurements and modeling, *J. Geophys. Res.*, *113,* D12307, doi:10.1029/2007JD009057.

Sassi, F., R. Garcia, B. Boville, and H. Liu (2002), On temperature inversions and the mesospheric surf zone, *J. Geophys. Res., 107*(D19), 4380−4391.

Savastiouk, V., and C. T. McElroy (2005), Brewer spectrophotometer total ozone measurements made during the 1998 middle atmosphere nitrogen trend assessment (MANTRA) campaign, *Atmos. Ocean., 43(4),* 315–324.

Schiller, C., A. Wahner, U. Platt, H-P. Dorn, J. Callies, and D. H. Ehhalt (1990), Near UV atmospheric absorption measurements of column abundances during Airborne Arctic Stratospheric Expedition, January–February 1989, 2, OClO observations, *Geophys. Res. Lett.*, *17*(4), 501–504.

Schmidt, U., R. Bauer, A. Engel, R. Borchers, and J. Lee (1994), The variation of available chlorine, Cl_y, in the Arctic polar vortex during EASOE, *Geophys. Res. Lett., 21*(13), 1215–1218.

Schneider, M., T. Blumenstock, F. Hase, M. Höpfner, E. Cuevas, A. Redondas, J. M. Sancho (2005), Ozone profiles and total column amounts derived at Izaña, Tenerife Island, from FTIR solar absorption spectra, and its validation by an intercomparison to ECC-sonde and Brewer spectrometer measurements. *J. Quant. Spectrosc. Radiat. Transfer, 91*(3), 245–274.

Schneider, M. and F. Hase (2008), Technical Note: Recipe for monitoring of total ozone with a precision of around 1DU applying mid-infrared solar absorption spectra, *Atmos. Chem. Phys., 8,* 63–71.

Schoeberl, M. R., A. J. Krueger, and P. A. Newman (1986), The morphology of Antarctic total ozone as seen by TOMS, *Geophys. Res. Lett.*, *13*(12), 1217–1220.

Schoeberl, M. R. and D. L. Hartmann (1991), The dynamics of the stratospheric polar vortex and its relation to springtime ozone depletions, *Science, 251*(4989), 46–52.

Schoeberl, M. R., A. R. Douglass, R. S. Stolarski, D. Toohey, L. Avallone, J. G. Anderson, W. Brune, D. W. Fahey, and K. Kelly (1993), The evolution of ClO and NO along air parcel trajectories, *Geophys. Res. Lett.*, *20*(22), 2511–2514.

Schoeberl, M. R., A. R. Douglass, S. R. Kawa, A. E. Dessler, P. A. Newman, R. S. Stolarski, A. E. Roche, J. W. Waters, and J. M. Russell III (1996), Development of the Antarctic ozone hole, *J. Geophys. Res.*, *101*(D15), 20909 –20924.

Schönbein, C. F. (1840a), On the odour accompanying electricity and on the probability of its dependence on the presence of a New Substance, *Philos. Mag. (III), 17*, 293–294.

Schönbein, C. F. (1840b), Recherche sur la nature de l'odeur, qui se manifeste dans certaines actions chimiques, *C. R. Hebd. Seances Acad. Sci., C 10*, 706–710.

Scinocca, J. F., N. A. McFarlane, M. Lazare, J. Li, and D. Plummer (2008), The CCCma third generation AGCM and its extension into the middle atmosphere, *Atmos. Chem. Phys., 8,* 7055–7074.

Senten, C., M. De Mazière, B. Dils, C. Hermans, M. Kruglanski, E. Neefs, F. Scolas, A. C. Vandaele, G. Vanhaelewyn, C. Vigouroux, M. Carleer, P. F. Coheur, S. Fally, B. Barret, J. L. Baray, R. Delmas, J. Leveau, J. M. Metzger, E. Mahieu, C. Boone, K. A. Walker, P. F. Bernath, and K. Strong (2008), Technical note: New ground-based FTIR measurements at Ile de La Réunion: observations, error analysis, and comparisons with independent data, *Atmos. Chem. Phys., 8,* 3483–3508.

Shindell, D. T., J. M. Reeves, L. K. Emmons, and R. L. de Zafra (1994), Arctic chlorine monoxide observations during spring 1993 over Thule, Greenland, and implications for ozone depletion, *J. Geophys. Res*., *99*(D12), 25697–25704.

Solomon, S., R. R. Garcia, F. S. Rowland, D. J. and Wuebbles (1986), On the depletion of Antarctic ozone, *Nature, 321,* 755–758.

Solomon, P., B. Connor, R. deZafra, A. Parrish, J. Barrett, and M. Jaramillo (1987a), High concentrations of chlorine monoxide at low altitudes in the Antarctic spring stratosphere: secular variation, *Nature, 328,* 411–413.

Solomon, S., G. Mount, R. Sanders, and A. Schmeltekopf (1987b), Visible spectroscopy at Mc-Murdo Station, Antarctica 2. Observations of OClO, *J. Geophys. Res., 92*(D7), 8329–8338.

Solomon, S. (1988), The mystery of the Antarctic ozone 'hole', *Rev. Geophys., 26*(1), 131–148.

Solomon, S. (1999), Stratospheric ozone depletion: a review of concepts and history, *Rev. Geophys., 37*(3), 275–316.

Solomon, P., B. Connor, J. Barrett, T. Mooney, A. Lee, and A. Parrish (2002), Measurements of stratospheric ClO over Antarctica in 1996-2000 and implications for ClO dimer chemistry, *Geophys. Res. Lett., 29*(15), 1708−1712.

Somorjai, G. A. (1994), *Introduction to Surface Chemistry and Catalysis*, pp. 1–667, John Wiley, New York.

SPARC CCMVal, 2010: SPARC report on the evaluation of chemistry-climate models. V. Eyring, T. G. Shepherd, and D. W. Waugh, Eds., SPARC Rep. 5, WCRP-132, WMO/TD-1526.

Special Edition (1989a), AAOE Special Edition, *J. Geophys. Res., 94*(D9), 11179–11737.

Special Edition (1989b), AAOE Special Edition 2, *J. Geophys. Res., 94*(D14), 16437–16857.

Steinbrecht, W., H. Claude, F. Schönenborn, U. Leiterer, H. Dier, E. Lanzinger (2008), Pressure and temperature differences between Vaisala RS80 and RS92 radiosonde systems, *J. Atmos. Oceanic Technol., 25*(6), 909-927.

Stolarski, R. S., and R. J. Cicerone (1974), Stratospheric chlorine: A possible sink for ozone, *Can. J. Chem., 52*, 1610–1615.

Stolarski, R. S., A. J. Krueger, M. R. Schoeberl, R. D. McPeters, P. A. Newman, and J. C. Alpert (1986), Nimbus 7 satellite measurements of the springtime Antarctic ozone decrease, *Nature*, *322*, 808–811.

Strong, K., M. A. Wolff, T. E. Kerzenmacher, K. A. Walker, P. F. Bernath, T. Blumenstock, C. Boone, V. Catoire, M. Coffey, M. D. Mazière, P. Demoulin, P. Duchatelet, E. Dupuy, J. Hannigan, M. Höpfner, N. Glatthor, D. W. T. Griffith, J. Jin, N. Jones, K. Jucks, J. Kuttippurath, A. Lambert, E. Mahieu, J. C. McConnell, J.Mellqvist, S. Mikuteit, D. Murtagh, J. Notholt, C. Piccolo, P. Raspollini, M. Ridolfi, C. Robert, M. Schneider, O. Schrems, K. Semeniuk, C. Senten, G. P. Stiller, A. Strandberg, J. Taylor, C. Tétard, M. Toohey, J. Urban, T. Warneke, and S. Wood (2008), Validation of ACE-FTS N_2O Measurements, *Atmos. Chem. Phys., 8,* 4759–4786.

Sussmann, R., F. Forster, M. Rettinger, and N. Jones (2011), Strategy for high-accuracy-and-precision retrieval of atmospheric methane from the mid-infrared FTIR network, *Atmos. Meas. Tech., 4,* 1943–1964.

Tabazadeh, A., R. P. Turco, K. Drdla, and M. Z. Jacobson (1994), A study of type I polar stratospheric cloud formation, *Geophys. Res. Lett., 21*(15), 1619–1622.

Taylor, F.W., C. D. Rodgers, J.G. Whitney, S.T.Werrett, J.J. Barnett, G.D. Peskett, P. Venters, J. Ballard, C.W.P. Palmer, R.J. Knight, P. Morris, T. Nightingale, and A. Dudhia (1993), Remote sensing of atmospheric structure and composition by pressure modulator radiometry from space: The ISAMS experiment on UARS, *J. Geophys. Res., 98*(D6), 10799–10814.

Tiao, G. C., G. C. Reinsel, D. Xu, J. H. Pedrick, X. Zhu, A. J. Miller, J. J. DeLuisi, C. L. Mateer, and D. J. Wuebbles (1990), Effects of autocorrelation and temporal sampling schemes on estimates of trend and spatial correlation, *J. Geophys. Res., 95*(D12), 20507–20517.

Tie, X. X., C. Granier, W. Randel, and G. P. Brasseur (1997), Effects of interannual variation of temperature on heterogeneous reactions and stratospheric ozone, *J. Geophys. Res*., *102*(D19), 23519–23527.

Tilmes, S., R. Müller, J.–U. Grooß, and J. M. Russell III (2004), Ozone loss and chlorine activation in the Arctic winters 1991-2003 derived with the tracer-tracer correlations, *Atmos. Chem. Phys., 4*, 2181–2213.

Tolbert, M. A., M. J. Rossi, R. Malhotra, and D. M. Golden (1987), Reaction of chlorine nitrate with hydrogen chloride and water at Antarctic stratospheric temperatures, *Science*, *238*, 1258–1260.

Toohey, D. W., L. M. Avallone, L. R. Lait, P. A. Newman, M. R. Schoeberl, D. W. Fahey, E. L. Woodbridge, and J. G. Anderson (1993), The seasonal evolution of reactive chlorine in the Northern Hemisphere stratosphere, *Science*, *261*, 1134–1136.

Toon, O., P. Hamill, R. Turco, and J. Pinto (1986), Condensation of HNO_3 and HCl in the winter polar stratospheres, *Geophys. Res. Lett., 13*(12), 1284–1287.

Toon, O., R. Turco, and P. Hamill (1990a), Denitrification mechanisms in the polar stratospheres, *Geophys. Res. Lett., 17*(4), 445–448.

Toon, O. B., E. V. Browell, S. Kinne, and J. Jordan (1990b), An analysis of lidar observations of polar stratospheric clouds, *Geophys. Res. Lett., 17*(4), 393–396.

Toon, G. C., C. B. Farmer, P. W. Schaper, L. L. Lowes, R. H. Norton, M. R. Schoeberl, L. R. Lait, and P. A. Newman (1992), Evidence for subsidence in the 1989 Arctic winter stratosphere from airborne infrared composition measurements, *J. Geophys. Res., 97*(D8), doi:10.1029/91JD03115, 7963–7970.

Toon, G. C., J.-F. Blavier, and J. T. Szeto (1994), Latitude variations of stratospheric trace gases, *Geophys. Res. Lett.*, *21*(23), 2599–2602.

Toon, G. C., J.-F. Blavier, B. Sen, R. J. Salawitch, G. B. Osterman, J. Notholt, M. Rex, C. T. McElroy, and J. M. Russell III (1999), Ground based observations of Arctic O_3 loss during spring and summer 1997, *J. Geophys. Res., 104*(D21), 26497–26510.

Toon, O. B., A. Tabazadeh, and E. V. Browell (2000), Analysis of lidar observations of Arctic polar stratospheric clouds during January 1989, *J. Geophys. Res., 105*(D16), 20589–20615.

Traub, W. A., K. W. Jucks, D. G. Johnson, and K. V. Chance (1994), Chemical change in the Arctic vortex during AASE II, *Geophys. Res. Lett.*, *21*(23), 2595–2598.

Tuck, A., R. Watson, E. Condon, J. Margitan, and O. Toon (1989), The planning and execution of ER-2 and DC-8 aircraft flights over Antarctica, August and September 1987, *J. Geophys. Res., 94*(D9), 11181–11222.

Tung, K. K., M. K. W. Ko, J. M. Rodriguez, and N. D. Sze (1986), Are Antarctic ozone variations a manifestation of dynamics or chemistry?, *Nature*, *333*, 811–814.

Turco, R. P., O. B. Toon, and P. Hamill (1989), Heterogeneous physiochemistry of the polar ozone hole, *J. Geophys. Res., 94*(D14), 16493–16510.

Vigouroux, C., M. De Mazière, P. Demoulin, C. Servais, F. Hase, T. Blumenstock, I. Kramer, M. Schneider, J. Mellqvist, A. Strandberg, V. Velazco, J. Notholt, R. Sussmann, W. Stremme, A. Rockmann, T. Gardiner, M. Coleman, and P. Woods (2008), Evaluation of tropospheric and stratospheric ozone trends over Western Europe from ground-based FTIR network observations, *Atmos. Chem. Phys., 8*, 6865–6886.

Viscardy, S., Q. Errera, Y. Christophe, S. Chabrillat, and J.-C. Lambert (2010), Evaluation of ozone analyses from UARS MLS assimilation by BASCOE between 1992 and 1997, paper presented at 37th COSPAR Scientific Assembly, Montréal, Canada, A11-0123-08.

Voigt, C., J. Schreiner, A. Kohlmann, P. Zink, K. Mauersberger, N. Larsen, T. Deshler, C. Kröger, J. Rosen, A. Adriani, F. Cairo, G. D. Donfrancesco, M. Viterbini, J. Ovarlez, H. Ovarlez, C. David, and A. Dörnbrack (2000), Nitric acid trihydrate (NAT) in polar stratospheric clouds, *Science, 290,* 1756–1758.

Vömel, H., H. Selkirk, L. Miloshevich, J. Valverde-Canossa, J. Valdés, E. Kyrö, R. Kivi, W. Stolz, G. Peng, and J. A. Diaz (2007), Radiation dry bias of the Vaisala RS92 humidity sensor, *J. Atmos. Oceanic Technol., 24*(6), 953–963.

von Clarmann, T., H. Fischer, F. Friedl-Vallon, A. Linden, H. Oelhaf, C. Piesch, M. Seefeldner, and W. Völker (1993), Retrieval of stratospheric O_3, HNO_3 and $ClONO_2$ profiles from 1992 MIPAS-B limb emission spectra: Method, results, and error analysis, *J. Geophys. Res.*, *98*(D11), 20495–20506.

Wahner, A., R. Jakoubek, G. Mount, A. Ravishankara, and A. Schmeltekopf (1989), Remote sensing observations of daytime column NO_2 during the Airborne Antarctic Ozone Experiment, August 22 to October 2 1987, *J. Geophys. Res., 94*(D14), 16619–16632.

Wallace, J. M. and P. V. Hobbs (2006), *Atmospheric science: an introductory survey*, 2nd ed., Elsevier Inc, pp 483.

Washenfelder, R., G. Toon, J. Blavier, Z. Yang, N. Allen, P. Wennberg, S. Vay, D. Matross, and B Daube (2006), Carbon dioxide column abundances at the Wisconsin Tall Tower site, *J. Geophys. Res, 111,* D22305, doi:10.1029/2006JD007154.

Waters, J. W., L. Froidevaux, W. G. Read, G. L. Manney, L. S. Elson, D. A. Flower, R. F. Jarnot, and R. S. Harwood (1993), Stratospheric ClO and ozone from the Microwave Limb Sounder on the Upper Atmosphere Research Satellite, *Nature*, *362*, 597–602.

Weatherhead, E. C., G. C. Reinsel, G. C. Tiao, X.-L. Meng, D. Choi, W.-K. Cheang, T. Keller, J. DeLuisi, D. J. Wuebbles, J. B. Kerr, A. J. Miller, S. J. Oltmans, and J. E. Frederick (1998), Factors affecting the detection of trends: Statistical considerations and applications to environmental data, *J. Geophys. Res, 103*(D14), 17149–17161.

Webster, C. R., R. D. May, D. W. Toohey, L. M. Avallone, J. G. Anderson, P. Newman, L. Lait, M. R. Schoeberl, J. W. Elkins and K. R. Chan (1993), Chlorine chemistry on polar stratospheric cloud particles in the Arctic winter, *Science*, *261*, 1130–1133.

Wespes, C., L. Emmons, D. P. Edwards, J. Hannigan, D. Hurtmans, M. Saunois, P.-F. Coheur, C. Clerbaux, M. T. Coffey, R. Batchelor, R. Lindenmaier, K. Strong, A. J. Weinheimer, J. B. Nowak, T. B. Ryerson, J. D. Crounse and P. O. Wennberg (2011), Analysis of ozone and nitric acid in spring and summer Arctic pollution using aircraft, ground-based, satellite observations and MOZART-4 model: source attribution and partitioning, *Atmos. Chem. Phys., 12,* 237−259.

Williams, W. J., J. J. Kosters, and D. G. Murcray (1982), Nitric acid column densities over Antarctica, *J. Geophys. Res.*, *87*(C11), 8976–8989.

Williams, J. W., S. T. Jackson, J. E. Kutzbach (2007), Projected distributions of novel and disappearing climates by 2100AD. *P. Natl. Acad. Sci., 104*, 5738-5742.

Wofsy, S. C., M. B. McElroy, and Y. L. Yung (1975), The chemistry of atmospheric bromine, *Geophys. Res. Lett.*, *2*(6), 215–218.

Wolff, M. A., T. Kerzenmacher, K. Strong, K. A. Walker, M. Toohey, E. Dupuy, P. F. Bernath, C. D. Boone, S. Brohede, V. Catoire, T. von Clarmann, M. Coffey, W. H. Daffer, M. De Mazière, P. Duchatelet, N. Glatthor, D. W. T. Griffith, J. Hannigan, F. Hase, M. Höpfner, N. Huret, N. Jones, K. Jucks, A. Kagawa, Y. Kasai, I. Kramer, H. Küllmann, J. Kuttippurath, E. Mahieu, G. Manney, C. T. McElroy, C. McLinden, Y. Mébarki, S. Mikuteit, D. Murtagh, C. Piccolo, P. Raspollini, M. Ridolfi, R. Ruhnke, M. Santee, C. Senten, D. Smale, C. Tétard, J. Urban, and S. Wood (2008), Validation of HNO_3, $ClONO_2$, and N_2O_5 from the Atmospheric Chemistry Experiment Fourier Transform Spectrometer (ACE-FTS), *Atmos. Chem. Phys., 8*, 3529–3562.

Wood S., A. Goldman, P. Manning, N. Jones, J. B. Connor, and C. P. Rinsland (2000), Zephyr2: A Method for Automated Retrievals of Stratospheric and Tropospheric Molecular Constituent Profiles From Ground-Based Infrared Solar Absorption Spectra Using SFIT2, *Eos Trans. AGU*, *81*(48), Fall Meeting Suppl.

Wood, S. W., R. L. Batchelor, A. Goldman, C. P. Rinsland, B. J. Connor, F. J. Murcray, T. M. Stephen, and D. N. Heuff (2004), Ground-based nitric acid measurements at Arrival Heights, Antarctica, using solar and lunar Fourier transform infrared observation, *J. Geophys. Res.*, *109,* D18307, doi:10.1029/2004JD004665.

WMO (World Meteorological Organization), (1990), *Scientific Assessment of Ozone Depletion: 1989*, *Global Ozone Research and Monitoring Project—Report No. 20*, Geneva, Switzerland.

WMO (World Meteorological Organization), (1995), *Scientific Assessment of Ozone Depletion: 1994, Global Ozone Research and Monitoring Project—Report No. 37*, Geneva, Switzerland.

WMO (World Meteorological Organization), (1999), *Scientific Assessment of Ozone Depletion: 1998, Global Ozone Research and Monitoring Project—Report No. 44*, Geneva, Switzerland.

WMO (World Meteorological Organization), (2003), *Scientific Assessment of Ozone Depletion: 2002, Global Ozone Research and Monitoring Project—Report No. 47*, 498 pp., Geneva, Switzerland.

WMO (World Meteorological Organization), (2007), *Scientific Assessment of Ozone Depletion: 2006*, WMO Global Ozone Research and Monitoring Project–Report 50, Geneva, Switzerland.

WMO (World Meteorological Organization), (2011), *Scientific Assessment of Ozone Depletion: 2010*, WMO Global Ozone Research and Monitoring Project–Report 52, Geneva, Switzerland.

Wuebbles, D. J. (1983), Chlorocarbon emission scenarios: potential impact on stratospheric ozone, *J. Geophys. Res., 88*(C2), 1433–1443.

Wunch, D., P. O. Wennberg, G. C. Toon, B. J. Connor, B. Fisher, G. B. Osterman, C. Frankenberg, L. Mandrake, C. O'Dell, P. Ahonen, S. C. Biraud, R. Castano, N. Cressie, D. Crisp, N. M. Deutscher, A. Eldering, M. L. Fisher, D. W. T. Griffith, M. Gunson, P. Heikkinen, G. Keppel-Aleks, E. Kyrö, R. Lindenmaier, R. Macatangay, J. Mendonca, J. Messerschmidt, C. E. Miller, I. Morino, J. Notholt, F. A. Oyafuso, M. Rettinger, J. Robinson, C. M. Roehl, R. J. Salawitch, V. Sherlock, K. Strong, R. Sussmann, T. Tanaka, D. R. Thompson, O. Uchino, T. Warneke, and S. C. Wofsy (2011), A method for evaluating bias in

global measurements of CO_2 total columns from space, *Atmos. Chem. Phys., 11,* 12317–12337.

Xu, X., A.H. Manson, C.E. Meek, T. Chshyolkova, J.R .Drummond, C.M. Hall, D.M. Riggin, and R.E. Hibbins, R.E. (2009), Vertical and inter-hemispheric links in the stratosphere-mesosphere as revealed by the day-to-day variability of Aura-MLS temperature data, *Ann. Geophys., 27,* 3387-3409.

Yudin, V. A., M. A. Geller, B. V. Khattatov, A. R. Douglass, M. C. Cerniglia, J. W. Waters, L. S. Elson, A. E. Roche, and J. M. Russell III (1997), A UARS study of lower stratospheric polar processing in the early stages of northern and southern winters, *J. Geophys. Res*., *102*(D15), 19137–19148.

Yung, Y. L., J. P. Pinto, R. T. Watson, and S. P. Sander (1980), Atmospheric bromine and ozone perturbations in the lower stratosphere, *J. Atmos. Sci., 37,* 339–353.

Zander, R., P. Demoulin, E. Mahieu, L. Delbouille, G. Roland, F. Mélen, C. Servais, M. De Mazière, and M. Van Roozendael (1998), An overview of NDSC-related activities at the Jungfraujoch through high-resolution infrared solar observations, in Atmospheric Ozone: Proceedings of the XVIII Quadrennial Ozone Symposium, edited by R. D. Bojkov and G. Visconti, pp. 1005–1008, Edigrafital, Teramo, Italy.